PERFORMANCE AND WEAR CHARACTERISTICS OF A CENTRIFUGAL SLURRY PUMP HANDLING SOLID-LIQUID MIXTURES

Ph.D. THESIS

by

RAHUL TARODIYA

DEPARTMENT OF MECHANICAL AND INDUSTRIAL ENGINEERING
INDIAN INSTITUTE OF TECHNOLOGY ROORKEE
ROORKEE – 247 667 (INDIA)
SEPTEMBER, 2019

PERFORMANCE AND WEAR CHARACTERISTICS OF A CENTRIFUGAL SLURRY PUMP HANDLING SOLID-LIQUID MIXTURES

A THESIS

Submitted in partial fulfilment of the requirements for the award of the degree

of

DOCTOR OF PHILOSOPHY

in

MECHANICAL AND INDUSTRIAL ENGINEERING

by

RAHUL TARODIYA

DEPARTMENT OF MECHANICAL AND INDUSTRIAL ENGINEERING
INDIAN INSTITUTE OF TECHNOLOGY ROORKEE
ROORKEE – 247 667 (INDIA)
SEPTEMBER, 2019

INDIAN INSTITUTE OF TECHNOLOGY ROORKEE

STUDENT'S DECLARATION

I hereby certify that the work presented in the thesis entitled **"PERFORMANCE AND WEAR CHARACTERISTICS OF A CENTRIFUGAL SLURRY PUMP HANDLING SOLID-LIQUID MIXTURES"** is my own work carried out during a period from December 2014 to September 2019 under the supervision of Dr. B. K. Gandhi, Professor, Department of Mechanical and Industrial Engineering, Indian Institute of Technology Roorkee, Roorkee.

The matter presented in the thesis has not been submitted for the award of any other degree of this or any other Institute.

Dated: **(Rahul Tarodiya)**

SUPERVISOR'S DECLARATION

This is to certify that the above mentioned work is carried out under my supervision.

Dated: **(B. K. Gandhi)**
Supervisor

The Ph.D. Viva-Voce Examination of **Mr Rahul Tarodiya,** Research Scholar, has been held on……

Chairman, DRC **Signature of External Examiner**

This is to certify that the student has made all the corrections in the thesis.

Signature of Supervisor **Head of the Department**

ABSTRACT

Centrifugal pumps are being extensively used for hydraulic transportation of solids over short and medium distances through pipelines where the requirements of head and discharge are moderate. The performance and erosive wear behaviour of the pump components are the most critical design and selection parameters. An improvement in performance reduces the energy expenditure while the reduction in erosion enhances the service life.

The review of literature suggests that the efforts have been made to estimate the reduction in water performance of the pump for handling different types of solid particles and to find methods to mitigate it. Different correlations were proposed to estimate the pump performance handling slurry. Regarding the erosion of the pump components, different techniques were used to identify the zones of maximum localized wear. Two dimensional numerical modeling of the pump is generally performed to investigate the erosion of the components. The knowledge of the dominating parameters affecting the erosion of the pump components at different operating conditions is still not conclusive. There is a need to develop an understanding of erosive wear distribution of the components all along their length and width of the flow passages. The constants in the empirical models used to predict the erosion are generally varied with the properties of target material and erodent, and impact conditions.

In view of above, the present study is aimed to fill the aforementioned gaps from the experimental and numerical investigations of the performance and wear of a centrifugal slurry pump. The performance of a 50 mm centrifugal slurry pump is evaluated experimentally with solid-liquid mixture to investigate the effect of flow rate, particle size, solid concentration, and rotational speed on the performance. The slurries of fly ash-water and sand-water are used to conduct the experiments. The accuracy of the available correlations to predict the head drop due to slurry is compared with the experimentally measured data.

In search of an alternative approach to correctly predict the pump performance characteristics with solid-liquid mixture, the computational fluid dynamics (CFD) modeling of the centrifugal slurry pump model is performed using the commercial CFD code Fluent 19.0. Two modeling approaches namely Multiple Reference Frame (MRF) and Sliding mesh (SM) are used to predict the pump performance characteristics. The accuracy of predicting pump performance characteristic using the SM approach (unsteady) is found better than the MRF approach (steady). With the SM approach, a deviation below ±2.5% for complete head discharge characteristic and +5% for the complete efficiency discharge characteristic with respect the experimental data is obtained. Further, the multiphase modeling of the pump is performed

using SM approach with two models, Mixture and Eulerian-Eulerian multiphase. The equi-size particulate sand-water slurry is used for simulation. The Eulerian-Eulerian multiphase model predicted the effect of the solids on the pump performance close to the experimental results as compared to Mixture model. The obtained accuracy with Eulerian-Eulerian model for predicting the effect of solids on head and efficiency is around ±2% and ±3%, respectively. The predicted results using Eulerian-Eulerian model confirm that the head and efficiency of the pump decrease with the increase in particle size and solid concentration. The particles of high specific gravity show less reduction in head and efficiency of the pump. The effect of solids on head and efficiency ratios of the pump is not the same. The difference in head and efficiency ratios majorly depends on the specific gravity of solids. Further, the effect of variation in particle size and concentration on the flow field in the impeller and casing has also been analyzed at best efficiency point operation. Non-homogeneous suspension of particles inside the blade channels and casing passages is examined. The particulate concentration is observed higher near the impeller back shroud, pressure side of the blades, and non-suction side of the casing as compared to other locations. Furthermore, the numerical modeling of the pump is performed with multi-size solid particulate slurry to investigate the effect of variation in particle size distribution on pump performance. The numerical modeling for multi-size solid particulate slurry predicted the head and efficiency ratio with the deviation of ±2% and ±3.5%, respectively, as compared to the experiments. The predicted pump performance with different multi-size particulate slurries shows that the drop in head and efficiency increases with the increase in weight fraction of bigger size particles in the multi-sized slurry. The non-uniformity in the particle flow field inside the impeller and casing increased with the increase in weight fraction of bigger size particles in multi-sized slurry.

In the second phase of the study, erosion studies are performed in a laboratory test rig, pilot plant test setup and CFD code Fluent. A large size slurry pot tester of 270 liters capacity is used to investigate the erosion behavior of target materials namely steel 304L, grey cast iron (GCI) and high chromium white cast iron (HCWCI) in the velocity range of 9.0-18.5 m/s. The solid-liquid mixture is prepared using three different solids namely, sand, fly ash and iron ore by mixing with tap water to get 1% weight concentration. The erosion behaviour of the target materials is evaluated by varying the orientation angle from 15^{o}-90^{o}. The erosion rate (ER) in g/g of solids is found to increase with velocity having power index value varying between 2-3.5, which increases with increase in impact angle and depends on the target material and erodent. The ER of the material also increases with the increase in particle size with power index varying between 0.8-1.4 depending on the target material. Based on the generated

experimental data, empirical correlations are developed to estimate the ER of all the three target materials with three different particulate slurries as a contribution of cutting and deformation wear of the equipment handling solid-liquid mixture. The correlation developed to estimate the erosion rate (ER) of steel 304L with sand-water slurry is given as:

$$ER = ER_C + ER_{D90}\left(\sin\alpha\right)^2$$

where the cutting erosion rate (ER_c) is given as:

$$ER_C = 1.51\times10^{-11} f(\alpha) V^{2.15} d^{0.71}$$

and the deformation erosion rate (ER_{D90}) is given as:

$$ER_{D90} = 2.36\times10^{-13} V^{2.8} d^{0.98}$$

In the above expressions, V is the velocity, α is the particle impact angle, and d is the particle size.

To investigate the erosive wear profile of the pump casing experimentally and its relationship with numerically simulated flow field, experiments are conducted in a pilot plant test rig with two equi-sized sand particulate slurries at two pump speeds and two flow rates. Wear specimens (1.5 x 1.5 x 0.01 cm^3) of steel 304L are affixed at fourteen different locations along the centerline of the casing wall. The erosion of the specimens is determined based on the measurement of weight loss to study the wear pattern along the casing. Further, the flow field inside the pump is numerically simulated using Eulerian-Lagrangian modeling to correlate the particle impact condition with the measured wear. Scanning electron microscopic (SEM) images of worn out samples are also examined in each case to identify the dominant mechanism of erosion at different locations of the casing. It is observed that the wear at the volute tongue is contributed by both the cutting and deformation whereas, at all other locations, the material is removed due to cutting and ploughing.

Further, the developed correlation from the pot tester data for steel 304L is used to predict the erosion of the pump casing. The predicted erosion profile of the casing centerline showed reasonably good agreement with the experiments. The numerical simulations are further performed to study the effect of particle size and flow rate on erosion rate distribution in the casing and impeller blade surface of HCWCI.

On the basis of the present experimental and numerical studies on performance and wear characteristics of a centrifugal slurry pump, the following conclusions are drawn:

- The effect of pump speed, flow rate, solid concentration, specific gravity, particle size, and particle size distribution on the pump performance is established. The head ratio

and efficiency ratio are found to be different which was found to depend on the specific gravity of solids.

- An effective multiphase modeling approach to predict the pump performance characteristics using equi-size and multi-size particulate slurry is determined. The particle motion inside the wetted passage of the pump components is established.
- The effect of impact angle, particle size and velocity on erosive wear of steel 304L, GCI and HCWCI is established. CFD based empirical correlations are developed to estimate the erosion rate of the above target materials in the velocity range of 9.0 to 18.5 m/s with sand, fly ash and iron ore particulate slurry as contribution of cutting and deformation wear.
- The numerical modeling of the pump with the empirical correlations developed from pot tester data showed reasonably accurate prediction of casing erosion profile. The effect of particle size and flow rate on the erosion rate distribution along the length and width of the casing and impeller blade passages are established.

ACKNOWLEDGEMENT

Completing my Ph.D. degree has been probably the most challenging activity of my life. This would not have been possible without the valuable contributions of a number of people over the duration of my degree. Therefore, it is an honour for me to acknowledge their support and encouragement.

Foremost, I would like to thank my supervisor, **Dr. Bhupendra Kumar Gandhi**, Professor and Head of the Department of Mechanical and Industrial Engineering, Indian Institute of Technology Roorkee. I am extremely fortunate to have an advisor who guided me all the times when my steps faltered and acted as my mentor and guardian for last four and half years. He has been supportive since the first day I started my research work at IIT Roorkee. His extensive knowledge in the field, timely help, and constructive criticism raised my standards. My learning from Prof. Gandhi is not only confined into research. I strongly believe my experience of working under him will be an asset for the upcoming phases of my life.

I wish to acknowledge the Ministry of Human Resources and Development (MHRD), Government of India, for financial support in the form of monthly stipend to meet the living expenses.

I wish to sincerely thank my faculties at SGSITS Indore, especially, Dr. B.S. More, Mr. Pranabesh Ganai and Mr. Ashok Atulkar for their encouragement and suggestions to enroll for Ph.D. as well as the continuous interactions.

I express my sincere thanks to Dr. A.K. Sharma and Dr. Ankit Bansal for teaching me the subjects during the Ph.D. course work namely Friction and Wear, and Computational Fluid Dynamics (CFD), respectively, which gave me the confidence to work in this field.

I am very much thankful to the wonderful staff of the Fluid Mechanics and Machinery Laboratory and Slurry Research Laboratory, MIED namely, Inderpal Sharma Ji, Vijay Singh Ji, Shamsher Singh Ji, Akshay Kumar and late Babu Ram for their help with my experiments.

I would like to thank my friend Shrikant Jakhetiya, Senior Manager, Reliance Rosa Plant, for arranging fly ash from NTPC Dadri. I am thankful to Bhandari Foils Ltd. Dewas, and Divine Engineering, Bhagwanpur for providing the target materials for conducting experiments on erosion. I am thankful to Piyush Bhai (M.K. Mechanical Works, Roorkee) for his timely help in fabrication work during experimentation.

I would like to give special thanks to Mr. Subodh Khullar for helping me in the entire duration of the work. I really appreciate your time, support and cooperation.

I wish to thank all my friends and colleagues for their moral support and camaraderie to help keep things in perspective. I would like to specifically thank Dr. Manish Chauhan, Dr. Rajesh Kumar, Dr. Vikas Verma, Mr. Kamal Raj Sharma, Mr. Subodh Kumar, Mr. Sandeep Kumar, Mr. Shubham Sharma, Mr. Rohit Sahu, Mr. Jesim Hashmy, and Mr. Prince Kumar for their continuous support during best and worst moments of my doctoral journey.

I would like to express my reverence and great admiration for my parents **Shri Kailash Chandra Tarodiya** and **Smt. Kavita Tarodiya** for their blessings and endeavour to keep my moral high. I am grateful to my wife **Swati** for her sacrifices, patience, belief and encouragement in the successful completion of the present work. I am thankful to my brothers and sisters for their persistent encouragement and support.

At last, I would like to thank the almighty and all who have directly or indirectly helped me during the period of the present work.

I dedicate this Ph.D. Thesis to my parents.

RAHUL TARODIYA

TABLE OF CONTENT

LIST OF TABLE

LIST OF FIGURE

NOMENCLATURE

A	projected area of the particle, m^2
A_s	exposed surface area of the wear specimen, m^2
A_1	shifting coefficient
C_D	weighted mean drag coefficient
C_L	lift coefficient
C_V	volume concentration of solids, in fraction
C_{vm}	coefficient of virtual mass force
C_W	weight concentration of solids, in fraction
$C_{1,2,3\ldots}$	constants
D	diffusivity, m^2/s
D_2	impeller exit diameter, m
ER	erosion rate, (g/ g of solids)
ER_C	erosion due to cutting, (g/ g of solids)
ER_{Cmax}	maximum erosion rate due to cutting, (g/ g of solids)
ER_D	erosion due to deformation, (g/ g of solids)
ER_{D90}	erosion due to deformation at normal impact angle, (g/ g of solids)
E_w	wear in mm per year
F_s	particle shape factor
H	net head developed by the pump, meter of fluid column
H_B	hardness, (HB)
H_{vt}	hardness, (Hv)
$\bar{\bar{I}}$	identity tensor
I_{2D}	second invariant of the deviatoric stress tensor for solid phase
K	velocity component normal to surface below which no erosion takes place, m/s
K_H	head reduction factor
K_s	fitting erosion constant
$K_{(s/t)}$	a constant (equal to 0.42, 1.0, and 1.83 for $H_{vs}/H_{vt} \leq 6$, from 6 to 12.3 and $\geq$ 12.3, respectively)
K_η	efficiency reduction factor
$K_{1,2,3\ldots}$	proportionality constant
M	momentum exchange coefficient
N	pump speed, rpm
N_s	pump specific speed = $\frac{N\sqrt{Q}}{(H)^{3/4}}$ where Q is in m^3/hr
P	power, watts
P_p	particle overall perimeter of the projection, m
Q	flow rate, m^3/s
Q_r	flow ratio (ratio of delivered rate to the discharge rate at BEP)
Ri	constant for impact angle function
Re_p	particle Reynolds number
Re_s	relative Reynolds number
S	specific gravity
S_M	source term
S_d	scalar measure of deformation tensor
S_{ij}	strain rate tensor
T	torque input to pump shaft, N-m
U_2	peripheral velocity at impeller outlet, m/s

V	velocity, m/s
V_R	exit velocity from pump, m/s
V_{dr}	drift velocity, m/s
V_{f2}	flow velocity of solids at impeller exit, m/s
V_r	relative velocity, m/s
Vr,s	terminal velocity for the solid, m/s
V_{r1}	residual parallel component of particle velocity at small angles of attack
V_{sf}	slip velocity, m/s
V_{w2}	tangential velocity component at impeller exit, m/s
V'	reference impact velocity
W	unhindered particle settling velocity, m/s
W_L	mass loss, g
W_T	wear, grams
W_{c1}	cutting wear one, cm^3
W_{c2}	cutting wear two, cm^3
X	static head, meter
Y	potential head, meter
d	diameter of secondary phase
d_{wm}	weighted mass diameter, µm
d_{wn}	weighted mean diameter, µm
d_{50}	median diameter, µm
d'	reference particle size
e_{ss}	coefficient of restitution for particle collisions
f	maximum value of f(α)
f(α)	particle impact angle function
g	acceleration due to gravity, m/s^2
g_{0ss}	radial distribution function of solid phase
h	head loss due to flow phenomenon, meter of fluid column
Δh	additional head loss due to flow of slurries, meter of fluid column
k	turbulent kinetic energy, m^2/s^2
k_F	ratio of vertical to horizontal force component on particle
m	mass of particle, kg
n_s	dimensionless pump specific speed
$n_{1,2....}$	impact condition constant
p	pressure, pa
p_σ	constant plastic flow stress
q_n	flow rate characteristic number
sH	specific head
sP	specific power
sQ	specific flowrate
t	time, seconds

Greek Symbols

α	impact angle, degree
α_{s0}	impact angle at which horizontal velocity component has just become zero when particle leaves body, degree
α_0	transition angle, normally set as 15 degree
α_1	impact angle at which wear develops, degree
α_{max}	impact angle for maximum wear, degree
β	volume fraction
βs,max	maximum volumetric static settled concentration, fraction
γ	constant

$\dot{\gamma}$	shear rate, s^{-1}
γ_2	blade outlet angle, degree
δ	deformation wear factor, the amount of energy needed to remove unit volume
λ_s	bulk viscosity of solids, kg/m-s
θ	impact angle, degree
ρ	density, (kg/m^3)
ω	angular velocity, rad/s
μ	dynamic viscosity, kg/m-s
μ_t	turbulent viscosity, kg/m-s
μ_{eff}	effective viscosity, kg/m-s
μ_s	shear viscosity, kg/m-s
υ	kinematic viscosity, m^2/s
ε	turbulent dissipation rate, m^2/s^3
τ	shear stress, Pa
τ_y	yield stress, Pa
$\bar{\bar{\tau}}$	viscous stress tensor, Pa
$\bar{\bar{\tau}}_t$	Reynolds stress tensor, Pa
η	efficiency, %
η_p	plastic viscosity, Pa-s
Θ_s	granular temperature of solid phase, K
ϕ	internal friction angle taken as 30^o
σ_{sf}	dispersion Prandtl number taken as 0.75
χ	cutting wear factor, the quantity of energy needed to scratch out unit volume
ξ_h	head transformation ratio
Ψ	pressure index
Ψ_1	ratio of depth of contact to depth of cut

Subscripts

d	discharge
f	fluid
i	input
l	leakage
m	mixture of solid-liquid (slurry)
o	output
p	pump
q	q^{th} phase solid
s	solids
t	target material
w	water
imp	impeller
vol	volute
th	theoretical
sf	secondary flow
loc	local
suc	suction
mix	mixing
s,col	collisional part
s,kin	kinetic part
s,fr	frictional part

Superscripts

m	mixture

s	solids
w	water
β	constant, velocity exponent

CHAPTER 1: INTRODUCTION

1.1 Overview

Transportation of solids through slurry pipeline is one of the popular methods of conveying bulk solids over long to medium distances. A slurry pipeline is a two phase (i.e. mixture of solid and liquid) flow pipeline. The conveying fluid is normally water, however occasionally oil or other liquids may also be used. A slurry pipeline system inherently has a high degree of efficiency, reliability and round the year availability even for the routes over remote or difficult to traverse terrain, thus assuring continuous supply, with reduced storage cost, at the consumption point. The transportation of solids using slurry pipelines was first noticed in the mid-nineteenth century in California. The pipeline was used in placer mining operations [Abulnaga, 2002]. The interest in solid transportation using slurry pipelines was initiated in 1950's with simple tests of pumping sand and coal at moderate concentrations. Today there are several applications where slurry pipelines are used for carrying a variety of products including coal, coal-ash, limestone, copper concentrate, rock phosphate, tailings, and iron ore in many parts of the world. In India after the Second World War, slurry transportation systems were successfully installed in different coal mines [Indian Bureau of Mines, 2001]. In almost all the thermal power plants in India, slurry pipelines are being used for disposal of fly ash/bottom ash to the ash ponds [Kumar et al., 2003]. In recent years, Indian government and Indian steelmakers have shown big interest in slurry pipeline projects for the transportation of iron ore. Presently there are three operational iron ore slurry pipelines in India. Two slurry pipelines belong to Essar Steel and one to Brahmani River Pellets Ltd.

There are some other areas in which a slurry pipeline can be effectively used like in the extraction of mineral deposits from deep sea, and recycling of manure and treating sewage sludge for agriculture lands [Senapati, 2009]. There are three distinct stages in the basic slurry transportation system as shown in Fig. 1.1. The first stage is the slurry preparation stage wherein the material is procured and processed so that it becomes suitable for the subsequent stages. The second stage is the pipeline and pumps, and the third stage is the terminal stage wherein the material is prepared for eventual utilization.

The pumping unit is one of the most important components of the system. It feeds the pipeline and transmits required energy for the transportation. Pumps are broadly classified into two main categories namely positive displacement and roto-dynamic. In a positive displacement pump, a fixed volume of the fluid is positively displaced in a confined space to raise its pressure. In a roto-dynamic pump, the pressure of the fluid raises due to the action of the

rotating impeller. Roto-dynamic pumps generally possess wider flow passages for the smooth flow of solid particles. Centrifugal pump, a type of roto-dynamic pump, is mostly used in a large number of industries for small and medium distances transportation of slurries. It is normally preferred for the higher flow, low head operations, whereas positive displacement pumps are preferred for the low flow, high-pressure applications [Jacobs, 2005]. For a given duty, the centrifugal pumps have the following advantages as compared to positive displacement pumps [Willis and Truscott, 1978; Jacobs, 2005; Fact Sheet, 2014]:

(a) Simple in construction and less expensive. Available in wide range of materials.
(b) Can handle much larger solids.
(c) Low starting torques means they are less susceptible to blockages.
(d) Valves are not required for their operation.
(e) Steady delivery rate.
(f) Lower maintenance cost.

At the same time centrifugal pumps have some disadvantages which are as follows:

(a) Single stage pump can't develop high pressure.
(b) Poor efficiency, especially for small sizes.
(c) Performance gets reduced with increasing solid concentration or fluid viscosity.
(d) Wear of components reduces the performance with time.

1.2 Centrifugal Slurry Pump

A centrifugal slurry pump is the heart of slurry transportation system. It is used to increase the hydraulic energy of the slurry due to the dynamic action of a rotating impeller in the same manner as conventional centrifugal pumps for clear liquid. It is normally used as mainline pump, and also booster pump for providing necessary suction pressure for the operation of positive displacement pumps. While a rigorous, well-defined procedure for the design of the conventional centrifugal pump is established, the process for design of the centrifugal slurry pump is still being followed as modification of the former for slurry flow. The centrifugal slurry pump comprises of a number of components as shown in Fig. 1.2 which can be broadly classified into two categories, the first is the components which are rotating like the impeller, and the shaft, and second, the stationary components like the casing, throat bush, side liner, stuffing box, and bearings. To handle the solid particles, the design of the conventional centrifugal pump is being modified suitably for ensuring the clog free operation and minimum erosion of the pump components. To achieve this, the wetted components of the pumps are usually made robust, thicker and having large flow passages as compared to the conventional

centrifugal pumps. The impeller for these pumps is generally designed with less number of vanes in order to pass the bigger size solid particles and accommodate extra vane thickness. Fewer vanes result in a flatter head-discharge characteristic of these pumps with some reduction in efficiency [Wilson et al., 1992].

1.3 Centrifugal Slurry Pumps Performance Characteristics

Centrifugal slurry pumps normally have flat head-discharge characteristics. The clear water performance of the pump is generally reduced due to the presence of solids. Reduction in small change in head may result in large change in the flow rate [Sellgren et al., 2000]. An example of shifting of the operating point of the pump due to the reduction in pump head curve with solids is shown in Fig. 1.3. There are many parameters that have been reported to affect the performance of the pump. The parameters that majorly affect the pump performance are the solid concentration, slurry rheology, particle size and shape, and particle density [Wilson, 1987].

To determine the performance of these pumps with slurry, experiments are either performed with actual slurry or empirical correlations are used to estimate the performance based on performance with water [Wilson et al., 1992]. The correlations are generally developed to calculate the additional parameters defined as under.

$$\text{Head ratio } (\text{HR}) = \frac{\text{Head developeded by slurry at a given flow rate(m)}}{\text{Head developed by water at the same flow rate(m)}} \tag{1.1}$$

$$\text{Power ratio } (\text{PR}) = \frac{\text{Input power drawn by slurry at a given flow rate (kW)}}{\text{Input power drawn by water at the same flow rate(kW)}} \tag{1.2}$$

$$\text{Efficiency ratio } (\text{ER}) = \frac{\text{Efficiency of the pump for slurry at a given flow rate}}{\text{Efficiency of the pump for water at the same flow rate}} \tag{1.3}$$

Alternatively, the decrease in head and efficiency are also expressed in terms of reduction factors. The head reduction factor (K_H) is defined as 1-HR and the reduction factor for efficiency (K_η) is defined as 1-ER.

1.4 Erosive Wear of Centrifugal Slurry Pumps

Wear is an important consideration in the design and operation of centrifugal slurry pumps due to their application for abrasive slurry handling services like mining, earth moving, cement, ceramics, foundry, metal working, power generation, chemical processing, and dredging. Wear limits the operational life, hydraulic indices and the reliability of the pumps [Roco et al., 1984]. It is evaluated as a volume loss of surface material due to corrosion, cavitation, scaling and erosion mechanisms. Amongst them, the material loss due to corrosion and erosion phenomena

are generally encountered in centrifugal slurry pumps [Gandhi, 1998]. Corrosion is an electrochemical phenomenon. It is controlled either by monitoring the pH value of the slurry or adding oxygen inhibitors, which removes the dissolved and entrained oxygen from the slurry [Wasp et al., 1977]. Erosion is defined as the progressive removal of material from a surface due to repetitive impacts of solid particles at the surface. The complete elimination of erosion is not possible although it can be controlled by identifying the causes. Erosive wear of the pump wetted components has strong dependence on (i) the flow conditions like the velocity of particle, and particle impact angle, (ii) target material properties like hardness, ductility-brittleness and toughness, (iii) solid particle properties like their shape, size, specific gravity and hardness, (iv) design of the components (v) pump operation like the slurry discharge rate and pump rotational speed, (vi) carrier fluid properties like viscosity and density, and (vii) slurry properties like amount of solids loading and its rheological behavior. The dependence of erosion on such a large number of parameters makes the erosion phenomenon quite complicated. A little change in any operating parameter may affect the damage due to erosion significantly. Investigation of detailed erosion behavior of pump components at different operating conditions is essential to quantitatively establish the erosive wear characteristic of the pump components.

1.5 Mechanisms of Slurry Erosion Wear

To understand the erosion behavior of materials, the scratches produced by solid particles on the target surface were generally analyzed. The commonly accepted erosion mechanisms are classified as: (1) Cutting (2) Ploughing (3) Extrusion and forging and (4) Subsurface deformation and cracking [Desale, 2006]. Fig. 1.4 (a-d) shows the schematic representation of these mechanisms of material removal due to the impact of solid particles. The cutting wear is associated with a portion of target material displaced in the form of chips due to shearing of the surface by the particles along their flow trajectory. The material removal showing plough marks on the target surface is related to the ploughing mechanism. It occurs due to the tangential component of the impacting force being larger than the normal component. The material is extruded (by plastic deformation) ahead of a solid particle to form a raised lip (or ridge). These lips (or ridges) remain attached to the target surface but are vulnerable to subsequent impacts. The mechanism of extrusion and forging is also termed as platelet mechanism of material removal. In this, the particle hitting the target surface creates shallow craters and spreads the target material in platelets like pieces over the adjacent craters. On further impact of particles, these platelets will be easily removed from the surface. The removal

of material due to surface deformation and crack formation is generally observed when the normal component of the impacting force is too large compared to the tangential component. The particles penetrate and indent on the target surface which produces the indentation marks and cracks on the surface. With further impacts of particles, these cracks grow and divide the surface into smaller pieces which are removed easily by the subsequent particle impacts. The mechanisms of erosive wear are majorly dependent on the surface properties and the particle impact conditions. The variation in the flow field and the impact conditions of the particles produces an uneven wear along the wetted components of the pump. It is therefore essential to understand the mechanism of slurry erosion of pump materials for different particle impact conditions.

1.6 Numerical Simulation of a Centrifugal Pump

Flow in a centrifugal pump develops complex phenomenon like boundary layer separation, secondary flows, unsteadiness etc. The interaction between the rotating and stationary components not only affects the performance of the pump but also gives rise to dynamic forces on the components.

During the last few decades, significant improvement in Computational Fluid Dynamics (CFD) is noticed. Today, it has reached the level of predicting accurate results, in relatively shorter time. The cost of CFD simulation is considerably less than that of the prototype testing. With the aid of CFD, the complex flow field inside the pump can be understood, thus simplifying the product development process of the pumps.

Although the prediction of the pump internal flow is important, numerical simulation of pumps is not easy due to the usual CFD difficulties such as: modeling of turbulence, flow separation, boundary layer, etc. [Lakshminarayana, 1991]. In addition to these, there are also certain difficulties such as:

- Extremely complex geometry: large numbers of elements are needed to develop mesh model which increases the cost of computation.
- Hydraulic energy of the fluid increases by the transfer of energy due to impeller rotation. A cascade simulation is not valid [Gonjalez et al., 2002].
- The interaction between impeller and casing needs an unsteady simulation to solve the time dependent governing equations. This can be achieved in a quasi-steady way i.e. simulating the pump to obtain the steady solution with different angular positions of the impeller. Moreover, it is much better if the numerical model can simulate the unsteady flow and rotate the impeller for each time step. However, the cost of unsteady

simulation is typically 30 to 50 times higher than that of the quasi-steady simulation [Voorde et al., 2002].

Additionally some of the difficulties observed for simulation of the pumps for the solid-liquid flows are as under:

- Increase in computational time due to increase in governing equations for each phase.
- The accuracy of the results may be affected greatly if the interaction between the particles, particle-wall and particle-fluid is not modeled carefully.

CFD simulations of conventional centrifugal pumps were studied by many investigators [Gonzalez et al., 2002; Zhou et al., 2003; Cheah et al., 2007; Barrio et al., 2011; Yuchuan et al., 2015; Jiang et al., 2016; Shukla et al., 2017] in last two decades. However, the CFD studies on centrifugal slurry pumps are very few in literature. Moreover, due to the difficulties of the task, most of these studies were performed with simplifications of the problem either in the modeling approach or in the flow characteristics.

1.7 Motivation of the Present Study

Centrifugal slurry pumps are being normally used in slurry pipelines as an economical means of transporting solids over short to medium distances. Presence of solids reduces the performance of the pump. To accurately match the pump with the pipeline system, it is necessary to know the effect of solids on pump performance. Otherwise, the pump and the system may mismatch. Due to the complex nature of the problem, difficulties were encountered for generating large experimental data on pump performance for different solid-liquid mixtures. There are limited published methods for predicting the effect of solids on pump performance. CFD modeling of the pump for handling solid-liquid mixture may help in predicting the performance characteristics and the analysis of the complex flow field inside the pump components. This has motivated the author to investigate an effective numerical methodology to simulate the centrifugal slurry pump for multiphase solid-liquid flows.

Erosive wear is an important consideration in the design of these pumps for the longevity of the pump components. The knowledge of the dominant parameters affecting the erosion may help in design and operation of the pumps. This also has encouraged the author to carry out a systematic study on the erosion of the pump.

The numerical prediction of erosion of the components is majorly dependent on the accuracy of the erosion model. It is interesting to note that the erosion models developed using the bench scale tests showed variation with the change in properties of solid particles and target material. This prompted author to investigate the erosion behavior of different pump materials and the

development of a correlation for different pump materials to numerically estimate the erosion of pump components.

1.8 Organization of the Thesis

This thesis is presented in seven chapters. The organisation of the thesis is made in the following sequence:

Chapter 1 gives an overview of slurry transportation system. The performance and wear characteristics of centrifugal slurry pump are discussed and motivation of the present work on this area is presented.

Chapter 2 presents a literature review of the studies aimed to investigate pump performance and erosive wear using experimental and numerical methods. The laboratory studies performed to investigate the effect of different operating parameters on erosion and the correlations developed to predict the erosion are also reviewed. The objectives of the present work are also outlined in this chapter.

Chapter 3 presents the experimental investigations carried out in the present work to determine the pump performance characteristics with water alone, sand-water slurry, and fly ash-water slurry.

Chapter 4 presents the numerical modeling of the pump performed to investigate the pump performance and flow field with clear water, equi-sized and multi-sized particulate slurries.

Chapter 5 presents the experimental investigations carried out using laboratory test rig namely slurry pot tester, to determine the erosive wear behaviour of three pump materials (steel 304L, grey cast iron and high chromium white cast iron) due to sand, iron ore and fly ash particulate slurries. The development of the empirical correlations for erosion prediction using CFD with the obtained experimental data is also discussed.

Chapter 6 presents the experimental and numerical investigations carried out to determine the erosive wear behaviour of the pump components.

Chapter 7 lists the conclusions drawn based on the present investigation and the scope of the future works that may be taken up further for investigation on the performance and wear of the pumps.

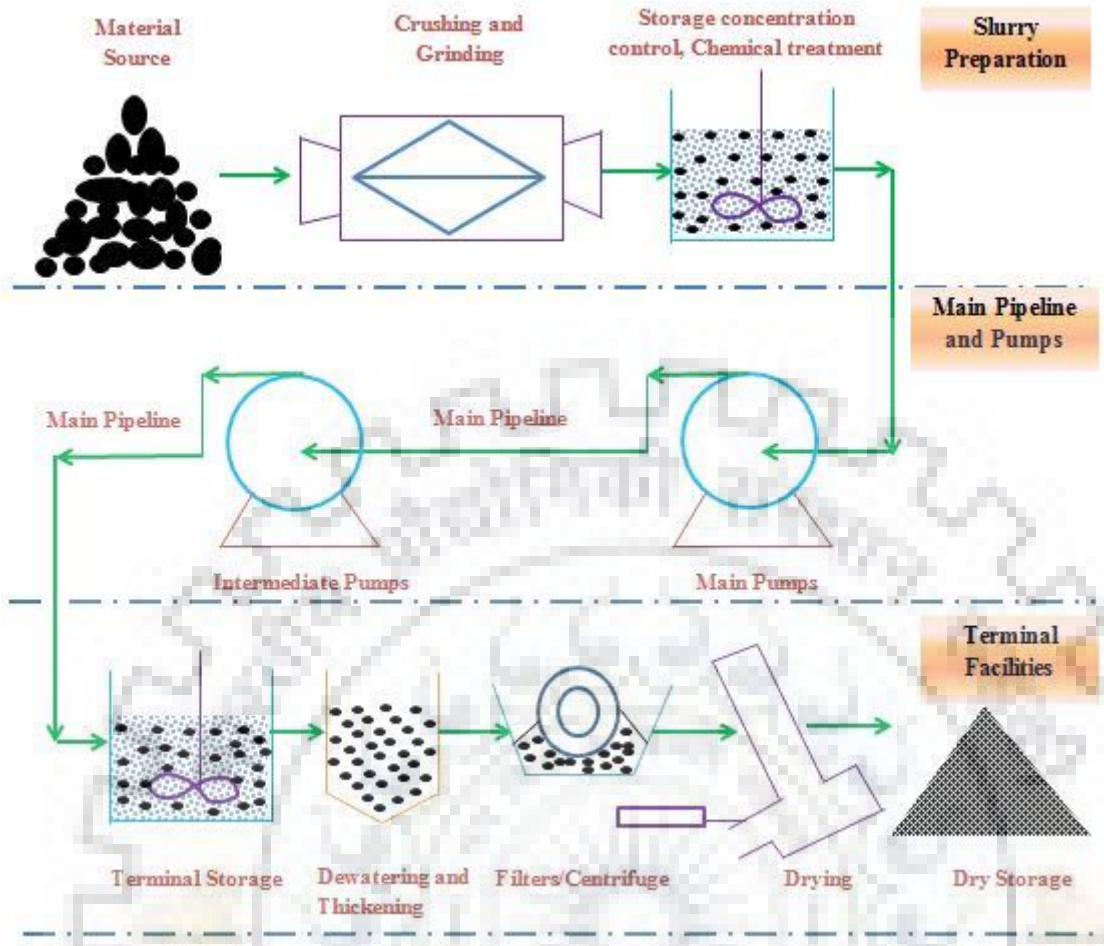

Fig. 1.1 Schematic layout of the basic slurry transportation system

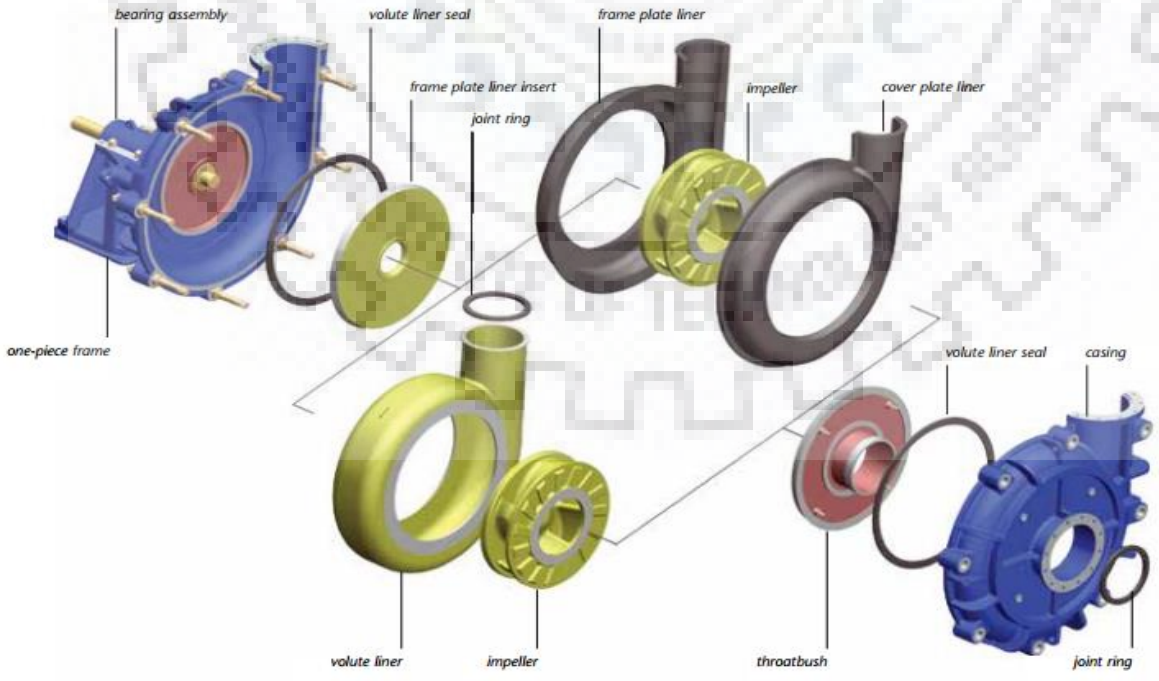

Fig. 1.2 Components of centrifugal slurry pump [Lum, 2013]

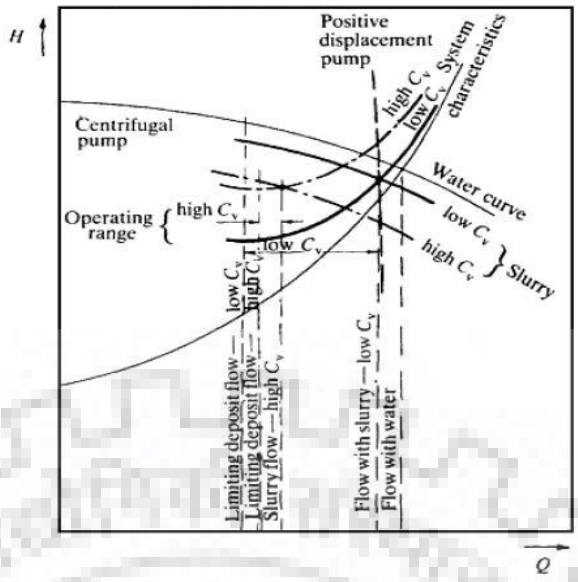

Fig. 1.3 Shift of operating point on pump head curve due to solids [Jacobs, 2005]

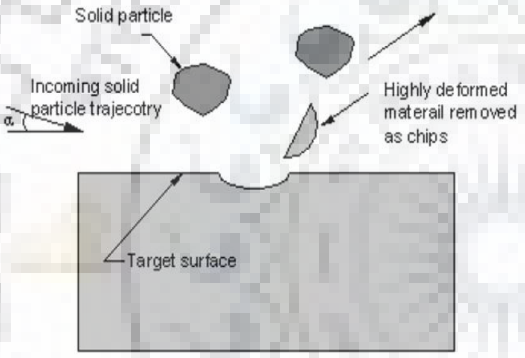

(a) Cutting erosion

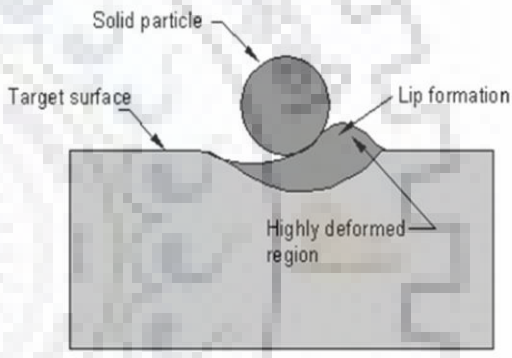

(b) Ploughing erosion

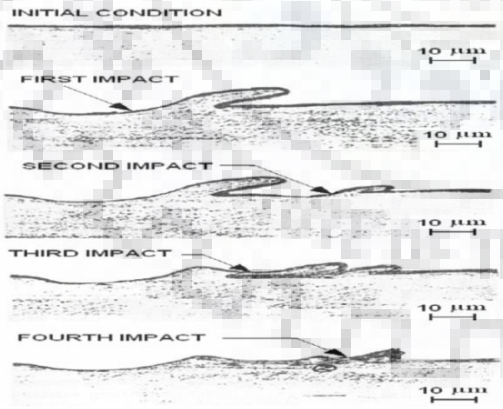

(c) Erosion due to extrusion and forging [Levy, 1986]

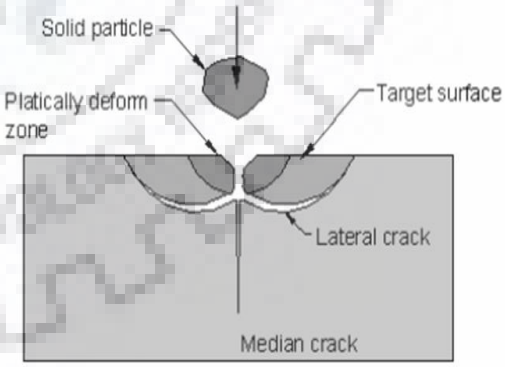

(d) Erosion due to subsurface deformation and cracking [Wensink and Elwenspoek, 2002]

Fig. 1.4 Schematic of different mechanisms of material failure due to solid particle impact [Desale, 2006]

CHAPTER 2: LITERATURE REVIEW

The performance of a centrifugal slurry pump plays an important role in the hydraulic transportation system for the trouble-free and economic transportation of solid-liquid mixtures. The performance of a centrifugal slurry pump is generally poor compared to the conventional centrifugal pump due to less number of impeller vanes, robust design, large running clearances and more thickness of the components. The performance of these pumps with water gets reduced due to the presence of suspended solids as shown in Fig. 2.1. The selection of these pumps for any application is based on two important design aspects (a) the amount of reduction in pump performance with the suspended solids, so that the correct matching of the pump to the hydraulic system can be achieved and (b) erosion resistance of the pump materials for a particular operating condition, so that its service life can be estimated. Over the years, attempts have been made to estimate the effect of solids on pump performance and erosive wear of the components. This chapter discusses some of the important experimental and numerical works conducted on the performance and wear estimation of centrifugal slurry pumps to gain an insight into the present state of knowledge.

2.1 Effects of Solids on Pump Performance

The effect of solids on the pump performance characteristics may be known a priory to minimize the energy consumption and reducing the chances of mechanical failure of the components due to high radial and thrust loads which occur when the pump operates at off-design conditions [Davidson, 1987]. Solids suspended in the liquid do not absorb, store or transmit pressure energy [Wilson, 1987]. The energy required to keep the solids suspended and to move them with the flow is imparted by the liquid [Gandhi, 1998]. Therefore, the performance of the pump is generally reduced while handling the solid-liquid mixture. Over the years, several experimental and numerical works were performed to investigate the reduction in performance of the pump due to the presence of solids.

2.1.1 Experimental Studies

The analysis of the effects of solid particles on the pump performance was initiated by Fairbank [1942]. He investigated the performance of a 3 inch centrifugal pump handling mud and suspension of two sands of median diameters of 34 μm and 800 μm. He observed that the head developed with slurry is similar to that with water for very fine size particles, but it reduces for bigger particle sizes. He found that the drop in head discharge characteristics at constant speed increased with increase in concentration and size of solid particles while the flow rate at

maximum efficiency remained unaffected. He developed an expression to evaluate the theoretical head using Euler's equation by assuming that the velocity of solid particles at impeller exit is higher than that of the water alone. He also reported that the affinity laws are applicable to the slurry pumps for change in the speed over a narrow range. The experimental work performed by different investigators namely, Mano [1955] on a 2 inch slurry pump, Hasegava et al. [1957] and Sasaki et al. [1958] on a 3 inch slurry pump, and Herbitch and Vallentine [1961] on a 4 inch slurry pump, all handling different solids, were summarized by Stepanoff [1965]. He concluded that the performance of the pump depends on the slurry rheological characteristics, particle size and solid concentration. The input power increased with increase in specific gravity of the slurry and the affinity laws for conventional pumps were also found to be applicable to the centrifugal slurry pumps. Widenroth [1970] used the cloud technique to calculate the speed of solid particles and water separately in a standard non-plugging type centrifugal slurry pump and a model-dredge pump. He injected a cloud of solid matter into the slurry and noted the time to pass it through certain distance. He observed no slip at the exit of the pump while at the inlet, the solid particles entered with slip. In order to test the performance of the slurry pumps, he used two pumps with thirteen samples of sand and gravel. He observed large variation in characteristics of the low specific speed pumps as compared to medium specific speed pumps and attributed this phenomenon to the difference in friction path of the flow inside the pump. He also conducted experiments to study the factors affecting the pump performance and proposed a correlation using non-dimensional parameters to estimate the head loss. Hunt and Faddick [1971] checked the dependency of pump performance on its size using three different size pumps handling aqueous solution of chip shaped particles and reported that the size of the pump affects the amount of head developed and efficiency. The selection of the operating point based on particle concentration was investigated by Vocaldo et al. [1974]. They reported that the total losses in the pump are contributed by pressure gradient required for carrier fluid, particle interactions and maintaining the particles under suspension. They used dimensional analysis to develop a semi-empirical correlation to predict the head reduction factor and determined the constants of the empirical correlation using experimental data of the metal and rubber-lined pumps. They used sand particles of different sizes and clay at two speeds, namely 1180 rpm and 1780 rpm. They observed that the head loss of rubber lined pump is higher than that of the metal pump due to better energy absorbing capacity of the former. They also observed that the affinity laws are applicable to the slurry pumps. Burgess and Reizes [1976] performed experiments on pump performance using the slurry of beach sand, river sand and heavy mineral particles at two speeds namely, 800 rpm and 1300 rpm. They

observed an increase in the drop of head with the increase in specific gravity of the solids. They also reported applicability of affinity laws for the pumps. They developed a correlation to predict the head reduction factor and reported its accuracy as ±5% for their experimental data. The experimental data was also used by Cave [1976] to develop a correlation for evaluating the head reduction factor. They accounted the effect of specific gravity of the particles on its terminal settling velocity and reported the variation in head reduction factor as proportional to (S_s-1). It relates to the Stokes flow where the terminal settling velocity varies as (S_s-1) for the particle Reynolds number less than one. Widenroth [1978] recommended for characterizing the solid particle with mean particle diameter for estimation of head losses. He conducted experiments at different speeds in three test loops of different pipe diameters to evaluate the pump performance for two impeller geometries and fifteen materials, mostly sand and gravels of different sizes. He reported dependency of dimensionless head capacity characteristic on the slurry concentration and the material type. Sellgren [1979] evaluated the performance of four blade rubber lined pump transporting ores and minerals at a speed of 760 rpm and 1140 rpm. Based on the experiments, he reported that the slurry with wide particle size distribution (PSD) influences the internal flow characteristic to lesser degree than the slurry of equi-size particles, and the reduction in head is independent of the pump speed. He also observed that the amount of reduction in head is equal to the reduction in efficiency up to 20% solid concentration (by weight), but at higher concentrations the reduction in efficiency is greater than that of the head. He proposed a correlation to predict the head reduction factor which shows an error of ±15% for his experimental data. Remisz [1983] experimentally evaluated the performance of centrifugal pump at 1480 rpm and 1720 rpm for handling fine particulate slurries ($d_{max} < 0.2$). He found that the head developed, efficiency and the flow rate at best efficiency point get reduced with increase in density of the mixture. He also proposed a correlation in terms of non-dimensional flow rate and mass density of the mixture to estimate the pump performance for solid-liquid mixtures. Walker and Goulas [1984] evaluated the performance characteristics of the pump handling non-Newtonian slurries of coal/water and kaolin/water mixtures. They observed instability of the pump-system curve at low flow rates as shown in Fig. 2.2. The pump performance was affected by the apparent viscosity of the mixture and the system curve intersects the pump characteristics at two or three points at low flow rates, while at high flow rate, the performance was reduced due to plastic viscosity of the mixture. They reported that the affinity laws are not applicable to the pump handling non-Newtonian slurries. Maz [1984] investigated the effect of solid properties and concentration on the performance of the slurry pump with channel type impellers of 150 mm and 300 mm diameters transporting coal and

gravel type materials. He observed that the reduction in head was linear for handling coarse size grain material with wide PSD. They concluded that the single size of the particle was unable to characterize the wide size distribution. Chand et al. [1985] investigated the effect of additives on the pump performance. They mixed guar-gum as drag reducing polymer in fly ash, sand, iron ore and coal dust slurries, of average mean particle size between 85 and 655 μm. They observed that the head developed by the slurry pump increases continuously with the addition of polymer in the slurry. Roco et al. [1986] developed an analytical procedure based on loss analysis to evaluate the pump performance handling solids. They developed a methodology to calculate the total head from the theoretical head by deducting head losses due to friction, mixing and secondary flow in the impeller for water and solid-liquid mixture, separately. They proposed semi-empirical correlations to estimate these losses and finally developed a computer program to estimate the head discharge characteristics of the pump handling slurry. They predicted the head discharge characteristics of seven pumps of different specific speeds for transporting silica sand up to 35% volumetric concentration using the proposed methodology and reported the average discrepancies of 1–2% from their experimental data. The experimental investigation of Sellgren and Vappling [1986] with two mine tailings of weight concentration up to 60% showed that the drop in head was maximum 15% compared to clear water and the reduction in head is less compared to reduction in efficiency for weight concentrations higher than 40%. At higher concentrations, they correlated the reduction in efficiency with the pump Reynolds number and the specific speed. Wilson [1987] analyzed the field test data of slurry pump for settling slurries and reported similar behaviour as observed by Sellgren and Vappling [1986] for reduction in head and efficiency. They also observed no change in the position of best efficiency point (BEP) for pumping settling slurries and reported that reductions in head and efficiency are independent of the flow rate, pump rotational speed, pump size and the pump specific speed. They also found that the pump power is directly proportional to the mixture specific gravity and the affinity laws are applicable to the slurry pumps. Sellgren and Addie [1989] investigated the effect of particle size on the pump performance. They showed that the reduction in head due to larger particle size is higher for a small size pump as compared to a large size pump. They also observed that the reduction in head is independent of the pump speed but depends weakly on the flow rate. In a further study, Sellgren et al. [1990] reported that the drop in head increases linearly with increase in weighted solid concentration up to 45% to 50%. The weighted mean diameter of particles was reported as a better choice to represent multi-sized slurries as compared to d_{50} for estimation of pump performance. Gahlot et al. [1992] investigated the performance of metal and rubber lined

centrifugal slurry pumps at 1450 rpm, using closed and open type impellers for transporting coal (S_s = 1.48, d_{50} = 900 μm) and tailing materials (S_s = 2.85, d_{50} = 170 μm). They observed that the reduction in head and efficiency is independent on the pump flow rate and increases linearly with increase in weighted solid concentration up to 50%. The drop in head and efficiency ratio increases with the increase in solids specific gravity. They observed large deviations in predicting the performance using existing empirical correlations compared to the experimental data which was attributed to either improper accounting of specific gravity of solids or use of d_{50} as a representative particle size. Finally they proposed an empirical correlation which showed an error of +20% and−15% in predicting the head reduction factor for their experimental data. The correlation developed by Gahlot et al. [1992] for head reduction factor was modified by Kazim et al. [1997] by conducting experiments on a centrifugal slurry pump at 1000 rpm to consider the effect of particle size, size distribution, specific gravity, and concentration. The correlation showed better accuracy of about ±10%. They also reported that the reduction in efficiency is higher as compared to that of the head which increases with increase in particle size, concentration and specific gravity of the solids. Gandhi et al. [1999a] compared their experimental results with the values of head and efficiency ratios estimated using some of the existing correlations. They reported that experimental values are function of pump speed and none of the correlation is able to predict them reasonably as shown in Fig. 2.3. In order to minimize the error band, they proposed that the pump speed may be considered as a parameter for the developing a correlation. They also found that the values of head ratio (HR) and efficiency ratio (ER) are not always equal and separate correlations are needed to estimate each one separately. Sellgren et al. [2000] studied the effect of adding clay in sand on the performance of centrifugal slurry pump using four radial vanes type metal pump and reported around 1/3rd reduction in the head loss with the addition of clay. The drop in ER was less compared to drop in HR, while reductions in both the HR and ER are equal at about 35% solid concentrations by weight. They also varied the pump speed from 500 to 900 rpm and observed that the effect of solids on pump performance is independent of pump speed. Finally they developed a correlation to evaluate the head reduction factor. The experimental work performed by Gandhi et al. [2001a] on 50 mm and 100 mm centrifugal pumps with three solid materials namely bed ash, fly ash and zinc tailings of different particle sizes showed dependency of reduction in head and efficiency on particle size and slurry characteristic. They observed higher head drop for the slurry of bed ash (S_s = 2.44, d_{50} = 135 μm) particles of low specific gravity compared to slurry of zinc tailing (S_s = 2.82, d_{50} = 145 μm) particles. They investigated the effect of adding fine particles in coarse size slurry

and reported that the losses due to presence of bigger particles reduce with addition of fine particles and increase in the pump size. Engin and Gur [2001] investigated the effect of impeller tip clearance on the performance of an open impeller pump transporting slurry. They conducted the tests for several tip clearances ranging from 1.25–8 mm. They observed that the increase in the tip clearance increases the losses. They proposed a correlation to estimate the HR for both shrouded and un-shrouded impellers within an error band of −20% to +15% for their experimental results. Gandhi et al. [2002] investigated the applicability of affinity laws to centrifugal slurry pump handling water and slurry separately. They observed that the affinity laws are applicable for water while in case of slurry, the affinity laws show good agreement only up to 20% weight concentration of solids at different pump speeds. At higher concentrations, they proposed to apply corrections in these laws. Engine and Gur [2003] compared different correlations available to predict HR using 216 experimental data of 11 different slurries. They observed that their correlation gives the lowest deviation in HR prediction compared to other correlations, and Kazim et al. [1997] correlation is the second most accurate. They found a large deviation in the prediction using d_{50} as compared to weighted mean size of the particles. The effect of slurry concentration with solids particle of washed phosphate of diameter 3 mm on the performance of six blade metal impeller pump was studied by Benretem et al. [2007]. They observed that for volumetric concentration <15%, the reductions in head and efficiency are almost equal and vary linearly with concentration. They reported that the PSD is very significant for determining the pump performance, and helps in predicting wear and selection of material for pump parts.

Yassine et al. [2010] investigated the effect of solid concentration on the performance of a shrouded impeller pump handling sand-water slurry at 2900 rpm and reported reduction in pump performance with increase in solids loading. To estimate the reduction factor at different flow rates, they proposed separate correlations depending on solid concentration (up to 15% by weight) of sand slurries. They observed that the reduction in HR and ER is independent of the flow rate and the error is within ±9% of the tested concentrations. Chandel et al. [2011] evaluated the performance characteristic of centrifugal slurry pump transporting high concentrated fly ash slurry (50% to 70% by weight). They observed that the HR and ER for the centrifugal slurry pumps at the rated speed are reduced with increase in solid concentration and are independent of pump flow rate. They also observed higher reduction in the HR as compared to the ER with increase in solid concentration. Khalil et al. [2013] investigated the effect of transporting soft slurries of aquatic weeds at different concentrations up to 18% (by weight) on the pump performance at 2900 rpm. They observed reduction in head and efficiency of the

pump with the increase of solid concentration and specific gravity. They also proposed an empirical correlation to evaluate the head reduction factor as a function of solid concentration (by weight), specific gravity and the particle size having accuracy within an error band of ±10%. Kumar et al. [2014] investigated the effect of adding fly ash in bottom ash on the performance of centrifugal slurry pump. They reported that addition of fly ash in the bottom ash reduces the viscosity of the slurry and also reduces the reduction in the head and efficiency of the pump. Salim et al. [2015] investigated the effect of size and concentration of the clinker slurry on the performance of the slurry pump at different speeds and reported that the performance of the pump is dependent on the size and concentration of the particles along with the pump speed. Mrinal et al. [2016] investigated the effect of viscosity on pump performance handling mixture of bentonite powder, water, and Na_2CO_3. They observed the reduction in head and efficiency of the pump with the increase in slurry viscosity. Wang and Qian [2017] investigated the effect of size and concentration on the performance of the double suction centrifugal pump. They reported that decrease in head increases with the increase in size and concentration of the particles.

A close scrutiny of all these experimental studies reveals that the head and efficiency of the centrifugal pump decreases whereas the input power increases with the increase of particle size, and solid concentration. The affinity laws appears to be applicable for low solid concentration and may need corrections at higher solid concentrations for Newtonian slurries, however these laws are not applicable for handling non-Newtonian slurries. The effect of PSD and solid specific gravity on pump performance is still not conclusive. Theoretically the understanding of the effect of particle's specific gravity on pump performance is related with the effect of the specific gravity to the terminal settling velocity of the particles. It is observed that investigators [Vocaldo et al., 1974; Burgess and Reizes, 1976; Sellgren, 1979; Gahlot et al., 1992; Kazim et al., 1997, Gandhi et al., 2001a] found difficult to get an individual effect of solids specific gravity by keeping other operating parameters constant in the experiments. The pump performance may be improved either with the addition of finer particles in the coarse size slurry or by changing the rheological characteristic of the slurry [Chand et al., 1985; Chandel et al., 2011]. The proper size consideration of the particle is necessary for the correct estimation of the pump performance [Maz, 1984; Sellgren et al., 1990; Gahlot et al., 1992; Kazim et al., 1997; Gandhi et al., 2001a; Engin and Gur, 2003]. Many semi-empirical and empirical correlations were proposed to evaluate the pump performance. A summary of the available empirically and semi-empirical correlations is listed in Table 2.1.

2.1.2 Numerical Studies

CFD based approach is being increasingly used nowadays for investigating the solid-liquid flows. It allows investigating the three dimensional multiphase flow over a wide range of operating conditions, which is difficult with the experiments due to time, labour and complexity of the problem. A summary of the detailed modeling strategies adopted for the simulation of centrifugal pumps for handling solid-liquid mixture is presented in Table. 2.2. It is seen that the effect of solids on pump performance was predicted for a wide range of solid properties and concentrations. Wang et al. [2012] investigated the effect of particle concentration on the performance of the slurry pump transporting equi-size particles. At high volumetric concentration, they observed that the reduction in pump performance is large due to increase in friction losses and the collision between the particles and particles with impeller surfaces. Li et al. [2012] analyzed the effect of increase in size of equi-size particles along with volumetric concentration of solids. They reported that the reduction in head generation is increased with increase in particle size and flow rate except at the maximum flow rate. The particle volume fraction (PVF) had more impact on efficiency as compared to particle size. With increase in PVF, the maximum limit of flow rate was reduced and the BEP was shifted towards the low flow rate. Zhang et al. [2013] analyzed the effect of particle size, volumetric concentration and particle density on a low specific speed pump performance. They observed dominant effect of particle size and concentration on the pump performance as compared to the particle density.

Numerical studies conducted to investigate the effect of solids on pump performance with wide range of particle properties showed that the estimation of the pump performance with solids through simulation is an economic and effective tool to compliment the experimental studies. However, it is seen that the accuracy of the multiphase numerical modeling of the pump is not reasonable to determine the effect of solids on the pump performance. The large deviation in the predicted pump performance using CFD with the experimental studies may be attributed to the selection of the multiphase model and the approach to model the pump for numerical simulation like steady or unsteady. Most of the simulations were carried out with steady state modeling of the pump using 'Mixture' multiphase model [see Table 2.2]. It is also observed from the numerical studies that these are mainly focused to estimate the effect of solids on the pump performance. Since, the design of the centrifugal slurry pump is different compared to the conventional pumps, the flow characteristics inside the former may not be similar to the conventional centrifugal pumps. Therefore, the knowledge of the flow field and particle flow

behaviour inside the pump flow passage is desirable to improve the performance and to mitigate the erosion wear of the components.

Also, equi-size particles were used for simulation whereas the actual slurry comprises of particles with size variation up to three orders in magnitude. It is observed that the PSD affected the pump performance and hence to get the reasonable accuracy in the predicted results, the representative diameter of multi-sized slurry need to be identified.

2.2 Solid Particle Erosion of Centrifugal Slurry Pumps

Erosion of wetted components of the pump is a major concern associated with the hydraulic transportation system [Truscott, 1972]. The measurement of material loss due to erosion during field test requires a long period of operation. Generally experiments in the pilot plant test rig are performed to investigate the erosion behaviour of the components handling solid-liquid mixture. Due to the complexity of different pump components, it is not possible to effectively evaluate the material loss due to erosion for each component at different operating conditions for different combinations of slurry and target materials. Various techniques were used to analyze the erosion of the pump components namely, paint wear method [Widenroth, 1970; Roco et al., 1984], measurement of reduction in the wall thickness [Widenroth, 1993; Walker et al., 1994; Wood et al., 2004], the weight loss measurement of individual components [Rayan and Shawky, 1989; Gupta et al., 1995; Padhy and Saini, 2011] or wear pieces fixed inside the geometry through suitable arrangements [Mishra et al., 1998; Gandhi et al., 2001b], or pasting thin wear samples inside the flow passages [Padhy and Saini, 2012; Zeng et al., 2014], and numerical simulation using the erosion models developed through accelerated wear test rigs [Minemura and Zhong, 1995; Roudnev et al., 2009; Pagalthivarthi et al., 2013; Noon and Kim, 2016]. The major components of the pump which fail due to erosion are the impeller and the casing [Wilson, 1973]. The experimental and numerical studies have been performed to determine the zones of erosive wear along the wetted region of different pump components and also the factors affecting it.

2.2.1 Experimental Studies

Widenroth [1970] experimentally determined the erosion of the impeller and the pump casing using paint wear method. He reported that due to increase in grain size, the point of wear gradually moves from suction to the pressure side of the blade and with the increase in flow rate, the point of wear shifted from inlet to the outlet of the pump. He also reported that the increase in material loss of softer material was comparatively less at high impact angle. Mueller

et al. [1978] evaluated the erosion by measuring the depth of material loss of the test specimens affixed inside the pump casing and correlated their results with the erosion rate of test specimens used in simple impingement type laboratory test setup. They selected eight different materials mostly used in coal slurry pumps for the investigation, which also covered wide range of hardness. They observed that the cemented tungsten carbide (K-703) showed better wear resistant properties amongst all the material tested. They recommended hard facing materials for the volute wall and impeller flow passage surfaces due to their good wear resistance characteristic at low impingement angles. Read [1982] used an ultrasonic device to measure the reduction in casing wall thickness due to erosion wear of large dredge pump running in a sand mining operation. He reported the region along the periphery of the casing where most of the erosion took place. In the outer vanes of the impeller, he observed deep pits and proposed to evaluate the localized and irregular wear to capture the pits. Roco et al. [1984] applied thin layer of polyamide and epoxy resin materials to determine the wear inside the pump components. They selected three different pump geometries and tested them for dilute and dense slurries of sand-water. They observed that the erosion of the pump components is contributed by directional impact, random impact, and sliding of the solid particles. The average wear rate of the casing was found higher than that of the other components which reduced with increase in the flow rate. They reported that the maximum average erosion rate of the casing along width at the rated flow rate occurred in the region between 285^{o} to 315^{o} from the volute tongue in the direction of impeller rotation. Widenroth [1984] evaluated the wear behavior of impeller through weight loss technique and also by measuring the reduction in the thickness through an ultrasonic device. He used four impellers and observed higher erosion rate for harder material at high impingement angle of the particles. This reduced the vane thickness and changed the shape of the vane. He further used weight loss technique and reported that the wear resistance of harder material impellers is higher. He also measured the wear rate inside the concentric type casing at 5 different positions and reported that the wear rate distribution along the casing wall is nearly uniform. Rayan and Shawky [1989] used weight loss technique to estimate the erosion rate of cast steel impeller for dilute slurry (2% to 4% by volume). They reported that the material loss due to erosion is similar to the loss due to cavitation at low concentration. The wear was varied with the cubic power of velocity and increased with the increase in solid concentration. Widenroth [1993] used four radial blades dismountable impeller in a model dredge pump and estimated the wear along the suction and pressure side of impeller blade by scanning through inductive displacement transducer. He reported that the minimum wear occurred at BEP. The effect of slurry flow rate and particle size on wear rate of

the pump components was evaluated by Walker et al. [1994]. They reported that the minimum wear along the pump components occurred at about 80% BEP flow rate compared to the BEP flow rate. They also reported that the material loss of impeller is large for coarse size particulate slurry which increased chances of its early failure, whereas the life of the throat bush is limited for fine particulate slurry. Gandhi et al. [2001b] measured the average mass loss due to erosion of the wear specimens to study the casing wear profile. They welded a mild steel strip inside the flow passage of the casing and fixed the straight wear samples to cover the complete casing width at different locations inside the casing. They observed that the location of the maximum wear was around 180^{o} from the volute tongue, and it did not change with the change in flow rate or solid concentration.

It is seen that very few attempts were made to determine the erosion of the pump components experimentally. It may be due to the difficulties involved in setting up the experiments to perform the wear tests in different components [Gandhi, 1998]. The studies were performed to identify the zones of maximum wear in the pump components. The average erosion data is used to analyse the components wear. The knowledge of the dominate parameters affecting the erosion of the pump components at different operating conditions is still not conclusive.

2.2.2 Numerical Studies

Due to the complexity in measurements, the erosion of pump components is also predicted using the numerical tools. These are performed to identify the zones of high erosive wear in the pump and factors affecting it.

Ahmad et al. [1986] developed a numerical code to study the internal flow field and particle trajectory along the wetted region of the impeller. They further used the code to predict the zones of the maximum wear inside the impeller. They reported that at low particle concentration, the pressure side of the blade erodes faster and location of the maximum wear is its leading edge. Roco and Addie [1987] used energy approach for simulating slurry pumps numerically through finite element and finite volume techniques. They estimated the velocity of solid particles and concentration near the wall of the pump components to predict the wear. They reported that pump geometry cab be optimized by adjusting the flow conditions and material thickness along the wetted walls. In a further study, Addie et al. [1987] compared the predicted erosion from energy approach with the field data for volute, semi-volute and annular casings along with the casing for large dredge pumps. They reported large error in predicting the absolute wear but the wear distribution profile was found similar for first three casings except the dredge pump casing. Pagalthivarthi and Hemly [1992] developed a numerical model to predict erosion inside the pump casing. They incorporated the coefficients of impact and

sliding wear in a model, developed through the laboratory test rigs, and reported over-prediction of the estimated wear values as compared to the actual measurements. Minemura and Zhong [1995] employed two-dimensional Lagrangian finite volume approach to numerically predict the erosion of a pump casing. They reported that the dominant mechanisms of erosion are deformation and cutting, and the location of maximum wear at BEP flow rate was 300^{o} from the volute tongue. Sellgren et al. [2005] estimated the wear rate at different operating conditions of the slurry pump through numerical simulations. They reported that for high specific speed pump, casing showed better erosion resistance while for low specific speed pump, the erosive wear in the impeller and the suction liner is less. Dong et al. [2009] observed different stages of material removal due to wear namely saturation wear, steady wear and sharp wear. They developed a methodology using finite element technique, and obtained the pump wear and its variation with particle size, shape and the impact angle. They reported that the vane outlet, vane inlet, internal surface of rear cover plate and the middle of the vane are the most affected region of impeller, and in the casing the most affected region is the volute tongue. Roudnev et al. [2009] predicted the wear rate along the casing using three-dimensional steady state and transient simulations using commercial CFD code Ansys CFX. They reported the need of transient simulation of the complete pump model for the better prediction of the casing wear. They reported that the zones of the maximum velocity shifted on changing the flow rate which changes the location of the maximum wear of casing wall. They also observed that the three dimensional multi-domain transient simulation predicts the wear along the casing close to the actual wear. Kruger et al. [2010] reported that the wear of impeller geometry of the pump depends on the parameters like particle impact angle, solid concentration and flow pattern, vortices and secondary flows. They used Euler-Euler approach and evaluated the erosion of the pump impeller. They observed the impact wear at the leading edge while sliding wear along the trailing edge and the side plate of the impeller. Batalovic [2010] developed a mathematical model to predict the erosion of the pump impeller and to estimate its service life. The model was used to optimize the pump operation during slurry transportation. He also proposed that the model may be used during material selection of the pump impeller. Pagalthivarthi et al. [2013] performed two-dimensional numerical simulation of the pump casing using finite element modeling. They observed that the distribution of wear is non-uniform along the casing with two local peaks. The first peak was located at the tongue and the second peak was observed in the region of 285^{o} to 315^{o} from the volute tongue. They reported that the flow conditions significantly affect the erosion profile of the casing. Peng et al. [2015] used the Euler-Lagrangian modeling approach to numerically simulate the impeller and casing

wear. They used erosion model of Finnie [1972] to evaluate the relative erosion rate and observed dependency of erosive wear on the concentration of the solid particles. They further discussed that the amount of relative wear in both the casing and impeller is generally high at low flow rate and the minimum for the pump operating at BEP flow rate. They also reported that the amount of relative wear of the casing surface was higher than that of the impeller surface. Noon and Kim [2016] performed steady three dimensional frozen rotor simulation of a centrifugal slurry pump for handling lime slurry using the Euler-Lagrangian model of Ansys CFX. They estimated the average erosion rate over the width of the volute casing at different angular locations to show the effect of particle size and concentration. They observed two local peaks in the erosion profile under different operating conditions. First was at the tongue of the casing and second was at around 265^{o} from the tongue. Recently, Dong et al. [2019] performed steady three dimensional frozen rotor simulation of double suction centrifugal pump to estimate the slit erosion behavior of the pump impeller. They predicted the zones of maximum erosion on impeller blade surfaces and compared them with experimentally obtained results using paint wear method. They reported that the variation in particle size significantly affect the erosion distribution on blades, whereas the variation in solid concentration only increases the magnitude of erosion.

The numerical simulation showed good agreement with the experimental result in identification of zones of the maximum wear at different operating conditions. The investigations were done based on the change in average erosion profile of the components at any operating condition. The understanding on the effect of operating condition in local changes of erosion profile of pump components may substantially help the designer for mitigation of erosive wear of the components.

2.3 Parameters Affecting Slurry Erosion of Materials

Studies on erosive wear in the field or pilot plant require a long period of operation, large amount of material and labour work. To overcome these problems, researchers have developed an alternate method to evaluate the erosion of materials using accelerated laboratory test rigs [Rohnisch and Vollmer, 1970; Barker and Truscott, 1974; Roco et al., 1984]. Testing under conditions of accelerated erosion is well accepted for comparing the relative erosive wear behavior of different materials [Koirala et al., 2017]. It also helps to understand the mechanism of erosive wear of material at different operating conditions. Over the years various erosion studies were performed using different wear test rigs [Javaheria et al., 2018]. A summary of the experimental studies performed using laboratory test rigs to investigate the erosion is listed in

the Table 2.3. It gives the information about the type of test rig used by the investigators, details of the erodent and target materials, ranges of different parameters studied, and some major outcomes of the work.

It is seen that the two test rigs are generally used in literature: (a) Slurry jet impingement tester (JIT) [Elkholy, 1983; Turenne et al., 1989; Lin and Shao, 1991a; Burstein and Sasaki, 2000; Divakar et al., 2005; Nguyen et al., 2014] and (b) Slurry pot tester [Tsai et al., 1981; Bree et al., 1982; Clark, 1991; Gupta et al., 1995; Gandhi et al., 2003; Desale et al., 2005; Lindgren and Perolainen, 2014; Rawat et al., 2017]. In a slurry jet impingement tester, a flat specimen is subjected to a jet of solid-liquid mixture [Zu et al., 1990]. The erosive wear of the materials can measured at different impact angles by orientating the specimen in the desired direction in the range of 0^o to 90^o. In a slurry pot tester, generally two cylindrical test specimens were rotated in a pot containing solid–liquid mixture and the average mass or thickness loss of the specimens is measured to evaluate the wear [Clark, 1991; Gupta et al., 1995]. Gandhi et al. [2003] modified the available design of the pot tester. They used flat specimens and made provision to orient them from 0^o-90^o in the direction of flow to determine the effect of impact angle on erosion behaviour of flat brass specimens at 3.48 m/s and 8.18 m/s. Desale et al. [2005] further modified the design proposed by Gandhi et al. [2003] by inserting a propeller from the tank bottom and rotated it independently to obtain the uniform suspension of solid-liquid mixture during test. Using the modified design, Desale et al. [2006] have reported the erosion of ductile materials in the velocity range of 3-8 m/s. For the measurement of erosion at higher velocities Gandhi [2015] further modified the design of slurry pot tester to evaluate the erosive wear of materials for the impact velocities up to 32 m/s.

2.3.1 Particle Size

The solid properties that predominantly affect the erosion of the target materials are the shape, size and hardness [Al-Bukhaiti et al., 2016]. Particle size is one of the critical parameters that affect the erosion of the materials. It is generally observed that the thickness of the pump components due to erosion reduces more with the increase in particle size [Addie et al., 1987]. Some of the investigators [Desale et al., 2009; Abouel-Kasem, 2011] proposed a power law relationship between erosive wear and particle size as below,

$$\text{Erosion rate } \alpha \text{ (particle size)}^n \qquad (2.1)$$

Some other investigators [Iwai and Nambu, 1997; Nguyen et al., 2016; Lin et al., 2018] reported that the erosion increases with particle size up to a particular size and then decreases with further increase in the size based on experiments with JIT. Nguyen et al. [2016] reported that the effect of particle-particle interactions dominated for the bigger particle size in JIT

which decreases the velocity of particles impacting on the target material for bigger particles and thus reduces the erosion. Apart from the laboratory test rig, difficulties are also encountered to perform experiments with completely uniform size particles for investigation of particle size effect [Clark and Hartwich, 2001].

In literature [Gupta et al., 1995; Gandhi and Borse, 2004; Desale, 2006] the representative size of samples of non-uniform size particles is generally be taken as either mean, median, weighted mean or weight mass diameter which are defined as (a) Mean diameter is the the average of minimum and maximum size of particles present in the solid samples. (b) Median diameter (d_{50}) is the size of the sieve through which 50% of solid particles will pass. (b) Weighted mean diameter (d_{wn}) is the equivalent size of particle having an average weight of all the particles present in the samples. It is expressed as

$$d_{wn} = \sum_{i=1}^{N} f_i d_i \tag{2.2}$$

Where N is the total number of size groups, f_i is the fraction of solids in each size groups and d_i is the average diameter of two successive sieve sizes, one on which the solids are retained and the other through which it passed completely.

(c) Weighted mass diameter (d_{wm}) is based on the weighted average mass of all the particles available in the sample. It is expressed as

$$d_{wm} = \left\{ \sum_{i=1}^{N} f_i d_i^3 \right\}^{1/3} \tag{2.3}$$

Gandhi and Borse [2004] performed the experimental investigations to determine the most appropriate representative particle size for multi-size particulate slurry. They found that the predicted erosion rate with weighted mass diameter was close to that observed with multi-size solids slurry.

Some investigators [Desale et al., 2009; Abouel-Kasem, 2011] determined the effect of particle size on the variation in erosion rate of target materials and its mechanism using mean size solids samples. Misra and Finnie [1981] observed that the extent of particle size affects the erosion of materials which further depends on the properties of the target surface. Lynn et al. [1991] investigated the effect of particle size with SiC particles on the steel specimen. They concluded that the erosion rate of the material for the particle size greater than 100 µm is proportional to the kinetic energy of the impacting particle whereas, for smaller size particles (< 100 µm), it is higher. Desale et al. [2009] also reported the critical particle size as 200 µm for the erosion of Aluminum. They reported that higher erosion by smaller particles is associated with the change in the mechanism of material removal from impact erosion to three-

body abrasion. Iwai and Nambu [1997] reported the critical particle size for elastomer, polyurethane, and rubber as 208 μm, 91 μm, and 42 μm respectively, using jet impingement tester. Abouel-Kasem [2011] reported the critical particle size as 200 μm for 5117 steel and the erosion below this size is less than that of the erosion predicted by a power law correlation. He reported that the reduction in erosion by smaller particles is associated with the change in the mechanism of material removal from ploughing to indentation.

2.3.2 Particle Shape

The particle shape is another important parameter affecting the erosion of materials. Variation in particle shape may change the power law exponent of particle size [Desale, 2006]. Salik et al. [1981] reported that the variation in particle shape can change the erosion value by an order of magnitude. To estimate the particle shape effect, Cox [1927] specifies the parameter, namely 'Shape Factor' to quantify the particle shape. It is also known as circularity. It is defined as the ratio of the projected area of the particle (A) to the overall perimeter of the projection (P_p) as under:

$$\text{Shape Factor} \qquad \text{S.F.} = \frac{4\pi A}{P_p^{\,2}} \tag{2.4}$$

The shape factor of the particles ranges from 0 to 1, where 1 represents the circular shape of the particles, and lower values represent the deviation of the particles from circularity. Levy and Chik [1983] investigated the effect of particle shape on AISI 1020 carbon steel. They reported that the angular particles were four times more erosive than the rounded or spherical particles. Desale et al. [2006] investigated the effect of particle shape on erosion of ductile materials due to cutting and deformation. They observed that the mechanism of cutting wear was more affected by the particle shape as compared to the deformation wear.

2.3.3 Hardness of Erodent and Target Material

It is generally observed that the erosion rate increases with the increase in hardness ratio i.e. the ratio of erodent hardness to the target material hardness. This increment is up to a certain value of hardness ratio beyond which the effect may not be significant [Levy and Chik, 1983; Elkholy, 1983; Sundararajan and Roy, 1997; Desale et al., 2008]. This is attributed to the fact that the particles of higher hardness show less tendency to break up during impact whereas break up and adherence of soft particles to the surface reduce the kinetic energy which decreases the erosion rate [Levy and Chik, 1983]. Elkholy [1983] determined the functional relationship of hardness ratio with erosion rate using the four different target materials of hardness ranging from 150 to 400 HB and particles of silica sand of hardness 710 HB. He used

power law correlation to correlate the hardness ratio with erosion rate and reported the power law index of hardness ratio of 3.82 up to the transition limit of 1.9 and beyond that limiting ratio as 0.27. Shipway and Hutchings [1996] also examined the effect of erodent and target material on erosion behaviour. They reported that the increase in hardness ratio toward unity rapidly increases the erosion rate and reduces the velocity exponent of erosion rate. The effect of hardness ratio more than one on erosion rate was investigated by Desale et al. [2008]. They reported three regions of hardness ratio in which the erosion rate remains almost constant under normal impact condition. The three regions of hardness ratio were as 4.2–5.2, 6.9–12.1 and 12.5–27.5.

2.3.4 Particle Impact Angle

Particle impact angle is the angle between the target surface and the direction of particle velocity during impact. It is generally agreed that the erosion rate is also a function of particle impact angle. Based on the dependence of erosion of material with impact angle, the materials are characterized as ductile or brittle. For ductile materials, the maximum erosion rate is generally for the impact angle between 15^{o}-40^{o}, whereas for brittle material, the maximum erosion rate is near to 90^{o} [Harsha and Thakre, 2007; Abd-Elrhman et al., 2014; Syamsundar et al., 2015]. Zhong and Minemura [1996] observed that for the material showing ductile erosion behaviour, the contribution of cutting to the total wear is much higher up to the angle of the maximum wear as compared to the deformation wear and beyond that angle, the contribution of cutting wear decreases with the impact angle. Desale et al. [2006] observed that for ductile materials, the angle of maximum erosion is a function of target material properties and is independent of the erodent.

2.3.5 Particle Impact Velocity

The particle impact velocity is one of the dominating factors influencing the erosion rate of materials. At higher impact velocity, even a small size particle may cause significant erosion [Rai et al., 2017]. Several studies [Lin and Shao, 1991a; Stack et al., 1996; Lindsley and Marder, 1999; Lopez et al., 2005; Oka and Yoshida, 2005; Aminul-Islam and Farhat, 2014; Syamsundar et al., 2015] were performed to investigate the effect of particle impact velocity on the erosion rate of the materials. It is generally observed that the erosion rate of materials increases with increase in the velocity and follows a power law relationship between erosion rate and velocity as shown

$$\text{Erosion rate } \alpha \text{ (particle velocity)}^{n} \qquad (2.6)$$

Where, the exponent 'n' is the power index for velocity. It varies in the range of 2-4 for ductile materials [Desale, 2006], showing the dependence of erosion on the kinetic energy of the impacting particles ($1/2\ mV_s^2$). The increase in material loss with velocity is attributed to the increase in kinetic energy of the impacting particles.

It is generally observed that the investigations to determine the effect of velocity were more focused towards the estimation of power index value for the correct prediction of erosion of materials. Finnie [1972] discussed that the variation in power index may arise due to wide variations in experimental and particle impact conditions. Lindsley and Marder [1999] also reported that the power index may relate to the experimental conditions and not the properties of target material and mechanism of erosion. Lin and Shao [1991a] observed that the power index is not constant for a material and varies with the impact angle and target material properties. Oka and Yoshida [2005] reported the variation in power index with the hardness of the target materials. Desale et al. [2011] found different values of power index for cutting and deformation of the materials. Aminul-Islam and Farhat [2014] suggested that the value of power index may depend on the mechanism of erosion. They reported that the variation in power index value with impact angle is significantly more at high impact velocity compared to low velocity.

2.3.6 Solid Concentration

In slurry erosion, the material loss is majorly affected due to the particle-particle interactions with the increase in solid concentration [Parsi et al., 2014]. The effect of particle concentration on erosion rate was investigated by many investigators [Bree et al., 1982; Clark, 1991; Gupta et al., 1995; Gandhi et al., 2003; Desale et al., 2011; Rawat et al., 2017]. Increase in solid concentration increases the frequency of particle impact on the target surface that results in more material loss from the target surface. However, the rate of material loss in terms of g/g of solids was observed to decrease with the increase in solid concentration [Bree et al., 1982; Mens and Gee, 1986; Gandhi et al., 2003; Desale et al., 2011]. This phenomenon can be attributed to the reduction in particle impact velocity with the collision of particles rebounded from the wall to the impacting particle, also known as "shielding effect", [Brown et al., 1981; Deng et al., 2005] and with the increase in particle-particle interactions at higher solid concentrations [Desale, 2006].

2.4 Erosion Models

Due to the industrial importance, several attempts were made to develop a model that can predict the erosion of materials close to the field data. Some of these studies were performed

from the data taken during experimental investigation and other studies were based on deriving the erosion model using the understanding of solid mechanics. A summary of some of the models proposed to evaluate erosion is presented in Table. 2.4. It gives the information of their mathematical form and test conditions used for their development or validation and are discussed in following sections.

2.4.1 Theoretical Erosion Models

Finnie [1960] was amongst the earliest to propose a theoretical model to predict the erosion of ductile materials based on single particle analysis. He made following assumption to derive the model from the equation of particle motion (a) the particle rotation during cutting is negligible, (b) the ratio of the depth of contact to the depth of cut is constant, (c) the particle cutting face is of uniform width and large compared to depth of cut, (d) constant plastic flow is reached upon impact of particles. The model showed good agreement with the experimentally measured erosion values at low impact angle. However, at normal impact the model gives no erosion.

Bitter [1963a] derived a model based on the hypothesis that the wear at any angle is contributed by cutting and deformation wear. The cutting and deformation wear being occurred due to tangential and normal component of particle velocity with respect to target surface respectively. He first developed a theoretical model for deformation wear of ductile materials by using the Hertzian contact theory and energy balance equation. Further Bitter [1963b] proposed two alternate models for cutting wear for the cases (a) particles that still have a tangential velocity component when they leave the target surface (W_{c1}), (b) particles with zero tangential velocity component during the collision (W_{c2}). He proposed to estimate the total wear rate as the sum of cutting and deformation wear rates. To estimate the wear from the Bitter [1963a,b] models experimental data are needed for the calculation of cutting and deformation wear coefficients. This exercise involves lengthy and complex calculations [Desale et al., 2011].

Neilson and Gilchrist [1968] derived an erosion model based on the correlations proposed by Finnie [1960] and Bitter [1963a,b] to estimate the erosion rate for ductile and brittle materials. They also suggested a simple approach to estimate the contribution of cutting and deformation wear at any impact angle. According to them, the total wear at normal impact angle was contributed only by deformation wear. The normal component of velocity needed to initiate the erosion can be neglected as it usually small compared to particle velocity. With these assumptions, the experimental data at normal impact angle can be used to determine the deformation wear coefficient. By assuming the constant value of deformation wear coefficient for other impact angles, the contribution of cutting wear is also estimated.

2.4.2 Empirical Erosion Models

Different empirical models were proposed by many investigators [Elkholy, 1983; Ahlert, 1994; Haugen et al., 1995; Gupta et al., 1995; Gandhi et al., 1999b; Zhang et al., 2007; Desale et al., 2011; Okita et al., 2012; Vieira et al., 2016] based on large experimental data generated through laboratory test rigs. It is observed that the empirical models were generated based on two approaches (a) the effect of particle-particle interaction was incorporated in the model itself using the laboratory test data (b) The effect of particle-particle interaction was not included in the model and suggested to capture it through numerical modeling. The advantage with empirical models is that they can be easily incorporated in the numerical simulations to predict the erosion.

Elkholy [1983] proposed a correlation to estimate wear of pump materials based on the size of solid particle, slurry concentration, impact angle and the ratio of hardness of the erodent and target material using JIT. For the correlation, he tested aluminium and cast iron samples with sand water slurry in the velocity range of 5 to 30 m/s and solid volume concentration up to 20%. Ahlert [1994] developed an erosion model for AISI 1018 steel using the experimental data obtained through direct impact tester. The proposed correlation was primarily used to predict the erosion in chokes, pipe, elbows, and oil and gas production equipment based on the information of particle shape, target material hardness, impact velocity, and impact angle. The model is also commonly known as E/CRC (Erosion/Corrosion Research Center) model. Haugen et al. [1995] used the generalised erosion relationship and experimentally determined the values of velocity exponent and impact angle relationship for 28 different materials covering six standard steels, ten surface coatings, and twelve ceramics and tungsten carbide materials. The correlation is also commonly known as DNV (Det Norske Veritas) erosion model and is frequently used to predict the erosion in pipelines and fittings using numerical tool. Gupta et al. [1995] proposed two correlations, obtained from data generated for equisized particulate slurries in the pot tester to predict the expected thickness loss rate for two pipe materials, namely brass and mild steel. The proposed correlations were used to predict the extent of uneven erosion in a slurry pipeline using local concentration, local effective particle size and average velocity. Oka et al. [2005] investigated the influence of parameters of erodents and target materials on the erosion behavior using sandblast type erosion test rig. They proposed a correlation for estimating erosion rate from the knowledge of the properties of erodent and target materials, impact angle and flow velocity. Zhang et al. [2007] performed the experiments in direct impact tester and proposed a new functional relationship of impact angle for E/CRC model. Desale et al. [2011] developed a correlation using the data generated for the

erosion testing of seven ductile materials (aluminum alloy, copper, brass, mild steel, AISI 304L stainless steel, AISI 316L stainless steel, and turbine blade steel) in a slurry pot tester. They proposed the correlation to evaluate the erosion rate, using separate correlation for deformation and cutting wear rate. The correlation needs the particle size, slurry concentration, ratio of target material and erodent hardness, shape factor, velocity and impingement angle of the particles to evaluate the erosion of components in slurry transportation.

Different models were developed for prediction of erosion. It is observed that the accuracy of the empirical models depends on the type of laboratory test rig used.

Once the model is developed, it can be used for different applications. However, the biggest problem encountered with the empirical models is that the constants in the models are generally fixed. However, in actual case, they vary with the properties of target material and erodent, and impact conditions. From the close scrutiny of the available erosion models, it is observed that the models were generally developed based on gas-solid erosion process for higher velocities and solid-liquid erosion for lower velocities. It was well established that the impact velocity of solid particles has a dominant effect on the erosive weight loss [Elkholy, 1983; Gandhi et al., 2003; Oka and Yoshida, 2005; Desale et al., 2011]. Hence, extrapolation of available correlations of solid-liquid mixture to high velocity for erosion prediction may incur a large error. In view of above, generally correlations developed for gas-solid erosion are used to simulate the solid-liquid erosion at high velocities [Kang et al., 2016; Khanal et al., 2016]. However the mechanism of erosion of gas-solid mixture and liquid-solid mixture is different and this assumption may be one of the reasons for large error in numerical prediction. Further the materials of construction of slurry handling equipment are varied widely depending on the service condition [Xie et al., 2015]. However, the variation in the value of constants in the model for different materials was not well studied so far which may limit the use of numerical tools for reasonable prediction of erosion of components of centrifugal slurry pump of different materials.

2.5 Objectives of the Work

Review of literature reveals that the difficulties are encountered with the experimental studies to investigate the performance and wear characteristics of the centrifugal slurry pumps. The knowledge of different parameters affecting the performance and wear behaviour of the pumps is still not conclusive. There exists a need to develop a numerical methodology that can effectively predict the performance and wear characteristics of centrifugal slurry pumps while handling solid-liquid mixture. Another important aspect is the need of an empirical correlation

that can predict the erosion of pump materials. In view of the above, the present work has been undertaken with the following objectives.

1. To experimentally evaluate the effect of properties of solids and operating conditions on the pump performance characteristics while handling solid-liquid mixture.
2. To numerically model a centrifugal slurry pump to predict the pump performance using steady and unsteady techniques. Experimentally measured data are to be used to check the accuracy of the modeling technique.
3. Investigate an effective CFD model for carrying out the multiphase simulations of a centrifugal slurry pump for handling equi-sized and multi-sized slurries.
4. To experimentally evaluate the erosive wear behaviour of different pump materials with different slurries under different operating conditions in a high speed slurry pot tester and to develop an empirical correlation for prediction of erosive wear of the pump materials.
5. To perform the experiments for evaluating the erosion behaviour of a centrifugal slurry pump casing and its variation with respect to particle size, flow rate and pump speed.
6. To numerically model the pump for predicting the erosive wear of its components and identifying the factors affecting the wear zones.

Table 2.1: Available correlations for estimation of head reduction factor of centrifugal slurry pump

Investigator(s)	Existing Correlation for Head Reduction Factor "K_H"
Fairbank [1942]	$\dfrac{\left[1-\dfrac{(1-C_V)}{S_m}\right]-S_sC_V\left(U_2-V_{f2}{}^{s}\mathrm{Cot}\gamma_2\right)}{S_m\left(U_2-V_{f2}{}^{w}\mathrm{Cot}\gamma_2\right)}$ where, $V_{f2}{}^{s}$ = f(d_{50},W,Q)
Widenroth [1970]	$3.16\times10^{-4}\dfrac{C_V}{\psi_w}(N_s)^{-2.46}(Re_p)^{1/3}$
Vocaldo et al. [1974]	$\dfrac{C_V(S_s-1)}{S_m}\left[0.167+B_1\sqrt{\dfrac{d_{50}(S_s-1)}{D_2}}\right]$ where, B_1=10 for rubber lined and 6.02 for metal pumps
Burgess and Reizes [1976]	$1-(1-C_W)^n$ where, n = f(S_s,d_{50})
Cave [1976]	$0.0385(S_s-1)\dfrac{S_s+4}{S_s}C_W\ln\left(d_{50}/22.7\right)$
Sellgren [1979]	$0.32C_W{}^{0.7}(S_s-1)^{0.7}C_D{}^{-0.25}$ where, $C_D=\dfrac{4g}{3}\dfrac{d_{wn}(S_s-1)}{W^2}$
Remisz [1983]	$1-\xi_h$ where, ξ_h = f(S_m-1,q_n)
Baz [1984]	$0.02C_V(1+Q_r{}^2)\left[\dfrac{(S_s-1)}{(S_m-1)}\right]$
Roco et al. [1986]	$\dfrac{\sum\Delta h_m}{H_{th}-\sum h_w}$ where, $H_{th}=\dfrac{U_2{}^2-U_1{}^2}{g}\dfrac{Q_{th,max}-Q}{Q_{th,max}}$ $h_w=(h_{sf})^w+(h_{loc})^w+(h_f)^w$ = f(pump configuration) $\Delta h_s=(\Delta h_{sf})^m+(\Delta h_{loc})^m+(\Delta h_f)^m$ = f(C_V, S_s-1, Re_p, N_s, W and pump configuration)
Gahlot et al. [1992]	$0.00056(S_s-1)^{0.72}C_W\dfrac{S_s+3}{S_s}\ln(50d_{wn})$
Kazim et al. [1997]	$0.13C_W\sqrt{S_s-1}\ln\left(d_{wn}/20\right)$
Gandhi et al. [2000]	$1-\dfrac{(H_{th}-h_{loss})^m}{(H_{th}-h_{loss})^w}$ where, h_{loss}= h_{slip} + h_{mix} + $h_{f,imp}$ +$h_{f,vol}$ at Q_d = Q_{imp} – Q_l
Sellgren et al. [2000]	$\dfrac{C_1V_RWV_{w2}\left(2/gD_2\right)^{0.5}C_W\times(1-C_W)}{gH_w}$
Engin and Gur [2001]	$0.11C_W\left(S_s-1\right)^{0.64}\ln\left(44d_{wn}\right)$
Engin and Gur [2003]	$2.705C_W(S_s-1)^{0.64}\left(d_{wn}/D_2\right)^{0.313}$
Khalil et al. [2013]	$0.0236C_W{}^{0.7754}S_s{}^{0.2358}d_{wn}{}^{0.1426}$
Cheng and Song [2013]	$(1-C_W)^n$ where, $n=(0.21+0.066\ln d_{50})S_s$

Table 2.2: Summary of numerical investigations of performance characteristics of the centrifugal slurry pump with solid-liquid mixture

Author	**Operating Parameters**	**CFD Code**	**Analysis Type**	**Mesh Details**		**Multi-phase Model**	**Deviation from Experiments with Slurry**	
				Type	**Elements** (millions)		**Head**	**Eff.**
Liu et al. [2009]	S_s = 1.21 d_s = 50-150 C_v = 5-25 N = 990	Fluent	Steady	Un-structured	1.2	Mixture	Not compared	Not compared
Wang et al. [2012]	S_s = 1.61 d_s = 200 C_v = 3-10 N = 1650	Fluent	Steady	Un-structured	0.4	Eulerian-Eulerian	+9.5%	+4.5%
Li et al. [2012]	S_s = (---) d_s = 100-1000 C_v = 1- 4 N = 2900	---	Steady	Not discussed	Not discussed	Mixture	+7%	+8%
Zhao et al. [2012]	S_s = 1.61 d_s = 30-200 C_v = 1-15 N = 1450	Fluent	Steady	Un-structured	0.4	Mixture	+9.4%	+8.8%
Zhang et al. [2013]	S_s = 0.5-3 d_s = 10-250 C_v = 5-18 N = 1450	---	Steady	Un-structured	0.5	Mixture	+2%	+7%
Tao et al. [2017]	S_s = 2.3 d_s = 500 C_v = 10 N = 2900	CFX	Unsteady (Time step size = 1.72414 x10^{-4} sec)	Structured	4.0	Not discussed	Not compared	Not compared

Table 2.3: Erosion study on accelerated laboratory test rigs

Author (s)	Test Rig	Slurry	Solid Size (µm)	Target Materials	Solid Fraction (%)	Velocity (m/s)	Impact Angle (Degree)	Remark
Tsai et al. [1981]	Slurry Pot Tester with Propeller	Coal+ Kerosene SiC+ Kerosene	24 150	A-53 Mild Steel, Stainless Steel 304 and 316	C_w = 30 and 50	6.1, 9.14 and 12.2	-----	The erosion rate increased with increase in particle velocity, concentration and temperature. Sic particles erode 40-100 times more than that of coal.
Bree et al. [1982]	Slurry Pot Tester	Sand + Water,	260 and 990	Steel 142 and CBR 315.3	C_v = 14 and 33	4, 15 and 30	10-90	Erosive wear has direct functional relationship with the particle size and concentration. Erosion rate relates with velocity through power law relationship with an exponent between 3 and 4.
Levy and yau [1984]	Jet Impingement Tester	Coal + Kerosene, SiO_2 + Water	200	1018,1020, 4340 Steels, 410, 304, 321 Stainless Steel, Two low Chromium steels	C_w = 30	12 to 30	20-90	The maximum erosion observed at an angle of 90^o. Due to the effect of viscosity the erosivity of the solid particles gets reduced compared to gas-solid erosion process. The velocity exponent decreases with increase in impact angle.
Mens and Gee [1986]	Slurry Pot Tester	Sand + Water	290, 700, and 1900	Steel C22 and Natural Rubber	C_v = 10, 14, 22 and 33	4 and 30	10-90	Angle of maximum erosion is at 40^o for Steel C22 and 10^o for natural rubber. Velocity exponent depends on impact angle and varies between 2.7 to 3.2.
Lin and Shao [1991a]	Falling Jet Apparatus	Sand + Water	150	Aluminum, 1020 Steel, High Chrome Cast Iron	C_w = 5	10 to 70	15-90	The velocity exponent is decreased with increase in hardness. The viscous effect of fluid is reduces the velocity exponent in comparison with gas-solid particle erosion test.

Lin and Shao [1991b]	Falling Jet Apparatus	Sand + Water	150	Aluminum, 1020 Steel, High Chrome Cast Iron, Ceramic and Glass	$C_w = 5$	19.1 to 62.4	15-90	The angle of maximum erosion is increases with the increase in the hardness. Lower the impact velocity smaller the maximum angle of erosion to be occur.
Clark [1991]	Slurry Pot Tester	Sand+ Oil	53-180	Steels (P110, N80 and K55)	C_w = 0.5-4	9.35 and 18.7	-----	The velocity exponent for erosion is 2.4. The rate of erosion can be reduced due to decrease in collision efficiency at susceptible regions in the flow regime.
Lynn et al. [1991]	Slurry Pot Tester	SiC + Oil	20-423 40, 57.5, 75, 115.5, 163.5, 250, 323.5 and 423	P110 Steel	$C_w = 1.2$	18.7	-----	For particle size greater than 100 µm the erosion rate is directly proportional to the kinetic energy dissipated by particles during impact but for particle size below that the material removal predominant by other mechanisms.
Gandhi et al. [2003]	Slurry Pot Tester with Four Bladed Propeller	Tailings + Water	223.5, 448.5 and 890	Brass	C_w = 20 and 40	3.48 ad 8.18	15-90	Maximum wear occurs at 30◦ orientation angle, which is 3-4.5 times higher than the erosion at 90◦ orientation angle. The power index is lower than 2 for velocity, whereas for particle size it is a function of orientation angle also.
Gandhi and Borse [2004]	Slurry Pot Tester with Four Bladed Propeller	Sand + Water	112.5, 225, 505 and 855	Grey Cast Iron	C_w = 20 and 40	3.62	30 and 75	Weighted mass particle size is a better choice to represent multi-sized particulate slurries. Addition of fine particle in multi-sized slurry reduces the erosion.

Tian and Addie [2005]	Coriolis Wear Tester	Sand + Water	22-1428	Aluminum Alloys and High Chromium White Iron	C_v = 1.52, 3.03, 6.06 and 12.12	----	0	High chromium white iron showed 27-140 times higher wear resistance compared to aluminium alloy.
Desale et al. [2006]	Slurry Pot Tester with Four Bladed Propeller	Quartz+ Water, Alumina + Water and Silicon carbide + Water	550	Aluminum Alloy (AA6063) and SS 304L	C_w = 10	3	7.5-90	The maximum angle for erosive wear is a function of target material properties and does not depend on the erodent. The erosion rate of ductile materials varies with the erodent shape and density rather than its size and hardness.
Desale et al. [2008]	Slurry Pot Tester with Four Bladed Propeller	Quartz+ Water, Alumina + Water and Silicon carbide + Water	362.5, 550 and 655	AA6063, Copper, Brass, Mild Steel, SS 304L, SS 316L, and Turbine Blade Steel	C_w = 10, 20 and 30	3, 6 and 8.33	90	The erosive wear of ductile materials at normal impact condition is a function of the ratio of erodent hardness to target material hardness. Erosive wear at normal impact has strong dependence on velocity and particle size but relatively weak dependence on solid concentration.
Desale et al. [2009]	Slurry Pot Tester with Four Bladed Propeller	Quartz + Water	37.5, 112.5, 181, 256, 362.5, 462.5, 550 and 655	Aluminum Alloy (AA6063)	C_w = 20	3	30 and 90	The critical particle size is 200 µm for the erosion of aluminum. Below the critical particle size the erosion rate is high compared to power law relationship due to change in the mechanism of material removal from impact to three-body abrasion
Walker and Robbie [2013]	Jet tester (JT), Slurry Jet Erosion Tester (SJT) , Coriolis Tester (CT)	Sand + Water	212-300	50 Duro Natural Rubber, 27% Cr White Cast Iron, 35% Cr White Cast Iron	C_w = 10	20 (JT), 16 (SJT), 14-24 (CT)	30(JT), 20 (SJT), 0-8 (CT)	The erosion mechanism is different in the field wear and the laboratory test rig due to lack of consideration of field wear situation in the laboratory test rigs.

Nguyen et al. [2014]	Slurry Erosion Test Rig	Sand + Water	160	Stainless Steel SUS304	C_v = 0.5	10 to 30	90	Erosion rate of stainless steel SUS304 was initially high and reduced to a critical value over the testing time. Plastic deformation mechanism dominated at high impact angles.
Yao et al. [2015]	Jet Impingement Tester	Sand + Water	180, 250 and 300	SS 304 and SS 316	C_w = 1.5	20	20-45	Erosion resistance of SS-316 is more as compared to SS-304. Ploughing and micro-cutting are the dominant mechanism of material removal of these materials.
Nguyen et al. [2016]	Slurry erosion Test Rig	Sand + Water	50, 80, 150, 350, 450 and 750	Stainless Steel SUS304	C_v = 0.5	30	90	The erosion rate increases as particle size increases, however, it reaches a maximum value at particle size of 150 μm, and then gradually decreases as particle size becomes bigger.
Al-Bukhaiti et al. [2017]	Slurry Whirling-Arm Test Rig	Sand + Water	510-755	High Chromium White Cast Irons (HCWCI)	C_w = 1	5, 10 and 15	30, 45, 60 and 90	The erosion resistance of HCWCI was more at the normal impact and the lowest at 30^o. The change of impact velocity resulted in changing the slurry erosion mechanisms.
Rawat et al. [2017]	Slurry Pot Tester, With Four Bladed Propeller	Fly Ash + Water	60.32	Brass	C_w = 50-70	1 to 4	0-90	The functional dependence of erosive wear is much stronger for solid concentration in comparison to velocity
Nandre and Desale [2018]	Slurry Pot Tester with Four Bladed Propeller	Quartz+ Water, Alumina + Water and Silicon Carbide + Water	256,362.5, 462.5, and 550	Aluminum Alloy (AA6063)	C_w = 3-35	1.82 to 7.02	45,90	The erosive wear of material is majorly affected with the variation in kinetic energy of impacting particles, particle shape and the mechanism of erosion.

Table 2.4: Erosion models

Author (s)	Correlation	Remark
Finnie [1960]	$ER = \frac{V_s^2}{p_\sigma \psi_1 k_F}(\sin(2\alpha) - \frac{6}{k_F}\sin^2(\alpha))$ for $\tan\alpha \le \frac{k_F}{6}$ $ER = \frac{V_s^2}{p_\sigma \psi_1 k_F}(\frac{k_F \cos^2\alpha}{6})$ for $\tan\alpha \ge \frac{k_F}{6}$	Model Type: theoretical Test rig: erosion tester Slurry: silicon carbide + air Target material: copper, 1020 steel, aluminum Particle size range: 250 µm Impact angle range: 10^o–90^o Velocity range: ≤150 m/s.
Bitter [1963a,b]	$ER_D = \frac{1}{2}\frac{(V_s \sin\alpha - K)^2}{\delta}$ $ER_C = \frac{2V_s(V_s\sin\alpha - K)^2}{(V_s\sin\alpha)^{1/2}}\left\{V_s\cos\alpha - \frac{C(V_s\sin\alpha - K)^2}{(V_s\sin\alpha)^{1/2}}\chi\right\}$ for $\alpha \ge \alpha_{s0}$ $ER_C = \frac{\frac{1}{2}\left[V_s^2\cos^2\alpha - K_1(V_s\sin\alpha - K)^{3/2}\right]}{\chi}$ for $\alpha \le \alpha_{s0}$ $ER = ER_C + ER_D$	Model Type: theoretical Test rig: free-falling apparatus Slurry: cast iron + air, Target material: aluminum, copper, 1055 steel Particle size range: 300 µm Impact angle range: 10^o–90^o Velocity: 107 m/s
Neilson and Gilchrist [1968]	$ER = \frac{\frac{1}{2}\left[V_s^2\cos^2\alpha - V_{r1}^2\right]}{\chi} + \frac{1}{2}\frac{(V_s\sin\alpha - K)^2}{\delta}$ for $\alpha < \alpha_{s0}$ $ER = \frac{\frac{1}{2}V_s^2\cos^2\alpha}{\chi} + \frac{1}{2}\frac{(V_s\sin\alpha - K)^2}{\delta}$ for $\alpha > \alpha_{s0}$	Model Type: theoretical Test rig: single particle test Slurry: aluminum oxide + air Target material: aluminum Particle size range: 210 µm Impact angle range: 10^o–90^o Velocity range: 108-192 m/s
Elkholy [1983]	$W_T = 1.342\times10^{-5} C_V^{0.682}\left(\frac{H_{Bs}}{H_{Bt}}\right)^{r_1} d_s^{0.616} V_s^{2.39}$ $\times\left\{1+\sin\left(\frac{\alpha-\alpha_1}{90-\alpha_1}180-90\right)\right\}$ where, $r_1 = 3.817$ if $\frac{H_{Bs}}{H_{Bt}} < 1.9$ and $r_1 = 0.268$ if $\frac{H_{Bs}}{H_{Bt}} > 1.9$	Model Type: empirical Test rig: JIT Slurry: sand+ water Target material: aluminum, cast iron Particle size: 410-500 µm Impact angle range: 15^o–90^o Velocity range: 5-30 m/s Concentration:5-20%by vol.
Ahlert [1994]	E/CRC Model $ER = A_1(H_{Bt})^{-0.59} F_s f(\alpha) V_s^\beta$ $f(\alpha) = a\alpha^2 + b\alpha \quad \alpha \le \alpha_o$ $f(\alpha) = x\cos^2\alpha\sin(w\alpha) + y\sin^2\alpha + z \quad \alpha > \alpha_o$ where a,b,c,x,y, and z are constants	Model Type: empirical Test rig: direct impact test Slurry: sand+ water Target material: carbon steel
Haugen et al. [1995]	DNV Erosion Model $ER = C_2 f(\alpha) V_s^\beta$ $f(\alpha) = \sum_{i=1}^{8}(-1)^{i+1} A_i \alpha^i$	Model Type: empirical Test rig: JIT Slurry: sand + water Target material: 28 Particle size: 200-250 µm Impact angle:7.5^o, 22.5^o, 90^o Velocity range:18-20, 40-45, 200-220 m/s

Gupta et al. [1995]	For Brass $E_w = 0.178 V_s^{2.4882} d_s^{0.291} C_W^{0.516}$ For Mild Steel $E_w = 0.223 V_s^{2.148} d_s^{0.344} C_W^{0.556}$	Model Type: empirical Test rig: slurry pot tester Slurry: zinc tailings + water Target material: brass, and mild steel Particle size: 37.5-448.5 µm Impact angle range: 0^o Velocity range: 3.9-8.06 m/s Concentration:15-45% by wt.
Gandhi et al. [1999]	$E_w = 2.57 V_s^{2.56} d_s^{0.85} C_W^{0.83}$	Model Type: empirical Test rig: slurry pot tester Slurry: zinc tailings + water Target material: brass Particle size: 223.5-890 µm Impact angle range: 0^o Velocity range: 3.2-8.18 m/s Concentration:20-40% by wt.
Oka et al. [2005]	$ER = f(\alpha) ER_{D90}$ where $f(\alpha) = (\sin\alpha)^{n_1} (1 + H_{vt}(1 - \sin\alpha))^{n_2}$ $ER_{D90} = 1x10^{-9} \rho_T K_s (H_{vt})^{K_1} \left(\frac{V_s}{V'}\right)^{K_2} \left(\frac{d_s}{d'}\right)^{K_3}$	Model Type: empirical Test rig: sand blast type Slurry: SiO_2, SiC and glass beads (GB) particles + air Target material: cast iron, aluminum, and stainless steel Particle size : 49-428 µm Impact angle range: 5^o-90^o Velocity range: 50-150 m/s
Zhang et al. [2007]	E/CRC Erosion Model $ER = C_3 (H_{Bt})^{-0.59} F_s f(\alpha) V_s^{\beta}$ $f(\alpha) = \sum_{i=1}^{5} R_i \alpha^i$	Model Type: empirical Test rig: direct impact test Slurry: sand + water, sand+ air Target material: inconel 625 Particle size range: 150 µm Impact angle: 0^o-90^o Velocity range: 2.5-10 m/s (Water), 10-28 m/s (Air) Concentration: 0.5% (water), 0.0002-0.006% (Air) by vol.
Desale et al. [2008]	$ER_{D90} = 6.62 \times 10^{-14} \times K_{(s/t)} V_s^{2.02} d_s^{1.62} C_W^{-0.283}$ $ER = ER_{D90} (\sin\alpha)^3 + ER_C$ where $ER_C = 6.62 \times 10^{-12} \times f(\alpha) (MSF)^{-0.80} (H_{vt})^{-0.72} V_s^{2.35} d_s^{1.55} C_W^{-0.11}$ $f(\alpha) = 0.99 \left[\sin\left(\frac{\pi}{2}\right)\left(\frac{\alpha}{\alpha_{max}}\right) \right]^{0.58}$ for $0\,\text{deg} \le \alpha \le \alpha_{max}$ $f(\alpha) = 0.92 \left\{ \sin\left[\left(\frac{\pi}{2}\right) - \left(\frac{\pi}{2}\right)\left(\frac{\alpha - \alpha_{max}}{90 - \alpha_{max}}\right) \right] \right\}^{4.30}$ for $\alpha_{max} \le \alpha \le 90\,\text{deg}$	Model Type: empirical Test rig: slurry pot tester Slurry: quartz, alumina, silicon carbide particles + water Target material: aluminum alloy (AA6063), copper, brass, mild steel, AISI 304L stainless steel, AISI 316L stainless steel, and turbine blade steel Particle size : 362.5, 550, 655 µm Impact angle range: 7.5^o–90^o Velocity range: 3.6-8.33 m/s Concentration:10-30% by wt.

Okita et al. [2012]	E/CRC Erosion Model $ER = C_4 \left(H_{Bt}\right)^{-0.59} F_s f\left(\alpha\right) V_s^{\beta}$ where $H_{Bt} = \frac{\left(H_{vt} + 0.1023\right)}{0.0108}$ $f\left(\alpha\right) = \frac{1}{f}.\left(\sin\alpha\right)^{n1}.\left(1 + H_{vt}^{n_3}\left(1 - \sin\alpha\right)\right)^{n_2}$	Model Type: empirical Test rig: direct impact test Slurry: sand + air Target material: aluminum 6061-T6 Particle size: 150 and 300 µm Impact angle: 0^o-90^o Velocity range:13, 24, 42 m/s Concentration:0.1% by vol.
Vieira et al. [2016]	$ER = 2.16x10^{-8} F_s f\left(\alpha\right) V_s^{2.41}$ where $f\left(\alpha\right) = 0.65\left(\sin\alpha\right)^{0.15}\left(1 + 1.48\left(1 - \sin\alpha\right)\right)^{0.85}$	Model Type: empirical Test rig: direct impact test Slurry: sand+ air Target material: SS 316 Particle size range: 300 µm Impact angle: 15^o-90^o Velocity range: 8.9-35.5 m/s

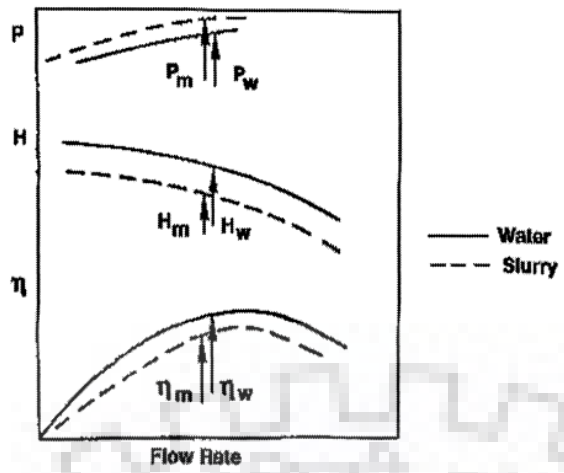

Fig. 2.1 Effect of slurry on centrifugal slurry pump performance characteristic [Wilson et al., 1992]

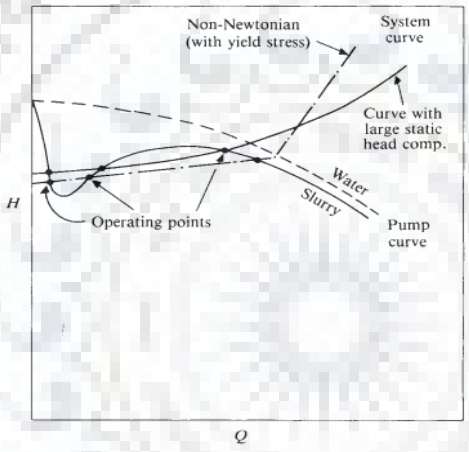

Fig. 2.2 Pump-system instability when handling non-Newtonian slurries [Walker and Goulas, 1984]

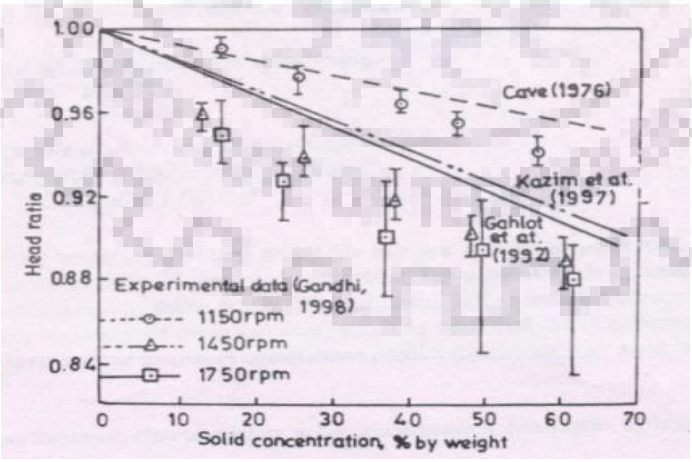

Fig. 2.3 Variation of experimental and predicted values of head ratio with fly ash slurry [Gandhi et al., 1999a]

CHAPTER 3: PERFORMANCE CHARACTERISTICS OF A CENTRIFUGAL SLURRY PUMP

Centrifugal slurry pumps are an integral component of any pipeline system transporting solids over short to medium distances. The performance characteristics of these pumps are greatly affected due to the presence of suspended solids. The flow behavior of the solid-liquid mixture inside the wetted passage of the components at different operating conditions also changes the pump performance. Thus for designing a slurry transportation system, it is necessary to know the effect of suspended solids and operating conditions on the performance of the centrifugal slurry pump. This chapter presents the experimental investigations carried out to find the effect of operating parameters namely particle size, particle concentration, flow rate and rotational speed on the pump performance.

3.1 Experimental Set-up

Experiments are performed in a slurry pilot plant test rig available in the slurry research laboratory of Mechanical and Industrial Engineering Department, IIT Roorkee. The schematic diagram and photographic view of the experimental setup are shown in Figs. 3.1 (a) and (b), respectively. A "50M WILFLEY" (Make: Hindustan Dorr-Oliver Ltd. Bombay) centrifugal slurry pump is used to perform the experiments. The details of centrifugal slurry pump are given in Table 3.1. The pump impeller is a closed type and consists of five identical backward curved blades. The diameter of the impeller at eye and tip are 110 mm and 265 mm, respectively. Impeller inlet and outlet blade angles are 23^o and 25^o, respectively. The pump is designed with side suction to allow easy service of the parts without affecting the inlet or discharge pipe line. The sectional view of the pump is shown in Fig. 3.2.

A short loop of 50 mm pipe diameter is used for the measurement of pump performance characteristics with water and slurry. The slurry is prepared in a hopper-shaped mixing tank. The height of the mixing tank is 1.55 m and has a square shape at the top (1.00 m x 1.00 m). The maximum capacity of the tank is 0.76 m^3. A suitable stirring arrangement is made for keeping the solids in suspension during experiments. The stirrer is inserted from the top of the mixing tank and rotated around 50 rpm using a 3 phase induction motor (1450 rpm) through 1:30 reduction gear box. The slurry is drawn from the mixing tank by the pump and returned after passing through the pipe loop to either the mixing tank or measuring tank. An arrangement is made to deflect the flow into either mixing tank or the measuring tank. The measuring tank is used to calibrate the flow meter during experimentation. The rise in the level of slurry in measuring tank over a known time period is measured to obtain the flow rate. The

return line from the measuring tank enables to empty this tank after each measurement. Plug valves are provided to vary the flow rate.

For monitoring of the flow rate, a pre-calibrated electro-magnetic flowmeter is installed in the vertical pipe section as shown in the schematic diagram (See Fig. 3.1a). An efflux sampling tube fitted with a plug valve in the vertical pipe section is used for collection of the slurry sample to monitor the solid concentration. Separators are installed at two diameters upstream and downstream of the suction and delivery flanges of the pump. The purpose of a separator is to eliminate entrance of solid particles in the pipe connected to pressure transducers. The separators are made with a transparent acrylic pipe in order to ensure pressure measurements without air entrapment in the separators. The arrangement of the separator is shown in Fig. 3.3. Two pressure transducers are connected with separators to measure the total static head developed by the pump. Air is purged off from the pipeline and the separators, before taking measurements. The pump is driven by 7.5 kW, 440 V and 14.5A induction motor (Type: 3 phase square cage). For the variation of motor speed, a frequency modulator is used.

3.2 Instrumentation

Different instruments are used to measure the various operating parameters required to obtain the pump performance and slurry property. Details of the instruments are discussed in the following paragraphs.

3.2.1 Flow Rate Measurement

The flow rate in the pipe loop is continuously monitored using an electromagnetic flowmeter (Magmeter, Make: Iotaflow). The measuring tank is used to calibrate the flowmeter during experiments. Flow rate measurement shows an accuracy of ±0.5% of the flowmeter. The calibration of the electromagnetic flowmeter is presented in Fig. 3.4. It is seen that the deviations are within ±0.5%. The calibration of the meter is also regularly checked with slurries during experimentation.

The specifications of the electromagnetic flowmeter are as below.

1	Pipe diameter	50 mm NB
2	Range of discharge rate	0- 18 L/s
3	Application	Abrasive slurry flow measurement
4	Output flow volume signals	4-20 mA
5	Maximum operating pressure	20 bar
6	Maximum liquid temperature	80˚ C
7	Accuracy	±0.5%
8	Display	3 1/2 digit digital display for discharge and average velocity
9	Material for Tube, Liner, and Electrode	SS 304, PTFE, and SS316

3.2.2 Pressure Measurement

The pressure at the suction and delivery sides of the pump is measured using two pressure transducers (LD301, Make: Smar) connected through the separators at two diameters upstream and downstream of the suction and delivery flanges, respectively. At the suction side, a pressure transducer is used to measure the absolute pressure. Similarly, at the delivery side, a pressure transducer is used for gauge pressure measurement. Both the transducers are calibrated using the pressure calibrator (PPC4, Make: Fluke) of range 0-14 bar of accuracy ±0.015%. The calibration curve of the transducers is shown in Fig. 3.5 (a,b). The accuracy of both the transducer is observed ±0.75% of full scale. The specification of the pressure transducers are as follows:

1	Type	Gauge
	Operating Pressure Range	0.21 to 2.5 bar
2	Type	Absolute
	Operating Pressure Range	0.02 to 2.5 bar

3.2.3 Speed Measurement and Its Variation Arrangement

The pump speed is measured by a non-contact type tachometer having an accuracy of ±1 revolutions per minute (rpm). To operate the pump at different speeds, a variable frequency drive (VFD) of 7.5 kW (Make: ABB Ltd.) is employed to run the induction motor which is connected to the pump.

3.2.4 Measurement of Input Power to the Pump

For measurement of shaft power, the shaft torque is measured through a torque transducer (T22-M, Make: M/s HBM LTD, Germany) installed between the pump and the motor shafts. The range of the torque transducer is 0.1 Nm to 200 Nm with an accuracy of ±0.2%.

3.2.5 Properties of Solid Particles and the Solid-Liquid Mixture

In the present work, the slurry of water and solid particles, namely Indian standard sand (Tamil Nadu minerals Ltd.) and fly ash (NTPC, Dadri) are considered. Standard laboratory tests are performed to determine the physical and rheological properties of solids and solid-liquid mixture. The test method used and the measured parameter with these tests are presented in the sections below.

3.2.5.1 Particle Density

The density of solids plays an important role on the performance of slurry pumps [Gandhi, 1998]. It decides the settling characteristic of the particles. To determine the density of solid particles, standard pycnometer tests are performed. The measured density of Indian standard sand and fly ash is 2650 kg/m^3 and 2010 kg/m^3, respectively.

3.2.5.2 Particle Size and Its Distribution

It is not possible to collect identical size particles of the solid materials. For conducting the test with the nearly same size of particles, the particles of Indian standard sand are sieved using narrow range of sieve sizes. The average of the two successive sieve sizes, in between which the particles are retained, is considered as particles mean size. The mean particle size of 200 µm (+ 150 –250), 400 µm (+300 –500), and 605 µm (+500 –710) are collected to perform the experiments. The numbers in the parenthesis represent the successive sieve sizes. The fly ash particles are used in multi-size form as received. To determine the particle size distribution of fly ash particles, sieve analysis is performed. The detail of particle size distribution of fly ash particles is presented in Table 3.2.

3.2.5.3 Static Settled Concentration

The static settled concentration of slurry suspension represents the maximum value of solid concentration under static condition and generally used for transportation through the pipeline. It depends on the properties of solid particles and the carrier fluid [Mishra, 1996]. To determine the static settled concentration of the slurry, the gravitational settling method is used as discussed by Gandhi [1998]. The measured value of static settled concentration for sand and fly

ash particles is presented in Table 3.3. The maximum settled concentration for sand (200 μm) and fly ash particulate slurry is found as 72.81% and 60.48% by weight, respectively.

3.2.5.4 pH Value

A digital pH meter was used to determine the pH value of solid-liquid mixture at different particulate concentrations. The measured pH value of the sand and fly ash particulate slurries is presented in Table 3.4. The pH values of sand-water and fly ash-water slurries up to 50% weight concentration lies in the range of 7.65 to 7.74 and 7.38 to 7.65, respectively, which indicate that these slurries are non-reactive.

3.2.5.5 Rheological Tests

Rheological characteristic of the carrier fluid plays a significant role on the performance of the centrifugal slurry pump [Roco et al., 1986]. The rheological characteristic of the carrier fluid varies with the addition of solid particles and changes other than Newtonian if the mixing of solids increases beyond a certain limit [Biswas et al., 2000].

In the present study, the rheological characteristic of the sand-water and fly ash-water slurry is determined through measurement of the variation in shear stress with shear rate. The MCR 102 rotational rheometer (Make: Anton Paar Company Ltd., Germany) is used to determine the rheological characteristics of the slurry. A pictorial view of MCR 102 rheometer installed in the Fluid Mechanics laboratory of Mechanical and Industrial Engineering Department, IIT Roorkee is shown in Fig. 3.6. It consists of a high resolution optical encoder, an air bearing supported synchronous electrically commutated (EC) motor (also called DC motor), a cooling unit to control the temperature of the fluid and a compressor to supply the compressed air to the air bearing. It covers a wide operating range of torque and temperature. The detailed specifications of MCR 102 rheometer are as below:

1.	Torque Range	Min- 0.05 μNm Max- 200 mNm
2.	Speed Range	0-18840 rpm
3.	Temperature Range	-20 to +70 ºC
4.	Normal force range	0.01 to 50 N

The rheometer is connected to a desktop computer and operated via software programme Rheoplus. A standard measuring system consists of a cup (CC27-SS) and bob (CC27-35377) geometry is available to perform the rheology of fluids. Before conducting the rheological measurements, the measuring cup and bob are cleaned and air dried.

For measurements, around 30 ml of slurry is prepared at a particular concentration and poured in the cup. An electronic weighing machine having least count of 0.1 mg is used to measure the mass of the solids. The measuring cup is kept stationary with a locking device and a bob is inserted vertically into the cup and allowed to rotate at known fixed speed. In the cup, the slurry is subjected to shearing action due to the rotation of bob. The rheology of the sand (mean size = 200 μm) and fly ash slurry is measured for the solid concentration range of 10-50% by weight. The measurements are conducted under the controlled shear rate ranging from 60 to $300s^{-1}$ at a constant temperature of $25^{o}C$. To ascertain the reproducibility of the measured data, the experiments are conducted for at least two samples of the same material.

The results of the rheological studies of sand and fly ash slurries are tabulated in the Table 3.5. The non-zero value of yield stress implies that the slurry is showing Non-Newtonian behaviour and is represented as Bingham plastic fluid. The mathematical form of the equation representing Bingham fluid behaviour is given by

$$\tau = \tau_y + \eta_p \dot{\gamma} \qquad (3.1)$$

where, τ is the shear stress (Pa), τ_y is the yield stress (Pa), η_p is the plastic viscosity of the Bingham fluid (Pa-s), and $\dot{\gamma}$ is the shear rate (per seconds).

From shear stress and shear rate data, the values of yield stress and plastic viscosity of fluids are determined using the method of least square. The relative viscosity of the slurry is calculated by dividing the Bingham plastic viscosity or Newtonian dynamic viscosity of the slurry to the viscosity of water under similar experimental conditions. Table 3.5 shows the variation in the relative viscosity of the sand and fly ash at different solid concentrations (by weight). As usual, it is observed that the relative viscosity of the slurry increases with the increase in solid concentration. This is mainly attributed to the increase in inter-particle interactions [Senapati et al., 2009]. At higher solid concentration, the presence of number of solid particles is relatively more and hence higher shear stress is needed to initiate shearing. Further, the yield stress values of the slurries presented in Table 3.5 shows that the sand slurry shows Newtonian behaviour up to the tested range of solid concentration (i.e. C_w = 50%) whereas fly ash slurry shows Newtonian behaviour only up to 30% weight concentration and beyond this it shows Bingham fluid behaviour.

3.3 Uncertainty in Measurements

The range within which the true value of a measured quantity can be expected to lie with a suitably high probability is termed as "uncertainty of the measurement" [IEC 60041]. All the experimental measurements involve uncertainty in spite of all care and precautions which may

be attributed to all possible sources of error in measurements. This error may be due to geometrical in-accuracy in the test apparatus, in-accuracy of measuring instruments, and human error. To estimate the uncertainty in the measured pump performance characteristics, the root-sum-square of all the individual uncertainties is determined. The calculated uncertainty in the head, input power, and efficiency is ±1.35%, ±0.26%, and ±1.37%, respectively.

3.4 Range of Parameters Studied

Experiments are carried out to investigate the effect of flowrate, particle size, solid concentration, and rotational speed on pump performance while handling solid-liquid mixture. The pump clear water performance characteristic is measured at three speeds namely 1200 rpm, 1050 rpm, and 900 rpm. Experiments are conducted at 1200 rpm with fly ash slurry at six different weight concentrations namely 7.2%, 13.3%, 21.2%, 27.8%, 35.1%, and 44.3% by varying the flowrate in the range of 6-13 L/s at each concentration. The measurements on fly ash slurry are used to investigate the effect of flowrate on the pump performance. The experiments are also performed with three different mean size sand particulate slurries namely 200 µm, 400 µm and 605 µm at different weight concentrations in the range 10-40% at best efficiency point (BEP) and 0.75 BEP flowrate at the speed of 1200 rpm. The effect of speed on pump performance is investigated by conducting the experiments with sand particulate slurries of mean size 400 µm at the speeds of 1050 rpm, and 900 rpm at different weight concentrations in the range 5-40% at BEP flowrate.

3.5 Experimental Procedure and Data Analysis

Before starting the experiment, the mixing tank, the pump, and separators are filled with water. The entrapped air is purged-off from the separators. All the measuring instruments are connected to the power supply line and zero setting is checked. The motor is switched on and the speed at which the experiments are desired to perform is set using VFD connected to the motor. The delivery plug valve is adjusted to achieve the desired flowrate. After achieving the stabilized conditions, the readings of different instruments namely electromagnetic flowmeter, pressure transducers, torque sensor, and tachometer are noted. The measurements are taken for different openings of delivery valve to cover the operating range of the pump. The same procedure is followed for measurements at all the three speeds namely 900, 1050, and 1200 rpm with clear water.

After the completion of measurements with clear water, the performance characteristic of the pump is measured with the solid-liquid mixture for different solid concentrations. Initially, the above procedure is repeated with water, then a known mass of solid particles are added in the

mixing tank at different intervals to get the measurements at various solid concentrations. The stirrer is continuously rotating for proper mixing of solids in the mixing tank. During each measurement, two efflux samples are collected to monitor the solid concentration. These samples are further analyzed to check the particle attrition, if any. No significant change in the particle size is observed over the total duration of any tests.

Further, the analysis of the collected data is carried out to estimate the pump performance. The calculation of slurry density, net head developed, pump input, output power, pump efficiency, head ratio, efficiency ratio, power ratio, and affinity laws equations are given below:

The density of the slurry mixture is calculated as [Abulnaga, 2002]:

$$\rho_m = \frac{100}{C_w / \rho_s + (100 - C_w) / \rho_w} \tag{3.2}$$

Where,

C_w = concentration by weight, %

ρ_m = density of mixture, kg/m^3

ρ_s = density of solid, kg/m^3

ρ_w = density of water, kg/m^3

The net head developed by the pump is calculated as [Gandhi, 1998]:

$$H = X_d + \frac{V_d^2}{2g} + Y_d - (\pm X_{suc} + \frac{V_{suc}^2}{2g} + Y_{suc}) \quad \text{meters} \tag{3.3}$$

Where,

X_{suc} = static head at the suction end of the pump, meter

X_d = static head at the delivery end of the pump, meter

V_{suc} = flow velocity in the suction pipe, m/s

V_d = flow velocity in the delivery pipe, m/s

Y_{suc} = potential head at the suction measured from pump centerline, meter

Y_d = Potential head at the delivery measured from pump centerline, meter

Power output from the pump calculated as:

$$P_o = \rho_m g Q H \quad \text{watts} \tag{3.4}$$

Where, Q is the flowrate in m^3/s.

Power input to the pump is calculated as:

$$P_i = \frac{2\pi NT}{60} \quad \text{watts} \tag{3.5}$$

Where, N is the rotational speed of the pump shaft (rpm), and T is the torque input to pump shaft (N-m).

Efficiency of the pump is calculated as:

$$\eta_p = \frac{P_o}{P_i} x100 \qquad \% \tag{3.6}$$

Head ratio (HR) is calculated as

$$HR = \frac{H_m}{H_w} \tag{3.7}$$

Where H_m, and H_w are the net head developed by the pump with mixture (meter of slurry) and clear water (meter of water), respectively at the same flowrate.

Efficiency ratio (ER) is calculated as

$$ER = \frac{\eta_{p,m}}{\eta_{p,w}} \tag{3.8}$$

Where $\eta_{p,m}$, and $\eta_{p,w}$ are the efficiency of the pump with the mixture and clear water, respectively at the same flowrate.

Power ratio (PR) is calculated as

$$PR = \frac{P_m}{P_w} \tag{3.9}$$

Where P_m, and P_w are the power input to the pump with mixture (kW) and clear water (kW), respectively at the same flowrate.

The affinity laws used are as below:

$$\text{Specific head}, sH = \frac{gH}{N^2 D_2^{\,2}} \tag{3.10}$$

$$\text{Specific flowrate}, sQ = \frac{Q}{N D_2^{\,3}} \tag{3.11}$$

$$\text{Specific power}, sP = \frac{P_i}{\rho_m N^3 D_2^{\,5}} \tag{3.12}$$

Where, N = pump speed, revolutions/sec, D_2 = characteristic pump dimension (generally impeller outlet diameter), meters.

3.6 Results and Discussion

The pump performance with clear water and slurry is calculated from the measured data. The obtained results are discussed below:

3.6.1 Pump Performance Characteristics with Clear Water

Experiments are initially conducted with clear water at three pump speeds, namely 900 rpm, 1050 rpm, and 1200 rpm to determine the variation of pump performance characteristics with the speed. The performance data of the pump with clear water at the different speeds are listed in Table 3.6. The estimated performance characteristic of the pump with clear water at 900 rpm, 1050 rpm, and 1200 rpm is presented in Fig. 3.7 (a-c). It is observed that the head-discharge characteristic of the pump is almost flat and the maximum pump efficiency is around 50% which is very low as compared to the conventional centrifugal pumps of same specific speed. This may be attributed to the less number of thick impeller vanes and large flow passages for clog-free operation [Wilson et al., 1992]. The maximum efficiency of the pump at 900 rpm, 1050 rpm, and 1200 rpm is observed as 46.41%, 47.81%, and 50.70%, respectively. The corresponding values of flow rate, head developed, and input power at the maximum efficiency point are 7.92 L/s, 6.74 m, and 1.128 kW, respectively at 900 rpm, 10.1 L/s, 9.17 m, and 1.9 kW, respectively at 1050 rpm, and 11.93 L/s, 11.60 m, and 2.68 kW, respectively at 1200 rpm (Table 3.6).

Further, the experimental data for different speeds are used to check the applicability of affinity laws for a centrifugal slurry pump handling clear water. The values of the specific head, specific flowrate, and specific power from the test data at different speeds are calculated using the Eqs. (3.10) to (3.12). The variation in specific head and specific power with specific flowrate at all the three speeds is shown in Fig. 3.8. It is observed that the values of the specific head decrease with the increase in specific flowrate at each rotational speed. It is also observed that the deviation in the specific head values is not much at different speeds. The maximum deviation in the specific head values for all the three speeds is within ±2% over the entire measuring range of specific flowrate. It shows that the affinity law for the estimation of head developed by a conventional centrifugal pump is also applicable for the centrifugal slurry pump for handling clear water. This is in line with the studies reported in the literature [Hunt and Faddick, 1981; Wilson et al., 1992; Gandhi et al., 2002]. Further, the variation in specific power with specific flowrate is observed to be linear and a large variation is seen in the values of specific power at different rotational speeds. The increase in rotational speed reduces the specific power at any specific flowrate. This may be attributed to the reduction in the overall

losses in the pump with increase in rotational speed [Gandhi et al., 2002]. The maximum reduction in the specific power is around 10% with 25% increase in pump speed from 900 rpm to 1200 rpm. The variation in specific power values with speed shows that the affinity laws for the estimation of input power for the conventional pumps is not applicable to the slurry pumps. Similar observation of non-applicability affinity laws for estimation of input power required for slurry pumps at different speeds was reported in the literature [Hunt and Faddick, 1981; Wilson et al., 1992; Gandhi et al., 2002].

3.6.2 Pump Performance with Solid-Liquid Mixture

Experiments are performed to determine the effect of operating parameters on the pump performance while handling solid-liquid mixture. The effect of flow rate, particle size, solid concentration and rotational speed on the pump performance for slurry is determined and discussed in the following sections.

3.6.2.1 Effect of Flow Rate

To investigate the effect of flowrate on the characteristics of the pump handling solid-liquid mixture, experiments are performed using the fly ash-water slurry at 1200 rpm. The measured performance of the pump with fly ash-water slurry at different flowrates (varied in the range of 6-13 L/s), and weight concentrations (varied in the range of 7.2-44.3%) are listed in Table 3.7. The estimated performance characteristics of the pump with fly ash slurry are presented in Fig. 3.9 (a-c). It is observed that the performance characteristics of the pump with fly ash slurry appear similar to the performance characteristics with clear water. However, the head developed and efficiency of the pump reduces with the increase in weight concentration of fly ash slurry (Fig. 3.9 (a,c)). The maximum reduction in net head developed, and pump efficiency at BEP flowrate compared to clear water is around 1.46 m, and 7.36 %, respectively, for the weight concentration of 44.3%. Fig. 3.9 (b) shows that the required input power to the pump increases with the increase in weight concentration of fly ash particles. The maximum increase in input power at BEP flowrate compared to clear water results is around 0.79 kW up to the weight concentration of 44.3%. Further, it is seen that the flowrate at maximum efficiency of the pump remains unaffected with the increase in the weight concentration of fly ash particles (Fig. 3.9 (c)). A similar observation was also reported in the literature [Kazim et al., 1997; Yassin et al. 2010].

The variations of HR, PR, and ER with flowrate and solid concentration are also determined and presented in Fig. 3.10 (a-c). It is observed that the HR, PR, and ER at any given concentration is nearly constant and the maximum variation is within 5%, 9%, and 10%,

respectively, in the entire range of tested flowrate. In literature, Chandel et al. [2011] observed the variation within 5% in the HR and ER of the pump with flowrate for high concentration fly ash water slurries. Yassin et al. [2010] reported the variation in HR, ER, and PR within ±9% with flowrate for sand-water slurries. Hence it is generally assumed that the reduction in the performance of the pump is almost independent of the flowrate.

3.6.2.2 Effect of Particle Size and Solid Concentration

To investigate the effect of particle size on pump performance, experiments are conducted at 1200 rpm with three different samples of sand water slurries of mean particle size of 200 µm, 400 µm, and 605 µm. The effect of particle size is determined with the variation in weighted solid concentration in the range of 10-40% while keeping the flowrate and pump speed constant. With the earlier understanding of the effect of flowrate on pump performance, measurements are performed at only two flowrate conditions i.e. BEP and 0.75 BEP flowrate with water to further observe the effect of flowrate with the variation in particle size. The measured pump performance with sand water slurry at BEP and 0.75 BEP flow rate is given in the Table 3.8. The effect of particle size on the HR, ER, and PR with the variation in weighted solid concentration for BEP and 0.75 BEP flowrate conditions is presented in Fig. 3.11 (a-c) and 3.12 (a-c), respectively. It is observed from Fig. 3.11 (a,b) that the reduction in HR and ER increases linearly with the increase in weighted solid concentration for each particle size. This may be attributed to the increase in particle-particle interaction and the energy required for pushing the particles inside the pump flow passage as the number of particle increases with increase in solid concentration. Further, it is also observed that the increase in particle size increases the drop in HR and ER. This may attribute to the increase in energy required to suspend the bigger size particles inside the pump flow passage [Gandhi et al., 2001a]. At nearly 10% weighted concentration, the drop in HR and ER is around 3%, whereas at nearly 40% weighted concentration, the reduction is around 8%. The increase in particle size at higher concentrations may attribute to the more energy loss of bigger size particles due to particle-particle interaction. The variation of PR with particle size and solid concentration is shown in Fig. 3.11 (c). It is seen that with the variation in particle size for the same mass of solid loading, there is no significant change in PR. It increases with the increase in solid concentration. The trend of variation in PR with solid concentration is seen almost similar to the variation in slurry specific gravity with solid concentration. The variation of PR with solid concentration similar to that of slurry specific gravity was also reported by Ni et al. [1999] for the sand-water mixture of mean particle size up to 372 µm. Further Fig. 3.11(c) shows that the value of slurry specific gravity is more than the value of the PR. It shows that the reduction in HR and ER with the

variation in solid concentration is not the same. The drop in HR is more than the drop in ER. The estimated maximum difference in HR and ER values with the present test data is around 2%. Higher drop in HR around 2% to 10% as compared to ER were also observed by Gahlot et al. [1992] and Gandhi et al. [2001a] for coal, bed ash, fly ash and zinc tailing slurry.

Further to see the effect of particle size and solid concentration with the variation in flowrate, the estimated head ratio, efficiency ratio, and power ratio at 0.75 BEP flowrate for different particle sizes and solid concentrations are presented in Fig. 3.12 (a-c). It is observed that the variation in HR, ER, and PR with particle size and weight concentration at 0.75 BEP flowrate is similar to that of the BEP flowrate. Hence it can be assumed that the effect of particle size and solid concentration on pump performance is independent of the flowrate.

3.6.2.3 Effect of Pump Speed

To study the effect of speed on pump performance, experiments are performed with 400 μm size sand particulate slurry for different weighted concentrations at the rotational speed of 1200 rpm, 1050 rpm, and 900 rpm corresponding to the BEP flow rate of clear water. The estimated performance at 1050 rpm and 900 rpm is listed in Table 3.8. Fig. 3.13 (a,b) shows the variation in HR and ER with pump speed and solid concentration. It is seen that the trend of linear reduction of HR and ER with the increase in solid concentration does not change with the pump speed. Also with the variation in speed, the change in drop of HR and ER is not significant. The maximum variation in the HR and ER with speed is within 2%. Thus, it can be assumed that the variation of HR and ER is independent of the rotational speed. These observations are in line with the study of Vocaldo et al. [1974], Burgess and Riezes [1976], Kazim et al. [1997] and Gandhi et al. [2002] for coarse particulate slurries.

3.6.3 Comparison with Existing Correlations

The comparison between measured and computed values of the HR from different correlations (see Table 2.1) is shown in Fig. 3.14. It is seen that the accuracy of prediction of the HR varies for different correlation. The accuracy of HR prediction with correlations of Vocaldo et al. [1974], Burgess and Reizes [1976], Gahlot et al. [1992], Kazim et al. [1997] and Engin and Gur [2003] are around +11% to -1%, +11% to -6%, +13% to -2.5%, +7% to -9% and +6% to -8%, respectively. It shows that none of the correlations gives satisfactory results to predict the HR very close to experimental data. Therefore, an alternative approach may be required to accurately predict the performance of the pump with solid-liquid mixture.

3.7 Concluding Remarks

Based on the present experimental investigation, the following conclusions can be drawn:

- The rotational speed and flowrate are not much significantly affecting the variation in head and efficiency of the pump. It can be assumed that the HR, ER, and PR are independent of the flowrate and the speed.
- The HR and ER decreases almost linearly with the increase in solid concentration. For bigger particle size, the particle-particle interaction is more at higher solid concentrations and therefore the reduction in these ratios are more.
- For the same mass loading, the variation in particle size has no effect on the PR. The PR increases with the increase in solid concentration. The trend of variation in PR with solid concentration is almost similar to the variation in slurry specific gravity with solid concentration.
- The accuracy of the available correlations in literature to predict the HR is poor. An alternative approach may be investigated to accurately predict the performance of the pump with solid-liquid mixture.

Table 3.1: Details of “50M wilfley” centrifugal slurry pump model

Specification	
Impeller Details	
(i) Type	Closed
(iii) Number of blades	5
(iv) Impeller eye diameter (mm)	110
(v) Impeller outlet diameter (mm)	265
(vi) Impeller width at eye (mm)	44.2
(vii) Impeller width at the outlet (mm)	68.6
(viii) Impeller inlet vane angle (degree)	23
(ix) Impeller outlet vane angle (degree)	25
(x) Blade thickness (mm)	22.4
Casing Details	
(i) Type	Semi-volute
(iii) Base volute diameter (mm)	275
(iv) Volute width (mm)	85
(V) Impeller-tongue radial gap (mm)	31
Inlet passage diameter (mm)	100
Outlet passage diameter (mm)	50

Table 3.2: Particle size distribution of fly ash

Weighted mean diameter (d_{wn}) = 60 µm				Median diameter (d_{50}) = 62 µm					
Particle Size, (µm)	>300	250	212	180	150	106	90	75	45
% Finer (by weight)	100	98	97	94.6	89	81.2	78	67.4	20.4

Table 3.3: Static settling value of the slurry at 30% weighted solid concentration

Solid particle	Mass of solid (gram)	Amount of water (ml)	Total slurry volume (ml)	Interface reading (ml)	Void water (ml)	Water in settled mass (ml)	Maximum settled concentration	
	a	b	c	d	e = c-d	f = b-e	By weight	By volume
Sand (200 µm)	64.287	150	174	48	126	24	72.81	50.24
Fly ash	64.287	150	182	74	100	50	60.48	36.60

Table 3.4: pH values of slurry at different particulate concentrations (by weight)

Solid particle	Solid concentration (% by weight)						
	0	1	10	20	30	40	50
Sand (200 µm)	7.65	7.66	7.69	7.70	7.71	7.72	7.74
Fly Ash	7.65	7.66	7.62	7.56	7.50	7.43	7.38

Table 3.5: Rheological properties of sand and fly ash slurry for different solid concentrations (by weight) at constant temperature of 25^{o}C

Solid concentration (% by weight)	Sand			Fly Ash		
	Yield stress (Pa)	Relative viscosity	Flow behaviour	Yield stress (Pa)	Relative viscosity	Flow behaviour
0	0	1	Newtonian	0	1	Newtonian
10	0	1.11	Newtonian	0	1.22	Newtonian
20	0	1.16	Newtonian	0	1.48	Newtonian
30	0	1.31	Newtonian	0	2.41	Newtonian
40	0	1.43	Newtonian	0.0118	4.46	Non-Newtonian
50	0	1.52	Newtonian	0.1128	19.64	Non-Newtonian

Table 3.6: Data sheet of the pump performance with clear water at 1200 rpm, 1050 rpm, and 900 rpm pump speed

Pump Speed (rpm)	**Flow rate (L/s)**	**Suction pressure (mmH2O)**	**Delivery Pressure (kg/cm^2)**	**Pressure head (m)**	**Velocity head (m)**	**Potential head (m)**	**Net head (m)**	**P_o (kW)**	**Torque (N-m)**	**P_i (kW)**	**η_p (%)**
1200	4.01	10319	1.2	12.009	0.199	0.5	12.709	0.500	14.02	1.762	28.38
	6.08	10265	1.19	11.963	0.458	0.5	12.922	0.771	16.14	2.028	38.00
	7.82	10202	1.1	11.126	0.758	0.5	12.385	0.950	17.26	2.169	43.80
	9.06	10149	1.07	10.880	1.018	0.5	12.397	1.102	18.65	2.344	47.02
	10.12	10097	1.02	10.432	1.270	0.5	12.202	1.211	19.9	2.501	48.44
	11.13	10041	0.95	9.788	1.536	0.5	11.824	1.291	20.63	2.592	49.80
	11.93	9992	0.9	9.337	1.765	0.5	11.602	1.358	21.31	2.678	50.70
	12.98	9929	0.82	8.600	2.089	0.5	11.190	1.425	22.62	2.843	50.13
	14.08	9867	0.71	7.563	2.458	0.5	10.521	1.453	23.27	2.924	49.70
1050	4.1	10236	0.93	9.393	0.208	0.5	10.102	0.406	12.14	1.335	30.44
	5.1	10209	0.9	9.120	0.322	0.5	9.9423	0.497	12.93	1.422	34.99
	6.2	10186	0.87	8.843	0.476	0.5	9.820	0.597	13.47	1.482	40.31
	7.26	10145	0.83	8.484	0.653	0.5	9.638	0.686	14.36	1.579	43.48
	7.93	10119	0.81	8.310	0.780	0.5	9.590	0.746	14.87	1.635	45.64
	9.04	10072	0.77	7.957	1.013	0.5	9.470	0.839	16.25	1.787	46.98
	10.1	10027	0.71	7.403	1.265	0.5	9.166	0.908	17.28	1.900	47.81
	10.94	9970	0.64	6.760	1.484	0.5	8.744	0.938	17.92	1.970	47.63
	11.52	9940	0.59	6.290	1.646	0.5	8.436	0.953	18.3	2.012	47.39
900	3.79	10176	0.64	6.554	0.178	0.5	7.232	0.269	9.21	0.868	30.97
	5.10	10149	0.62	6.381	0.323	0.5	7.204	0.360	10.12	0.953	37.78
	5.90	10126	0.6	6.204	0.432	0.5	7.136	0.413	10.53	0.992	41.61
	6.97	10093	0.58	6.037	0.602	0.5	7.139	0.488	11.6	1.093	44.65
	7.92	10068	0.52	5.462	0.779	0.5	6.740	0.524	11.97	1.128	46.41
	8.91	9995	0.5	5.335	0.984	0.5	6.819	0.596	13.8	1.300	45.83
	9.77	9968	0.44	4.763	1.184	0.5	6.446	0.618	14.42	1.359	45.46

Table 3.7: Pump performance at 1200 rpm with fly ash slurry

Q (L/s)	H (m)	P_i (kW)	η_p (%)	HR	PR	ER
Water only						
13.1	10.642	2.759	49.557	1	1	1
11.97	11.52	2.682	50.448	1	1	1
11.18	11.842	2.587	50.196	1	1	1
10.08	12.293	2.45	49.601	1	1	1
9.05	12.595	2.317	48.256	1	1	1
7.83	12.865	2.202	44.883	1	1	1
7.05	13.006	2.13	42.229	1	1	1
6.03	13.115	2.032	38.18	1	1	1
Weight Concentration = 7.2% (S_m = 1.038)						
13.04	10.603	2.888	48.729	0.983	1.038	0.981
11.98	11.249	2.748	49.906	0.987	1.033	0.990
10.94	11.728	2.633	49.603	0.985	1.034	0.987
9.89	12.087	2.532	48.049	0.980	1.041	0.975
7.60	12.742	2.293	43.012	0.984	1.048	0.973
5.86	12.852	2.104	36.534	0.979	1.047	0.969
Weight Concentration = 13.3% (S_m= 1.072)						
13.28	10.135	2.989	47.336	0.953	1.064	0.959
12.12	11.036	2.906	48.388	0.974	1.085	0.961
10.91	11.506	2.755	47.901	0.965	1.083	0.953
9.40	12.075	2.534	47.094	0.966	1.065	0.970
7.49	12.425	2.339	41.823	0.958	1.075	0.953
5.82	12.658	2.206	35.118	0.965	1.101	0.938
Weight Concentration = 21.2% (S_m = 1.119)						
13.01	10.167	3.087	47.075	0.941	1.111	0.947
12.14	10.796	3.007	47.862	0.954	1.122	0.951
11.14	11.244	2.904	47.374	0.951	1.131	0.941
9.55	11.717	2.666	46.082	0.941	1.113	0.944
8.07	12.131	2.488	43.215	0.944	1.112	0.948
5.87	12.377	2.307	34.584	0.943	1.149	0.918
Weight Concentration = 27.8% (S_m = 1.163)						
12.95	9.975	3.147	46.818	0.920	1.136	0.941
12.08	10.680	3.127	47.040	0.941	1.170	0.934
11.35	11.002	3.063	46.511	0.939	1.182	0.923
9.95	11.609	2.884	45.693	0.943	1.183	0.925
8.06	11.865	2.628	41.500	0.923	1.176	0.911
5.77	12.229	2.458	32.738	0.932	1.230	0.879

Q (L/s)	H (m)	P_i (kW)	η_p (%)	HR	PR	ER
Weight Concentration = 35.1% (S_m = 1.214)						
13.16	9.780	3.356	45.675	0.913	1.201	0.922
12.02	10.443	3.231	46.299	0.918	1.212	0.919
11.09	10.823	3.127	45.742	0.914	1.220	0.909
9.98	11.378	2.982	45.371	0.925	1.221	0.918
8.02	11.668	2.767	40.268	0.907	1.240	0.886
6.21	11.785	2.651	32.893	0.899	1.297	0.840
Weight Concentration = 44.3% (S_m = 1.287)						
13.04	9.456	3.571	43.589	0.876	1.284	0.878
11.98	10.012	3.436	44.067	0.878	1.291	0.874
11.05	10.433	3.325	43.763	0.880	1.300	0.870
10.13	10.920	3.192	43.738	0.892	1.299	0.882
8.34	11.261	3.055	38.798	0.880	1.349	0.838
6.04	11.356	2.804	30.881	0.866	1.384	0.804

Table 3.8: Pump performance with sand-water slurry

C_w (%)	H (m)	P_i (kW)	η_p (%)	HR	PR	ER
Mean Particle Size = 200 µm, Flowrate = 11.99 L/s, Pump Speed = 1200 rpm						
0	11.707	2.723	50.571	1	1	1
10.8	11.477	2.891	50.079	0.981	1.062	0.992
15.2	11.306	2.960	49.628	0.966	1.087	0.983
20.4	11.162	3.074	48.943	0.954	1.129	0.969
25.1	11.027	3.183	48.310	0.942	1.169	0.956
30.1	10.953	3.301	48.036	0.936	1.212	0.950
34.6	10.811	3.413	47.517	0.923	1.253	0.939
39.6	10.628	3.552	46.722	0.908	1.304	0.925
Mean Particle Size = 400 µm, Flowrate = 11.92 L/s, Pump Speed = 1200 rpm						
0	11.784	2.742	50.259	1	1	1
10.2	11.377	2.880	49.371	0.965	1.051	0.982
14.9	11.271	2.985	48.739	0.956	1.089	0.970
20.6	11.009	3.098	47.697	0.934	1.130	0.949
25.9	10.766	3.220	46.661	0.914	1.174	0.928
31.2	10.517	3.344	45.654	0.892	1.219	0.908
35.5	10.319	3.465	44.696	0.876	1.264	0.889
40.1	10.097	3.576	43.983	0.857	1.304	0.875
Mean Particle Size = 605 µm, Flowrate = 11.97 L/s, Pump Speed = 1200 rpm						
0	11.776	2.713	50.965	1	1	1
11.3	11.211	2.874	49.289	0.952	1.059	0.967
15.7	11.001	2.962	48.328	0.934	1.092	0.948
20.1	10.779	3.064	47.222	0.915	1.129	0.927
24.7	10.547	3.175	46.083	0.896	1.170	0.904
31.2	10.189	3.323	44.664	0.865	1.225	0.876

C_w (%)	H (m)	P_i (kW)	η_p (%)	HR	PR	ER
34.3	10.044	3.396	44.130	0.853	1.252	0.866
39.1	9.790	3.526	43.070	0.831	1.299	0.845
Mean Particle Size = 200 µm, Flowrate = 9.08 L/s, Pump Speed = 1200 rpm						
0	12.473	2.334	47.598	1	1	1
8.7	12.154	2.416	47.337	0.974	1.035	0.995
15.0	11.898	2.546	45.975	0.954	1.091	0.966
18.9	11.711	2.598	45.587	0.939	1.113	0.958
24.3	11.478	2.718	44.256	0.920	1.164	0.930
29.6	11.319	2.831	43.591	0.908	1.213	0.916
34.2	11.222	2.910	43.510	0.900	1.247	0.914
39.4	10.964	3.053	42.207	0.879	1.308	0.887
Mean Particle Size = 400 µm, Flowrate = 8.94 L/s, Pump Speed = 1200 rpm						
0	12.537	2.292	47.938	1	1	1
7.2	12.152	2.378	47.196	0.969	1.037	0.985
13.2	11.747	2.454	46.131	0.937	1.071	0.962
20.4	11.398	2.568	44.813	0.909	1.120	0.935
26.5	11.018	2.673	43.297	0.879	1.166	0.903
31.6	10.769	2.784	42.184	0.859	1.214	0.880
35.1	10.659	2.866	41.620	0.850	1.250	0.868
39.7	10.374	2.969	40.563	0.827	1.295	0.846
Mean Particle Size = 605 µm, Flowrate = 9.06 L/s, Pump Speed = 1200 rpm						
0	12.463	2.300	48.137	1	1	1
8.5	11.710	2.435	45.473	0.940	1.059	0.945
21.3	10.939	2.634	42.672	0.878	1.145	0.886
Mean Particle Size = 605 µm, Flowrate = 9.06 L/s, Pump Speed = 1200 rpm						
26.4	10.678	2.718	41.882	0.857	1.182	0.870
31.3	10.506	2.840	40.853	0.843	1.235	0.849
35.59	10.254	2.937	39.817	0.823	1.277	0.827
41.36	9.879	3.056	38.594	0.793	1.329	0.802
Mean Particle Size = 400 µm, Flowrate = 10.08 L/s, Pump Speed = 1050 rpm						
0	9.254	1.915	47.773	1	1	1
14.8	8.731	2.064	45.985	0.943	1.077	0.963
21.97	8.570	2.184	44.998	0.926	1.140	0.942
26.34	8.438	2.246	44.346	0.912	1.173	0.928
31.25	8.364	2.357	43.559	0.904	1.231	0.912
36.33	8.212	2.471	42.297	0.887	1.290	0.885
40.43	8.075	2.601	40.743	0.873	1.358	0.853
Mean Particle Size = 400 µm, Flowrate = 8.06 L/s, Pump Speed = 900 rpm						
0	6.755	1.151	46.380	1	1	1
5.18	6.666	1.181	46.025	0.987	1.026	0.992
11.52	6.542	1.215	45.811	0.968	1.056	0.988
22.80	6.269	1.299	44.279	0.928	1.128	0.955
26.54	6.225	1.358	43.213	0.922	1.180	0.932
35.70	6.046	1.463	41.764	0.895	1.271	0.900

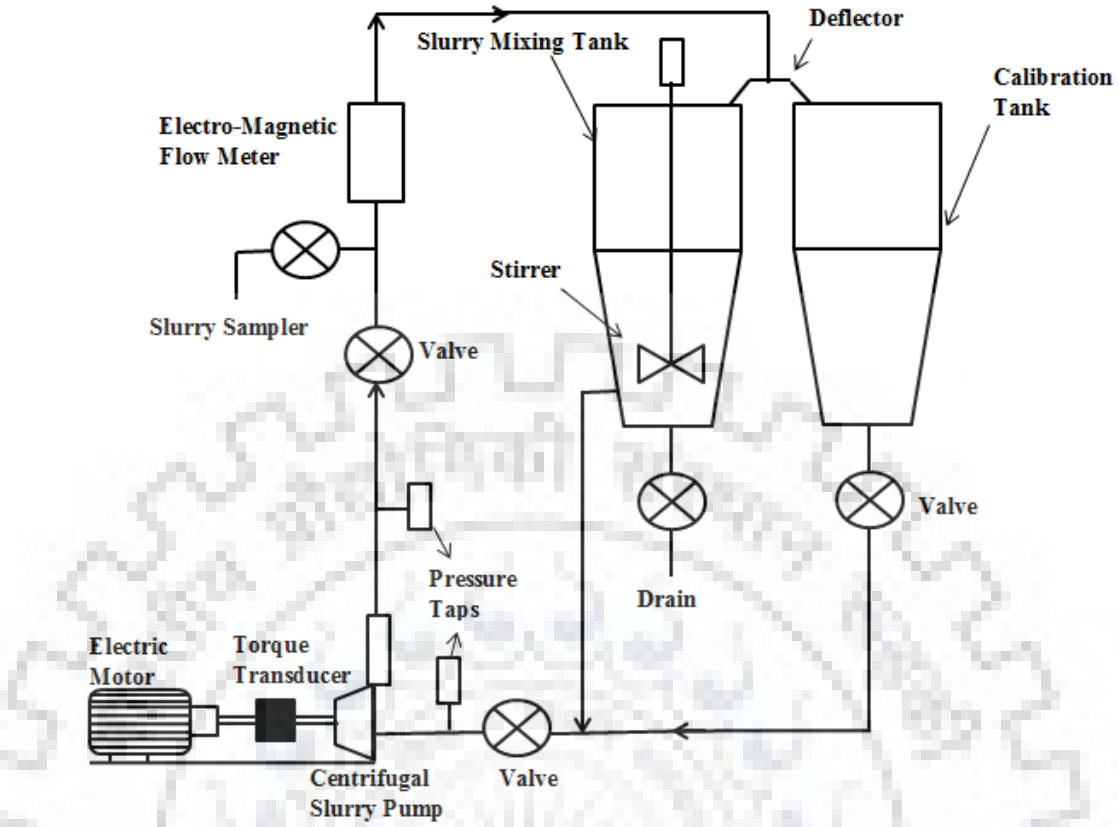

(a)

(b)

Fig. 3.1 Slurry pilot plant test setup (a) Schematic view (b) Photographic view

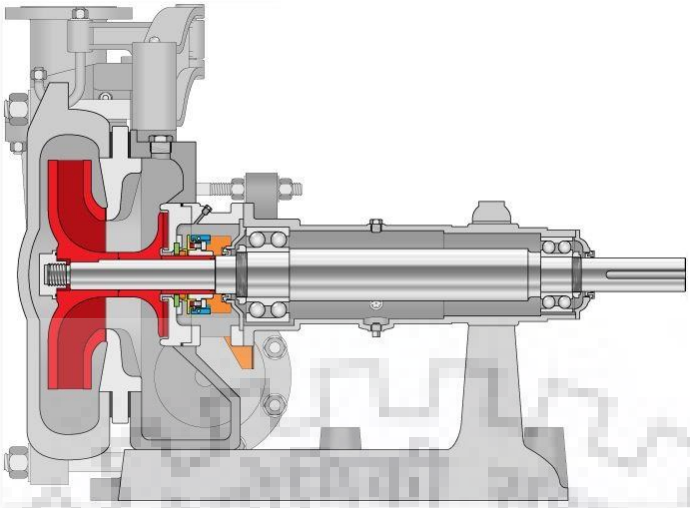

Fig. 3.2 Sectional view of the centrifugal slurry pump [Wilfley, 2006]

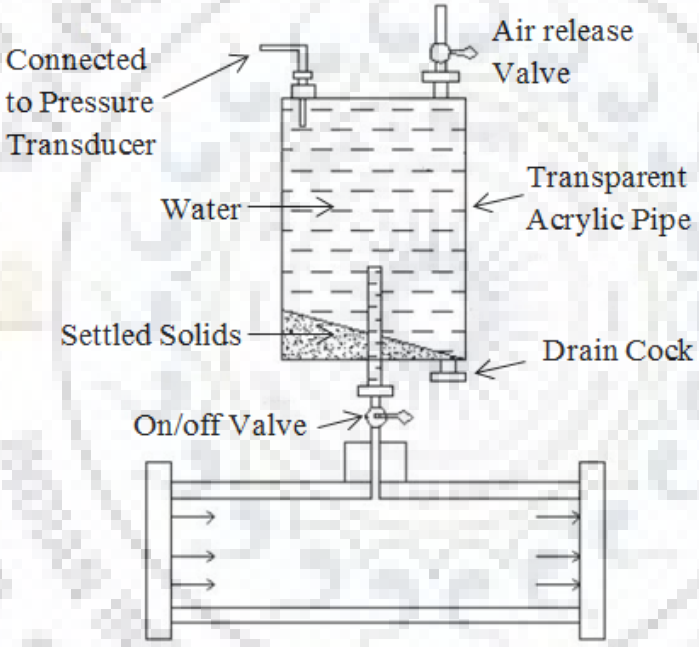

Fig. 3.3 Schematic diagram of the separator

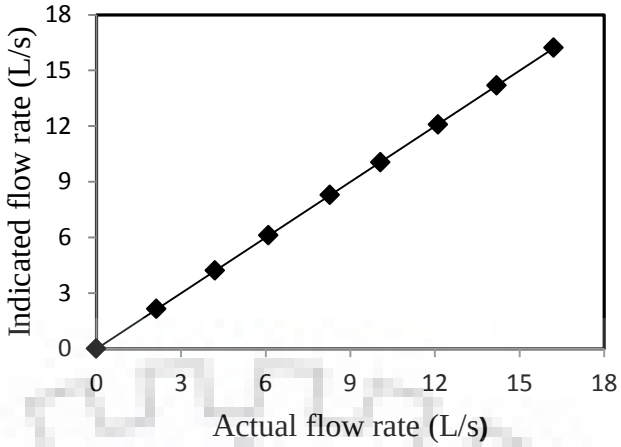

Fig. 3.4 Calibration of electro-magnetic flowmeter

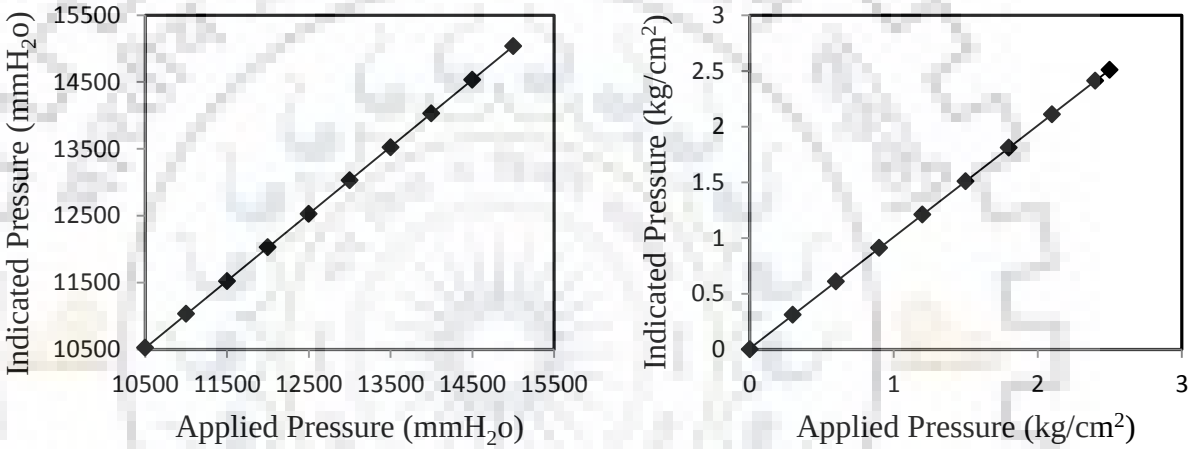

(a) (b)

Fig. 3.5 Calibration of pressure transducers (a) LD 301 (Absolute) at pump inlet (b) LD 301 (Gauge) at pump outlet

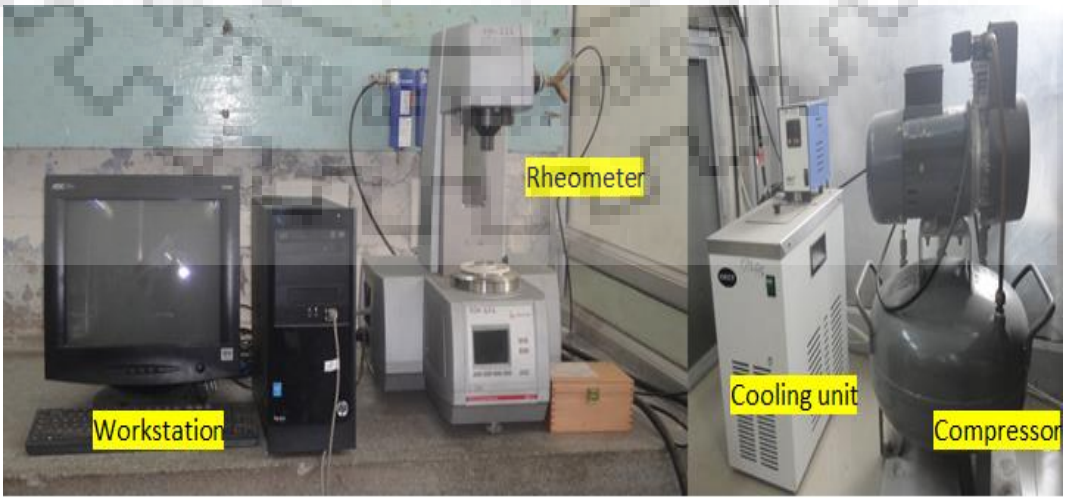

Fig. 3.6 MCR-102 rheometer (Anton Paar Company Ltd., Germany)

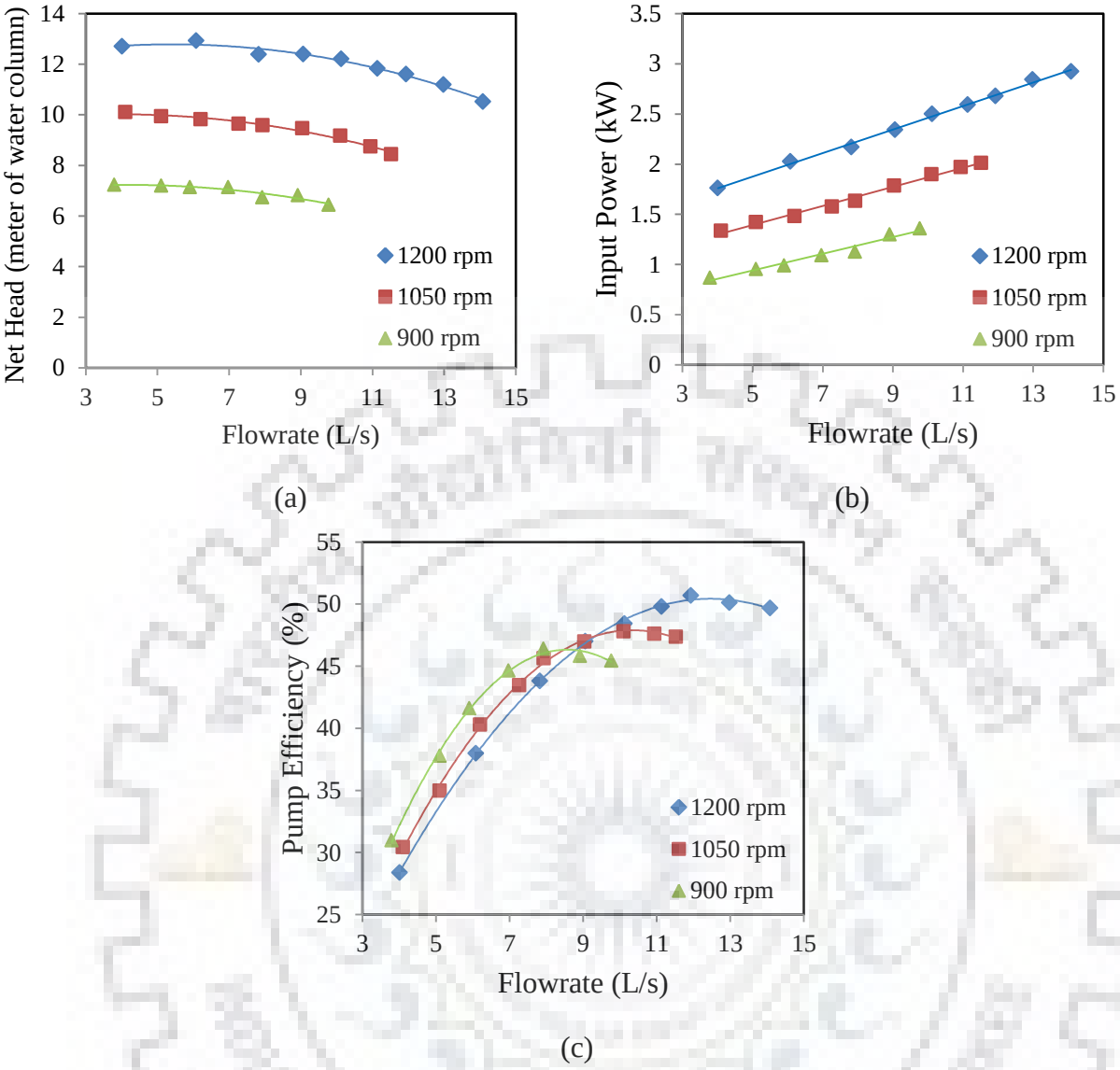

Fig. 3.7 Performance characteristics of the pump at different speeds with clear water (a) Head-Flowrate characteristics (b) Input Power-Flowrate characteristics (c) Efficiency-Flowrate characteristics

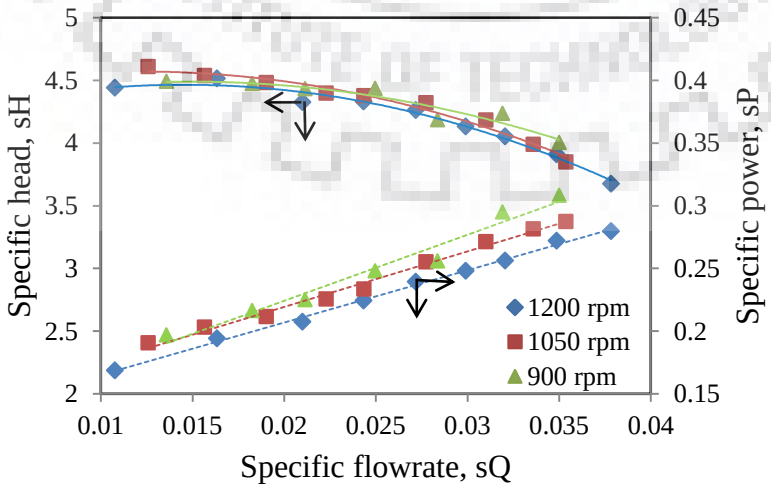

Fig. 3.8 Specific head and specific power characteristics of the pump with clear water

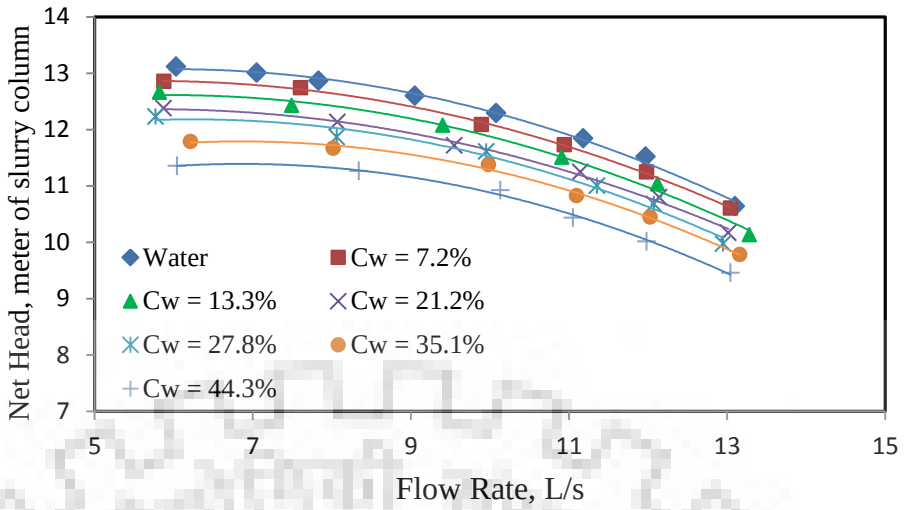

(a)

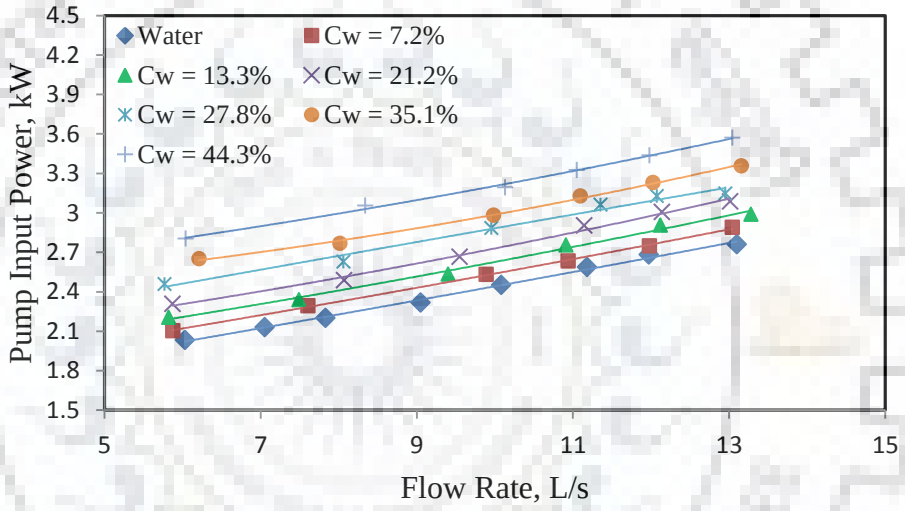

(b)

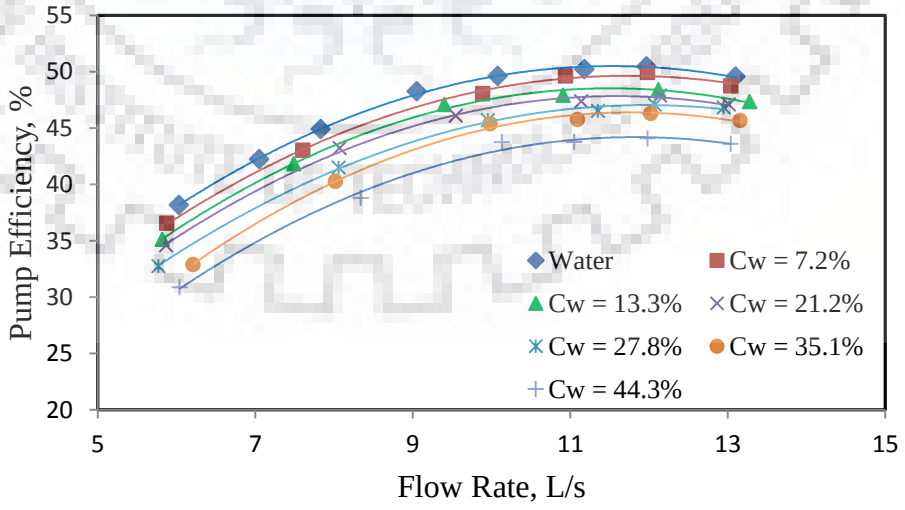

(c)

Fig. 3.9 Performance characteristics of the pump with fly ash slurry at 1200 rpm (a) Head-Flowrate characteristics (b) Input Power-Flowrate characteristics (c) Efficiency-Flowrate characteristics

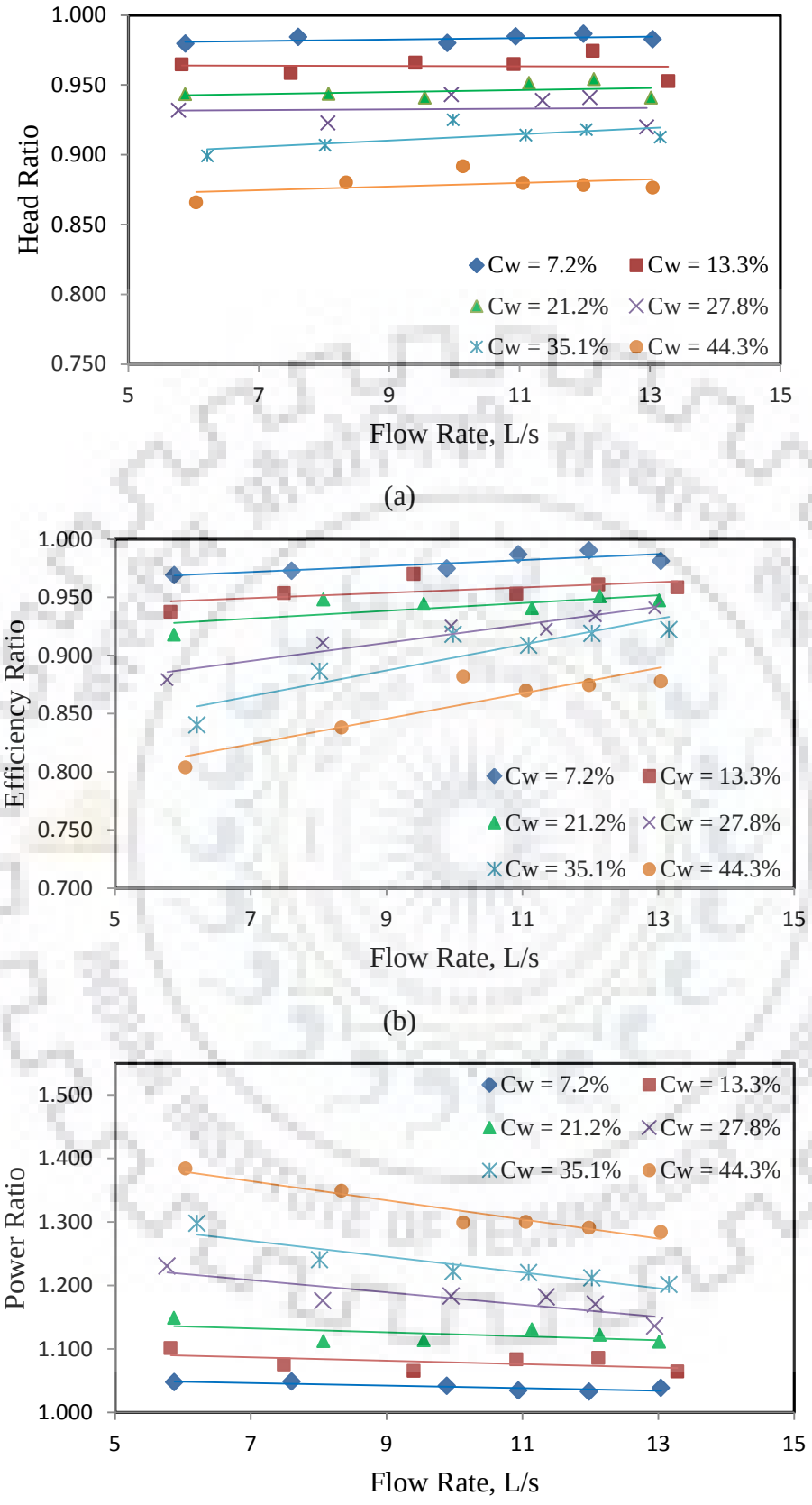

Fig. 3.10 Variation in (a) head ratio, (b) efficiency ratio, and (c) power ratio with flow rate for different weight concentrations of fly ash slurry

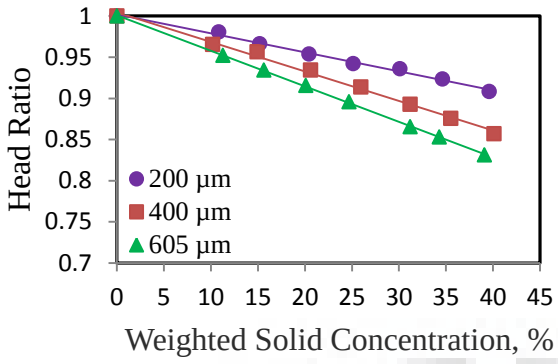

(a)

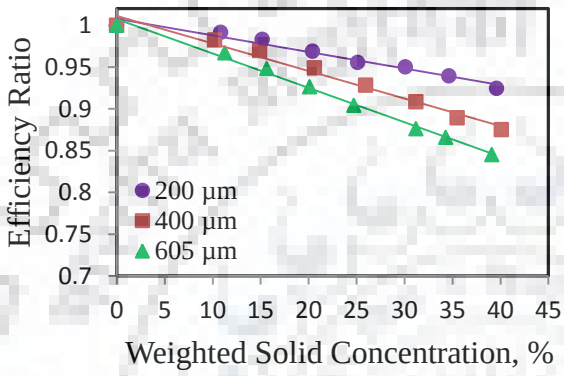

(b)

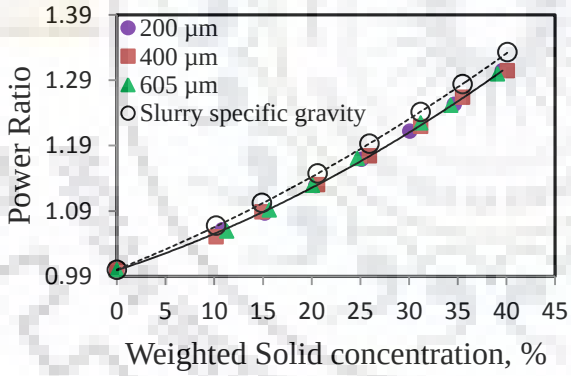

(c)

Fig. 3.11 Effect of particle size on (a) head ratio, (b) efficiency ratio and (c) power ratio for different weighted solid concentrations at BEP flowrate for 1200 rpm rotational speed

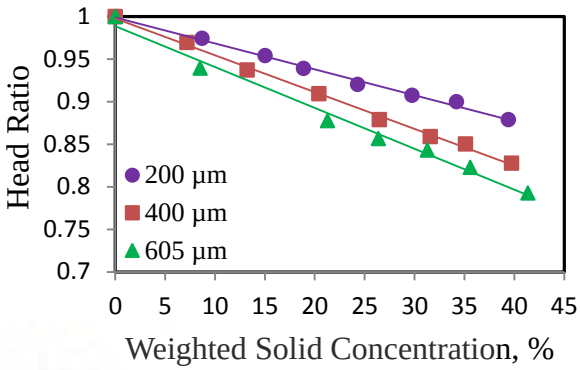

(a)

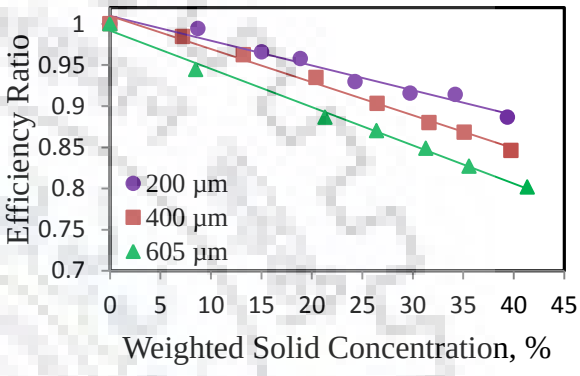

(b)

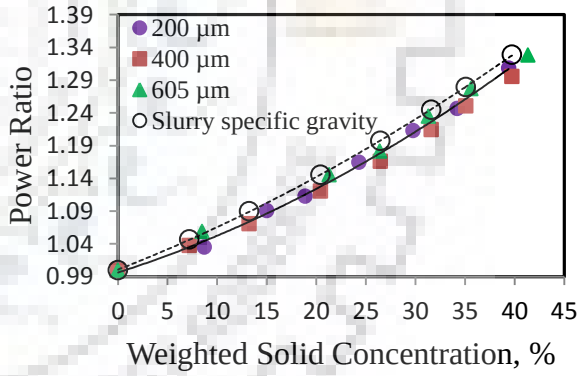

(c)

Fig. 3.12 Effect of particle size on (a) head ratio, (b) efficiency ratio and (c) power ratio for different weighted solid concentrations at 0.75 BEP flowrate for 1200 rpm rotational speed

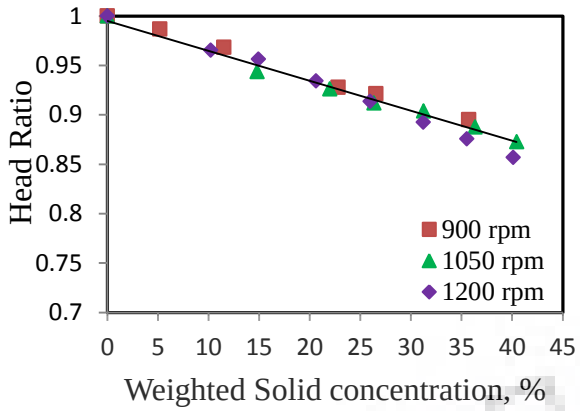

(a)

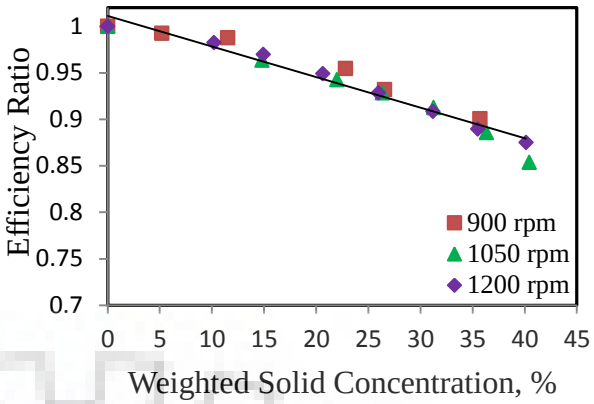

(b)

Fig. 3.13 Variation in (a) head ratio, and (b) efficiency ratio with 400 µm sand particles at different solid concentrations and rotational speeds

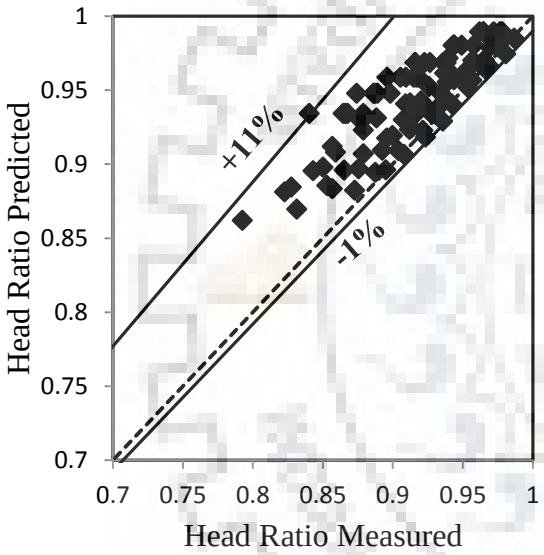

(a) Correlation of Vocaldo et al. [1974]

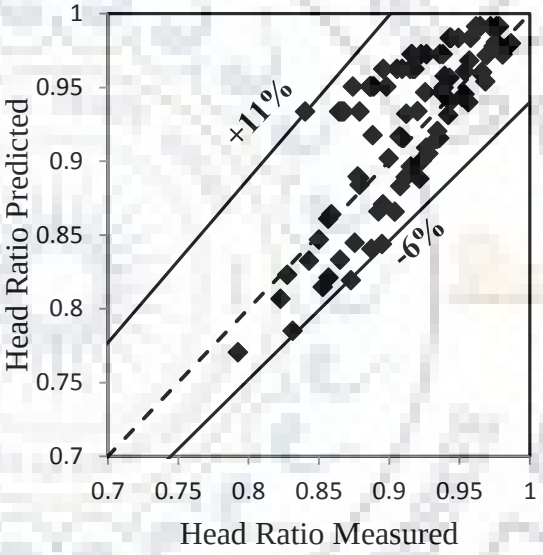

(b) Correlation of Burgess and Reizes [1976]

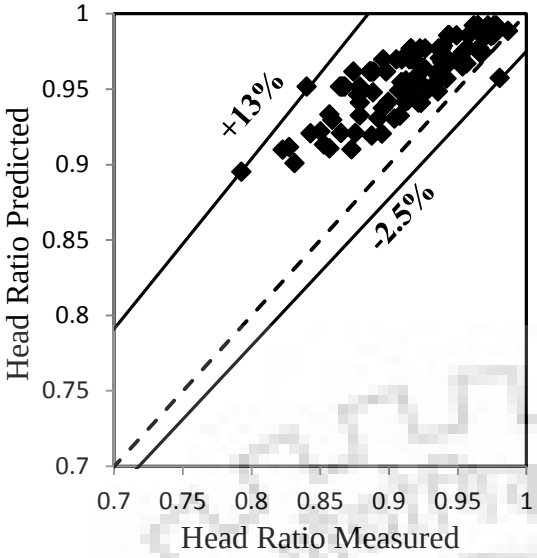

(c) Correlation of Gahlot et al. [1992]

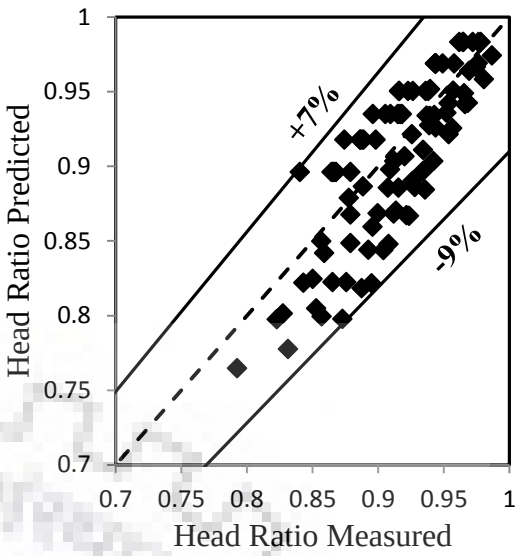

(d) Correlation of Kazim et al. [1997]

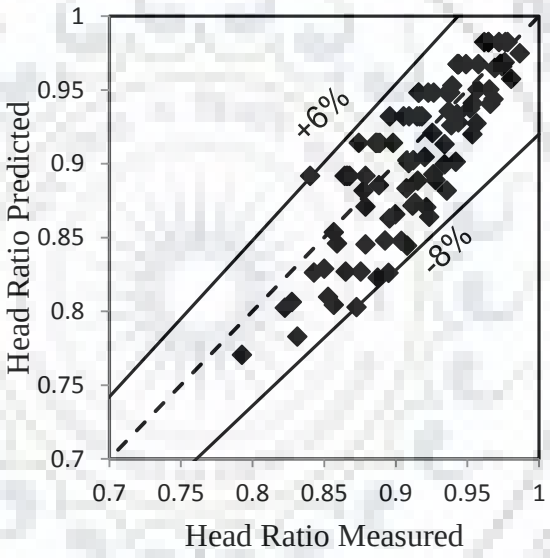

(e) Correlation of Engin and Gur [2003]

Fig. 3.14 Comparison of measured and predicted head ratio using different available correlations in literature

CHAPTER 4: NUMERICAL PREDICTION OF A CENTRIFUGAL SLURRY PUMP PERFORMANCE

The effect of solids on the performance of a centrifugal slurry pump is of major concern to the designers of a slurry transportation system. In recent years, the CFD has become an attractive approach for simulation of multiphase flows [Krishnan et al., 2010]. Literature [Liu et al., 2009; Zhang et al., 2013; Tao et al., 2017] reveals that limited efforts are made to carry out the numerical investigation of centrifugal slurry pump for estimating its performance and the flow field. In commercial CFD codes, two different approaches are available to model the dense slurry flow, namely Eulerian-Eulerian and Mixture models. Most of the investigations on pump has been carried out using one of the two models, however, the use of one approach over another has not been completely justified in literature [Liu et al., 2009; Wang et al., 2012; Zhao et al., 2012; Zhang et al., 2013; Tao et al., 2017]. Thus, an understanding of difference between the two multiphase modeling approaches in CFD for prediction of pump performance is still uncovered which may be useful for designer during selection and design optimization of pump for different industrial applications. The particle flow field studies using CFD [Zhao et al., 2012; Zhang et al., 2013], inside the pump components are mostly reported at the impeller mid-plane and there is some ambiguity regarding the location of high concentration which is one of the critical parameters affecting the erosion. An understanding of the three dimensional particle flow behavior inside the pump flow passages may help the designer to mitigate the uneven erosion of the components. Literature [Liu et al., 2009; Wang et al., 2012; Zhao et al., 2012; Zhang et al., 2013; Tao et al., 2017] reveals that the efforts were made to numerically evaluate the pump performance using only equi-sized slurry. It may be primarily attributed to the requirement of less computational efforts with single size particles as compared to the multi-size particles. However, wide particle size distribution (PSD) is generally present during pipeline transportation of solids in process industries. The variation in particle size distribution significantly affects the pump performance [Benretem et al., 2007]. The study of the effects of multi-size solid particles on pump performance characteristics with variation in PSD is at best incomplete. An understanding of the effect of particle gradation on pump performance and particle flow field may help the designer in designing the slurry pipeline for better flow stability.

In the present study, three-dimensional numerical simulations of a centrifugal slurry pump are performed with multiple moving reference frames (MRF) approach and the sliding mesh approach using commercial CFD code ANSYS Fluent 19.0. The accuracy of the pump

modeling approach is checked by comparing the performance characteristics of the pump obtained numerically and experimentally with water. Further, a study has been performed to develop an effective model for CFD simulation of the pump handling solid-liquid mixture. Two multiphase modeling approach "granular Eulerian-Eulerian" and "granular Mixture" are compared with the experimental measurements with sand-water slurry. An unsteady modeling approach is applied to carry out the complete investigation. Equi-sized particles are used for the simulations. The effects of particle size, solid concentration, and specific gravity on the pump performance and flow field are investigated. Further, a study has been carried out to determine the effect of PSD on the pump performance and flow field. For this purpose, the numerical modeling of the pump is performed with multi-sized particulate slurry using granular Eulerian-Eulerian multiphase model. The accuracy of the modeling approach is compared with the experimentally obtained pump performance for multi-size fly ash slurry.

4.1 Introduction to CFD

CFD is a branch of fluid mechanics that uses numerical methods and algorithms to solve and analyse problems that involve fluid flow or heat transfer. It is being widely used by the modern research community to determine the approximate solution of the fluid flow and heat transfer problems.

Even though, CFD gives an approximate solution but benefits like low cost, flexibility and universality emphasis its importance as compared to experimental and theoretical methods [Zikanov, 2010]. CFD is also helpful in solving problems involving complex geometry and abnormal operating conditions which are difficult to achieve in laboratory tests. Currently, a number of commercial CFD codes are available, like ANSYS FLUENT, ANSYS CFX, FLOTRAN, FLO EFD etc., which can be used to simulate the problems.

The whole CFD approach can be classified into three main steps:

i. **Pre-processing:** This step includes modeling of the components, mesh generation and imposing the boundary conditions. The first step is modeling of the geometry of flow domain. The fluid is considered as a continuous medium with occupying the shape of geometry. Second step is then discretization of the flow domain into small units known as cells and this process is called meshing. Third step is to define the boundary conditions to the problem, however, before that the flow conditions have to be understood completely. The boundary conditions include fluid used, operating conditions, flow parameters etc., and they play a vital role in achieving accurate and converging solution.

ii. **Solver:** In this step the governing equations of the fluid flow are solved. To solve these equations a suitable CFD code is chosen to solve the problem defined in the previous stage. The solution is obtained after achieving the specified convergence criteria.

iii. **Post processing:** In this step the obtained results are analysed with different methods like graphs, contour plots, vector plots, streamlines, etc.

4.2 Numerical Modeling of a Centrifugal Slurry Pump Handling Clear Water

In this study, 3D numerical simulations of centrifugal slurry pump handing clear water is performed using the commercial CFD code Fluent 19.0. This code works on finite volume approach to solve the governing equations for steady or unsteady fluid flows. The steady and unsteady simulations of the pump are performed using multiple reference frame (MRF) and sliding mesh (SM) approaches. The accuracy of the numerical simulations is checked through the experimentally obtained pump performance characteristics.

4.2.1 Mathematical Model

4.2.1.1 Continuity Equation:

It states that the rate of change of mass within a control volume is equal to the net inflow of mass. For three-dimensional incompressible unsteady flow in stationary frame, it can be mathematically written as:

$$\frac{\partial \rho}{\partial t} + \nabla \bullet (\rho V) = 0 \tag{4.1}$$

4.2.1.2 Momentum Equation:

According to law of conservation of momentum, the net force acting on the control volume is equal to rate of change of momentum within the control volume and rate at which the momentum is leaving the control volume. For three-dimensional incompressible unsteady flow in stationary frame, it can be mathematically written as:

$$\frac{\partial (\rho V)}{\partial t} + \nabla \bullet (\rho V V) = -\nabla p + \nabla \bullet \bar{\bar{\tau}} + \rho g + S_M \tag{4.2}$$

Where $\bar{\bar{\tau}}$ is the stress tensor expressed as:

$$\bar{\bar{\tau}} = \mu \left(\nabla V + (\nabla V)^T - \frac{2}{3} \delta \nabla \bullet V \right) \tag{4.3}$$

For flow in a rotating frame of reference, rotating at a constant angular velocity (ω), additional sources of momentum are required to consider the effects of Coriolis force and the centrifugal force:

$$S_{M,rot} = S_{cor} + S_{cfg} \tag{4.4}$$

Where $S_{cor} = -2\rho\omega \times V_r$ and $S_{cfg} = -\rho\omega \times (\omega \times r)$,

and where 'r' is the location vector and V_r is the relative velocity. The absolute velocity (V) and the relative velocity (V_r) are related by the following equation

$$V_r = V - (\omega \times r) \tag{4.5}$$

4.2.1.3 Turbulence Models

Turbulence is a chaotic state which is characterised by random fluctuation of flow parameters such as velocity, pressure etc. with respect to space and time. These fluctuations can be of small scale and high frequency. The computational cost to simulate these fluctuations in practical engineering problems is very high. Therefore, for computationally less expensive solutions, the instantaneous governing equations are solved using time-averaged, ensemble-averaged based approach (Reynolds averaging) or otherwise through a filter based approach. This includes additional unknown variables in the governing equations, and turbulence models are required to estimate these in terms of known quantities. For complex turbulent flows, time averaged Reynolds Averaged Navier-Stokes (RANS) equation is widely adopted in practical engineering problems to get the solution as the "filtered" Navier-Stokes equations (Large Eddy Simulation) are computationally more expensive.

In RANS, the solution variables in the instantaneous Navier-Stokes equations are decomposed into two components, one the mean component (ensemble-averaged or time-averaged) while the other represents the fluctuating nature. For example, a velocity (v) may be divided into an average component (V) and a fluctuating component (v') as shown in Eq. (4.6).

$$v = V + v' \tag{4.6}$$

Substituting the flow variables in this form into the instantaneous Navier-Stokes equations and taking a time (or ensemble) average yields RANS equations. The RANS equations can be written in Cartesian form as:

$$\frac{\partial \rho}{\partial t} + \nabla \bullet (\rho V) = 0 \tag{4.7}$$

$$\frac{\partial (\rho V)}{\partial t} + \nabla \bullet (\rho V V) = -\nabla p + \nabla \bullet \left\{ \bar{\bar{\tau}} - \rho \overline{v' v'} \right\} + \rho g + S_M \tag{4.8}$$

The general form of RANS equations is similar to the instantaneous Navier-Stokes equations, with flow variables now representing time-averaged values. The additional term, $-\rho\overline{v'v'}$ is known as the Reynolds stress. It represents the effects of turbulence and need to be modeled for the closure of the Eq. (4.8).

Generally, the Boussinesq hypothesis is used to relate the Reynolds stress to the mean velocity gradients:

$$-\rho\overline{v'v'} = \mu_t\left(\nabla V + (\nabla V)^T\right) - \frac{2}{3}\delta\left(\rho k + \mu_t \nabla \bullet V\right) \tag{4.9}$$

This approach was used in Spalart-Allmaras model, the k-ε models, and the k-ω models. The benefit of this approach is the less computational resources requirement to compute the turbulent viscosity (μ_t). Subject to this hypothesis, the Eq. (4.8) becomes:

$$\frac{\partial(\rho V)}{\partial t} + \nabla \bullet (\rho V V) = -\nabla p' + \nabla \bullet \left(\mu_{eff}\left(\nabla V + (\nabla V)^T\right)\right) + \rho g + S_M \tag{4.10}$$

where μ_{eff} is the effective viscosity expressed as:

$$\mu_{eff} = \mu + \mu_t \tag{4.11}$$

and p' is the modified pressure expressed as:

$$p' = p + \frac{2}{3}\rho k + \frac{2}{3}\mu_t \nabla \bullet V \tag{4.12}$$

4.2.1.3.1 Standard k-ε Model

The standard k-ε model is the simplest of the two-equation models. It is the semi-empirical model based on the turbulent kinetic energy (k) and its dissipation rate (ε) given by Launder and Spalding [1972]. In this the turbulent viscosity is linked to k and ε via relation:

$$\mu_t = \rho C_\mu \frac{k^2}{\varepsilon} \qquad \text{where, } C_\mu = 0.09 \tag{4.13}$$

The k and ε values are determined from transport equations:

$$\frac{\partial(\rho k)}{\partial t} + \nabla \bullet (\rho V k) = \nabla \bullet \left[\left(\mu + \frac{\mu_t}{\sigma_k}\right)\nabla k\right] + p_k - \rho\varepsilon \tag{4.14}$$

$$\frac{\partial(\rho \varepsilon)}{\partial t} + \nabla \bullet (\rho V \varepsilon) = \nabla \bullet \left[\left(\mu + \frac{\mu_t}{\sigma_\varepsilon}\right)\nabla \varepsilon\right] + \frac{\varepsilon}{k}\left(C_{\varepsilon 1} p_k - C_{\varepsilon 2}\rho\varepsilon\right) \tag{4.15}$$

where $C_{\varepsilon 1} = 1.44$, $C_{\varepsilon 2} = 1.92$, $\sigma_k = 1.0$ and $\sigma_\varepsilon = 1.3$. The p_k in above equations is the turbulence kinetic energy production term. For incompressible flow it is expressed as:

$$p_k = \mu_t \nabla V \bullet \left(\nabla V + \nabla V^T\right) - \frac{2}{3}\nabla \bullet V\left(3\mu_t \nabla \bullet V + \rho k\right) \tag{4.16}$$

4.2.1.3.2 RNG k-ε Model

In this the equations of the k-ε model was derived using renormalisation group theory. The analytical solution results in a model with constants different from those in the standard k-ε model.

$$\frac{\partial(\rho k)}{\partial t}+\nabla\bullet(\rho V k)=\nabla\bullet\left[\left(\mu+\frac{\mu_t}{\sigma_k}\right)\nabla k\right]+p_k-\rho\varepsilon \tag{4.17}$$

$$\frac{\partial(\rho \varepsilon)}{\partial t}+\nabla\bullet(\rho V \varepsilon)=\nabla\bullet\left[\left(\mu+\frac{\mu_t}{\sigma_\varepsilon}\right)\nabla \varepsilon\right]+\frac{\varepsilon}{k}\left(C_{\varepsilon 1}p_k-C^*_{\varepsilon 2}\rho\varepsilon\right) \tag{4.18}$$

where

$$C^*_{\varepsilon 2}=C_{\varepsilon 2}+\frac{C_\mu\eta^3\left(1-\eta/\eta_o\right)}{1+\beta_{RNG}\eta^3} \tag{4.19}$$

and $\eta=S_d k/\varepsilon$, $S_d=\sqrt{2S_{ij}S_{ij}}$

$$S_{ij}=\frac{1}{2}\left(\frac{\partial v_j}{\partial x_i}+\frac{\partial v_i}{\partial x_j}\right) \tag{4.20}$$

The turbulent viscosity is being calculated in the same manner as with the standard k-ε model. All the constants (except β_{RNG}) are derived explicitly in the RNG procedure. They are given as; C_μ = 0.0845, $C_{\varepsilon 1}$ = 1.42, $C_{\varepsilon 2}$ = 1.68, σ_k = 0.7194, σ_ε = 0.7194, η_o = 4.38 and β_{RNG} = 0.012 (derived from experiments).

4.2.1.3.3 Realizable k-ε Model

This model is a modification of the standard k-ε model which differs in two important ways. It uses a modified equation for dissipation rate and a different formulation for the turbulent viscosity. However, one limitation with this model is that it produces non-physical turbulent viscosities while modeling the computational domain using MRF and SM approaches.

The transport equation for dissipation rate is expressed as:

$$\frac{\partial(\rho \varepsilon)}{\partial t}+\nabla\bullet(\rho V \varepsilon)=\nabla\bullet\left[\left(\mu+\frac{\mu_t}{\sigma_\varepsilon}\right)\nabla \varepsilon\right]+\rho C_1 S\varepsilon-\rho C_2\frac{\varepsilon^2}{k+\sqrt{\nu\varepsilon}} \tag{4.21}$$

where, $C_1=\max\left[0.43,\frac{\eta}{\eta+5}\right]$, C_2 = 1.9, σ_k = 1.0 and σ_ε = 1.2.

The turbulent viscosity is calculated similar to the standard k-ε model. However in this, C_μ is no longer constant. It is computed from

$$C_\mu=\frac{1}{A_0+A_s\frac{kV^*}{\varepsilon}} \tag{4.22}$$

where
$$V^*=\sqrt{S_{ij}S_{ij}+\tilde{\Omega}_{ij}\tilde{\Omega}_{ij}} \tag{4.23}$$

and
$$\tilde{\Omega}_{ij}=\Omega_{ij}-2\varepsilon_{ijk}\omega_k$$

$$\Omega_{ij}=\overline{\Omega_{ij}}-\varepsilon_{ijk}\omega_k$$

where $\overline{\Omega_{ij}}$ is the mean rate of rotation tensor viewed in rotating reference frame with the angular velocity ω_k. The model constants A_0 and A_s are given as:

$$A_0 = 4.04,\ A_s = \sqrt{6}\cos\phi$$

where $$\phi = \frac{1}{3}\cos^{-1}\left(\sqrt{6}W\right),\ W = \frac{S_{ij}S_{jk}S_{ki}}{\tilde{S}},\ \tilde{S} = \sqrt{S_{ij}S_{ij}}$$

4.2.1.3.4 k-ω Model

This model solves two equations, one for turbulent kinetic energy (k) while the other one for turbulent frequency (ω) defined as ratio of dissipation rate (ε) and turbulent kinetic energy (k). The k-ω model predicts better results for flows having adverse pressure gradients and boundary layer separation. However it is highly sensitive to the changes in values of k and ω outside the shear layer. The transport equations involved in k-ω model are:

k-equation

$$\frac{\partial(\rho k)}{\partial t} + \nabla\bullet(\rho V k) = \nabla\bullet\left[\left(\mu + \frac{\mu_t}{\sigma_k}\right)\nabla k\right] + p_k - \beta'\rho k\omega \qquad (4.24)$$

ω-equation

$$\frac{\partial(\rho\omega)}{\partial t} + \nabla\bullet(\rho V \omega) = \nabla\bullet\left[\left(\mu + \frac{\mu_t}{\sigma_\omega}\right)\nabla\omega\right] + \gamma\frac{\omega}{k}p_k - \beta\rho\omega^2 \qquad (4.25)$$

P_k is the production rate of turbulence, which is calculated as in the k-ε model. The constants in the model are given as: $\beta' = 0.09$, $\alpha = 5/9$, $\beta = 0.075$, $\sigma_k = 1/2$ and $\sigma_\omega = ½$.

4.2.1.4 Near Wall Flow Modeling

In the turbulent flow along, the turbulence is directly affected by the presence of a solid boundary, as viscosity is dominant in the vicinity of the solid boundary. The solution variables have large gradients, and the momentum and other scalar transports occur most vigorously. Therefore, near wall treatment is essential for successful flow predictions in wall bounded turbulent flows. Generally, the near wall region is commonly divided into three layers: turbulent layer, buffer layer and viscous sublayer. The nearest region to the wall is the viscous sublayer as shown in Fig. 4.1.

In the CFD code Fluent, there are two approaches for modeling the near-wall region termed as "wall function" and "near wall modeling" presented in Fig. 4.2. In wall function, semi-empirical formulas are used to bridge the viscosity-affected region (viscous sublayer and buffer layer) between the wall and the fully-turbulent region. In near wall modeling, the viscosity-affected region needs to be resolved with a mesh throughout the wall, including the viscous

sublayer. In most high-Reynolds-number industrial flow simulations, wall function approach is mostly preferred, because it is economical, robust, and reasonably accurate.

In the CFD code Fluent, the standard wall functions are based on the proposal of Launder and Spalding [1974]. The law of the wall for mean velocity is given by:

$$V^* = \frac{1}{\kappa}\ln(Ey^*) \tag{4.26}$$

Where,

$$V^* = \frac{V_p C_\mu^{1/4} k_p^{1/2}}{\tau_w / \rho} \tag{4.27}$$

$$y^* = \frac{\rho C_\mu^{1/4} k_p^{1/2} y_p}{\mu} \tag{4.28}$$

κ = von Karman constant (=0.4187), E = empirical constant (=9.793), V_p = mean velocity of fluid at point P, k_p = turbulent kinetic energy at point P, y_p = distance from point P to the wall, μ = dynamic viscosity of fluid

The logarithmic wall function for mean velocity is known to be valid for $30<y^*<300$.

4.2.2 Geometry and Meshing of Pump Components

The geometry of the flow domain for the numerical simulations is to be generated on a suitable platform. In the present study, the pump chosen was "50M WILFLEY" centrifugal slurry pump which is installed in the slurry research laboratory of IIT Roorkee. The pump geometry details (Table 3.1) are used to generate a CAD model in PRO-E. After modeling different pump components, the flow domain i.e. the region in which the fluid flows inside the pump is obtained using the cut-out operation in Pro-E and is shown in Fig. 4.3 (a,b). The second step after modeling the geometry is discretization of the whole domain into small parts or elements. This process of discretization is termed as meshing of the domain. For this purpose, the modeled flow domain is imported in ANSYS ICEM. It is divided into different sub-domains namely suction, impeller, and casing. Unstructured mesh consists of hexahedral, tetrahedral, and prism element is generated for each sub-domain as shown in Fig. 4.4 (a-c). The mesh of separate computational domains is then connected through interfaces to obtain the complete mesh model of the pump as shown in Fig. 4.4 (d). The y+ value for the computational domain is varied in the range of 50 to 160. Further, to obtain a solution, independent of mesh resolution, mesh independency check is also performed, as discussed later.

4.2.3 Solution Strategy

4.2.3.1 Modeling of Relative Motion of Stationary and Rotating Components

The interfaces between rotating and stationary components, namely, impeller to suction (Interface I) and impeller to casing (Interface II) (see Fig. 4.3b), can be modeled using two different approaches: MRF or SM.

4.2.3.1.1 MRF Approach

In this approach, the mesh remains fixed during simulation. For the numerical simulations of the pump model, the calculation domain is divided into three cell zones. The suction and casing cell zones are kept stationary, while the impeller cell zone is given a rotation. The rotating and stationary equations are solved separately. At the interface, the coupling of the cell zones is performed using velocity transformation. Flow variables at the interface of these cell zones are assumed steady. This assumption allows predicting the complete flow field of the pump through steady-state calculations to save simulation time.

4.2.3.1.2 SM Approach

SM approach applies time-dependent simulations. The impeller zone is allowed to slide relative to the casing and suction zone, with no mesh distortion. All the three zones share the same inertial reference frame and connected through sliding mesh algorithm. It accounts the relative motion between the zones, and determines the flow variables and face fluxes across the interfaces using conservative interpolations. The simulations may be initialized with the solution of MRF model for faster convergence.

4.2.3.2 Boundary Conditions

The velocity inlet and pressure outlet are set as boundary conditions at inlet and outlet of the pump, respectively. The rotational speed of the impeller is set to be 1200 rpm. Table 4.1 shows the solution methodology adopted for the numerical simulations.

4.2.3.3 Data Evaluation

The net head developed by the pump is estimated from the difference of the total head (sum of pressure head, velocity head, and potential head) at outlet and inlet. The calculation of efficiency is performed as,

$$\eta_p = \frac{\rho g Q H}{T.\omega} \tag{4.29}$$

4.2.4 Optimization of Time Step Size and Number of Impeller Revolutions

Centrifugal pumps are normally operated under high-speed conditions. To achieve high accuracy in results along with numerical stability, sufficiently small time step size is required [Cheah et al., 2011]. However, decrease in time step size increases the cost of computation. In literature, Gonzalez et al. [2002] used the time step size of 2.94 $x10^{-4}$ seconds (2.857 degree) for simulating the pump at a rotational speed of 1620 rpm (= 169.65 rad/s). Barrio et al. [2011] used 5.8 $x10^{-5}$ seconds (0.9 degree) for simulating the pump at a rotational speed of 2600 rpm (= 272.27 rad/s). In the present case, the pump speed is different, which is 1200 rpm (= 125.66 rad/s). Therefore, to choose an optimum time step size for reasonably accurate results, simulations are performed initially for different time step sizes. Five different time steps of 1.25×10^{-3}, 8.33×10^{-4}, 5.55×10^{-4}, 4.167×10^{-4} and 2.778×10^{-4} seconds that are equivalent to 9^{o}, 6^{o}, 4^{o}, 3^{o} and 2^{o} of impeller rotation, respectively, are being selected for the study. The simulations with each time steps are performed at a rotational speed of 1200 rpm and flow rate of 12 L/s for the mesh size of approximately 2.72 million elements. The net head predicted at different time steps is plotted in Fig. 4.5. It is observed that the prediction of the net head developed by pump is reduced with the reduction in the time step size. However, after reduction in the time step size corresponding to 3^{o} of impeller rotation, there is no significant variation is observed in the net head values. Hence the time step size for 3^{o} impeller rotation which is equivalent to 4.167×10^{-4} seconds is selected to obtain the performance characteristics of the pump.

In unsteady simulations, the results should reach to a stable periodicity for convergence. Gonzalez et al. [2002] and Barrio et al. [2011] reported that at least five impeller revolutions were required to achieve unsteady convergence in the results with stable periodicity. Zhang et al. [2016] obtained the stable periodicity in the results for nearly 30 impeller revolutions. Therefore, to get the information about the minimum number of impeller revolutions required to achieve a stable solution, initial simulations are performed for each time step as shown in Fig. 4.5. It is observed that the solution started to become stable after nine impeller revolutions. Hence to achieve the solution independency on impeller rotation, total ten impeller revolutions are selected for initial simulation. The average data of the one complete impeller revolution of eleventh rotation is used for further analysis.

4.2.5 Mesh Independency

In complex numerical problems, the near-wall region becomes a major source of vortices and turbulence. In this region, the gradient of quantities is high and to obtain numerical solutions of high accuracy, fine grids are required. It may increase the cost of computation and also requires

a large memory to store them. Hence, the wall function approach is generally favoured to model the flow over the near wall region discussed earlier in section 4.2.1.4. With this approach the high gradient shear layers near walls can be modeled with relatively coarse meshes, yielding substantial savings in computational time and storage. Apart from the mesh size, the quality of the mesh is another parameter which needs to be considered to get better accuracy and stability of the results. The orthogonal quality check is required to observe the mesh quality which varies from 0 to 1. Close to 1 is the good quality mesh. For complex geometries, the orthogonal quality should be greater than 0.2 [Fluent 6.3, 2006]. To obtain the optimum mesh, grid independency test is needed to perform. For this purpose, six different mesh geometries named as G1 to G6 are developed with mesh elements in the range of 1.20 million to 4.93 million. The details of the number of elements in the mesh for each component and the minimum orthogonal quality achieved with the complete mesh model are listed in Table 4.2. The simulation with different meshes is performed at flowrates of 6 L/s, 9 L/s, and 12 L/s for the pump speed of 1200 rpm. The predicted pump performance with all the meshes is shown in Fig. 4.6. It is observed that the predicted net head and efficiency values decrease with the mesh G1 to G6. The percent decrease in net head values at 12 L/s flow rate with G2, G3, G4, G5, and G6 mesh corresponding to G1 mesh is 5.43%, 8.55%, 9.51%, 10.07%, and 10.23%, respectively. The percentage decrease in predicted efficiency values at 12 L/s flowrate with G2, G3, G4, G5, and G6 mesh corresponding to G1 mesh is 10.65%, 16.14%, 20.16%, 20.28%, and 20.31% respectively. Similar trend of decrease in the predicted results with different meshes were also observed at the flow rate of 6 L/s and 9 L/s. It is seen that the decrease in head and efficiency results from G4 to G6 mesh corresponding to G1 mesh is <1%. However the number of mesh elements increases to almost 1.43 times and 1.81 times of G4 mesh for G5 and G6 mesh, respectively. Hence to save the computational cost along with good accuracy in the result, the G4 mesh having the minimum orthogonal quality of 0.32 is selected to simulate the pump performance characteristics.

4.2.6 Turbulence Models Comparison

To select a suitable turbulence model, the simulations are performed with four two-equation turbulence models, namely Standard k-ε, Realizable k-ε, RNG k-ε and Standard k-ω at a rotational speed of 1200 rpm for 6 L/s, 9 L/s, and 12 L/s flowrate. The predicted net head with different turbulence models is presented in the Table 4.3. It is observed that the predicted net head values obtained with different turbulence models is not showing significant variation. The standard k-ε turbulence model predicted little higher net head than the other turbulence models and is about 0.38% higher than that of the standard k-ω turbulence model. However, in terms of

convergence speed, standard k-ε turbulence model is the fastest and more robust. Therefore, the standard k-ε model is selected for the present work.

4.2.7 Validation of Numerical Method

The head-discharge and efficiency-discharge characteristics of the pump with water are evaluated at 1200 rpm by conducting experiments in the test rig. It is seen that the maximum pump efficiency is 50.7% for the head and flowrate of 11.60 m and 11.93 L/s, respectively. The characteristics are compared with the numerical results, as shown in Fig. 4.7. It is observed that the numerical data obtained with SM approach are close to the experimental one, whereas the MRF approach over-predicts. The maximum difference between the experimental and numerical head-discharge characteristic of the pump over the operating range is ±2.5% and +7.0% for SM and MRF approach, respectively. The difference for the efficiency-discharge characteristic is 5% and 9% for sliding mesh and MRF approach, respectively. The accuracy of the numerical prediction of the efficiency is less because the mechanical losses are not considered. However, it is observed that the accuracy of SM is better than the MRF for the pump performance prediction and therefore the former is used for further analysis.

4.3 Numerical Simulations of a Centrifugal Slurry Pump with Solid-Liquid Mixture

To investigate the pump performance with solid-liquid mixture, the numerical modeling of the pump is performed using the multiphase models of the CFD code Fluent 19.0. It offers four models for multiphase simulation namely, Volume of fluid (VOF), Mixture, Eulerian-Eulerian and Discrete phase model (DPM). The first three are based on the Eulerian-Eulerian approach, whereas the last one (DPM) is based on Eulerian-Lagrangian approach. The VOF model is designed for two or more immiscible fluids. It is used where the position of the interface between the fluids is of interest. Hence for the simulation with solid-liquid mixture the remaining three models are more appropriate. Further, the choice of a particular multiphase model (Discrete Phase, Mixture, and Eulerian-Eulerian) depends on the volume fraction of solids to be handled along with the correct estimation of the desired results from the models. The application of discrete phase model is limited only for the slurry having solids within volumetric percentage less than 10% [Fluent 6.3, 2006]. For simulating dense slurry flows, Mixture and Eulerian-Eulerian multiphase models are the appropriate choice in CFD code Fluent.

In the present work, two multiphase models, granular Mixture and granular Eulerian-Eulerian are selected. Granular forms of model are selected to consider the effect of friction and collisions between particles in slurry flows. The details of each model are discussed below:

4.3.1 Eulerian-Eulerian model

In the Eulerian-Eulerian model, two phases, fluid (f), and solid (s), are assumed to coexist at every point in the space in the form of interpenetrating continua, so that, $\beta_f + \beta_s = 1$ where β_f and β_s are the volume fraction of fluid and solid phases, respectively. The continuity and momentum equations for the two phases are solved separately. The coupling between the phases is achieved with the interphase exchange coefficients.

4.3.1.1 Continuity Equation

$$\frac{\partial \rho_t}{\partial t} + \nabla \bullet (\beta_t \rho_t V_t) = 0 \text{ , where, t is either 's' or 'f'.} \tag{4.30}$$

4.3.1.2 Momentum Equations

For fluid phase:

$$\begin{aligned}\frac{\partial(\rho_f V_f)}{\partial t} + \nabla \bullet (\beta_f \rho_f V_f V_f) = &-\beta_f \nabla p + \beta_f \rho_f g + \nabla \bullet (\bar{\bar{\tau}}_f + \bar{\bar{\tau}}_{t,f}) + M_{sf}(V_s - V_f) \\ &+ C_{vm}\beta_s\rho_f(V_s \bullet \nabla V_s - V_f \bullet \nabla V_f) \\ &+ C_L\beta_s\rho_f(V_f - V_s)\times(\nabla \times V_f)\end{aligned} \tag{4.31}$$

For solid phase:

$$\begin{aligned}\frac{\partial(\rho_s V_s)}{\partial t} + \nabla \bullet (\beta_s \rho_s V_s V_s) = &-\beta_s \nabla p + \beta_s \rho_s g - \nabla p_s + \nabla \bullet (\bar{\bar{\tau}}_s + \bar{\bar{\tau}}_{t,f}) + M_{fs}(V_f - V_s) \\ &M_{sq}(V_s - V_q) + C_{vm}\beta_s\rho_f(V_f \bullet \nabla V_f - V_s \bullet \nabla V_s) \\ &+ C_L\beta_s\rho_f(V_s - V_f)\times(\nabla \times V_f)\end{aligned} \tag{4.32}$$

Where, ∇p is the static pressure gradient, ρg is the body force, ∇p_s is the solid pressure gradient, $C_{vm}\beta_s\rho_f(V_f \bullet \nabla V_f - V_s \bullet \nabla V_s)$ is the virtual mass force, and $C_L\beta_s\rho_f(V_f - V_s)\times(\nabla \times V_f)$ is lift force acting on the particles. The coefficient of virtual mass force (C_{vm}) and lift coefficient (C_L) are taken as 0.5 [Gopaliya and Kaushal, 2015].

For solid phase, the solid pressure (p_s) is estimated from the correlation given by Lun et al. [1984], and expressed as:

$$p_s = \beta_s\rho_s\Theta_s + 2\rho_s(1+e_{ss})\beta_s^2 g_{0,ss}\Theta_s \tag{4.33}$$

Where $g_{0,ss}$ is the radial distribution function for a solid phase and is calculated using the correlation [Lun et al., 1984] as,

$$g_{0,ss} = \left[1 - \left(\frac{\beta_s}{\beta_{s,max}}\right)^{\frac{1}{3}}\right]^{-1} \tag{4.34}$$

For more than one solid phase, the solid pressure (p_s) is estimated as [Lun et al., 1984]

$$p_s = \beta_s \rho_s \Theta_s + \sum_{q=1}^{N} 2\frac{d_{sq}^3}{d_s^3}(1+e_{sq})\rho_s \beta_s \beta_q g_{0,sq} \Theta_s \tag{4.35}$$

where d_{sq} (= $d_s/2 + d_q/2$) is the average of the s^{th} and the q^{th} phase particle diameters d_s and d_q, $g_{0,sq}$ is the radial distribution function for solid phases and calculated as [Lun et al., 1984]:

$$g_{0,sq} = \left[1 - \left(\frac{\beta_s}{\beta_{s,max}}\right)^{\frac{1}{3}}\right]^{-1} + \frac{1}{2} d_s \sum_{q=1}^{N+1} \frac{\beta_q}{d_q} \tag{4.36}$$

The granular temperature of solid (Θ_s) is calculated using the equation [Ding and Gidaspow, 1990] as,

$$\frac{3}{2}\left[\frac{\partial}{\partial t}(\rho_s \beta_s \Theta_s) + \nabla \bullet (\rho_s \beta_s V_s \Theta_s)\right] = \left(-p_s \bar{\bar{I}} + \bar{\bar{\tau}}_s\right) : \nabla V_s + \nabla \bullet (k_{\Theta_s} \nabla \Theta_s) - \gamma_{\Theta_s} + \phi_{fs} \tag{4.37}$$

where the term $\left(-p_s \bar{\bar{I}} + \bar{\bar{\tau}}_s\right) : \nabla V_s$ is the creation of fluctuation energy due to shear in the solid phase, $k_{\Theta_s} \nabla \Theta_s$ is the diffusion flux of granular energy.

The diffusion coefficient of granular temperature (k_{Θ_s}) is calculated using the correlation [Syamlal et al., 1993] as,

$$k_{\Theta_s} = \frac{15 d_s \rho_s \beta_s \sqrt{\Theta_s \pi}}{4(41-33\eta)}\left[1 + \frac{12}{5}\eta^2(4\eta-3)\beta_s g_{0,ss} + \frac{16}{15\pi}(41-33\eta)\eta\beta_s g_{0,ss}\right] \tag{4.38}$$

where $\eta = \frac{1}{2}(1+e_{ss})$

The collisional dissipation of energy (γ_{Θ_s}) is calculated using the correlation [Lun et al., 1984] as,

$$\gamma_{\Theta_s} = \frac{12(1-e_{ss}^2) g_{0,ss}}{d_s \sqrt{\pi}} \rho_s \beta_s^2 \Theta_s^{3/2} \tag{4.39}$$

The transfer of kinetic energy of random fluctuation in particle velocity from the solid phase to the fluid phase (ϕ_{fs}) is calculated using the correlation [Fluent 6.3, 2006] as,

$$\phi_{fs} = -3 M_{fs} \Theta_s \tag{4.40}$$

In Eqs. (4.31) and (4.32), $\bar{\bar{\tau}}_s$ and $\bar{\bar{\tau}}_f$ are the stress-strain tensors for solid and fluid phase respectively, and are expressed as

$$\bar{\bar{\tau}}_s = \beta_s \mu_s \left(\nabla V_s + \nabla V_s^T\right) + \beta_s \left(\lambda_s - \frac{2}{3}\mu_s\right) \nabla \bullet V_s \bar{\bar{I}} \tag{4.41}$$

and

$$\bar{\bar{\tau}}_f = \beta_f \mu_f \left(\nabla V_f + \nabla V_f^T \right) \tag{4.42}$$

where λ_s is the bulk viscosity of the solid particles calculated using the correlation [Lun et al., 1984] as,

$$\lambda_s = \frac{4}{3} \beta_s \rho_s d_s g_{0,ss} \left(1 + e_{ss}\right) \left(\frac{\Theta_s}{\pi} \right)^{1/2} \tag{4.43}$$

and μ_s is the shear viscosity of solids defined as [Fluent 6.3, 2006]

$$\mu_s = \mu_{s,col} + \mu_{s,kin} + \mu_{s,fr} \tag{4.44}$$

The collisional, kinetic and frictional part of the shear viscosity of solid phase is calculated from the correlations of the form [Gidaspow et al., 1992; Syamlal et al., 1993; Schaeffer, 1987]:

$$\mu_{s,col} = \frac{4}{5} \beta_s \rho_s d_s g_{0,ss} \left(1 + e_{ss}\right) \left(\frac{\Theta_s}{\pi} \right)^{1/2} \tag{4.45}$$

$$\mu_{s,kin} = \frac{\beta_s \rho_s d_s \sqrt{\Theta_s \pi}}{6\left(3 - e_{ss}\right)} \left[1 + \frac{2}{5} \left(1 + e_{ss}\right) \left(3e_{ss} - 1\right) \beta_s g_{0,ss} \right] \tag{4.46}$$

$$\mu_{s,fr} = \frac{p_s \sin\phi}{2\sqrt{I_{2D}}} \tag{4.47}$$

The Reynolds stress tensor for fluid phase in the Eqs. (4.31) and (4.32) is estimated using the equation [Fluent 6.3, 2006] as,

$$\bar{\bar{\tau}}_{t,f} = -\frac{2}{3} \left(\rho_f k_f + \rho_f \mu_{t,f} \nabla \bullet V_f \right) \bar{\bar{I}} + \rho_f \mu_{t,f} \left(\nabla V_f + \nabla V_f^T \right) \tag{4.48}$$

where $\mu_{t,f}$ is the turbulent viscosity, computed from

$$\mu_{t,f} = \rho_f C_\mu \frac{{k_f}^2}{\varepsilon_f} \qquad \text{where, } C_\mu = 0.09 \tag{4.49}$$

The prediction of turbulent kinetic energy k_f and its rate of dissipation ε for the fluid phase are obtained from the following transport equations

$$\frac{\partial}{\partial t} \left(\beta_f \rho_f k_f \right) + \nabla \bullet \left(\beta_f \rho_f V_f k_f \right) = \nabla \bullet \left(\beta_f \frac{\mu_{t,f}}{\sigma_k} \nabla k_f \right) + \beta_f G_{k,f} - \beta_f \rho_f \varepsilon_f + \beta_f \rho_f \prod_{kf} \tag{4.50}$$

$$\frac{\partial}{\partial t} \left(\beta_f \rho_f \varepsilon_f \right) + \nabla \bullet \left(\beta_f \rho_f V_f \varepsilon_f \right) = \nabla \bullet \left(\beta_f \frac{\mu_{t,f}}{\sigma_\varepsilon} \nabla \varepsilon_f \right) + \beta_f \frac{\varepsilon_f}{k_f} \left(C_{1\varepsilon} G_{k,f} - C_{2\varepsilon} \rho_f \varepsilon_f \right) + \beta_f \rho_f \prod_{\varepsilon f} \tag{4.51}$$

where, $G_{k,f}$ is the production of turbulent kinetic energy in the flow estimated as

$$G_{k,f} = \mu_{t,f} \left(\nabla V_f + \nabla V_f^T \right) : \nabla V_f \tag{4.52}$$

$\prod_{kf}$ and $\prod_{\varepsilon f}$ represent the influence of the solid phase on the fluid phase and computed from below,

$$\prod_{kf} = \frac{K_{fs}}{\beta_f \rho_f} \left(k_{sf} - 2k_f + V_{sf} \bullet V_{dr} \right) \tag{4.53}$$

$$\underset{\varepsilon f}{\Pi} = C_{3\varepsilon}\frac{\varepsilon_f}{k_f}\underset{kf}{\Pi} \tag{4.54}$$

Where, $C_{1\varepsilon} = 1.44, C_{2\varepsilon} = 1.92, C_{3\varepsilon} = 1.2, \sigma_k = 1.0, \sigma_\varepsilon = 1.3$

V_{sf} is the slip velocity, the relative velocity between the fluid phase and solid phase given by

$$V_{sf} = V_s - V_f \tag{4.55}$$

V_{dr} is the drift velocity given by

$$V_{dr} = -\left(\frac{D_s}{\sigma_{sf}\beta_s}\nabla\beta_s - \frac{D_f}{\sigma_{sf}\beta_f}\nabla\beta_f\right) \tag{4.56}$$

The momentum exchange coefficient between the fluid and solid phase in the Eqs. (4.31) and (4.32) is estimated using the correlation [Fluent 6.3, 2006] as,

$$M_{sf} = M_{fs} = \frac{3\beta_s\beta_f\rho_f}{4V_{r,s}^2 d_s}C_D\left(\frac{Re_s}{V_{r,s}}\right)|V_{sf}| \tag{4.57}$$

Where, C_D is the drag coefficient given by Dalla Valle [1948] as below,

$$C_D = \left(0.63 + \frac{4.8}{\sqrt{Re_s / V_{r,s}}}\right)^2 \tag{4.58}$$

Re_s is the relative Reynolds number between solid and liquid phases is given by:

$$Re_s = \frac{\rho_f d_s |V_{sf}|}{\mu_f} \tag{4.59}$$

$V_{r,s}$ is the terminal velocity correlation for the solid phase determined by the correlation [Garside and Al-Dibouni, 1977] as below,

$$V_{r,s} = 0.5\left(A - 0.06Re_s + \sqrt{(0.06Re_s)^2 + 0.12Re_s(2B - A) + A^2}\right) \tag{4.60}$$

where,

$$A = \beta_f^{4.14}; B = 0.8\beta_f^{1.28} \qquad \text{for}\ \beta_f \le 0.85 \tag{4.61}$$

and

$$A = \beta_f^{4.14}; B = \beta_f^{2.65} \qquad \text{for}\ \beta_f > 0.85 \tag{4.62}$$

The momentum exchange coefficient between the different solid phases in the Eq. (4.32) is estimated as [Syamlal, 1987]:

$$M_{sq} = \frac{3(1+e_{sq})\left(\frac{\pi}{2} + C_{fr,sq}\frac{\pi^2}{8}\right)\beta_s\rho_s\beta_q\rho_q(d_s + d_q)^2 g_{0,sq}}{2\pi(\rho_s d_s^3 + \rho_q d_q^3)}|V_s - V_q| \tag{4.63}$$

4.3.2 Mixture Model

The mixture model works on the principal of single-fluid approach. It solves the continuity and momentum equations for the mixture of the two phases. This model allows the phases to move at different velocities using the concept of slip velocities.

4.3.2.1 Continuity Equation for the Mixture

$$\frac{\partial \rho_m}{\partial t} + \nabla \bullet (\rho_m V_m) = 0 \tag{4.64}$$

where V_m is the mass-averaged velocity and is determined using the expression [Fluent 6.3, 2006] given as,

$$V_m = \frac{\sum_{p=1}^{t} \beta_p \rho_p V_p}{\rho_m} \tag{4.65}$$

and ρ_m is the mixture density calculated using the equation as below,

$$\rho_m = \sum_{p=1}^{t} \beta_p \rho_p \tag{4.66}$$

4.3.2.2 Momentum Equation for the Mixture

$$\frac{\partial (\rho_m V_m)}{\partial t} + \nabla \bullet (\rho_m V_m V_m) = -\nabla p + \rho_m g + \nabla \bullet \left[\mu_m \left(\nabla V_m + \nabla V_m^T \right) \right] + \nabla \bullet \left(\sum_{p=1}^{n} \beta_k \rho_k V_{dr,p} V_{dr,p} \right) \tag{4.67}$$

Where, μ_m is the viscosity of the mixture calculated using the equation [Fluent 6.3, 2006] as,

$$\mu_m = \sum_{p=1}^{t} \beta_p \mu_p \tag{4.68}$$

and $V_{dr,p}$ is the drift velocity for the secondary phase calculated using the equation [Fluent 6.3, 2006] as,

$$V_{dr,p} = V_p - V_m \tag{4.69}$$

4.3.3 Numerical Modeling of a Pump for Handling Equi-size Particulate Slurry

4.3.3.1 Boundary Conditions and Solution Strategy

The boundary conditions at inlet and outlet of the pump as well as the rotational speed are set as similar to those presented in section 4.2.3.2. Additionally, the volume fraction of the solid is defined at the inlet boundary. Table 4.4 shows the solution methodology adopted for the numerical simulation of pump handling equi-size particulate slurry.

4.3.3.2 Range of Parameters for Simulation with Equi-size Particulate Slurry

Four sets of multiphase simulation of a pump are performed with equi-size particulate slurry at 1200 rpm and BEP flow rate. In the first set, the simulations are performed at 20%, 30%, and 40% weight concentrations using 200 µm, 400 µm, and 605 µm size particles (S_s = 2.65) with Eulerian-Eulerian model and Mixture multiphase model to determine the effective multiphase model for the pump handling dense mixture. In the second set, the simulations are performed using Eulerian-Eulerian model with 100 µm, 200 µm, 400 µm, 600 µm, and 800 µm size

particles (S_s = 2.65) at 20% and 30% weight concentration, to determine the effect of particle size on the pump performance. In the third series, the simulations are performed using Eulerian-Eulerian model at 20%, 30%, 40% and 50% weight concentration with 200 µm and 400 µm size particles (S_s = 2.65), to determine the effect of solid concentration on a pump performance. In fourth set, the numerical simulations are performed using Eulerian-Eulerian model for the solids of specific gravity 1.5, 1.9, 2.3, 2.65 and 3 at 20%, 30% and 40% weight concentration to investigate the effect of specific gravity of solids on pump performance.

4.3.3.3 Validation of the Model

To estimate the effect of solids numerically, the pump performance predicted with the solid-liquid mixture using Eulerian-Eulerian model and Mixture multiphase model is compared with the experimentally obtained performance as shown in Table 4.5. The performance characteristics of the pump are predicted for three different mean size sand particles (200 µm, 400 µm, and 605 µm) and three weight concentrations (Cw = 20%, 30%, and 40%). The experimentally measured head ratio (HR) and efficiency ratio (ER) are compared with the predicted results. For both the models, the drop in the head and efficiency increases with increase in either particle size or concentration, a trend normally reported in the literature [Vocaldo et al., 1974; Gahlot et al., 1992; Kazim et al., 1997]. However, the numerical results with the mixture model show large deviations with the experimental data. Eulerian-Eulerian model predicted the effects of solid on the performance close to the experimental data. The deviation is within ±2% for the HR and ±3% for ER. Therefore, Eulerian-Eulerian model is selected for the further analysis of the effects of solids on the pump performance and flow field.

4.3.3.4 Effect of Solids on Pump Performance

4.3.3.4.1 Effect of Particle Size

The predicted centrifugal slurry pump characteristics, in terms of HR and ER, for equi-size particles (S_s = 2.65) of 100 µm to 800 µm at BEP flowrate, and 20% and 30% weight concentrations are presented in Fig. 4.8. It is seen that the increase in particle size increases the drop in HR and ER. This is attributed to the increase in the inertial effect of bigger size particles for flow through the pump passages. At 20% weighted concentration, the estimated drop in HR and ER is the maximum as 9.3% and 7.8% respectively, whereas, at 30% weighted concentration, the drop in HR and ER is the maximum as 10.4% and 12.07% respectively. The drop may be attributed to the increase in particle-particle interaction and frictional effects at higher solids loading. Kazim et al. [1997] also reported on increase in drop in HR and ER with the increase in particle size for the mean particle size range of 180-460 µm.

4.3.3.4.2 Effect of Solid Concentration

Fig. 4.9 shows the effect of solid concentration on the performance of the pump in terms of HR and ER. The numerical values of the ratios are presented for 20% to 50% weighted concentration at BEP flowrate for 200 µm and 400 µm equi size sand particles (S_s = 2.65). It is clearly seen that the HR and ER decreases with increase in solid concentration. The reduction in HR and ER is attributed to the energy required to overcome the inertia of the particles, which increases with increase in solid concentration. The decrease in HR and ER with solid concentration was also observed by Gahlot et al. [1992] for zinc tailings slurry (S_s = 2.85, d_{50} = 170 µm) and coal slurry (S_s = 1.48, d_{50} = 900 µm), Kazim et al. [1997] for sand slurry (S_s = 2.65 , d_{50} = 230 µm), and zinc slurry (S_s = 5.51 , d_{50} = 455 µm), and Gandhi et al. [2001a] for fly ash slurry (S_s = 2.08, d_{50} = 42 µm) up to 50% concentration (by weight). The maximum drop in HR and ER with increase in weight concentration from 20% to 50% is around 9% and 15% for 200 µm and 400 µm size particles, respectively.

4.3.3.4.3 Effect of Specific Gravity of Solids

The specific gravity of solids is one of the critical parameters affecting the performance of the centrifugal slurry pump [Engin and Gur, 2003]. Over the years, investigators [Vocaldo et al., 1974; Burgess and Reizes, 1976; Sellgren, 1979; Gahlot et al., 1992; Kazim et al., 1997; Gandhi et al., 2001a] studied this effect experimentally. However, an understanding of the effects of specific gravity of solid on the pump performance is still not conclusive as it is difficult to get the particles of different specific gravity with the same physical properties. In the present study, CFD simulations are performed with 200 µm size solid particles of specific gravity varying from 1.5 to 3 while keeping the weight concentration, flowrate and rotational speed constant. For a constant flowrate, the number of particles and the slurry density varies with the specific gravity of solids as shown in Fig. 4.10. It is seen that at any weight concentration, an increase in solids specific gravity decreases the number of particles in the slurry and increases the slurry density.

The effect of specific gravity of solids on HR and ER is shown in Fig. 4.11 for 200 µm size particles at BEP flowrate. It is seen that the decrease in specific gravity of solids decreases the HR. This may be attributed to the increase in number of particles with the decrease in specific gravity for the same weight concentration and size (see Fig. 4.10). The increase in number of particles increases the particle-fluid and the particle-particle interactions, and therefore, more energy is required to push the particles through the pump. The present findings of variation of HR with the specific gravity at constant weighted concentration, flowrate and pump speed is in agreement with the earlier findings of Gandhi et al. [2001a]. Fig. 4.11 also shows that the

decrease in the specific gravity decreases the ER. However, it is observed that the values of ER and HR vary differently with the change in the specific gravity. Values of ER are found greater than HR for particles of specific gravity more than 2.2 and vice-versa. The relationship between ER and HR was also investigated in literature [Sellgren, 1979; Gahlot et al., 1992; Kazim et al., 1997; Gandhi et al., 2001a]. Sellgren [1979] reported nearly equal values of HR and ER for pumping ore and industrial minerals (S_s = 2.3 to 4.2) up to a volumetric concentration of 20-25%. At higher concentration, the drop in efficiency is more as compared to the head. Kazim et al. [1997] reported the drop in ER is around 5% more than HR for coal, zinc, iron and different sand samples of specific gravity 1.49, 5.51, 4.35, and 2.65 respectively. Gahlot et al. [1992] and Gandhi et al. [2001a] reported 2-10% higher values of ER compared to HR for coal, bed ash, fly ash, and zinc tailing slurry. Many investigators [Sellgren, 1979; Gahlot et al., 1992; Kazim et al., 1997; Gandhi et al., 2001a] reported that the drop in HR and ER is not same. The present findings suggest that the relationship between ER and HR is a function of specific gravity of solid particles.

4.3.3.5 Effect of Solids on Pump Flow Field

The simulated results are used to investigate the flow field inside the centrifugal slurry pump. Figs. 4.12 and 4.13 show the static pressure and velocity contours respectively around the impeller mid-plane at BEP with 20% weight concentration for 200 μm size particles. The impeller is rotated in a clockwise direction. The obtained flow field seems to follow the general flow principal of the pump like the flow enters through impeller eye, diverted to the blade-to-blade passage and passes along the casing after exiting from the impeller, with increase in static pressure of the mixture from inlet to outlet. The magnitude of velocity is highest at the tip of the impeller. It is due to the rotational motion of impeller imparting the kinetic energy to the slurry which increases along the blade passage and reaches the maximum at the impeller tip.

To further develop an understanding of the particle flow field in the flow passages along the complete width, flow passages of impeller and casing are examined separately. The parameters affecting the pump erosion wear namely, the particle velocity and solid distribution are studied to gain insight for mitigation of uneven slurry erosion of the impeller and casing. To study the flow field of the slurry inside the impeller flow passage, one blade passage of the impeller is analyzed. Four planes (R_1-R_4) at different radial locations from the inlet (R_1) to the outlet (R_4) of the blade passage are selected as shown in Fig. 4.14 (a,b). The radial locations are non-dimensionalised using the impeller outer radius (R) and four planes are selected at radius ratio (r/R) of 0.415, 0.6, 0.8, and 1 (see Fig. 4.14).

Fig. 4.15 shows the velocity contours of fluid phase and solid phase at different radial locations inside the impeller blade channel for the pump operating at BEP flow rate and 30% weight concentration for 100 µm, 400 µm and 800 µm size particles. It is observed from Fig. 4.15 (i,ii) that the velocity of both the phases is not uniform in the channel along the blade width at any radial location. The magnitude of both fluid and solid phase velocities are the maximum near the impeller front shroud and the minimum near the impeller back shroud at any radial distance. This may be attributed to wider flow passage designed to ensure a clog-free operation of the solid-liquid mixture. Further, it is observed that the velocity difference of the two phases for 100 µm size particles is not very significant and increases with increase in particle size. It may be due to the higher inertia of bigger size particles which results in higher particle slip velocity.

The effect of particle size on solids distribution inside the impeller blade channel is shown in Fig. 4.16 (a-d). The contours of normalized solid concentration, a ratio of local volume fraction of solids to the efflux volume fraction, are plotted at four different radial locations (R_1-R_4) inside the impeller blade channel for 100 µm, 200 µm, 400 µm, and 800 µm size particles at BEP flowrate and 30% weight concentration. It is observed that the particle distribution is skewed in both axial and radial positions inside the channel. The homogeneity in particle distribution improves as the particles accelerate from R_1 to R_4. Since the particle velocity is very less at position R_1 (see Fig. 4.15), the particles are distributed non-homogeneously and tend to accumulate near the back shroud. Comparatively at position R_2, the particle distribution improves slightly because of the increase in particle velocities due to impeller rotation, but still, the particles are more near the back shroud. The concentration of particles at position R_2 is also more near the pressure side of the blade which may be a result of the dominant outward centrifugal force that acts on the particles due to the rotation of the impeller. At position R_3, the energy of the particles is further increased. Therefore, the distribution of particles becomes more homogeneous as compared to R_2. However, particles, except 100 µm, deviate from the fluid streamline and are shifted more towards the pressure side of the blade due to their higher inertial effect. At the impeller tip (R_4), almost uniform distribution of solids is observed for 100 µm and 200 µm size particles. For larger particle size, the concentration of particles is non-uniform and skewed with a higher value near the pressure side and back shroud.

Further to study the effect of particle size on flow field in the space between the impeller outlet and casing wall, five different planes (L_1-L_5) are selected at different angular locations along the pump casing as shown in Fig. 4.17. The location '1' is the casing tongue, location '2' is 50^o to location '1' and the other locations are spaced 90^o to the consequent location along the flow direction.

The velocity contours of different size particles at the five locations in the space between the impeller and casing at BEP flow rate and 30% weight concentration is presented in Fig. 4.18 (a-d). It is seen that the velocity of the particles at the exit from the impeller is maximum. As the radial distance from the impeller outlet increases, the velocity of the particles reduces due to the inertia of the particles. The particle velocity distribution is observed to be non-uniform because of the large width of the casing being provided for clog-free operation. The velocity of the particles is less at the back side of the casing as compared to the center and front side at different cross-sections. With increase in particle size, the reduction in velocity is more near the casing back side due to increase in inertia effects.

Further, to examine the effect of particle size on the concentration distribution in the casing, the contours of normalized solid concentration are plotted as shown in Fig. 4.19 (a-d). It is seen that the particles flowing along the casing flow path are suspended more near the casing backside where the velocity of the particles is less (see Fig. 4.18a-d). This may be attributed to the centrifugal force exerted by the impeller on particles and the secondary flows in the casing [Gonzalez and Santolaria, 2006]. Due to centrifugal force, the particles exiting from the impeller move radially towards the wall of the casing whereas due to secondary flows, the particles move towards the casing side walls. Moreover, the particles along the casing backside may not be able to move towards the center because of the continuous push of the faster moving particles from center.

To study the effect of solid concentration on particle velocity distribution inside the impeller blade channel and the casing, the contours of particle velocity for 200 µm size particles (S_s = 2.65) at BEP flow rate and 20% to 50% weight concentration are plotted in Figs. 4.20 (a-d) and 4.21 (a-d), respectively. It is observed that the increase in solid concentration increases the uniformity of velocity in the flow passages of both the components. This may be attributed to the increase in number of particles with the increase in solid concentration, which suppresses the effect of secondary flows in the flow passages.

Further to observe the effect of solid concentration on the particle distribution inside the impeller blade channel and the impeller casing space, the contours of normalized solid concentration for 200 µm size particles (S_s = 2.65) at BEP flow rate and 20% to 50% weight concentrations are plotted in Figs. 4.22 (a-d) and 4.23 (a-d), respectively. It is seen that the increase in the solid concentration increases the homogeneity of the particle distribution in the flow passages. This may attribute to the increase in the interference effect between the particles with increase in solid concentration [Chen et al., 2009]. Mishra et al. [1998] also reported that the homogeneity of particles increases with increase in solid concentration for the slurry flow

along straight pipelines and bends. They attributed the homogeneity of particles distribution at higher solid loading to the increase in particle-particle interactions.

4.3.4 Numerical Modeling of a Pump for Handling Multi-size Particulate Slurry

To determine the effect of particle size distribution on pump performance characteristics, numerical modeling of the pump is performed with multi-size particulate slurry using granular Eulerian-Eulerian multiphase model.

4.3.4.1 Boundary Conditions and Solution Strategy

Eulerian-Eulerian model with more than two phases (four/five) are considered for the simulation. Water is considered as a primary phase and the fly ash particles are considered as secondary phases. The velocity inlet and pressure outlet are set as a boundary condition at inlet and outlet of the pump, respectively. The rotational speed of the impeller is set to 1200 rpm. A time step of 4.16×10^{-4} s, equals to 3 degree impeller rotation, is set to perform the simulation at 1200 rpm. Table 4.6 shows the solution methodology adopted for the numerical simulations.

4.3.4.2 Range of Parameters for Simulation with Multi-size Particulate Slurry

Two sets of numerical simulation of the pump are performed with multi-size particulate slurry at 1200 rpm. In first set, the simulations are performed at 13.3% and 35.1% weight concentrations for three different operating flowrates of 7.8 L/s, 10.2 L/s and 12 L/s which are 65%, 85% and 100% of BEP flowrate, respectively, to validate the modeling of the pump with multi-size particulate slurry. The predicted pump performance is compared with the experimentally measured values. Three different mean size fly ash particles are considered for the multi-size particulate slurry. The initial weight fraction of each size is taken accordingly to PSD of fly ash particles (See Table 3.2) used during experimentation and calculated by multiplying the individual percentage weight for each size presented in Table 4.7 to the total weight fraction of the slurry. In second set, the simulations are performed with five different samples of PSD at 20% and 30% weight concentrations, and BEP flowrate, to investigate the effect of PSD on the pump performance. In this, the selection of particle sizes to prepare different multi-sized slurry samples is referred from the literature [Gandhi and Borse, 2004]. The particle sizes in multi-size slurry are taken as 112 µm (+75 –150), 225 µm (+150 –300), 505 µm (+300 –710), and 855 µm (+710 –1000). The numbers in parenthesis represent the successive sieve sizes. The different size particles are mixed in different proportions to obtain different PSD of multi-size slurry. The details of the variation in fraction of different size particles and the corresponding estimated representative particle size are listed in Table 4.8. Fig. 4.24 shows the variation in PSD of different slurry samples.

Simulations of the pump with equi-sized particulate slurry corresponding to different PSD, PSD-1 to PSD-5, is also performed at 20% and 30% weight concentrations, and BEP flow rate to study the effect of PSD on pump performance. The results obtained with multi-sized slurry and with the equi-sized slurry, based on weighted mean size (d_{wn}) and median size (d_{50}) are compared. The calculated single representative size of particles corresponding to different PSD is listed in Table 4.8.

4.3.4.3 Validation of the Model

Fig. 4.25 shows the measured and predicted performance characteristics of the pump with multi-sized fly ash slurry. It is seen that the maximum pump efficiency at 13.3% weight concentration is 48.39% for the head and flow rate of 11.04 m and 12.12 L/s, respectively. The increase in particulate weight concentration decreases the head and efficiency of the pump. At 35.1% weight concentration, the maximum pump efficiency reduced to 46.3% for the head and flow rate of 10.44 m and 12.02 L/s, respectively. The numerical model predicted the pump performance close to the experiments results. The numeric values in the plot are showing the deviation of the predicted results with the measured. The maximum deviations in the predicted head and efficiency are within ±2% and ±3.5%, respectively.

4.3.4.4 Effect of PSD on Pump Performance and Flow Field

The effect of PSD on pump performance is predicted at BEP flow rate for 20% and 30% weight concentrations with all the five aforementioned multi-size particulate slurries. The predicted values of HR and ER with slurries of different PSD are presented in Figs. 4.26 (a) and (b), respectively. It is seen that the variation in PSD significantly affect the pump performance. The drop in HR and ER increases with the variation in PSD from PSD-1 to PSD-5. This may be attributed to the decrease in weight fraction of small size particles and increase of bigger size particles as the PSD varied from PSD-1 to PSD-5 (Table 4.8). The reduction in HR due to large amount of small size particles present in multi-sized slurry was also observed by Gandhi et al. [2001a]. They reported that the small size particles help in suspending bigger size particles and therefore the energy required to keep the particles in motion is less. Moreover, the drop in HR and ER shows similar trend with variation in PSD from PSD-1 to PSD-5 for 20% and 30% weight concentrations. At 20% weight concentration, the percent decrease in HR for PSD-2 to PSD-5 compared to PSD-1 is 4.57%, 8.77%, 12.91% and 15.91%, respectively, whereas the percent decrease in HR at 30% weight concentration is 5.57%, 10.36%, 15.50%, and 19.40%, respectively. The higher drop in HR for 30% weight concentration shows that the increase in solids loading increases the effect of PSD on the pump performance. Similar observations are

noticed with the ER for the increase in solid concentration from 20% to 30% weight concentration with the variation in PSD.

Further, Fig. 4.26 (a,b) shows the comparison of HR and ER predicted from different PSD samples of multi-sized slurry to the predicted HR and ER values obtained with a single representative size of corresponding PSD of multi-sized slurry. It is seen that the predicted trend of HR and ER variation with PSD is different for multi-sized and equi-sized slurries. The predicted drop in HR and ER values with median size (d_{50}) slurry compared to multi-sized slurry is less, whereas the drop in HR and ER predicted from the weighted mean size is more. The maximum deviations in the reduction of HR and ER with median size (d_{50}) slurry at 30% weight concentration compared to multi-sized slurry for different PSD samples (1 to 4) are around -3% and -3.5%, respectively, whereas with weighted mean size the maximum deviations are around 3% and 2%, respectively.

In order to develop an understanding of PSD on particle flow field, the simulated results are used to examine the flow field of the particles inside the flow passages of impeller and casing. Figs. 4.27 (a-e) and 4.28 (a-e) shows the effect of PSD on solid concentration distribution inside the impeller blade channel and casing, respectively, at BEP flow rate and 30% weight concentration. The solids distribution contours in impeller blade channel (Fig. 4.27a-e) shows non-homogeneous distribution of solids in both axial and radial directions inside the channel. The variation in PSD significantly affects the flow of solids inside the blade channel. For PSD-5 (Fig. 4.27e) in which the fraction of bigger size particles are more, the solid distribution is highly skewed in both axial and radial positions inside the channel. The flow of solids is more near the back shroud (BS) and pressure side (PS) of the blade, whereas the zone of the minimum solid concentration is near the frond shroud (FS). The increase in flow of particles near the blade surfaces increases the chances of particle-particle and particle-wall collisions, which may increase the resistance for flow of particles. On reduction in fraction of bigger size particles and increase in small size particles with the variation in PSD from PSD-5 to PSD-1, the increase of homogeneity in flow of mixture is observed. The higher concentration of particles flowing near the back shroud and pressure side reduces, as the PSD changes from PSD-5 to PSD-1.

The distribution of solids inside the casing flow passage also shows that the homogeneity of particle distribution inside casing flow path is significantly affected with the variation in PSD (Fig. 4.28a-e). The particle concentration near the back side of the casing increases as the fraction of bigger size particles in the multi-sized slurry increases for PSD-1 to PSD-5.

Figs. 4.29 (a-d) and 4.30 (a-d) shows the effect of PSD on particle velocity distribution of different size particles inside the impeller blade channel and casing flow passages at BEP flowrate and 30% weight concentration. The particle velocity distribution in the blade channel is seen non-uniform at any radial location (Fig. 4.29a-d). Increase in particle size increases the non-uniformity. However for different PSD, the non-uniformity in particle velocity distribution is more with PSD-5. This may be attributed to the reduction in particle kinetic energy with increase in energy dissipation during particle-particle collision with higher fraction of bigger size particles.

The particle velocity distribution inside the casing flow passages shows that the velocity of the particles is non-uniform and significantly less near the back end of the casing. The comparison of particle velocity of different size particles shows that the PSD affects the velocity distribution of the particles in the casing also. The particle velocity is more non-uniform for the PSD with high weight fraction of bigger size particles.

4.4 Concluding Remarks

From the present numerical investigations of the effects of solids on the centrifugal slurry pump performance and flow field, the following conclusions can be drawn:

1. The Eulerian-Eulerian multiphase model predicted pump performance with slurry close to the experimental results as compared to Mixture multiphase model. The maximum deviation in head ratio and efficiency ratio predicted with the former is ±2% and ±3%, respectively, as compared to the experiments.
2. For same weight concentration and particle size, the increase in specific gravity of solids decreases the reduction in head and efficiency ratios of the pump. However, the effect of solids on head and efficiency ratios of the pump is not the same. The difference in head and efficiency ratios is observe to depend on the specific gravity of solids.
3. The particle velocity and solid concentration along the impeller and casing flow passages are non-uniform. This non-uniformity increases with increase in particle size but improves with increase in solid concentration.
4. The particle suspension along impeller flow passage is non-homogeneous, both in the axial and radial directions. It improves as the mixture progresses in the radial direction from the inlet to outlet of the blade. The region of higher concentration of particles is observed to be located near impeller back shroud and pressure side of the blade.

5. In the casing, the flow field of the particles is greatly influenced by the secondary flows. The concentration of the particles is particularly high near the non-suction side of the casing.
6. The Eulerian-Eulerian approach used for modeling multi-size solid particulate slurry predicted the head and efficiency ratio with the maximum deviation of ±2% and ±3.5%, respectively, with respect to the experiments.
7. The drop in head and efficiency increases with the increase in weight fraction of bigger size particles in the multi-size particulate slurry. The use of single representative particle size of multi-size particulate slurry for pump performance prediction is not capable to correctly capture the effect of PSD on pump performance.
8. The non-uniformity in particle velocity and solid concentration inside the impeller and casing increase with the increase in weight fraction of bigger size particles in multi-size particulate slurry.

Table 4.1: Solution methodology adopted for the numerical simulation with water alone

Parameters	Modeling
Components	Stationary domain: Casing and Suction Rotating domain: Impeller
Fluid	Water
Boundary conditions	Inlet: Velocity inlet Outlet: Pressure outlet
Discretization scheme	Momentum equation: First order upwind Turbulent kinetic energy: First order upwind Turbulent dissipation energy: First order upwind
Under relaxation factor	Pressure: 0.3 Momentum equation: 0.7 Turbulent kinetic energy: 0.8 Turbulent dissipation energy: 0.8
Pressure velocity coupling scheme	SIMPLE
Turbulence models	Standard k–ε with standard wall functions
Convergence control	rms of pressure, mass-momentum, and turbulent parameters ≤1.0E-5

Table 4.2: Mesh Details

Mesh type	Number of elements			Total number of elements	Mesh quality	Aspect ratio
	Impeller	Casing	Suction			
G1	229917	290784	680084	1200785	0.35	8.26
G2	581893	290784	680084	1552761	0.35	14.97
G3	1056115	290784	680084	2026983	0.35	15.41
G4	1056115	993667	680084	2729866	0.32	16.12
G5	2237111	993667	680084	3910862	0.32	18.45
G6	2237111	1396978	1300437	4934526	0.29	24.28

Table 4.3: Turbulence models comparison

Flow rate	Net head (meter of water column)			
	Standard k-ε	Realizable k-ε	RNG k-ε	Standard k-ω
6 lps	13.15	13.12	13.14	13.10
9 lps	12.44	12.41	12.43	12.39
12 lps	11.32	11.33	11.31	11.29

Table 4.4: Solution methodology adopted for the numerical simulation with equi-size particulate slurry

Parameters	**Modeling**
Velocity formulation	Absolute velocity formulation
Multiphase model	Eulerian-Eulerian (EE), Mixture (M)
No. of Phases	Two
Fluid	Primary phase: Water Secondary phase: Sand
Boundary conditions	Inlet: Velocity, Volume fraction Outlet: Pressure outlet
Discretization scheme	Momentum equation: First order upwind Volume fraction: First order upwind Turbulent kinetic energy: First order upwind Turbulent dissipation energy: First order upwind
Under relaxation factor	Pressure: 0.3 Momentum equation: 0.7 Volume fraction: 0.5 Turbulent kinetic energy: 0.8 Turbulent dissipation energy: 0.8
Pressure velocity coupling	Phase Coupled SIMPLE (EE), Presto (M)
Turbulence models	Standard k–ε with dispersed phase (EE), Standard k–ε (M)
Convergence control	rms of mass, momentum, volume fraction and turbulent parameters ≤1.0E-5

Table 4.5: Comparison of experimentally measured and numerically predicted on pump performance with different particle sizes at 12 L/s (BEP flowrate)

Particle Size (μm)	**Solids loading (%by weight)**	**Experimental**		**Eulerian-Eulerian**		**Mixture Model**	
		Head Ratio	**Efficiency Ratio**	**Head Ratio (deviation)**	**Efficiency Ratio (deviation)**	**Head Ratio (deviation)**	**Efficiency Ratio (deviation)**
200	20	0.957	0.972	0.964 (-0.783%)	0.984 (-1.255%)	0.891 (6.91%)	1.010 (-3.986%)
	30	0.934	0.951	0.924 (1.091%)	0.941 (0.948%)	0.828 (11.324%)	1.005 (-5.734%)
	40	0.910	0.926	0.899 (1.55%)	0.921 (0.496%)	0.763 (16.177%)	0.993 (-7.311%)
400	20	0.935	0.952	0.941 (-0.581%)	0.969 (-1.843%)	0.884 (5.478%)	0.998 (-4.852%)
	30	0.897	0.918	0.881 (1.881%)	0.915 (0.264%)	0.817 (8.93%)	0.980 (-6.805%)
	40	0.855	0.878	0.849 (0.696%)	0.858 (2.218%)	0.725 (15.208%)	0.923 (-5.085%)
605	20	0.915	0.918	0.919 (-0.374%)	0.941 (-2.578%)	0.878 (4.01%)	0.988 (-7.644%)
	30	0.869	0.875	0.876 (-0.742%)	0.887 (-1.442%)	0.801 (7.818%)	0.947 (-8.244%)
	40	0.821	0.831	0.823 (-0.155%)	0.825 (0.664%)	0.691 (15.857%)	0.857 (-3.169%)

Table 4.6: Solution methodology adopted for the numerical simulation with multi-size particulate slurry

Parameters	Modeling
Velocity formulation	Absolute velocity formulation
Multiphase model	Eulerian-Eulerian
No. of Phases	Four
Fluid	Primary phase: Water Secondary phase: Fly ash
Boundary conditions	Inlet: Velocity, Volume fraction Outlet: Pressure outlet
Discretization scheme	Momentum equation: First order upwind Volume fraction: First order upwind Turbulent kinetic energy: First order upwind Turbulent dissipation energy: First order upwind
Under relaxation factor	Pressure: 0.3 Momentum equation: 0.7 Volume fraction: 0.5 Turbulent kinetic energy: 0.8 Turbulent dissipation energy: 0.8
Pressure velocity coupling	Phase Coupled SIMPLE
Turbulence models	Standard k–ε with dispersed phase
Convergence control	rms of mass, momentum, volume fraction and turbulent parameters ≤1.0E-5

Table 4.7: Particle size distribution of fly ash used for experiment

Weighted mean diameter (d_{wn}) = 60 µm					**Median diameter (d_{50})** = 62 µm				
Particle Size, (µm)	>300	250	212	180	150	106	90	75	45
% Finer (by weight)	100	98	97	94.6	89	81.2	78	67.4	20.4
Mean Size (µm)	240				120			60	
Weight Fraction (%)	5.4				16.6			78	

Table 4.8: Particle size distribution in multi-sized slurry samples

Sample no.	Mean particle size (µm)				Weighted mean diameter, d_{wn} (µm)	Median diameter, d_{50} (µm)
	112	225	505	855		
	% weight fraction					
1	75	15	5	5	186	119
2	40	30	20	10	299	189
3	25	25	25	25	424	300
4	10	20	30	40	549	533
5	5	15	30	50	618	710

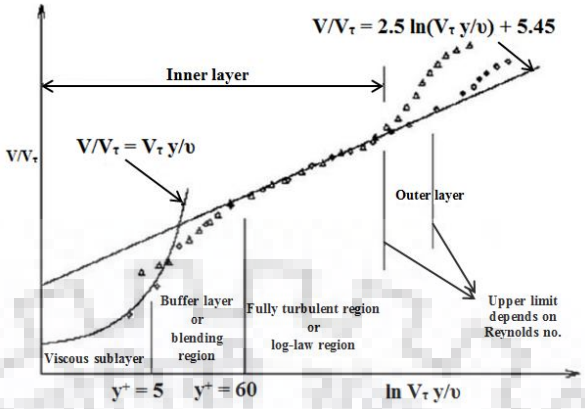

Fig. 4.1 Subdivisions of the near wall region [Fluent 6.3, 2006]

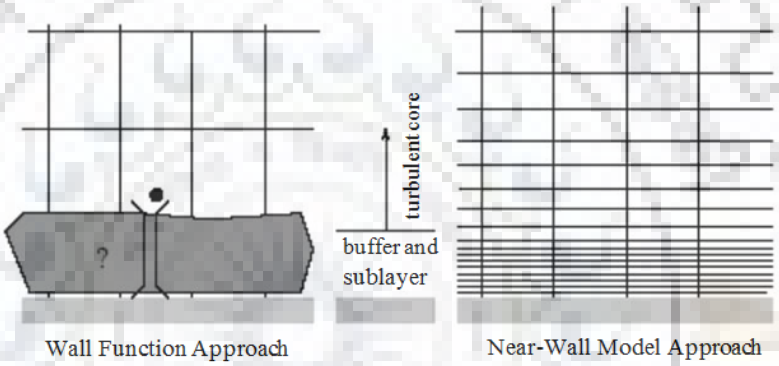

Fig. 4.2 Near wall treatments in Fluent [Fluent 6.3, 2006]

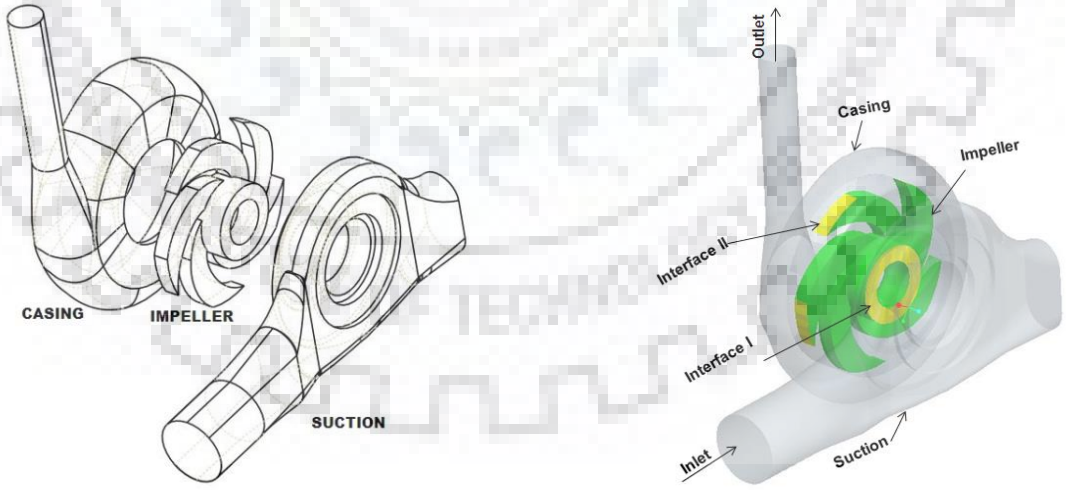

(a) Exploded view

(b) Assembled view with two interfaces namely Suction to Impeller (Interface I) and Impeller to Casing (Interface II)

Fig. 4.3 Computational domain of the centrifugal slurry pump

(a) Impeller

(b) Casing

(c) Suction

(d) Complete pump

Fig. 4.4 Mesh model of the components and complete pump

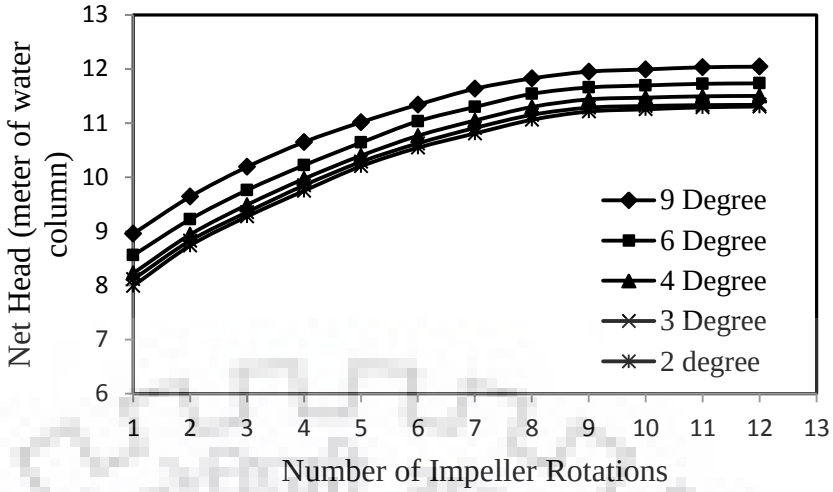

Fig. 4.5 Time step size and number of impeller rotation analysis of numerical predictions

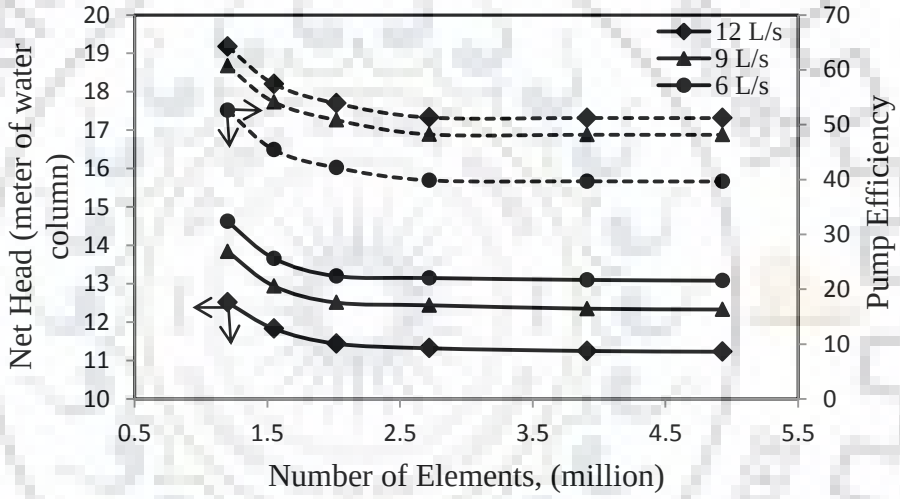

Fig. 4.6 Mesh independency analysis of numerical simulation

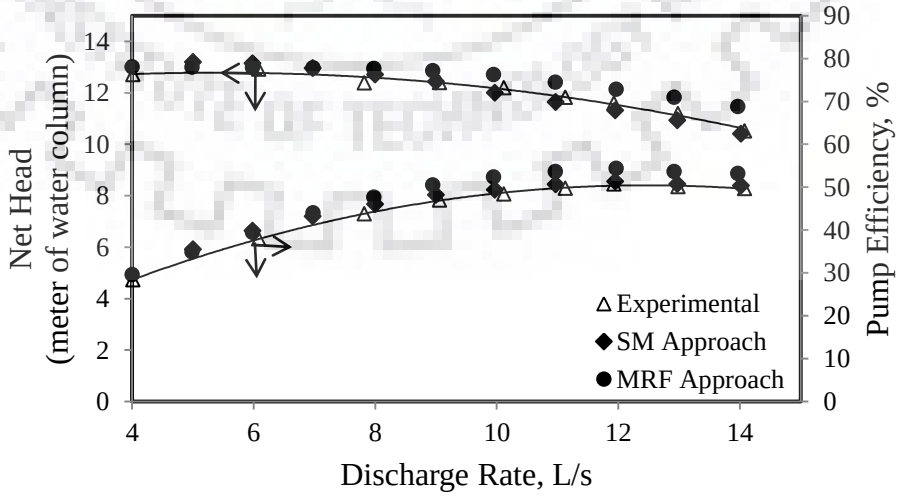

Fig. 4.7 Experimentally and numerically obtained centrifugal slurry pump performance characteristics with water at 1200 rpm

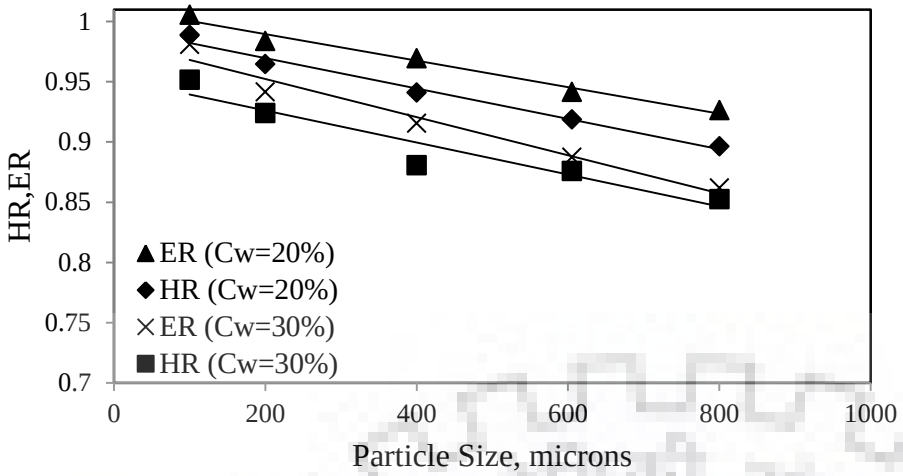

Fig. 4.8 Variation of head and efficiency ratio with a particle size (S_s = 2.65) at BEP flowrate of the pump for 20% and 30% weighted concentration

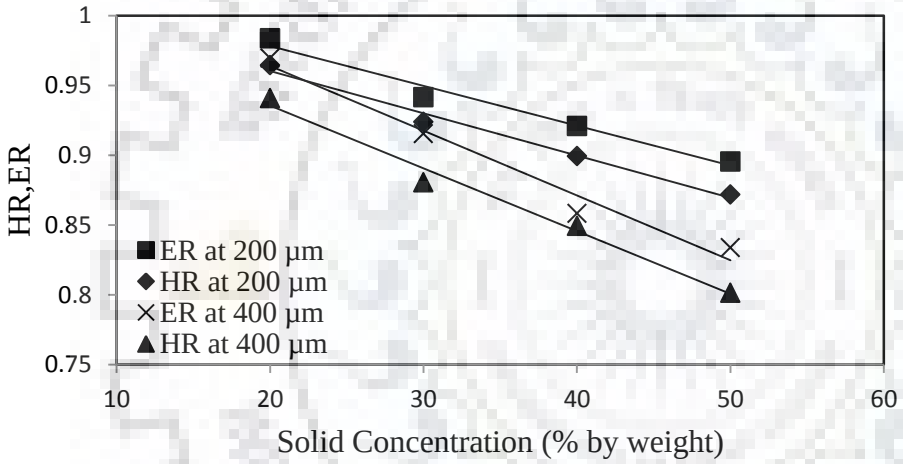

Fig. 4.9 Variation of the head and efficiency ratio with weight concentration at BEP flowrate of the pump running for 200 µm and 400 µm size particles (S_s = 2.65)

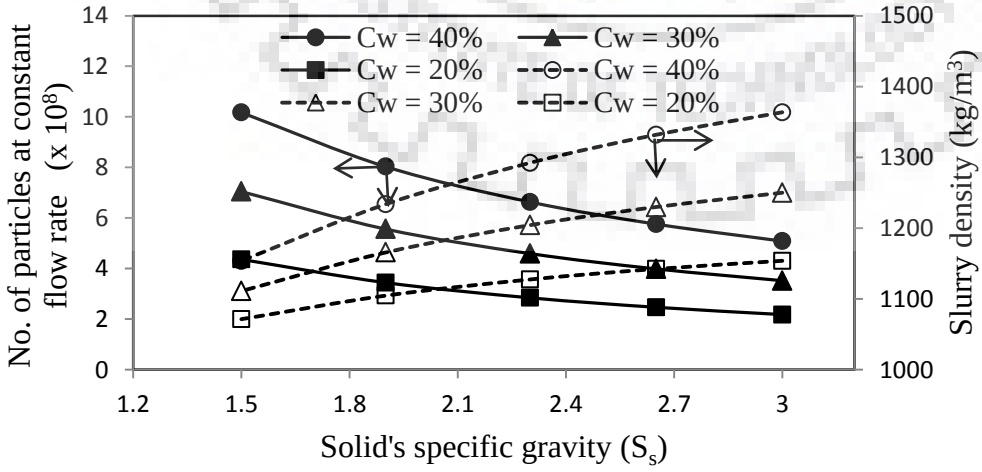

Fig. 4.10 Variation of the number of particles and slurry density at a constant flowrate (12 L/s) with solids specific gravity and weighted concentration for 200 µm size particles

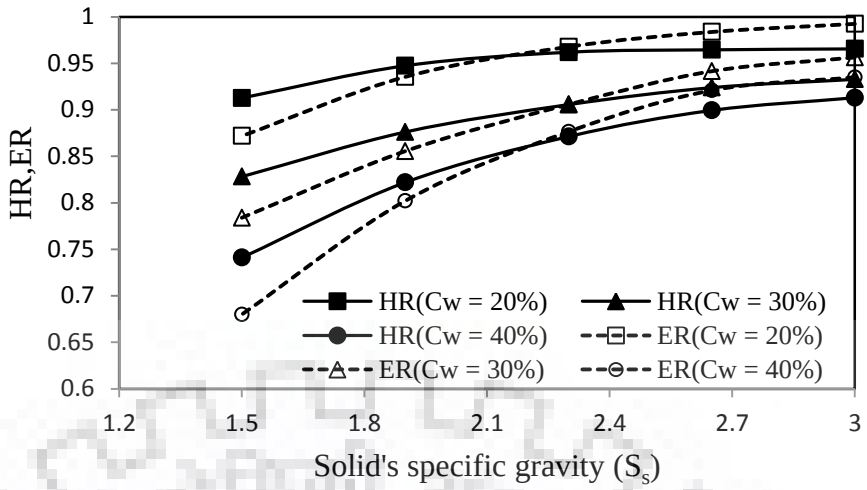

Fig. 4.11 Variation of head and efficiency ratio with specific gravity of solids and weighted concentration for 200 µm size particles at BEP flowrate

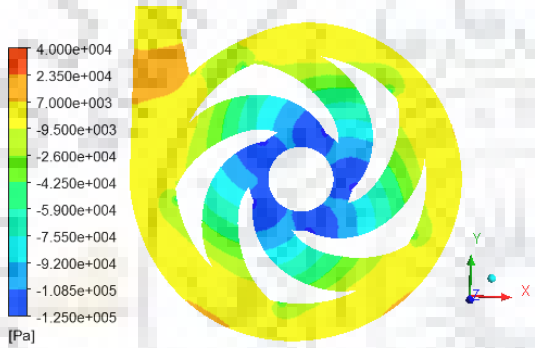

Fig. 4.12 Static pressure contour (Pascal) of mixture at impeller mid-plane at BEP flowrate for 200 µm size particles and Cw = 20%

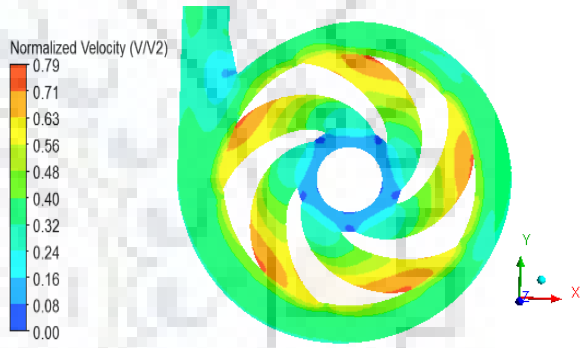

Fig. 4.13 Particle velocity contour at impeller mid-plane at BEP flowrate for 200 µm size particles and Cw = 20%

(a) Impeller mid plane view (b) Impeller isometric view

Fig. 4.14 Planes at different radial locations of the impeller blade

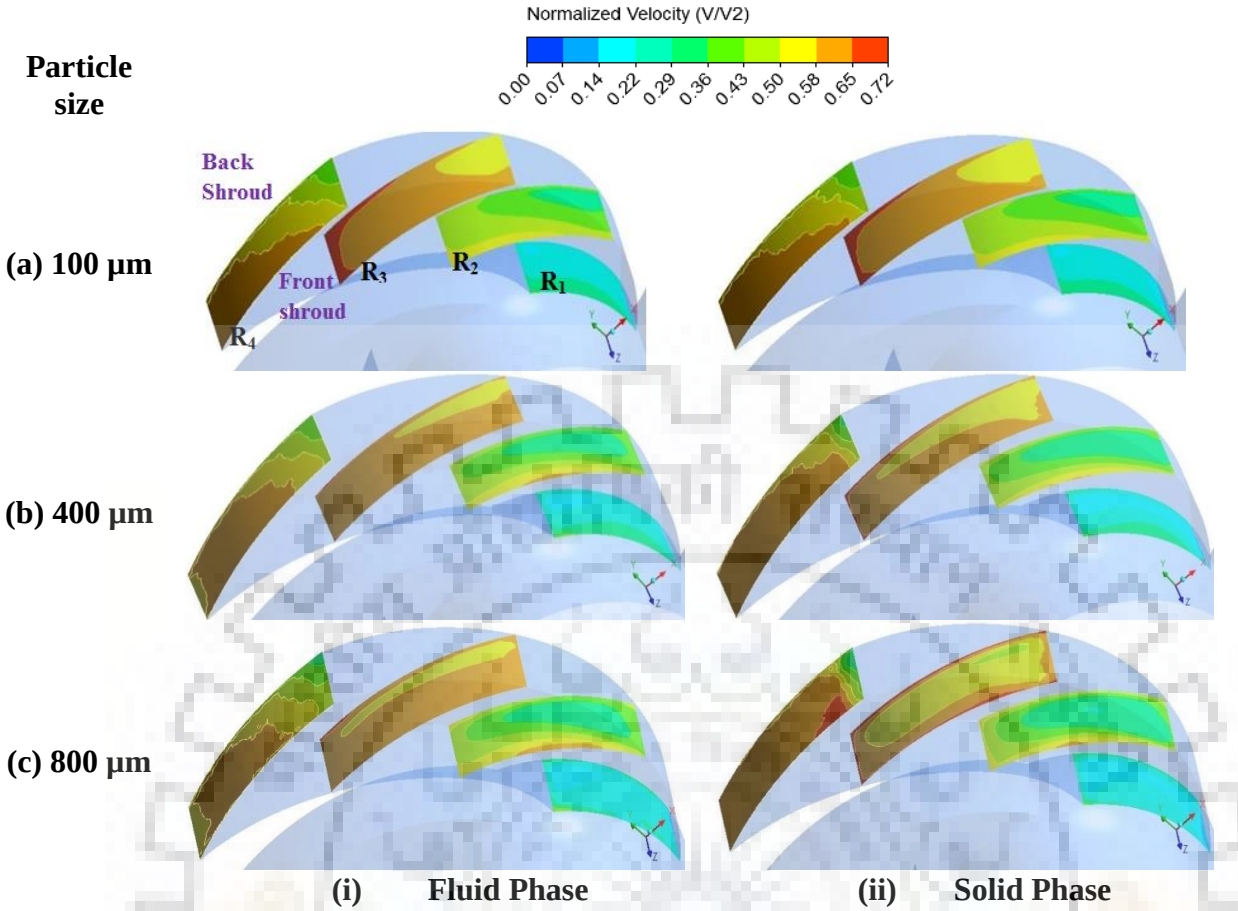

Fig. 4.15 Velocity contours of fluid and solid phases for 100 µm, 400 µm, and 800 µm size particles (S_s = 2.65) at different locations of impeller blade channel for BEP flow rate and Cw = 30%

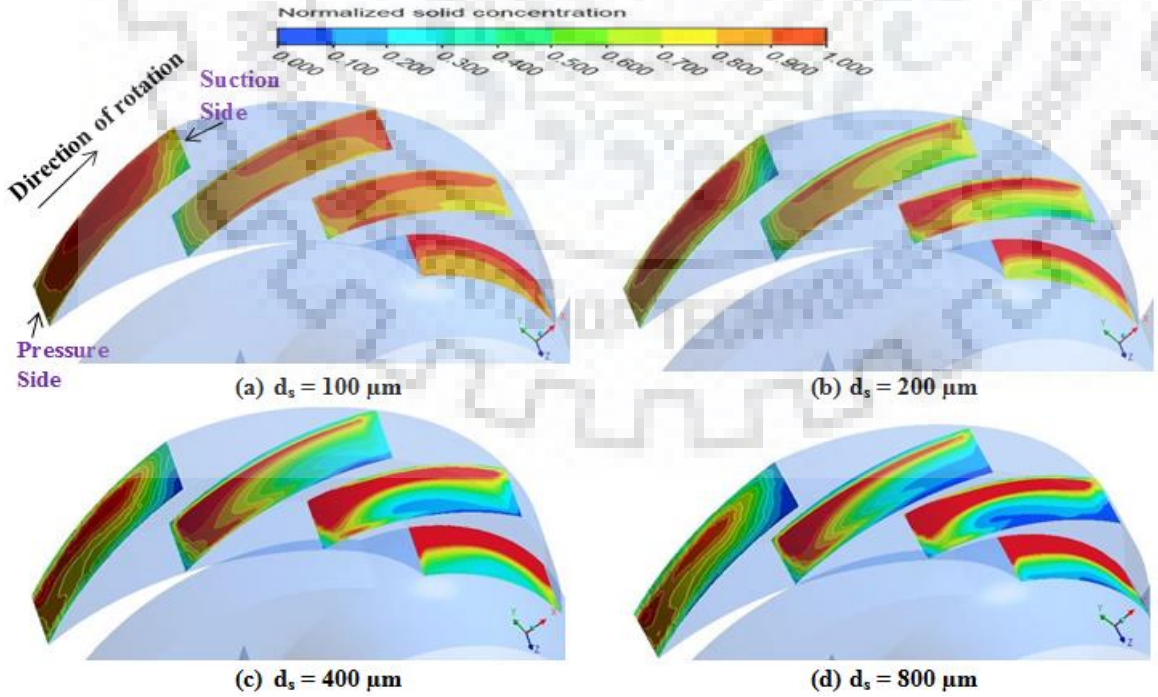

Fig. 4.16 Contours of normalized solid concentration for 100 µm, 200 µm, 400 µm, and 800 µm size particles (S_s = 2.65) at different locations of impeller blade channel for BEP flow rate and Cw = 30%

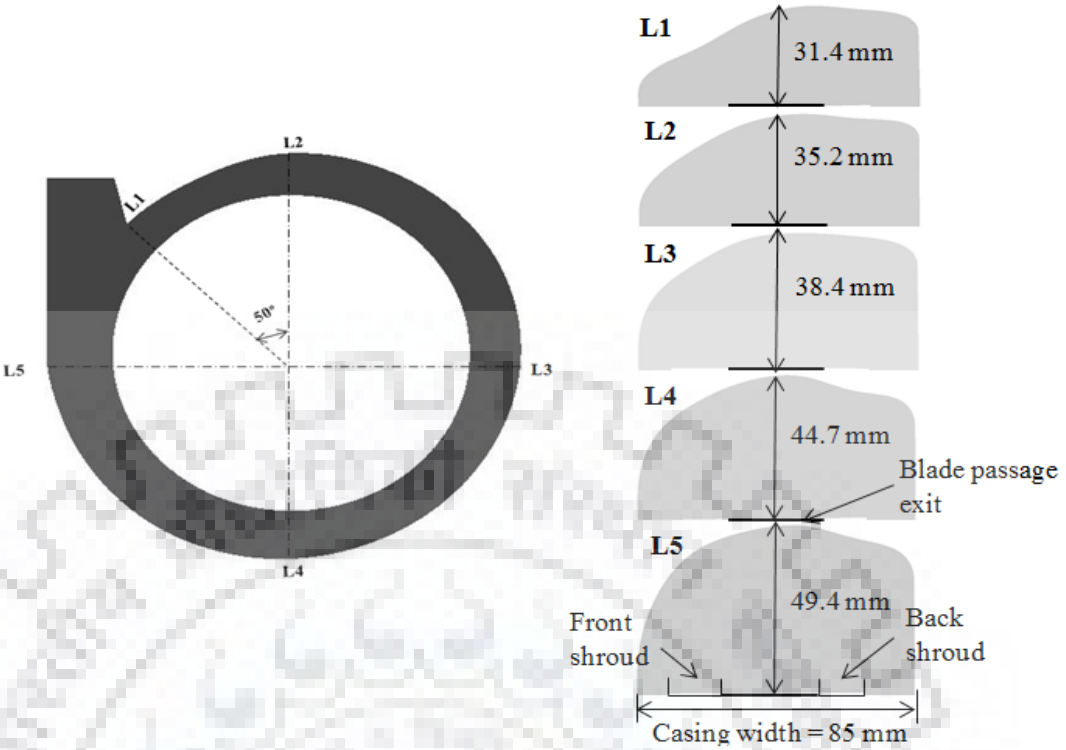

Fig. 4.17 Planes at different angular locations of the casing

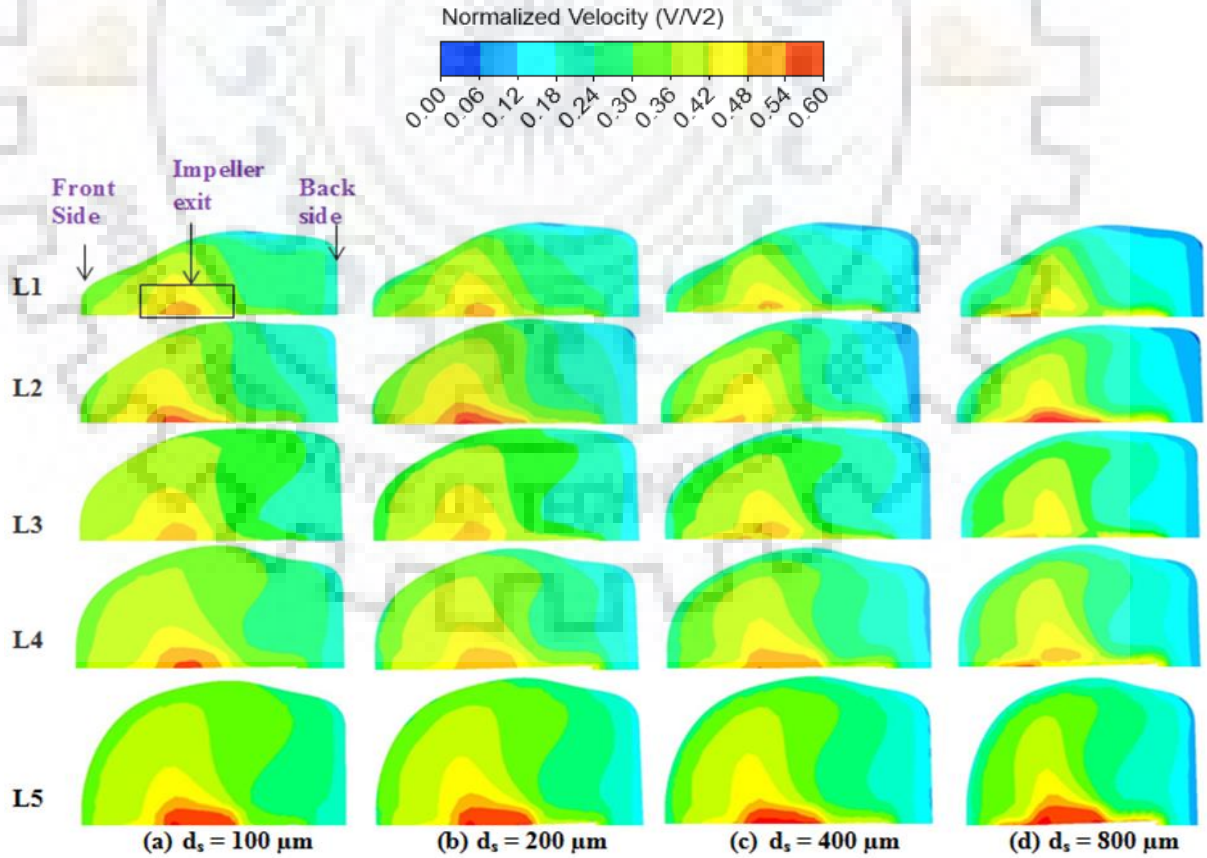

Fig. 4.18 Contours of particle velocity of 100 µm, 200 µm, 400 µm, and 800 µm size particles (S_s = 2.65) at different locations of the casing for BEP flow rate, Cw = 30%

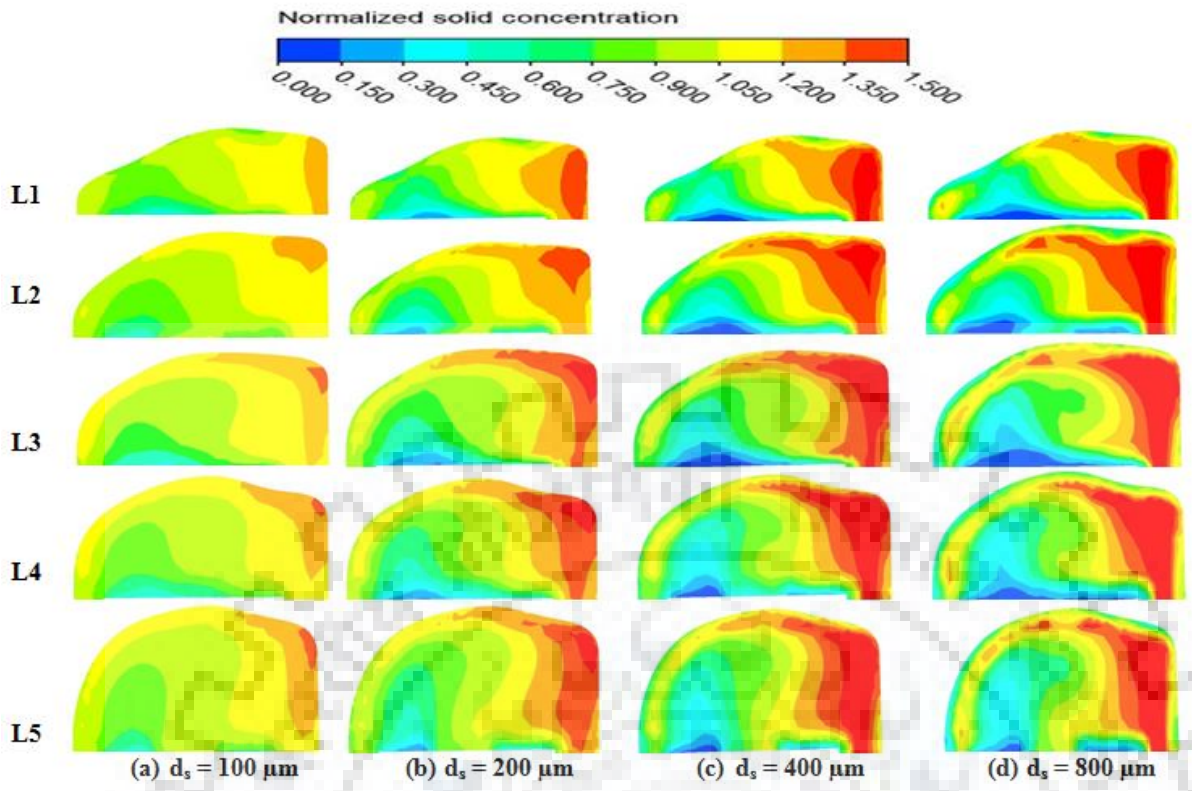

Fig. 4.19 Contours of normalized solid concentration of 100 µm, 200 µm, 400 µm, and 800 µm size particles (S_s = 2.65) at different locations of the casing for BEP and Cw = 30%

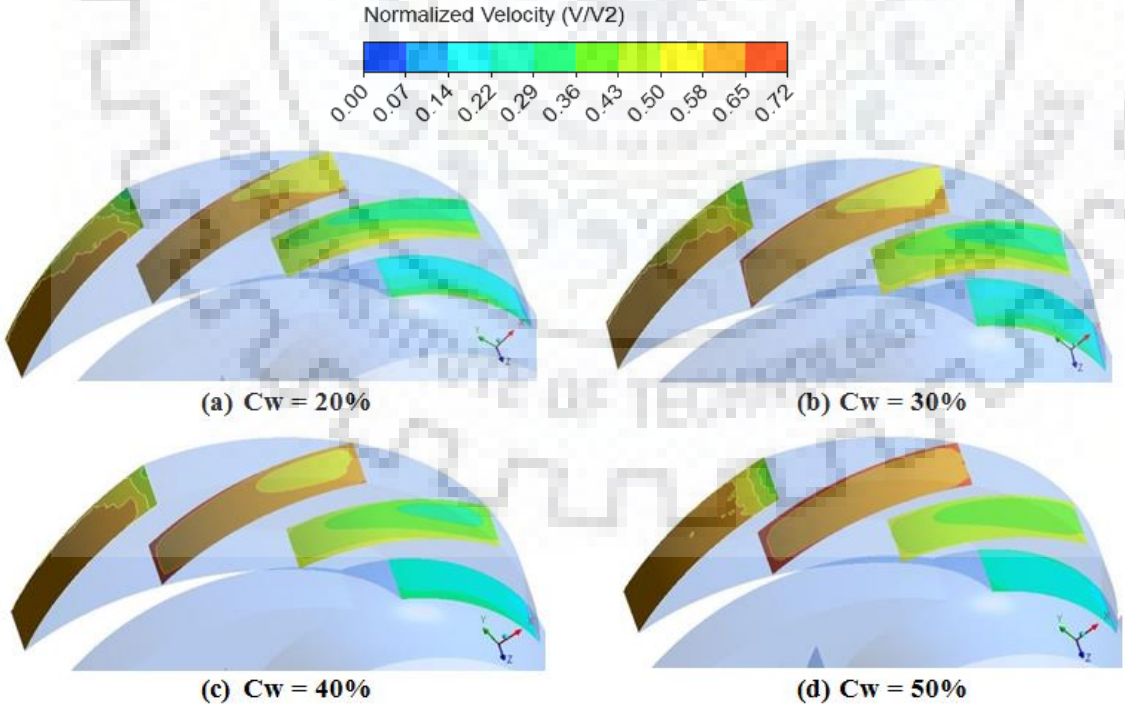

Fig. 4.20 Velocity contours of particle size of 200 µm (S_s = 2.65) at different locations of impeller blade channel for BEP flow rate and Cw = 20%, 30%, 40% and 50%

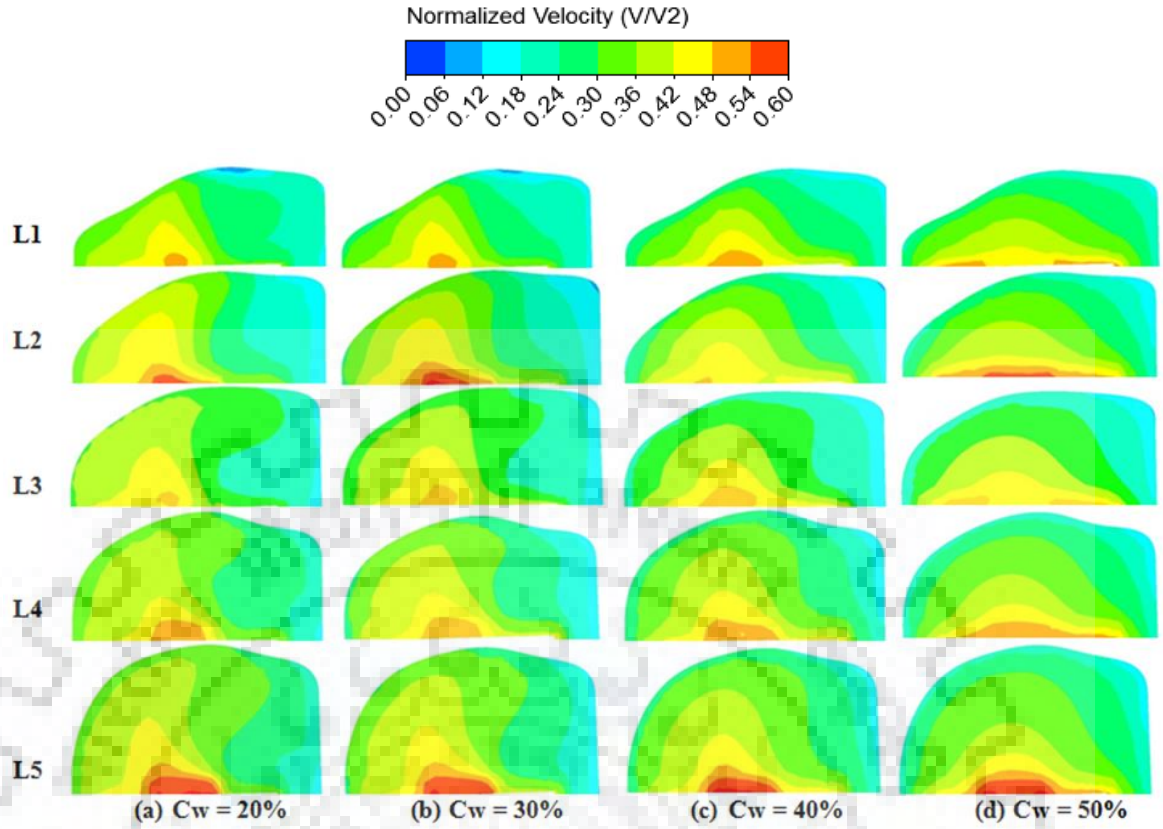

Fig. 4.21 Velocity contours of particle size of 200 µm (S_s = 2.65) at different locations of the casing for BEP flow rate and Cw = 20%, 30%, 40% and 50%

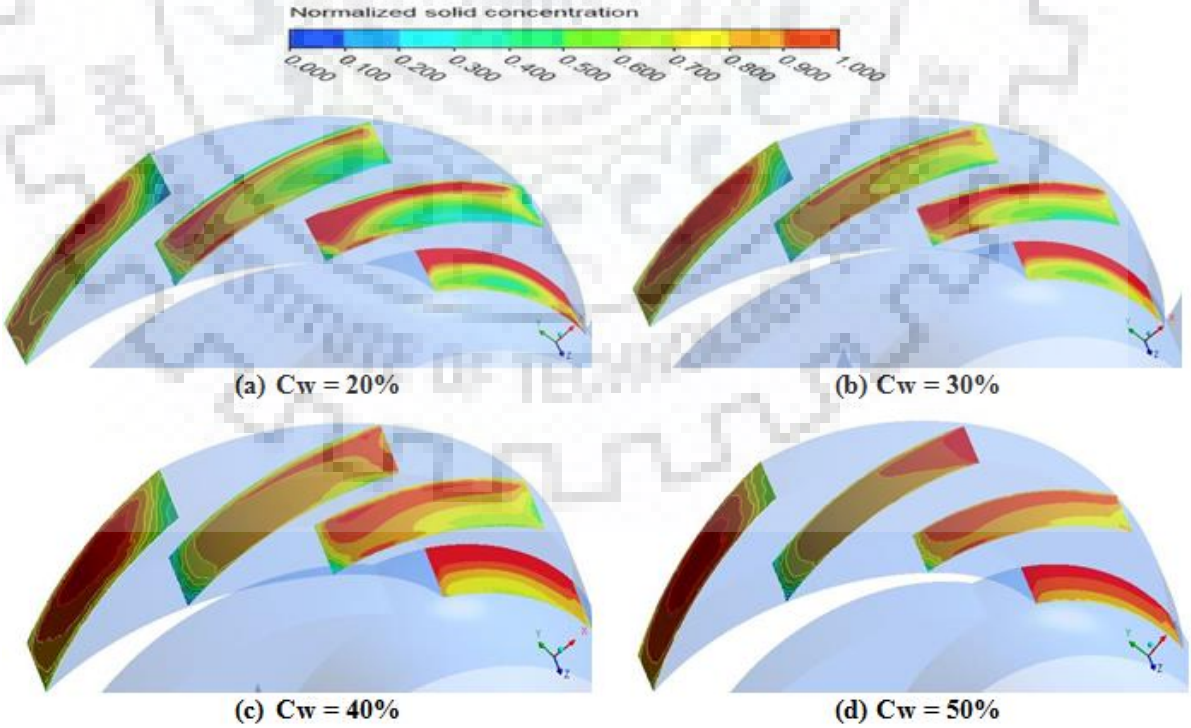

Fig. 4.22 Contours of normalized solid concentration of size 200 µm (S_s = 2.65) at different locations of impeller blade channel for BEP flow rate and Cw = 20%, 30%, 40% and 50%.

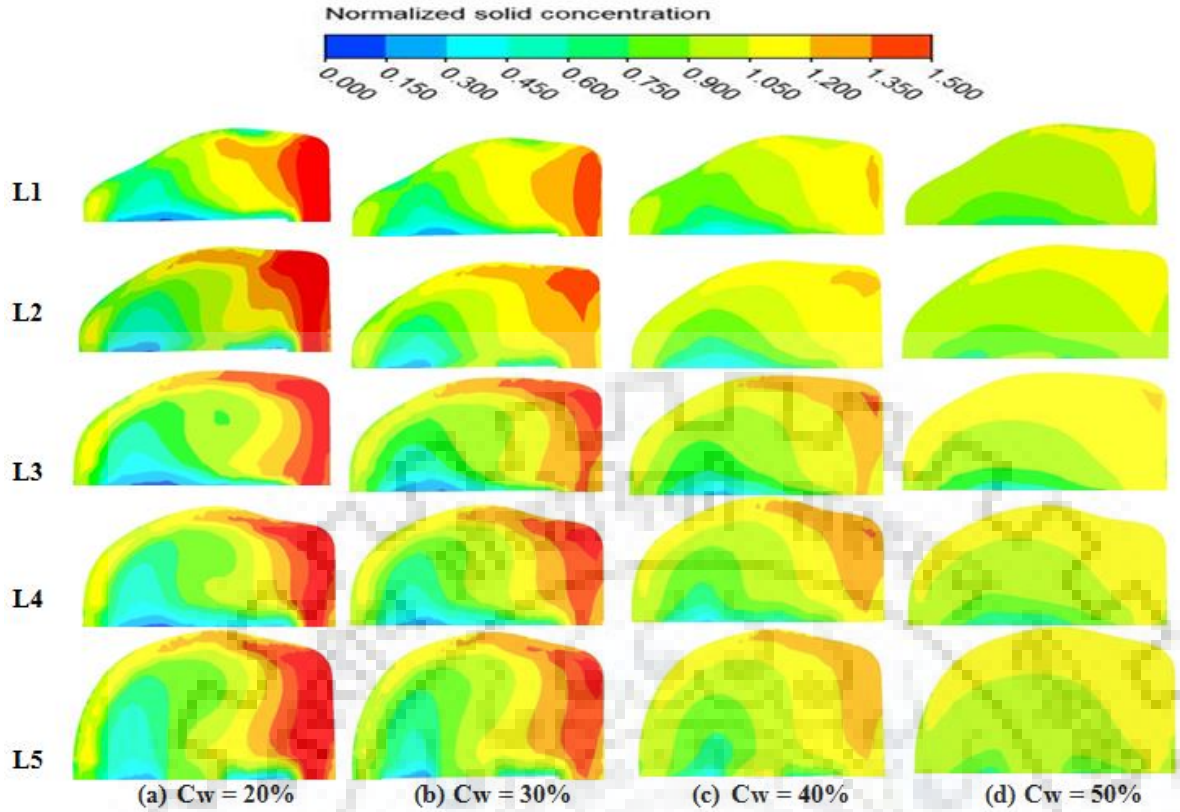

Fig. 4.23 Contours of normalized solid concentration of size 200 µm (S_s = 2.65) at different locations of the casing for BEP flow rate and Cw = 20%, 30%, 40% and 50%.

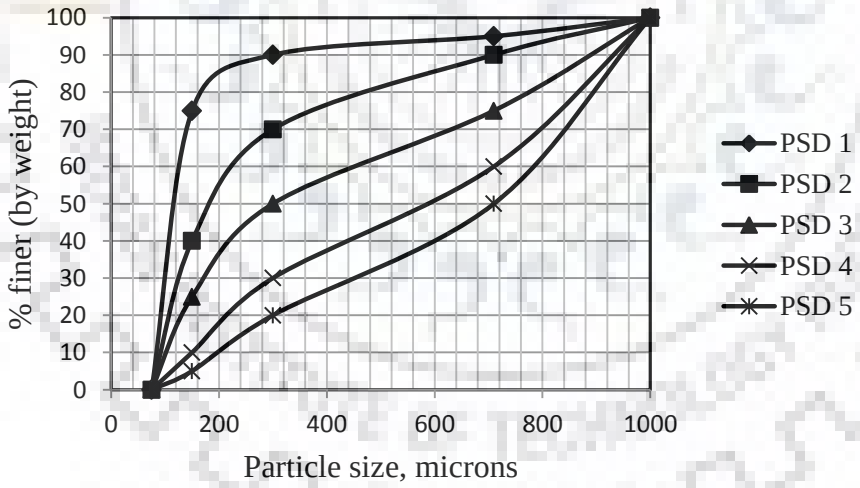

Fig. 4.24 Variation in particle size distribution of different multi-size slurry samples

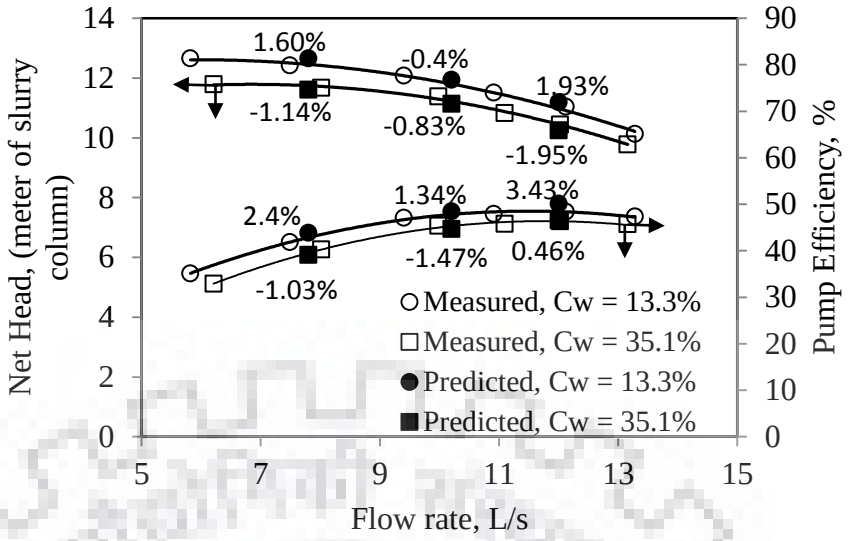

Fig. 4.25 Comparison of measured and predicted performance characteristics of pump handling fly ash-water slurry of 13.3% and 35.1% weight concentration at 1200 rpm

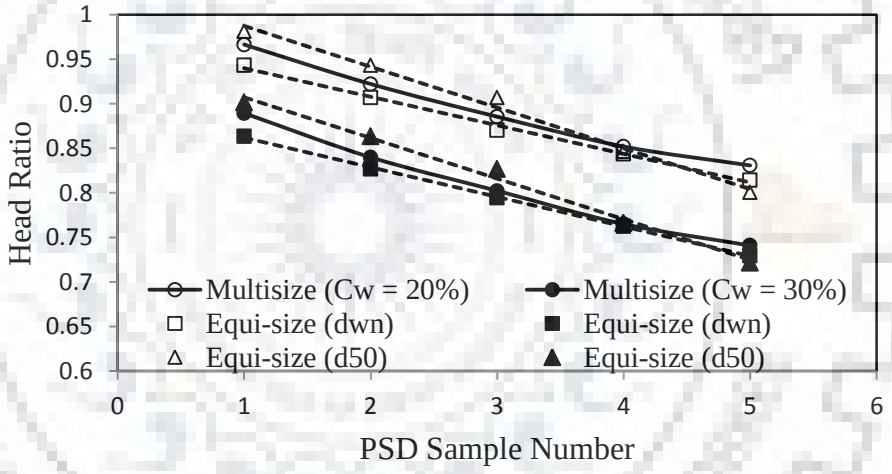

(a)

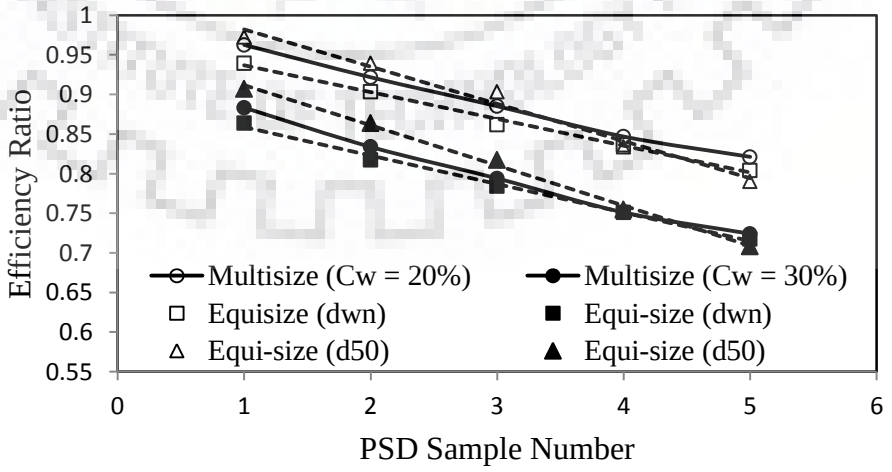

(b)

Fig. 4.26 Variation in head and efficiency ratio with change in particle size distribution of fly ash slurry at BEP flow rate for 20% and 30% weighted solid concentration

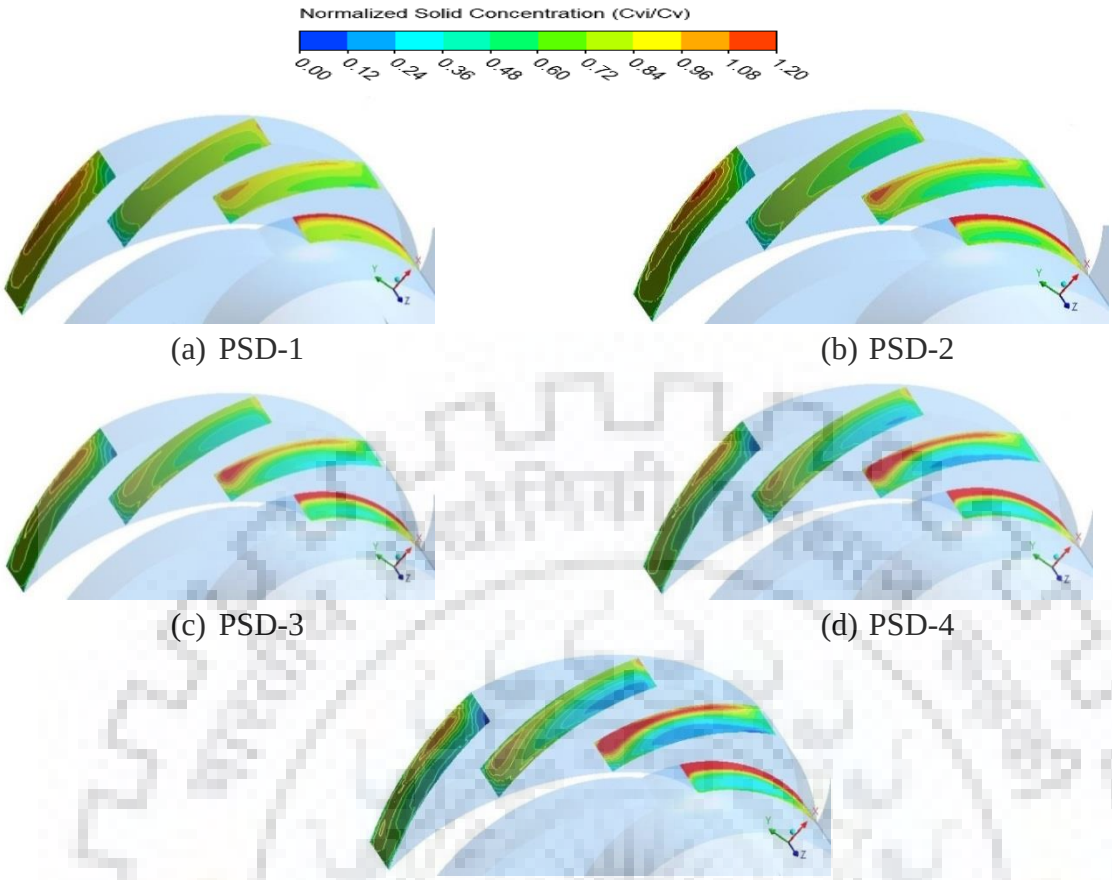

(a) PSD-1 (b) PSD-2

(c) PSD-3 (d) PSD-4

(e) PSD-5

Fig. 4.27 Contours of particle distribution at different locations of impeller blade channel with slurries of different PSD at BEP flow rate and C_w = 30%

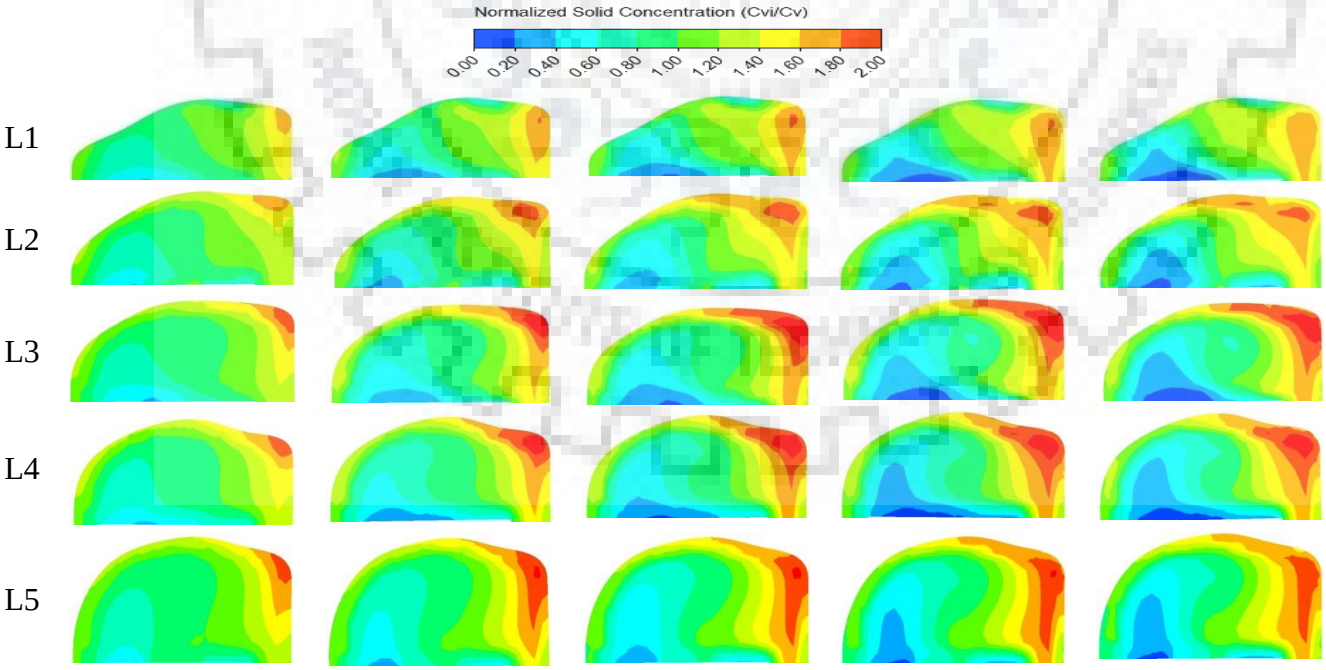

(a) PSD-1 (b) PSD-2 (c) PSD-3 (d) PSD-4 (e) PSD-5

Fig. 4.28 Contours of particle distribution at different locations of casing with slurries of different PSD at BEP flow rate and C_w = 30%

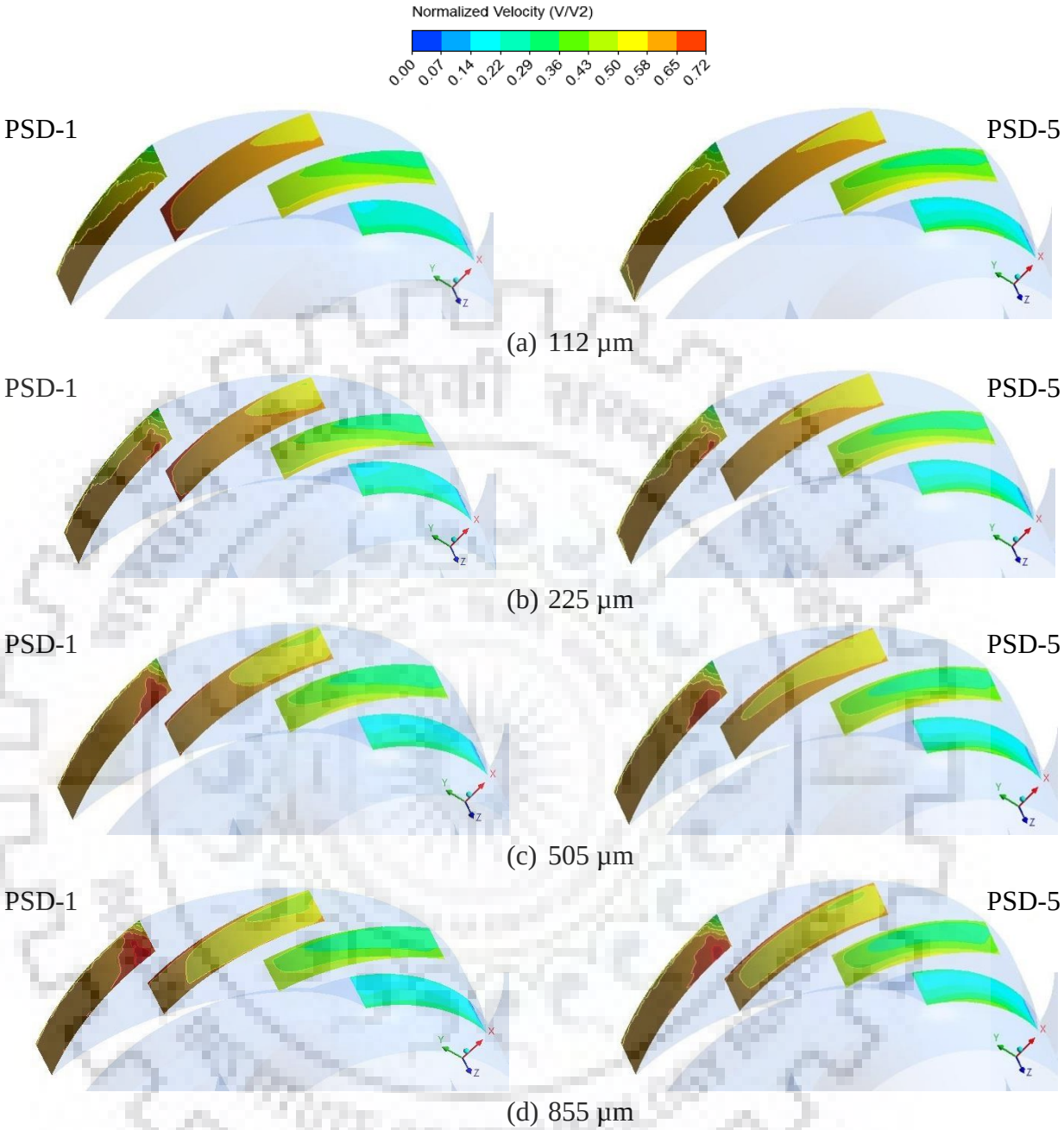

Fig. 4.29 Velocity contours of different size particles at different locations inside impeller blade channel for PSD-1 and PSD-5 at BEP flow rate and C_w = 30%

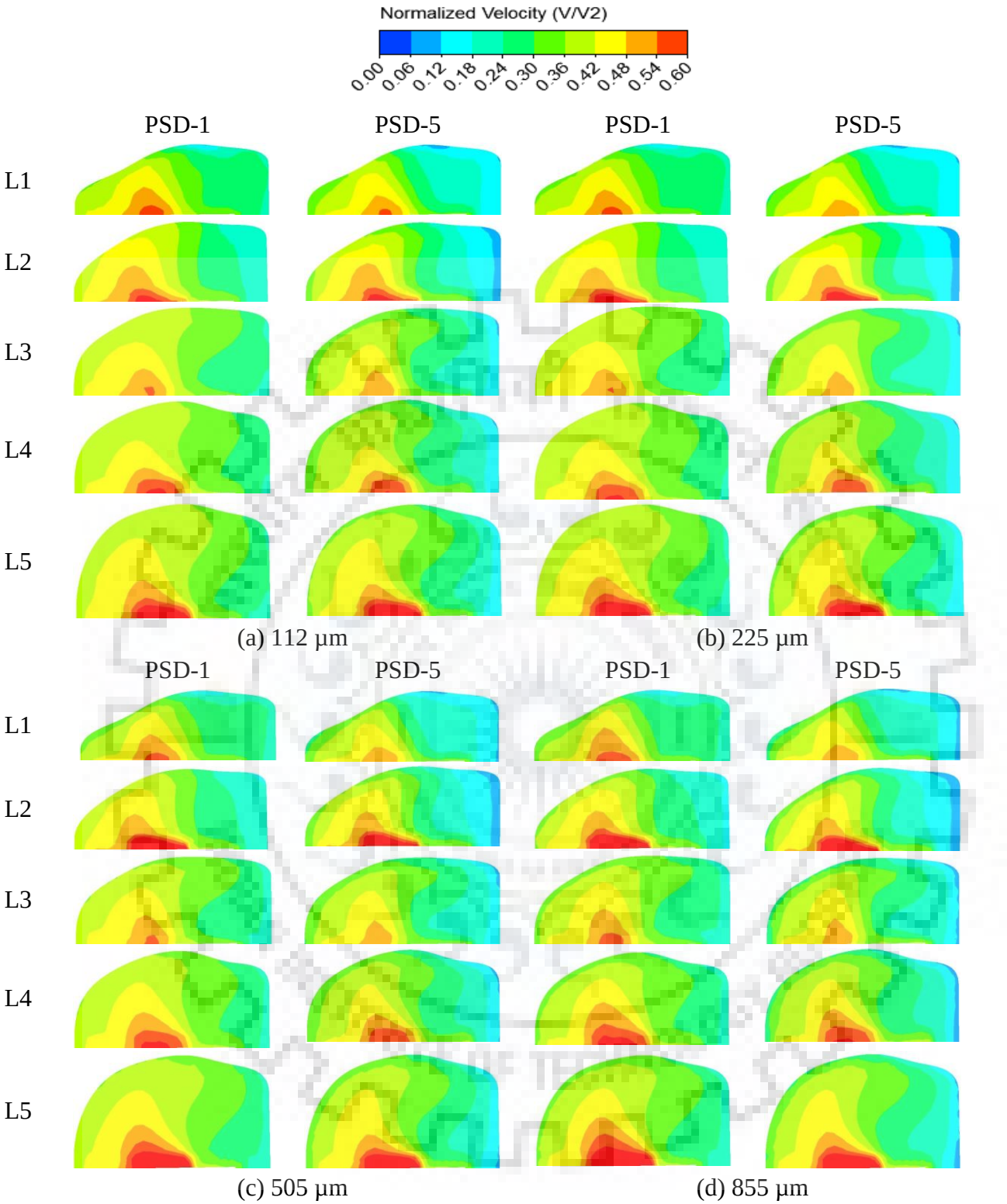

Fig. 4.30 Velocity contours of different size particles at different locations of casing for PSD-1 and PSD-5 at BEP flow rate and C_w = 30%

CHAPTER 5: LABORATORY TEST STUDIES ON SLURRY EROSION OF PUMP MATERIALS

Slurry erosion is a severe problem for components of a slurry transportation system including the centrifugal slurry pump. It affects the economy of the process as the component failures leads to downtime and component replacement costs. A fundamental requirement from the design perspective is to estimate the service life of the pump components subjected to slurry erosion. It requires understanding the mechanism of slurry erosion of the pump materials and the factors affecting it. The mechanism of slurry erosion depends on the properties of the solid particle, target material, as well as the impact conditions [Gandhi et al., 2003]. Bench-scale laboratory test rigs are generally preferred in comparison to in situ conditions or pilot plant test to perform a number of experiments under controlled environment. Slurry pot tester is one of the widely used test rigs to evaluate the erosive wear of the materials at an accelerated rate. Literature [Gupta et al., 1995; Gandhi et al., 2001b] shows that the experimental data of pot tester compares reasonably well with pump and pipeline wear. In the present study, the slurry erosion behaviour of pump materials is experimentally investigated using a large size pot tester developed by Gandhi [2015]. The effect of velocity, particle size, and impact angle on slurry erosion behaviour of pump materials namely steel 304L, grey cast iron, and high chromium white cast iron using three different solid particulate slurries, namely Indian standard sand, iron ore and fly ash are studied. An attempt is made to develop empirical correlations useful for incorporation in CFD for the erosion prediction of different slurries.

5.1 Experimental Program for Erosion Studies in Pot Tester

5.1.1 Experimental Setup

The schematic diagram along with the details of slurry pot tester used in the present investigation is shown in Fig. 5.1 (a-d) and its photographic view is shown in Fig. 5.1 (e). It consists of a stainless steel tank of capacity approximately 270 liters with an internal diameter of 800 mm and height 533 mm, respectively. It is mounted on the iron frame structure and fixed using nut-bolts. It is covered by a transparent acrylic sheet on the top for visualization during experiment. A shaft is inserted from the tank bottom in order to rotate a propeller for maintaining the uniform suspension of the solid particles. The minimum speed of the shaft required for the suspension of particles is determined from the literature [Tarodiya and Gandhi, 2016]. A pitched turbine blade propeller of diameter 560 mm is mounted on the shaft at a distance of 80 mm above the tank bottom and is rotated at 200 rpm by a 2.24 kW DC motor

through a V-belt pulley arrangement. Another shaft is inserted from the top to rotate the wear specimens inside the pot by a 7.45 kW, 440 V and 14.5 A induction motor. To perform the investigations at different speeds, a variable frequency drive (VFD) of ABB make is used. To prevent the leakage of solid-liquid mixture, a combination of oil-seal and mechanical seal is provided to both the shafts. Four stainless steel baffles of size 10 mm x 65 mm x 532 mm are fixed at the inner diameter of the cylindrical tank at equal distances with larger dimension on axial direction to break the vortex motion (if any) created by the propeller and rotating specimens. A drain hole is provided to drain out the solid-liquid mixture after the experiment.

Test fixture, similar to Desale et al. [2005], is fabricated to mount flat wear specimens as shown in Fig. 5.1 (b). The fixtures are made of high-chromium high-carbon steel and heat treated properly to achieve surface hardness of approximately 65 RC. The wear of fixture is lower in comparison to that of the specimens and thus the same fixture can be used for a number of test runs. A slot of size 30 mm x 5 mm x 2 mm, rounded at two ends, is provided at the test fixture to fix a wear specimen inside it. A rectangular tooth of 1 mm thickness and 2.5 mm width is provided on each fixture to place it at the required angle from 0^o to 90^o, in steps of 15^o, with respect to peripheral velocity, using slotted angular plate shown in Fig. 5.1 (c). Each test fixture is hanged on the rotating arm through its one end with the help of 4 mm screw. Two test fixtures are fitted at 180^o apart, at the end of the rotating arm of 237 mm radius to balance the dynamic forces with minimum interference of the wakes. The location of the test fixtures is 355 mm above the tank bottom which corresponds to 0.66 times of the height of the tank. Sharma et al. [2018] identified this location as the zone of minimum turbulence during flow field investigation in the pot tester using Particle Image Velocimetry (PIV) system. Since the volume swept by the wear specimens and the holding arms is very small in comparison to the total cylinder volume and also they are rotated in the direction opposite to the propeller rotational direction, it is assumed that the rotation of wear specimens may not cause substantial swirling motion inside the pot and particles will be impacting the wear sample at its orientation angle with peripheral direction.

The wear specimens of size 30 mm x 5 mm, rounded at both the ends as shown in Fig. 5.1 (d), have an exposed surface area of 144.64 mm^2. While fixing the wear specimen in the fixture, it is ensured that the top surface of the wear specimens and the face of the fixture remain in a single plane.

5.1.2 Properties of Target Materials and Solid Particles

Three different materials, used for manufacturing the pump components, are selected in the present work. The chemical composition of these materials is determined using energy

dispersive X-ray analysis (EDAX). A microhardness tester is used to measure the surface hardness of different target materials. The chemical composition, mass density and hardness of the target materials are listed in Table 5.1.

Three different solid particles namely, Indian standard sand, iron ore and fly ash are used to prepare solid-liquid mixtures with tap water to conduct experiments on erosive wear. For the purpose of conducting the tests on erosive wear, the solid particles of fly ash and iron ore are used in multi-size form, whereas, solid particles of Indian standard sand are sieved using a narrow range of sieve sizes and the particles retained between two successive sieves are used to prepare solid-liquid mixture of mean particle size. The physical and chemical properties of Indian standard sand are given in Table 5.2, which shows that its main constituent is silica. The properties of fly ash particles were discussed earlier in section 3.2.5. Similarly, the properties of iron ore particles are also determined. The measured density of iron ore particles is 2210 kg/m^3. The measured particle size distribution of multi-size iron ore particles using sieve analysis and the pH values of iron ore-water slurry are presented in the Tables 5.3 and 5.4, respectively.

To perform the experiments using sand particulate slurry, the mean particle size of 256 µm (+ 212 –300), 362.5 µm (+ 300 –425), 462.5 µm (+ 425 –500), 550 µm (+500 –600) and 655 µm (+600 –710) are collected. The numbers in the parenthesis represent the successive sieve sizes. Further to check the mean particle size and the shape of the sieved sand particles, scanning electron microscope (SEM) photographs of all five particle sizes are examined as shown in Fig. 5.2. It is observed that the particles of all sizes appear to be angular and almost similar in shape. Further, the SEM micrographs of all particle sizes are analysed by *ImageJ analyzer*. Diameter (d), area (A), and perimeter (P) of a single particle are measured in order to estimate the mean size of the particle and its shape factor (S.F.). The shape factor defined by Cox [1927] is determined using the following relation:

$$\text{Shape Factor} \qquad \text{S.F.} = \frac{4\pi A}{P_p^{\,2}} \tag{5.1}$$

The shape factor of the particles ranges from 0 to 1, where 1 represents the circular shape of the particles, and less value represent the deviation of the particles from circularity. A minimum of 50 particles from each size range is used to estimate its parameters. The results obtained from the image analysis of the particles are presented in Table 5.5. The average particle diameter of different size ranges of solid particles using image analysis is obtained within the successive sieve sizes as discussed above. The difference in the average size by sieve analysis and imaging technique is within 7%. The average shape factor of different size particles is also determined

and presented in Table 5.5. It is observed that the average shape factor of the particles of different size ranges is not the same. The maximum relative variation in the shape factor is within 4%. Since the variation in particle shape is small within the selected particle size ranges, therefore it is assumed that the effect of particle shape on the mass loss variation of the target material for different sand particle size ranges is negligible.

5.1.3 Range of Parameters

Preliminary experiments are performed in the pot tester to investigate the simulated wear conditions. The contribution of mass loss due to corrosion is investigated by rotating the wear specimens of each test material in water alone for the duration of 2 hrs. The specimens are fixed at 30^o orientation angle and rotated to achieve impingement velocity of 13 m/s. To investigate the effect of attrition and rounding-off of particles, experiments are performed with steel 304L wear samples at 13 m/s velocity, 1% weight solid concentration, 550 µm particle size and 30^o orientation angle of the specimens. The repeatability of measurements is checked by taking five measurements under similar operating conditions. For this purpose, the experiments are performed with wear specimens of steel 304L at 30^o and 90^o orientation angles of specimens at 13 m/s velocity, 1% weighted solid concentration, and 550 µm particle size. Experimental investigations on erosion behaviour of pump materials, namely steel 304L, grey cast iron, and high chromium white cast iron, are carried out using mixture of solid particles, namely Indian standard sand, iron ore, and fly ash, in water. The effect of orientation angle, velocity and particle size on erosion rate of all the three target materials is investigated. The range of parameters investigated is listed in Table 5.6. Furthermore, experiments are also carried out to establish the nominal particle size of multi-size slurry. Five different samples of multi-size sand particles are considered and the erosion rate of grey cast iron is measured at two orientation angle 30^o and 90^o, 13 m/s velocity, and 1% weighted solid concentration.

5.1.4 Experimental Procedure and Data Analysis

Fresh machined specimens are used for each experiment. For the similar initial condition of the target surface, the specimens are polished using #1500 emery paper prior to the experiment. The polished wear specimens are then cleaned with acetone and further dried using hot air blower. The slurry is prepared to conduct the experiments by mixing a predetermined mass of sand into the pot filled with water. The test fixtures are screwed on the rotating arm at known orientation angle. The pot is closed by tightening the acrylic cover. The propeller at the tank bottom is then rotated at the predetermined speed to maintain the uniform suspension of solids inside the pot. The rotating arm mounted on the upper shaft is rotated in the direction opposite

to that of propeller at 524 rpm to achieve the average peripheral velocity of 13 m/s of the specimens. The speed of the shaft is measured using a non-contact type tachometer.

An electronic weighing machine having least count of 0.1 mg is used to measure the mass loss of the wear specimen. Average of the mass loss of the two wear specimens, employed for each experiment, is used for further analysis. It is used to calculate the erosion rate of target material at known operating conditions. The erosion rate (ER) is defined as the ratio of the mass loss of the target surface (in gram) to the mass of impacting solid particles (in gram). It has been evaluated using Eq. (5.2) assuming that the particles are uniformly suspended and impacting the exposed surface area of the specimens at all the orientation angles.

$$ER = \frac{W_L \times 10^{-3}}{\rho_s C_v A_s V t} \tag{5.2}$$

Where ρ_s is the mass density of solid particles (kg/m^3), A_s is the exposed surface area of the wear specimen (m^2), C_v is solid concentration by volume (in fractions), V is the peripheral velocity of wear specimen (m/s), W_L is the average mass loss (g) of the specimen in time duration t (sec).

Further to identify the wear mechanism, the worn out surfaces are examined through a scanning electron microscope.

5.1.5 Preliminary Experiments

Preliminary experiments are performed in the pot tester under simulated wear conditions. The contribution of mass loss due to corrosion is investigated by rotating the wear specimens of each target material in water alone for duration of 2 hrs. The specimens are fixed at 30^o orientation angle and rotated to achieve impingement velocity of 13 m/s. The measurement of the mass of the specimens after the test duration did not show any considerable change. Therefore, it is concluded that during the test, the mass loss of the specimens is not contributed by the corrosion. Studies are also carried out to determine the maximum duration for negligible effect of attrition and rounding-off of particles on erosion. Experiments are performed with steel 304L wear samples at 13 m/s velocity, 1% weighted concentration, 550 μm particle size and 30^o orientation angle of the specimens. The variation in mass loss of the target material is measured after each 20 min interval for the total test duration of 80 min. The solid-liquid mixture is replaced periodically at the intervals of 20 min, 40 min, 60 min, and 80 min. The mass loss after 20 min interval for each case of slurry replacement is determined. Fig. 5.3 presents the rate of mass loss with time for four different times of the slurry replacement. It is observed that the mass loss of the samples increases as time duration of the experiment

increases. For the case of slurry replacement after 20 min, the mass loss with time showed linear behaviour. For the case of slurry replacement after 40 min, only little deviation in linearity is observed, and for the slurry replacement after 60 min, the deviation in linearity is significantly increased as compared to 40 min of slurry replacement time. Thus, the effect of attrition and rounding-off of the particles appears significant for slurry replacement time higher than 40 min at this velocity.

Experiments are also performed to check the repeatability of the measurements in the slurry pot tester. Five measurements are carried out at 30^o and 90^o orientation angle of steel 304L specimens at 13 m/s velocity, 1% weighted solid concentration, and 550 µm particle size. The measured mass loss for each measurement and the variation in the mass loss with the average mass loss of all the ten samples is tabulated in Table 5.7 and presented graphically in Fig. 5.4. The average mass loss of wear specimens at 30^o and 90^o orientation angle is obtained as 0.01738 g and 0.00651 g, respectively. It is observed that the measured mass loss data is scattered around the average mass loss under similar operating conditions for both the orientation angles. The estimated coefficients of variation of all the ten samples at 30^o and 90^o orientation angles are 3% and 4.3% around the mean value. Thus the maximum scatter in the mass loss measurement of wear specimens at any orientation angle may not be more than 4.3%. The scatter of data may further reduce for the average of the two specimens, considered in this study.

5.2 Parametric Investigation of Erosion Behaviour of Pump Materials

The slurry erosion behaviour of different pump materials is investigated experimentally using the pot tester. For each target material, the effect of dominating parameters, namely impact angle, particle size and velocity is determined. The obtained values of erosion rate of materials at different operating conditions are listed in Table 5.8 (a-i).

5.2.1 Effect of Impact Angle

Impact angle of the particles is one of the critical parameters affecting the erosion rate of the target material. It gives an idea about the maximum erosion of a slurry handling equipment [Gandhi et al., 2003]. Hence initially the erosion of the materials is evaluated at different impact angles in the pot tester at 13 m/s velocity and 1% weight concentration for two mean particle sizes. The wear specimens are positioned at different orientation angles, varying from 15^o to 90^o with respect to the flow direction, using a fixed slotted angular plate. The variation of mass loss of individual specimen (scatter bar) as well as average rate of erosion of target materials at different orientation angles is presented in Fig. 5.5 (a-c). It is seen from Fig. 5.5 (a-

c) that the erosion rate of the tested materials, namely steel 304L, grey cast iron, and high chromium white cast iron increases with increase in the orientation angle till 30^o and then decreases with further increase in orientation angle till 90^o for both the particle sizes. In literature, a similar trend of wear behavior was observed for steels [Desale et al., 2006; Aminul Islam and Farhat, 2014; Yoganandh et al., 2015; Javaheria et al., 2018], grey cast iron [Yildizli et al., 2006], and high chromium white cast iron [McDonald and Kelley, 1994; Al-Bukhaiti et al., 2017]. Further to compare the effect of particle size on the angle of the maximum erosion, it is observed that it is independent of the particle size for all the three target materials.

Investigation of the effect of impact angle on target material erosion rate with the fly ash and iron ores slurries is also carried out. The estimated erosion rate of the target materials, namely grey cast iron and steel 304L with fly ash and iron ore slurries is presented in Fig. 5.6. It is seen that the angle of maximum erosion of the target materials is independent to the change in erodent properties. However, the magnitude of erosion of the target materials is significantly changed for iron ore and fly ash particles. This may be attributed to the variation in the physical properties of the particles. This is in line with the observations of Desale et al. [2006]. They also examined the variation in erosion rate of materials with erodent properties and the dependence of angle of maximum erosion on target material properties for different erodents.

To identify the effect of impact angle on the material removal due to erosion, SEM micrographs of eroded surfaces are examined. The SEM micrographs of the eroded surfaces of steel 304L, grey cast iron and high chromium white cast iron are presented in Figs. 5.7 (a-f), 5.8 (a-f) and 5.9 (a-f), respectively. It is observed that the mechanism of material removal of the three target materials is similar at any orientation angle for the similar experimental condition. However, for all the materials, the mechanism of material removal significantly changes with the change in orientation angle. At 15^o orientation angle, fine scratches are displayed on all the surfaces (Figs. 5.7a, 5.8a and 5.9a). For orientation angle of 30^o and 45^o large cut marks and the ridges at the end of the cut marks is seen (Figs. 5.7b,c, 5.8b,c and 5.9 b,c). At higher orientation angles (60^o- 90^o), the material removal due to indentation and formation of material extruded lips on the surface is observed (Figs. 5.7d-f, 5.8d-f and 5.9).

The change in material removal mechanism with orientation angle can be related to the two components of the particle impact force i.e. normal and tangential components. At low orientation angle ($\leq 15^o$), the normal component is less as compared to the tangential component of particles impacting on the surface. Thus the impacting particles do not penetrate into the target surfaces and only produces fine scratches on the surfaces resulting in less erosion of target materials. With the increase in orientation angle ($15^o < \alpha \leq 45^o$), the normal component

of impact force increases due to which the particle penetration in to the target surface increases. Thus the particles gouge the surface and raise the material in front of their cutting path which is removed with the subsequent impact of the particles. This results in higher erosion of the target surface due to cutting and platelet deformation. With further increase in orientation angle ($45^o < \alpha \leq 90^o$), the particles impacting on the target surface have large normal component of impacting force compared to the tangential component. Thus, the particles penetrate and indent on the target surface. The deep indentation leading to the formation of raised lips. Some of these lips are removed due to fatigue with subsequent impacts of particles. Target surface also get work hardened and some mass may detach from the surface due to fatigue after large number of successive impacts. This results the small erosion rate of the target surface.

5.2.2 Effect of Velocity

To investigate the effect of velocity on the slurry erosion of target materials, experiments are conducted in the velocity range of 9.0-18.5 m/s. Initially, the measurements are performed at different orientation angles and velocities to determine their effect on different target materials. The measured erosion rate of the target materials, namely steel 304L and grey cast iron, at different orientation angles and velocities are presented graphically in Fig. 5.10 (a,b). It is seen that the increase in velocity increases the erosion rate of the materials. The increase in the material loss with velocity is attributed to the increase in kinetic energy of the impacting particles. The variation in erosion rate of the materials shows a similar trend with impact angle at all the velocities. The orientation angle at which the maximum erosion of the target material occurred is the same for all the velocities.

Many investigators [Finnie and Mcfadden, 1978; Lin and Shao, 1991a; Gupta et al., 1995; Gandhi et al., 1999; Oka and Yoshida, 2005; Desale et al., 2011; Aminul Islam and Farhat, 2014; Rawat et al., 2017] proposed power law relationship for erosion rate with velocity. The measured erosion rate of the materials with velocity for different orientation angles is plotted in Fig. 5.11 (a-c). It is observed that the velocity exponent for steel 304L varies from 2.31 to 2.77 with the variation of orientation angle from 15^o to 90^o (Fig. 5.11a). The obtained values of velocity exponent are in the range of 2-3 which is reported for steels in literature [Haugen et al., 1995; Oka and Yoshida, 2005; Javaheria et al., 2018]. The increase in velocity exponent with impact angle was also examined by Finnie and Mcfadden [1978] and Lin and Shao [1991a]. They attributed this variation to the change in mechanism of erosion of materials. The velocity exponent for cutting wear is generally less as compared to that for deformation wear [Lin and Shao, 1991a]. Thus the velocity exponent increases with increase in impact angle as the contribution of cutting wear decreases and deformation wear increases. The increase in velocity

exponent with impact angle is also seen with the other target materials, grey cast iron and high chromium white cast iron (Fig. 5.11b,c). The values of velocity exponent at 30^o and 90^o orientation angles are observed as 2.84 and 3.03 for grey cast iron and 2.73 and 2.88 for high chromium white cast iron, respectively. It is seen that the velocity exponent values of different target materials is not same. This may be attributed to the variation in the properties of the target materials. The variation in the velocity exponent with the change in target material properties were also reported by Lin and Shao [1991a] and Oka and Yoshida [2005].

Further, experiments are conducted with fly ash and iron ore particulate slurries at 30^o and 90^o orientation angles for all the three target materials in the velocity range of 11-18.5 m/s to investigate the effect of erodents. The measured material loss and the calculated erosion rate at different operating conditions are given in Table 5.8 (d-i). The variation in erosion rate of materials with velocity at 30^o and 90^o orientation angles for iron ore and fly ash particulate slurry is presented graphically in Figs. 5.12 (a-c) and 5.13 (a-c), respectively. The obtained velocity exponent values for steel 304L at 30^o and 90^o orientation angles are 2.48 and 2.82 respectively, with iron ore particles, and, 2.83 and 2.95, respectively, with fly ash particles. For grey cast iron the velocity exponent values at 30^o and 90^o orientation angles are obtained as 2.86 and 2.93, respectively with iron ore particles and 3.23 and 3.43, respectively with fly ash particles. For high chromium white cast iron, the velocity exponent values at 30^o and 90^o orientation angle are obtained as 2.84 and 2.9, respectively with iron ore particles and 3.27 and 3.49, respectively with fly ash particles. It is seen that the value of velocity exponent is varied with the change in properties of impacting particles. The dependence of velocity exponent with the change in erodent properties were also noticed in literature [Feng and Ball, 1999; Hussainova et al., 2001; Oka et al., 2005]. Feng and Ball [1999] reported that the increase in velocity exponent of the target materials is due to the reduction in hardness and toughness of the erodents. Hussainova et al. [2001] and Oka et al. [2005] reported increase in velocity exponent with decrease in particle hardness.

The SEM micrographs of worn out specimens are performed to identify the effect of velocity on the material removal due to erosion. The SEM micrographs of the eroded surfaces at 30^o and 90^o orientation angles for steel 304L, grey cast iron and high chromium white cast iron at three different velocities are presented in Figs. 5.14 (a-f), 5.15 (a-f) and 5.16 (a-f), respectively. It is observed that the dominant mechanism of material loss at the impact angle of 30^o and 90^o is cutting and deformation, respectively. The material loss due to cutting is related to the removal of the target material in the form of the chips by shear due to the erodent. While in deformation,

the material is lost due to the formation of craters which get flattened and fractured with the repeated impact of particles.

It is seen that for all the materials at 30^o and 90^o orientation angles, the mechanisms of material removal of the target surfaces is primarily due to cutting and deformation, respectively, and it does not change with the increase in velocity. At low velocity, a few cutting and indentation marks are seen on the surface (Figs. 5.14a,d, 5.15a,d and 5.16 a,d). With the increase in velocity, the intensity of cutting and deformation increases. At the velocity of 18.5 m/s, large number of cutting and indentation marks are seen on the surface (Figs. 5.14c,f, 5.15c,f and 5.16c,f) which is supported by the higher erosion rate of the surfaces at this velocity.

5.2.3 Effect of Particle Size

The effect of particle size on slurry erosion behaviour of target materials is determined using different mean size sand particulate slurries. Five narrow size ranges of sand particles of mean size ranging from 256 µm to 655 µm are used as erodents. The experiments are performed with all the three target materials for different particle sizes at two orientation angles, namely 30^o and 90^o, for 13 m/s velocity and 1% weight concentration. The effect of particle size at 30^o and 90^o orientation angles on erosion rate of the target materials is presented in Fig. 5.17 (a-c). It is observed that the increase in particle size increases the mass loss of materials, a phenomenon normally seen in the literature [Iwai and Nambu, 1997; Desale et al., 2009; Abouel-Kasem, 2011]. This is attributed to the increase in energy imparted by the solid particle to the target surface with the increase in its size.

Many investigators [Elkholy, 1983; Oka and Yoshida, 2005; Gupta et al., 1995; Desale et al., 2009; Abouel-Kasem, 2011; Rawat et al., 2017] proposed a power law relationship between erosive wear and particle size. It is seen from Fig. 5.17 (a-c) that the power law index of particle size for different materials varied for 30^o and 90^o orientation angles. For the 30^o orientation angle, the power law exponent is observed as 0.79, 1.21 and 0.84 for steel 304L, grey cast iron and high chromium white cast iron, respectively. The exponent for the 90^o orientation angle is found as 0.89, 1.30 and 1.4 for steel 304L, grey cast iron, and high chromium white cast iron, respectively. Higher values of particle size exponent for 90^o orientation angle compared to 30^o were also observed by Desale et al. [2009].

5.3 Development of Correlation for Estimation of Slurry Erosion

To predict the slurry erosion, the general form of empirical correlation is expressed as [Oka and Yoshida, 2005]

$$ER = K f(\alpha) V^{\beta} d^{\gamma} \quad (5.3)$$

Where ER is the erosion rate that is defined as the ratio of amount of mass loss of target material due to particle impact to the total mass of impacting particle, V is the velocity, α is the particle impact angle, d is the particle size; K, β, γ are the constants whose value may be a function of properties of target material, solid particle and the mechanism of material removal.

Based on the experimental data, an attempt has been made to develop empirical correlations to estimate the material loss due to erosion of the equipment handling solid-liquid mixture in the form of Eq. (5.3). The present experimental data shows the variation of the effect of particle size and velocity for 30^o and 90^o orientation angles, which may be attributed to the change in the dominant mechanism of erosion. Investigators [Bitter, 1963a,b; Neilson and Gilchrist, 1968; Huang et al., 2008; Desale et al., 2011] used separate correlations for cutting and deformation wear to incorporate the effect of impacting parameters on the total erosive wear. In view of above, the available experimental data are used to develop correlations as contribution of cutting and deformation wear for estimating the total wear as proposed earlier [Neilson and Gilchrist, 1968; Desale et al., 2011].

The erosion rate at 90^o impingement angle is assumed to be contributed by the only deformation (ER_{D90}). The erosion rate due to deformation at any other impact angles (ER_D) is determined using the following relationship proposed by Neilson and Gilchrist [1968].

$$ER_D = ER_{D90} (\sin\alpha)^2 \quad (5.4)$$

To determine the contribution of erosion rate due to cutting (ER_c) in total erosion rate (ER), the erosion rate due to deformation obtained from Eq. (5.4) is subtracted.

$$ER_C = ER - ER_D \quad (5.5)$$

The variation in cutting and deformation wear rate of the materials with orientation angles is determined and presented in Fig. 5.18. It is observed that the erosion of materials due to cutting shows increasing trend with the impact angle up to a certain angle and then decreases to zero at normal impact angle. Whereas, the variation in the erosion of materials due to deformation wear shows increasing trend with orientation angle and maximum at the normal impact angle. Zhong and Minemura [1996] also observed that the contribution of cutting wear to the total wear is more up to the angle of the maximum wear for the materials showing ductile erosion behaviour. Then it decreases leading to only deformation wear at normal impact angle.

To obtain the correlations, firstly a functional relationship of erosion rate with impact angle is determined. For this purpose, the dependence of erosion rate due to cutting with orientation angle is calculated in terms of the normalized cutting erosion rate (ER_c/ER_{cmax}). It is defined as

the ratio of the erosion rate due to cutting at any orientation angle to the maximum erosion rate due to cutting under the similar experimental conditions [Desale et al., 2011]. It is expressed as:

$$ER_C / ER_{Cmax} = f(\alpha) \tag{5.6}$$

The normalized cutting erosion rate of target materials at different velocities is plotted against the orientation angle as shown in Fig. 5.19 (a-c). It is assumed that at zero degree angle of orientation, no erosion takes place. In the present work, the turbulence inside the pot tester was minimised by using a propeller rotating at minimum speed. This may result in no deformation wear and also negligible cutting wear at zero degree angle. The normalized erosion rate is varied in the range of 0 to 1 for the orientation angle range between 0^o to 90^o, respectively. It is observed that despite the variation in velocity and particle size the trend of normalized cutting erosion of the target materials with impact angle remains almost similar. Thus to determine the functional dependence of cutting wear rate with orientation angle, a function has to satisfy the condition of ER_C/ER_{Cmax} equal to zero at 0^o and 90^o, and 1 at the angle of maximum erosion due to cutting. Two different functions are selected as below.

A function is selected to satisfy the condition of ER_C/ER_{Cmax} equals to zero at 0^o and 1 at the angle of maximum erosion due to cutting as below [Desale et al., 2011]:

$$f(\alpha) = a_1 \left[\sin\left(\frac{\pi}{2}\right)\left(\frac{\alpha}{\alpha_{max}}\right)\right]^{b_1} \qquad \text{for } 0 \text{ deg} \le \alpha \le \alpha_{max} \tag{5.7}$$

Similarly a function is selected to satisfy the condition of ER_C/ER_{Cmax} equals to 1 at the angle of maximum erosion due to cutting and zero at 90^o as below [Desale et al., 2011]:

$$f(\alpha) = a_2 \left\{ \sin\left[\left(\pi/2\right) - \left(\pi/2\right)\left(\frac{\alpha - \alpha_{max}}{90 - \alpha_{max}}\right)\right]\right\}^{b_2} \qquad \text{for } \alpha_{max} < \alpha \le 90 \text{ deg} \tag{5.8}$$

The constants a_1, b_1, a_2, and b_2 in the functions selected above are determined for each target materials from the normalized cutting erosion rate data using the method of least square. The obtained values of the constants a_1, b_1, a_2, and b_2 for all the target materials are presented in the Table 5.9.

The above functional relationships representing dependence of orientation angle to the cutting erosion rate [Eqs. (5.7) and (5.8)] are further used to develop correlations for the estimation of cutting erosion rate of target materials. Thus, the cutting erosion rate at any angle is divided by the function of orientation angle to determine the constant K and the exponent, β and γ in Eq. (5.3) for erosion due to cutting. A method of least square is used to find a relationship that yields a best-fit equation for cutting erosion of the target materials.

The relationship obtained to estimate the cutting erosion rate of the steel 304L is given as:

$$ER_C = 1.51\times10^{-11} f(\alpha) V^{2.15} d^{0.71} \quad (5.9)$$

Similarly the constant K and the exponent, β and γ in Eq. (5.3) are determined for the erosion due to deformation. For that the experimental data of erosion of target materials at 90° orientation angle is used.

The relationship obtained to estimate the deformation erosion rate of the steel 304L is given as:

$$ER_{D90} = 2.36\times10^{-13} V^{2.8} d^{0.98} \quad (5.10)$$

Finally the total erosion rate (ER) of steel 304L at any angle is calculated as

$$ER = ER_C + ER_{D90} (\sin\alpha)^2 \quad (5.11)$$

The obtained values of constant K and the exponent, β and γ for the cutting and deformation erosion of the materials with sand, iron ore and fly ash particulate slurries are listed in Table 5.10 (a-c).

5.4 Study on Representative Particle Size of Multi-size Particulate Slurry

In commercial slurry transportation, usually the particle size of the transported solids is varied over the three orders of magnitude (μm to mm) [Gandhi and Borse, 2004]. Variation in particle size distribution (PSD) of solids significantly affects the wear characteristics of the components of pumps and pipeline [Pagalthivarthi et al., 2013; Gupta et al., 1995]. Different approaches have been proposed to characterize the PSD of multi-size slurry for wear prediction. Roco and Cader [1988] have suggested for the use of d_{80} size for better erosion rate predictions. Gupta et al. [1995] reported that median (d_{50}) and weighted mean size (d_{wn}) can be used as representative size for the PSD to estimate erosion wear within an error band of ± 17 and $\pm$ 11%, respectively. Gandhi and Borse [2004] reported that the weighted mass particle size is more suitable representative particle size of the multi-sized slurry for the erosion prediction. Pagalthivarthi et al. [2013] reported that the average of d_{50} and d_{85} size was more suitable representative size of the multi-size slurry to predict erosion rate accurately.

The present study is performed to determine the representative particle size for the multi-size slurry. The experiments are carried out with multi-sized sand-water slurry in a slurry pot tester to determine the erosion rate of grey cast iron at 30° and 90° orientation angles for velocity of 16.5 m/s and 1% weight concentration. To conduct the experiments, five different samples of multi-size sand-water slurry are prepared. Each sample of multi-size sand slurry is prepared with four different mean size sand particles. For different mean particle sizes, sand particles are sieved using narrow sieve sizes. The mean particle size of 181 μm (+150 –212), 318.5 μm (+212 –425), 512.5 μm (+425 –600), and 725 μm (+600 –850) are collected to perform the experiments. The fraction of different mean size sand particles mixed to get multi-size sand

slurry samples and the correspondingly estimated representative particle size is listed in Table 5.11.

The obtained values of erosion rate of target material at 30^o and 90^o orientation angles with different multi-size sand slurry samples are listed in Table 5.12 and presented graphically in Fig. 5.20 (a,b). It is seen that the erosion rate of the target material increases with the increase in fraction of large size particles in the multi-sized slurry. This is attributed to the increase in energy imparted by the particles to the target surface with the increase in their size. Further, to investigate the representative particle size of multi-sized slurry, the erosion rate of grey cast iron is also predicted from the developed correlation with different representative particle sizes that are generally used to represent multi-size slurry. The predicted results and their deviation with experimental values for both the orientation angles are listed in Table 5.12. Fig. 5.20 (a-b) shows the comparison of the estimated erosion rate of grey cast iron with multi-sized slurry samples and the predicted erosion rate using different representative particle sizes at 30^o and 90^o orientation angles. It is seen that the variation in erosion rate prediction using different representative particle sizes with experimental data is observed at both the orientation angles. Among the five representative particle sizes, the weighted mass size, weighted mean size and the average of d_{50} and d_{85} size overestimated the erosion rate, whereas the median size under-predicts the erosion rate for sample number 1 to 3 and for other samples, it over-predicts. The deviation in prediction of the erosion rate with weighted mass size, weighted mean size, median size, and average of d_{50} and d_{85} size is around 72%, 25%, 20%, and 51%, respectively. The predicted erosion rate with the particle size, taken as the average of d_{50} and d_{wn} sizes, is close to the experimental results. For sample one to three, the maximum deviation is within ±5%. Moreover for sample number 4 and 5, it also over-predicts the erosion rate and the maximum deviation goes up to 15%. Based on the present work, the representative particle size for multi-size particulate slurries can be taken as the average of d_{50} and d_{wn} size. The assumptions of weighted mass size, weighted mean size, median size, and average of d_{50} and d_{85} size as the nominal particle size of the multi-sized slurry results in larger error in erosion rate prediction.

5.5 Concluding Remarks

Experiments are conducted in a pot tester to investigate the effect of impact angle, particle size and velocity on the erosive wear behaviour of the pump materials under varying conditions. The best representative size of multi-size particulate slurry is also investigated for wide range of PSD. Based on the results, the following conclusions can be drawn:

- The erosion behaviour of the pump materials, namely steel 304L, grey cast iron and high chromium white cast iron is ductile and shows maximum erosion around 30^{o} orientation angle. High chromium white cast iron has better erosion resistance compared to the other two target materials. With the change in particle size, velocity and the erodent properties, the trend of variation of erosion wear with the impact angle remains unaffected.
- The erosion increases with increase in particle size and velocity according to the power law relationship, and the exponent is a function of target material properties and orientation angle. At shallow orientation angles, the exponent values are less compared to that at high orientation angles. The change in the erodent properties also varies the exponent values of velocity.
- Cutting and deformation are the dominant mechanisms of material removal associated with the tangential and normal components of particle impacting force. As the kinetic energy of the particles decreases with decrease in the size and speed, the damage produced by the particles on the target surface reduces. No significant change in the mechanism of erosion of the target materials is observed with the variation in velocity.
- Separate correlations are developed to estimate the erosion rate (g/g) of the steel 304L, grey cast iron, and high chromium white cast iron for sand, iron ore and fly ash particulate slurries.
- Increase in weight fraction of small size particles in multi-size slurry significantly reduces the erosion rate of the target materials. The average of median and weighted mean size of the multi-sized particulate slurry is found to be a reasonable representative size for prediction of erosion rate of the target material.

Table 5.1: Properties of target materials

Target material	Chemical composition (Wt. %)	Density (kg/m^3)	Hardness (Hv)
Steel 304L	C-0.021, Mn-1.76, P-0.030, S-0.003, Si-0.22, Cr-18.08, Ni-8.06, Fe-bal.	7780	160
Grey Cast Iron	C-3.13, P-0.22, S-0.03, Si-1.68, Fe-bal.	7110	168
High Chromium White Cast Iron	C-3.21, Mn-1.08, P-0.04, Mo-0.54, Si-0.75, Cr-28.44, Ni-0.66, Cu-0.29, Fe-bal.	7480	782

Table 5.2: Physical and chemical properties of Indian standard sand

Color	Grayish White
Specific gravity	2.65
Shape of grains	Sub angular
SiO_2	99.30%
Fe_2O_3	0.10%

Table 5.3: Particle size distribution of iron ore

Weighted mean diameter (d_{wn}) = 215 µm								**Median diameter (d_{50})** = 206 µm						
Particle Size, (µm)	>850	710	600	500	425	300	250	212	180	150	106	90	75	45
% Finer (by weight)	100	98.8	95.2	89.2	85.2	79.2	55.2	51.2	44.2	30.2	25	20.4	18.6	4

Table 5.4: pH values of iron ore-water mixture

Solid particle	Solid concentration (% by weight)						
	0	1	10	20	30	40	50
Iron ore	7.65	7.66	7.58	7.65	7.68	7.74	7.76

Table 5.5: Estimated particle size and shape from image analysis of sand particles

Particle size range (μm)					
Mean sieve size (μm)	655	550	462.5	362.5	256
Average particle diameter (μm)	662.42	544.80	453.84	372.29	263.56
Standard deviation	65.88	45.39	36.23	42.84	40.00
Average shape factor	0.8395	0.8480	0.8278	0.8447	0.8478
Standard deviation	0.0637	0.0645	0.0692	0.0698	0.0467

Table 5.6: Range of parameters covered to study erosion of pump materials

Investigation	Erodent	Target material	Particle size, μm	Velocity, m/s	Solid concentration, % by weight	Impact angle, degree
Effect of orientation angle	Indian standard sand	Steel 304L	655,362.5	13	1	15,30,45,60, 75,90
		Grey cast iron	550, 256	13	1	15,30,45,60, 75,90
		High chromium white cast iron	550,362.5	13	1	15,30,45,60, 75,90
	Iron ore	Steel 304L	210	16.5	1	15,30,60, 90
		Grey cast iron	210	16.5	1	15,30,60, 90
	Fly ash	Steel 304L	61	16.5	1	15,30,60, 90
		Grey cast iron	61	16.5	1	15,30,60, 90
Effect of velocity	Indian standard sand	Steel 304L	655	9,11,16.5	1	15,30,45,60, 75,90
				18.5		30,90
		Grey cast iron	362.5	9,11,13	1	15,30,60,90
				16.5,18.5		30,90
		High chromium white cast iron	550	11, 13,16.5, 18.5	1	30,90
	Iron ore	Steel 304L	210	11,13,16.5, 18.5	1	30,90
		Grey cast iron	210	11,13,16.5, 18.5	1	30,90
		High chromium white cast iron	210	11,13,16.5, 18.5	2	30,90
	Fly ash	Steel 304L	61	11,13,16.5,	1	30,90

				18.5		
		Grey cast iron	61	11,13,16.5, 18.5	1	30,90
		High chromium white cast iron	61	11,13,16.5, 18.5	5	30,90
Effect of particle size	Indian standard sand	Steel 304L	256,462.5, 550	13	1	30,90
		Grey cast iron	462.5,655	13	1	30,90
		High chromium white cast iron	256,462.5, 655	13	1	30,90
Effect of particle size distribution	Indian standard sand	Grey cast iron	Multi-size (Five samples)	13	1	30,90

Table 5.7: Repeatability of mass loss measurement by slurry pot tester (target material: steel 304L, erodent material: sand, d = 550 µm, Cw = 1%, V = 13 m/s and T = 40 min)

Test run	Orientation angle, degree	Mass loss, mg		
		Sample 1	Sample 2	Average
1	30	17.3	17.1	17.2
2	30	18	17	17.5
3	30	17.5	16.6	17.05
4	30	17.1	17.4	17.25
5	30	18.2	17.6	17.9
Average of 10 samples				17.38
1	90	6.4	6.7	6.55
2	90	6.5	6.9	6.7
3	90	6.4	6.2	6.30
4	90	7	6.3	6.65
5	90	6.3	6.4	6.35
Average of 10 samples				6.51

Table 5.8: Measured erosion rate of pump materials at different operating conditions using slurry pot tester

(a) Target material: **Steel 304L**; Erodent: **Sand**

Particle size (µm)	Velocity (m/s)	Concentration Cw (%)	Impact angle (Degree)	Time (min)	Average mass loss (mg)	Erosion rate (g/g)x 10^{-7}
655	9	1	15	40	3.53	1.124
			30		5.13	1.633
			45		4.07	1.294
			60		3.20	1.018
			75		2.6	0.827
			90		2.13	0.679
655	11	1	15	40	7.84	2.040
			30		11.6	3.019
			45		9.04	2.353
			60		6.32	1.645
			75		5.44	1.416
			90		4.8	1.249
655	13	1	15	40	12.56	2.766
			30		19.76	4.352
			45		15.44	3.400
			60		12.16	2.678
			75		9.52	2.097
			90		7.92	1.744
655	16.5	1	15	30	20.25	4.685
			30		30.3	7.010
			45		24.52	5.674
			60		19.87	4.598
			75		16.88	3.904
			90		15	3.470
655	18.5	1	30	30	47.85	9.873
			90		25.5	5.261
362.5	13	1	15	40	8.08	1.779
			30		12	2.643
			45		9.52	2.097
			60		7.44	1.638
			75		5.84	1.286
			90		4.8	1.057
550	13	1	30	40	17.25	3.799
			90		6.55	1.442
462.5	13	1	30	40	14.6	3.215
			90		5.85	1.288
256	13	1	30	40	9.45	2.081
			90		3.35	0.738

(b) Target material: **Grey Cast Iron**; Erodent: **Sand**

Particle size (μm)	Velocity (m/s)	Concentration Cw (%)	Impact angle (Degree)	Time (min)	Average mass loss (mg)	Erosion rate (g/g)x 10^{-7}
550	13	1	15	40	22.9	5.043
			30		26.4	5.814
			45		21.95	4.834
			60		18.7	4.118
			75		16.6	3.656
			90		14.5	3.193
256	13	1	15	40	8.35	1.839
			30		10.6	2.334
			45		8.15	1.795
			60		6.7	1.475
			75		5.85	1.288
			90		5.4	1.189
362.5	9	1	15	40	2.6	0.827
			30		3.3	1.050
			60		2.3	0.732
			90		1.9	0.604
362.5	11	1	15	40	5	1.301
			30		7.5	1.952
			60		4.1	1.067
			90		3.8	0.989
362.5	13	1	15	40	11	2.422
			30		15.7	3.457
			60		10.3	2.268
			90		8.45	1.861
362.5	16.5	1	30	30	26.75	6.188
			90		14.35	3.320
362.5	18.5	1	30	30	39.3	8.109
			90		26.65	5.499
655	13	1	30	40	32.75	7.212
			90		18.3	4.03
462.5	13	1	30	40	21.3	4.691
			90		11.6	2.555

(c) Target material: **High Chromium White Cast Iron**; Erodent: **Sand**

Particle size (μm)	Velocity (m/s)	Concentration Cw (%)	Impact angle (Degree)	Time (min)	Average Mass loss (mg)	Erosion rate (g/g)x 10^{-8}
550	13	1	15	120	7.1	5.212
			30		10.65	7.818
			45		8.85	6.497
			60		7.7	5.652
			75		6.75	4.955
			90		6.3	4.625
362.5	13	1	15	120	4.4	3.230
			30		7.4	5.432

			45		6.2	4.551
			60		4.85	3.560
			75		4.25	3.120
			90		3.6	2.643
550	11	1	30	120	6.2	5.379
			90	160	4.7	3.058
550	16.5	1	30	90	21.3	16.425
			90		12.9	9.948
550	18.5	1	30	90	31.1	21.390
			90		19.15	13.171
655	13	1	30	120	13.1	9.616
			90		8.6	6.313
462.5	13	1	30	120	8.9	6.533
			90		4.9	3.597
			90		3.6	2.643
256	13	1	30	120	5.85	4.294
			90		2.25	1.652

(d) Target material: **Steel 304L**; Erodent: **Iron ore**

Particle size (μm)	Velocity (m/s)	Concentration Cw (%)	Impact angle (Degree)	Time (min)	Average mass loss (mg)	Erosion rate (g/g)x 10^{-7}
210	16.5	1	15	30	3	0.694
			30		4.5	1.041
			60		2.3	0.532
			90		1.8	0.382
210	11	1	30	40	1.6	0.416
	13			40	2.55	0.562
	18.5			30	7.3	1.506
	11	1	90	40	0.55	0.143
	13			40	1.1	0.242
	18.5			30	2.85	0.588

(e) Target material: **Grey Cast Iron**; Erodent: **Iron Ore**

Particle size (μm)	Velocity (m/s)	Concentration Cw (%)	Impact angle (Degree)	Time (min)	Average mass loss (mg)	Erosion rate (g/g)x 10^{-7}
210	16.5	1	15	30	6.2	1.434
			30		7.1	1.643
			60		4.65	1.076
			90		3.95	0.914
210	11	1	30	40	2.05	0.534
	13			40	3.4	0.749
	18.5			30	11	2.270
	11	1	90	40	0.95	0.247
	13			40	2.5	0.551
	18.5			30	5.9	1.217

(f) Target material: **High Chromium White Cast Iron**; Erodent: **Iron Ore**

Particle size (µm)	Velocity (m/s)	Concentration Cw (%)	Impact angle (Degree)	Time (min)	Average mass loss (mg)	Erosion rate (g/g)x 10^{-7}
210	11	2	30	160	1.5	0.048
	13			120	1.85	0.067
	16.5			90	4.1	0.157
	18.5			90	5.75	0.196
	11	2	90	160	0.85	0.027
	13			120	1.35	0.049
	16.5			90	2.15	0.082
	18.5			90	3.95	0.135

(g) Target material: **Steel 304L**; Erodent: **Fly Ash**

Particle size (µm)	Velocity (m/s)	Concentration Cw (%)	Impact angle (Degree)	Time (min)	Average mass loss (mg)	Erosion rate (g/g)x 10^{-7}
61	16.5	1	15	60	3.3	0.382
			30		5.3	0.613
			60		2.65	0.307
			90		2.05	0.237
61	11	1	30	80	1.65	0.215
	13			80	3.1	0.341
	18.5			60	8.85	0.913
	11	1	90	80	0.65	0.085
	13			80	1.15	0.127
	18.5			60	4.0	0.413

(h) Target material: **Grey Cast Iron**; Erodent: **Fly Ash**

Particle size (µm)	Velocity (m/s)	Concentration Cw (%)	Impact angle (Degree)	Time (min)	Average mass loss (mg)	Erosion rate (g/g)x 10^{-7}
61	16.5	1	15	60	4.95	0.573
			30		5.85	0.677
			60		3.65	0.422
			90		3.15	0.364
61	11	1	30	80	2.4	0.312
	13			80	3.75	0.413
	18.5			60	14.9	1.537
	11	1	90	80	0.8	0.104
	13			80	1.75	0.193
	18.5			60	6.6	0.681

(i) Target material: **High chromium white cast iron**; Erodent: **Fly Ash**

Particle size (μm)	Velocity (m/s)	Concentration Cw (%)	Impact angle (Degree)	Time (min)	Average mass loss (mg)	Erosion rate (g/g)x 10^{-7}
61	11	5	30	160	1.3	0.016
	13			120	1.55	0.022
	16.5			90	3.7	0.056
	18.5			90	6.4	0.086
	11	5	90	160	0.8	0.010
	13			120	0.95	0.014
	16.5			90	2.65	0.040
	18.5			90	4.2	0.056

Table 5.9: Constant values for functional relationship of impact angle to erosion rate

Target Material	a_1	b_1	a_2	b_2
Steel 304L	0.99	0.92	0.68	1.89
Grey Cast Iron	0.99	0.57	0.64	1.96
High Chromium White Cast Iron	0.99	0.86	0.73	1.93

Table 5.10: Values of constants of Eq. (5.10) for different pump materials for cutting and deformation erosion (a) sand-water slurry, (b) iron ore-water slurry and (c) fly ash-water slurry

(a) sand-water slurry

Target Material	Eq. (5.10) Constant and Exponents	Cutting Erosion (ER_C)	Deformation Erosion (ER_{D90})
Steel 304L	K	$1.51x10^{-11}$	$2.36x10^{-13}$
	β	2.15	2.8
	γ	0.71	0.98
Grey Cast Iron	K	$4.75x10^{-14}$	$3.79x10^{-14}$
	β	3.08	3.12
	γ	1.31	1.25
High Chromium White Cast Iron	K	$3.96x10^{-13}$	$3.88x10^{-15}$
	β	2.78	2.88
	γ	0.79	1.42

(b) iron ore-water slurry

Target Material	Eq. (5.10) Constant and Exponents	Cutting Erosion (ER_C)	Deformation Erosion (ER_{D90})
Steel 304L	K	$1.98x10^{-12}$	$8.75x10^{-14}$
	β	2.50	2.83
	γ	0.71	0.98
Grey Cast Iron	K	$4.75x10^{-14}$	$3.79x10^{-14}$
	β	3.08	3.12
	γ	1.31	1.25
High Chromium White Cast Iron	K	$6.63x10^{-14}$	$1.37x10^{-15}$
	β	2.82	2.90
	γ	0.79	1.42

(c) fly ash-water slurry

Target Material	Eq. (5.10) Constant and Exponents	Cutting Erosion (ER_C)	Deformation Erosion (ER_{D90})
Steel 304L	K	$1.94x10^{-12}$	$1.19x10^{-13}$
	β	2.64	2.96
	γ	0.71	0.98
Grey Cast Iron	K	$1.49x10^{-13}$	$1.58x10^{-14}$
	β	2.78	3.44
	γ	1.31	1.25
High Chromium White Cast Iron	K	$2.18x10^{-14}$	$6.07x10^{-16}$
	β	3.22	3.50
	γ	0.79	1.42

Table 5.11: Particle size distribution of multi-sized slurry samples

Sample no.	Mean particle size (μm)				Weighted mean diameter, d_{wn} (μm)	Median diameter, d_{50} (μm)	Average of d_{wn} and d_{50} (μm)	Average of d_{50} and d_{85} (μm)	Weighted mass diameter, d_{wm} (μm)
	181	318.5	512.5	725					
1	70	15	10	5	262	192	227	309	346
2	40	30	20	10	343	267	305	346	426
3	25	25	25	25	435	319	377	504	517
4	10	20	30	40	526	535	530	640	585
5	5	10	25	60	604	636	620	707	643

Table 5.12: Deviation in prediction of erosive wear caused by multi-size particulate slurry

Orientation angle	Experiments (multi-size slurry)		Predicted (representative particle size)				
	Sample no.	ER ($x10^{-8}$)	Weighted mean size ER ($x10^{-8}$) (Deviation)	Weighted mass size ER ($x10^{-8}$) (Deviation)	Median size ER ($x10^{-8}$) (Deviation)	Average d_{50} and d_{wn} ER ($x10^{-8}$) (Deviation)	Average d_{50} and d_{85} ER ($x10^{-8}$) (Deviation)
30 Degree	1	18.058	21.660 (19.9%)	31.109 (72.3%)	14.452 (-20%)	17.972 (-0.5%)	26.850 (48.7%)
	2	26.977	30.758 (14.0%)	40.784 (51.2%)	22.200 (-17.7)	26.398 (-2.1%)	31.109 (15.3%)
	3	33.584	41.910 (24.8%)	52.476 (56.3%)	27.987 (-16.7%)	34.786 (3.6%)	50.765 (51.2%)
	4	47.568	53.669 (12.8%)	61.637 (29.6%)	54.868 (15.3%)	54.201 (13.9%)	69.287 (45.7%)
	5	57.597	64.256 (11.6%)	69.710 (21.0%)	68.724 (19.3%)	66.481 (15.4%)	78.878 (36.9%)
90 Degree	1	9.910	11.940 (20.5%)	16.904 (70.6%)	8.096 (-18.3%)	9.981 (0.7%)	14.675 (48.1%)
	2	14.424	16.721 (15.9%)	21.923 (52.0%)	12.226 (-15.2%)	14.438 (0.1%)	16.904 (17.2%)
	3	18.058	22.504 (24.6%)	27.926 (54.6%)	15.271 (-15.4%)	18.818 (4.2%)	27.051 (49.8%)
	4	25.876	28.535 (10.3%)	32.590 (25.9%)	29.146 (12.6%)	28.806 (11.3%)	36.464 (40.9%)
	5	30.721	33.919 (10.4%)	36.678 (19.4%)	36.180 (17.8%)	35.045 (14.1%)	41.297 (34.4%)

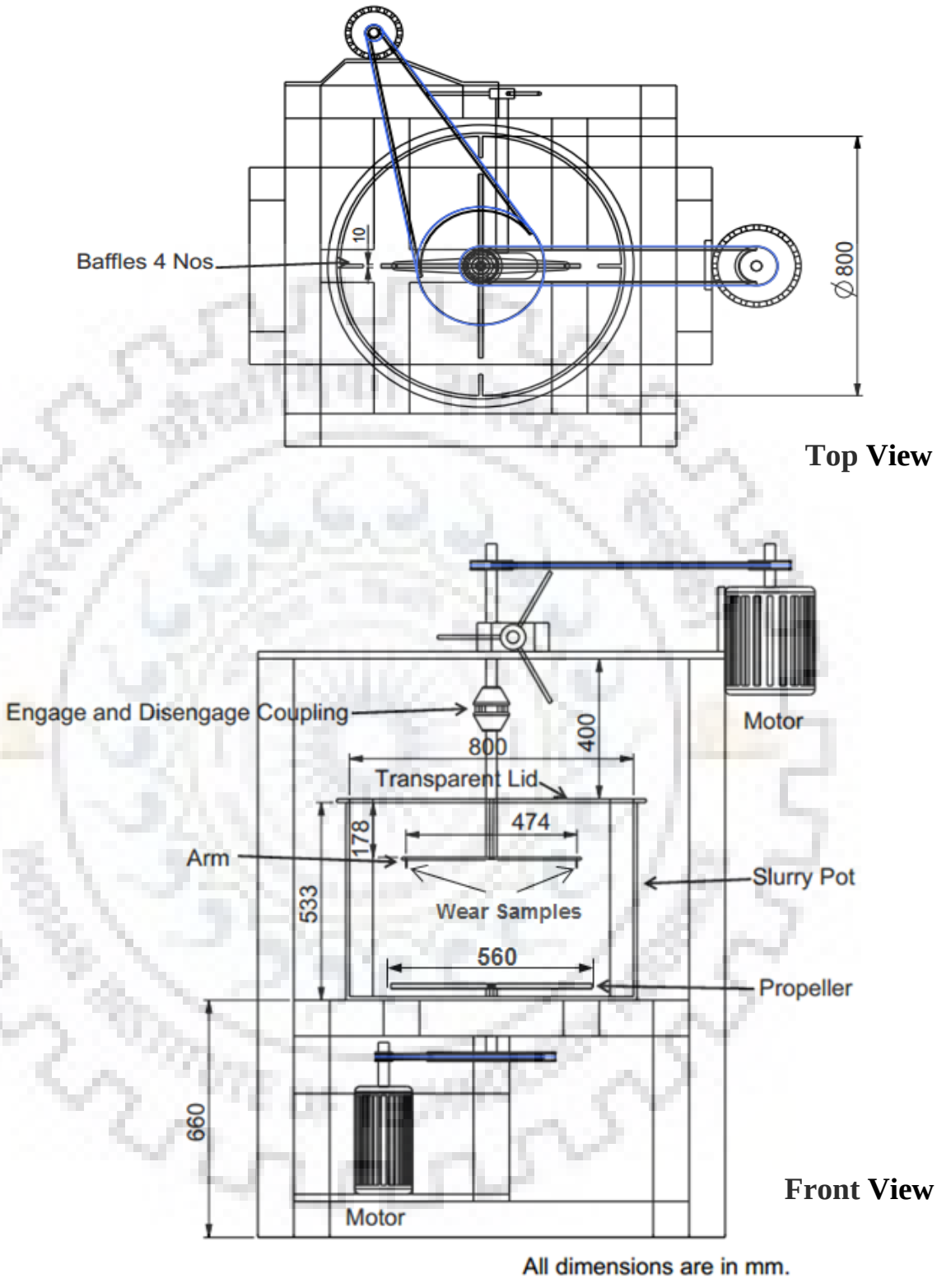

(a) Schematic diagram of the assembly

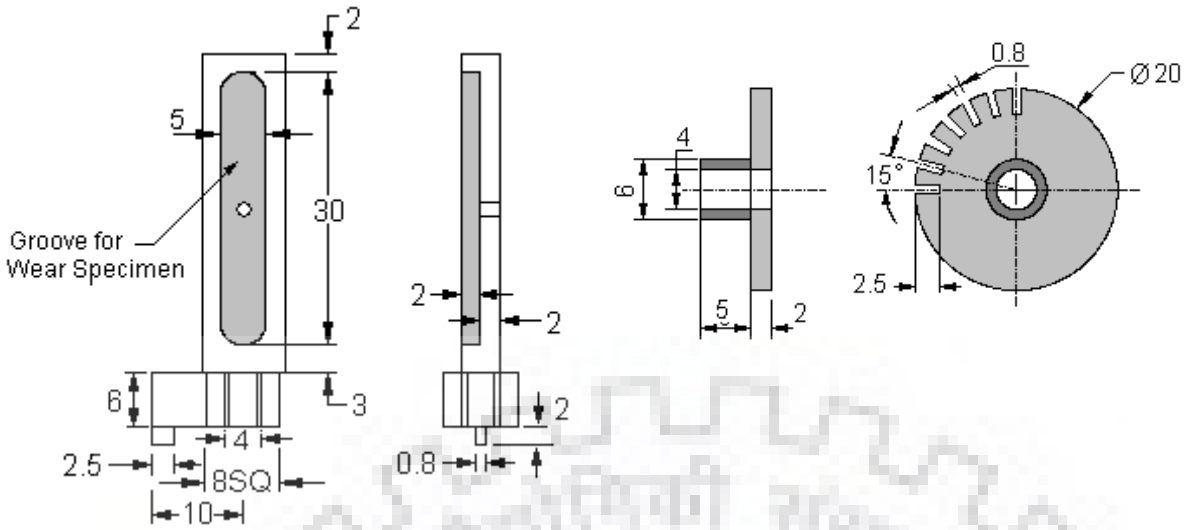

(b) Test Fixture (c) Slotted angular plate

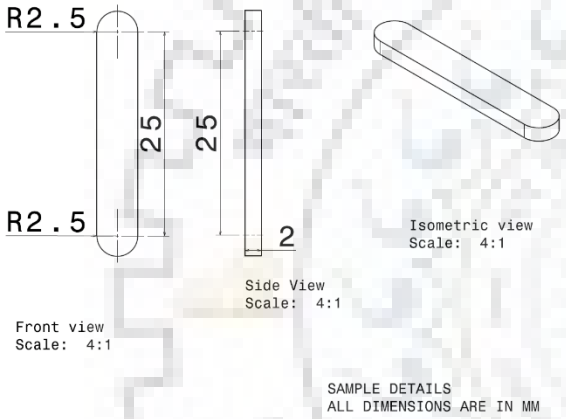

(d) Wear Sample

(All dimensions are in mm)

(e) Photographic View

Fig. 5.1 Slurry pot tester for erosion studies of pump materials (a) Schematic view (b) Test fixture (c) Slotted angular plate (d) Wear sample (e) Photographic view

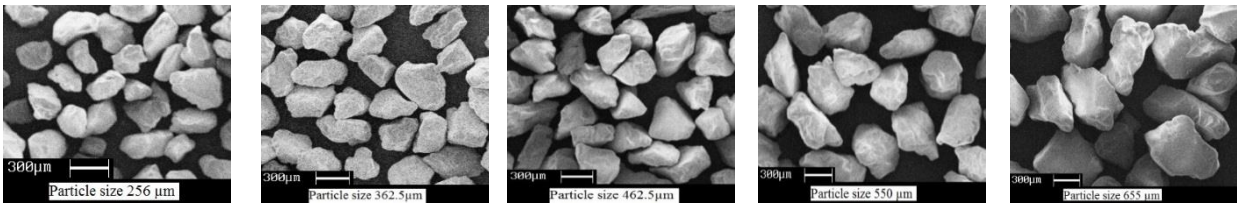

Fig. 5.2 SEM micrographs of different particle sizes

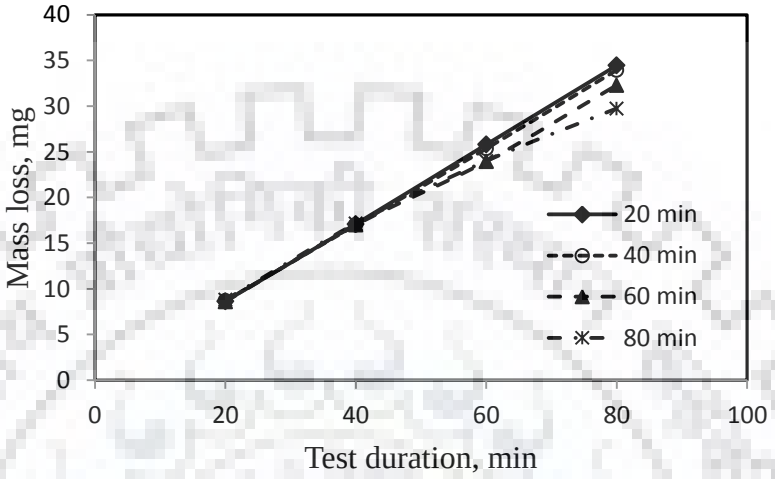

Fig. 5.3 Effect of slurry replacement time on erosion

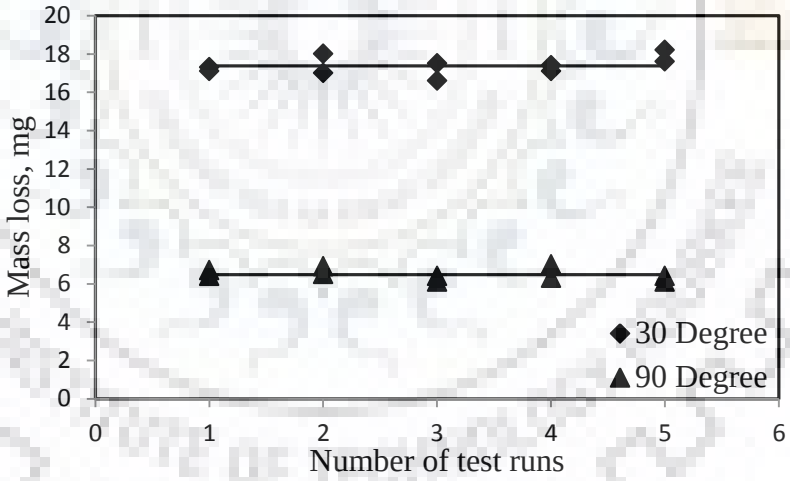

Fig. 5.4 Repeatability of mass loss at two orientation angles in the pot tester

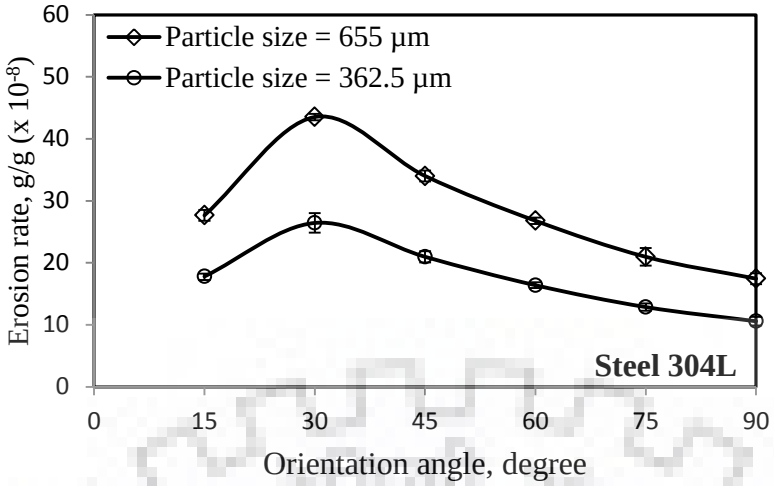

(a) Steel 304L

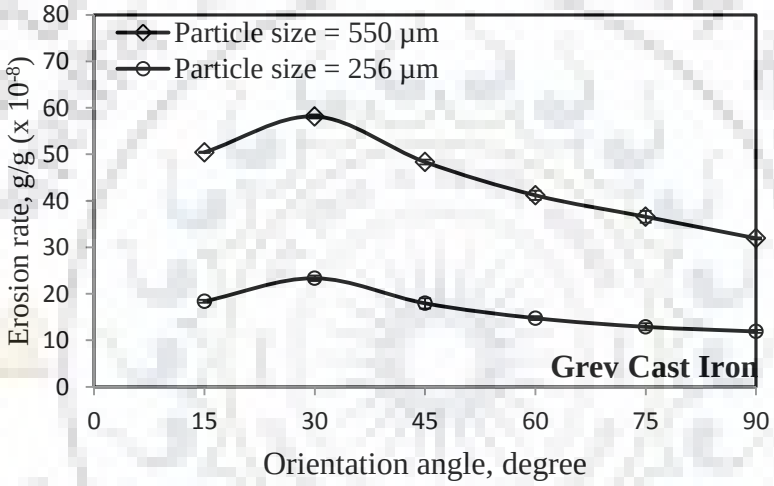

(b) Grey Cast Iron

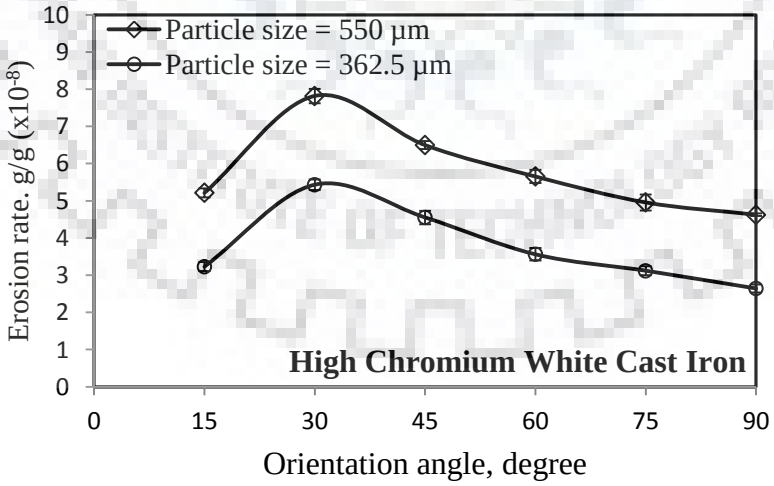

(c) High Chromium White Cast Iron

Fig. 5.5 Erosion rate variation of target materials with orientation angle and particle size at 13 m/s and 1% weighted solid concentration (a) Steel 304L (b) Grey cast iron (c) High chromium white cast iron

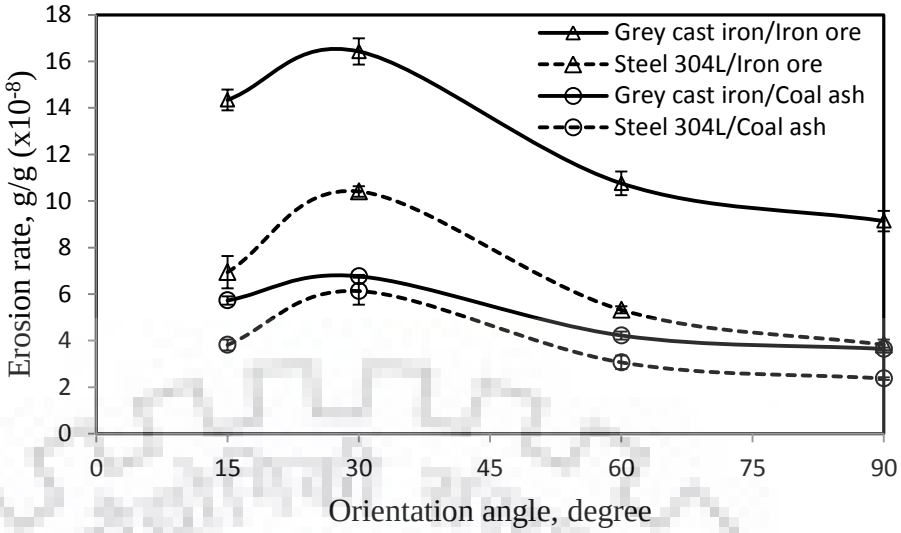

Fig. 5.6 Erosion rate variation of grey cast iron and steel 304L with iron ore and fly ash slurry at different orientation angle for 16.5 m/s velocity and C_w = 1%.

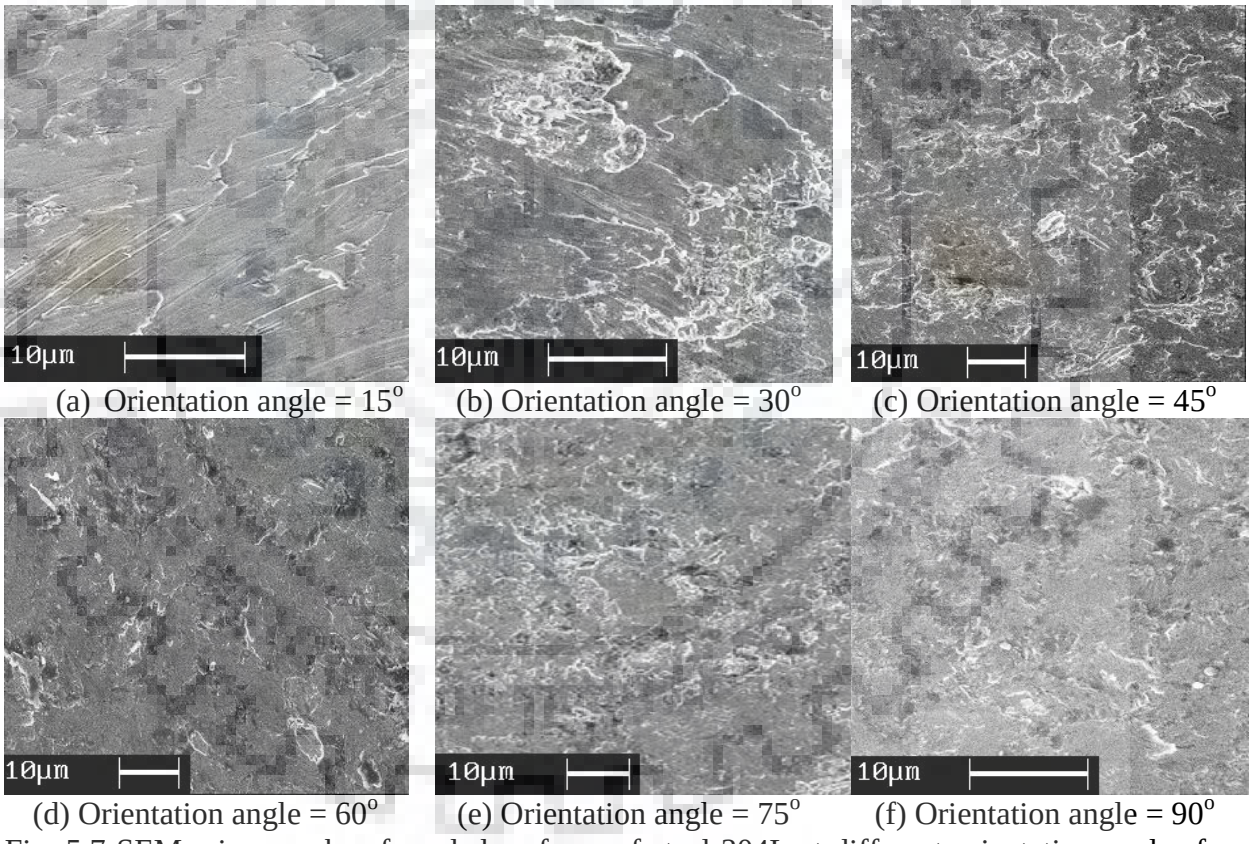

(a) Orientation angle = 15° (b) Orientation angle = 30° (c) Orientation angle = 45°

(d) Orientation angle = 60° (e) Orientation angle = 75° (f) Orientation angle = 90°

Fig. 5.7 SEM micrographs of eroded surfaces of steel 304L at different orientation angles for particle size = 655 µm, Cw = 1%, and V = 13 m/s.

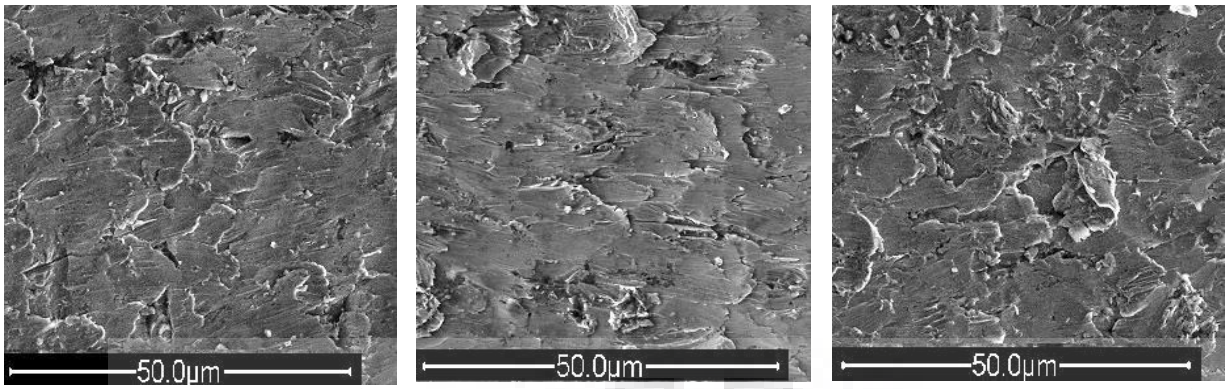

(a) Orientation angle = 15° (b) Orientation angle = 30° (c) Orientation angle = 45°

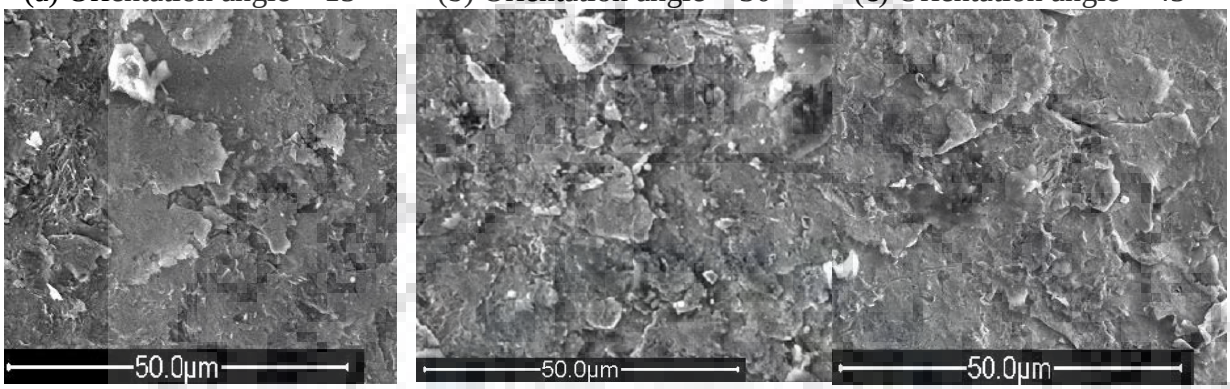

(d) Orientation angle = 60° (e) Orientation angle = 75° (f) Orientation angle = 90°

Fig. 5.8 SEM micrographs of eroded surfaces of grey cast iron at different orientation angles for particle size = 550 µm, Cw = 1%, and V = 13 m/s.

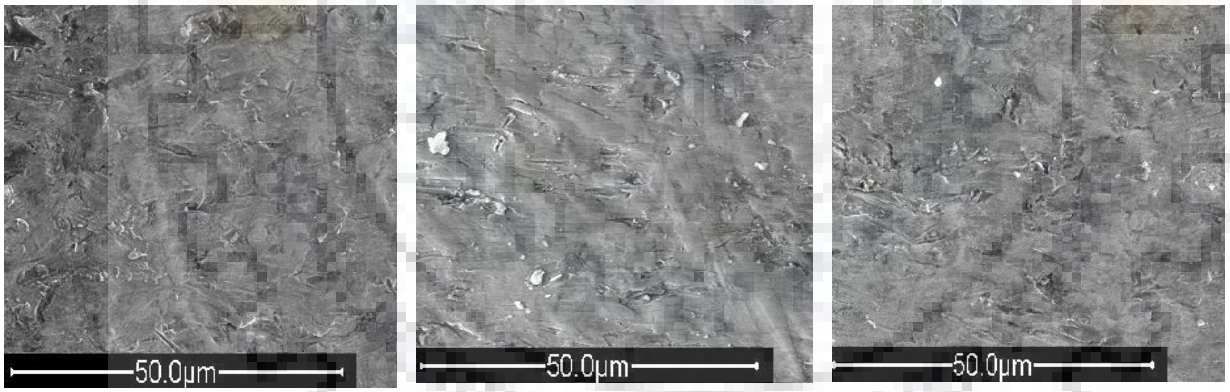

(a) Orientation angle = 15° (b) Orientation angle = 30° (c) Orientation angle = 45°

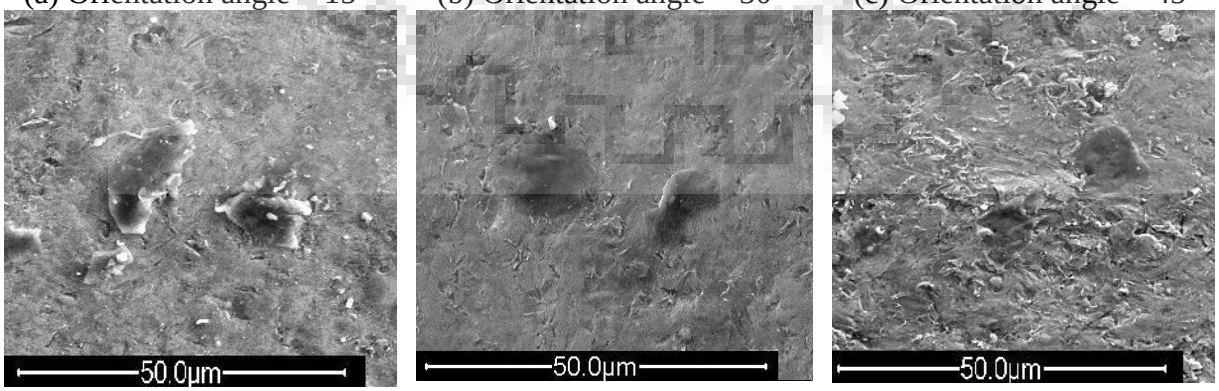

(d) Orientation angle = 60° (e) Orientation angle = 75° (f) Orientation angle = 90°

Fig. 5.9 SEM micrographs of eroded surfaces of high chromium white cast iron at different orientation angles for particle size = 550 µm, Cw = 1%, and V = 13 m/s.

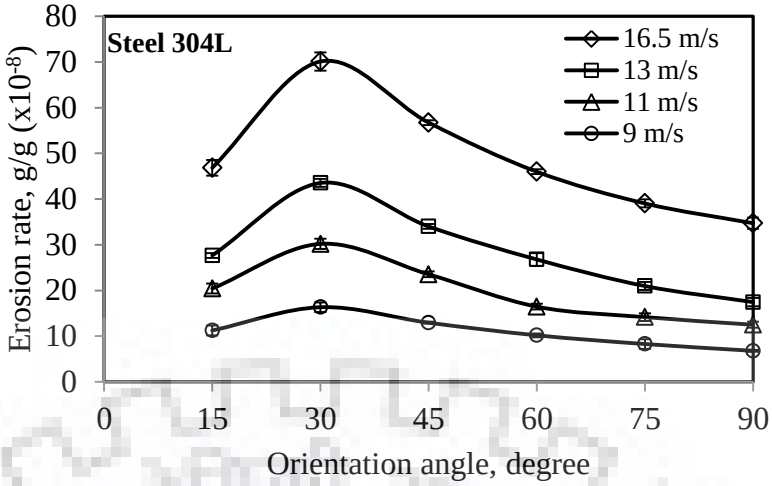

(a) Erosion rate of steel 304L with particle size of 655 µm

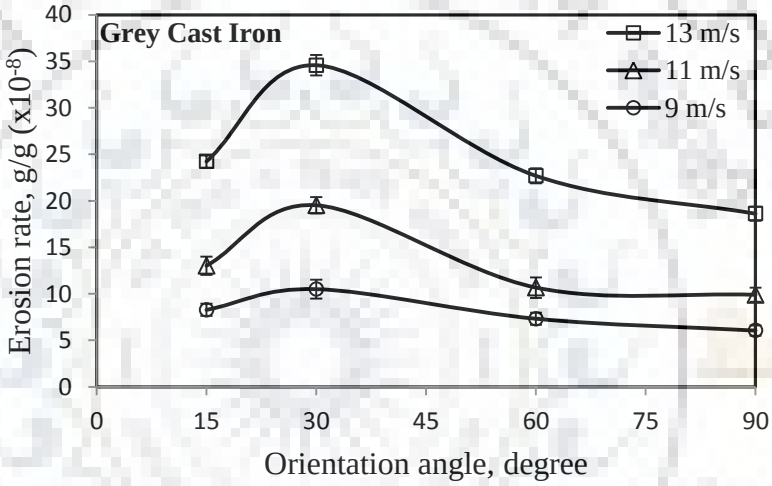

(b) Erosion rate of grey cast iron with particle size 362.5 µm

Fig. 5.10 Variation of erosion rate of target materials with orientation angle and velocity (a) Steel 304L and (b) Grey cast iron

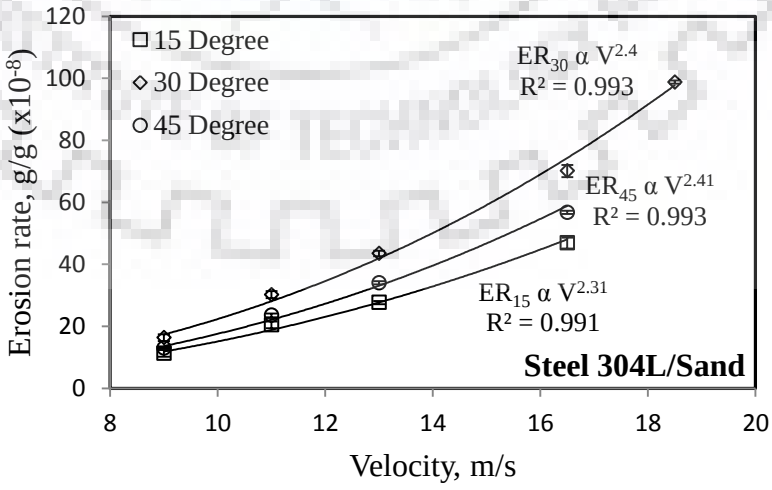

(i) For orientation angle 15 to 45 degree

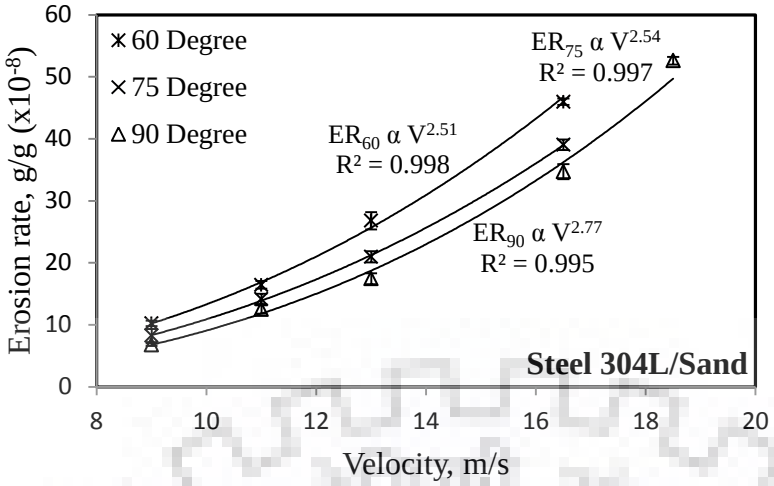

(ii) For orientation angle 60 to 90 degree

(a) Erosion rate of steel 304L with particle size of 655 µm

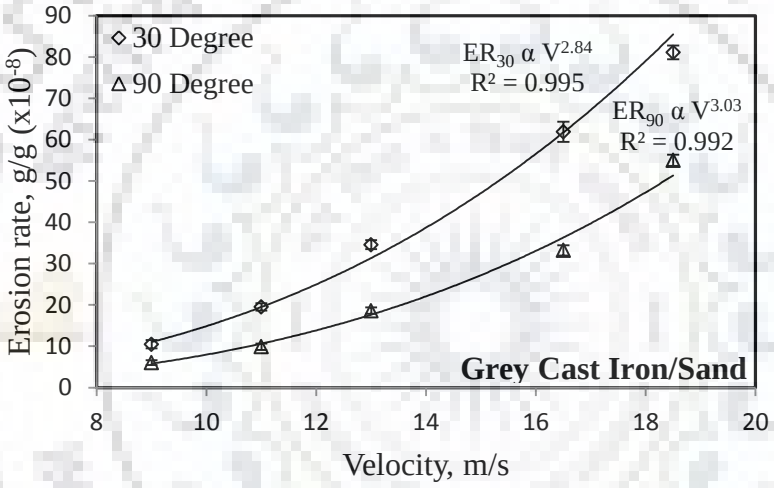

(b) Erosion rate of grey cast iron with particle size 362.5 µm

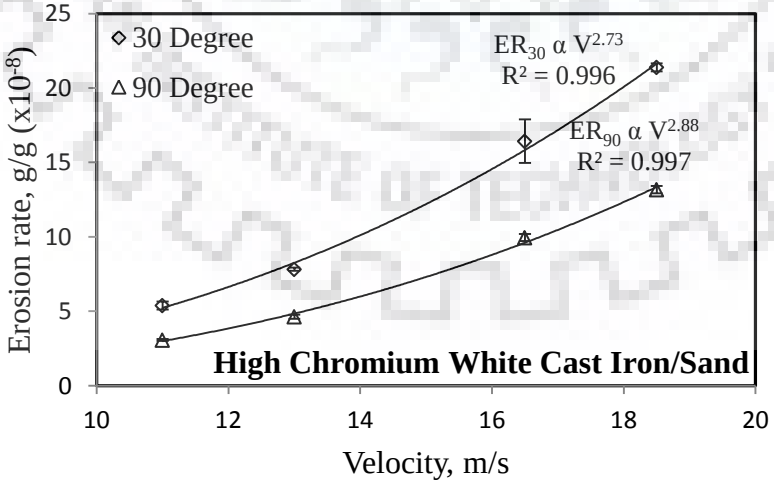

(c) Erosion rate of high chromium white cast iron with particle size of 550 µm

Fig. 5.11 Variation in erosion rate of target materials with velocity for different orientation angles (a) Steel 304L, (b) Grey cast iron, and (c) High chromium white cast iron

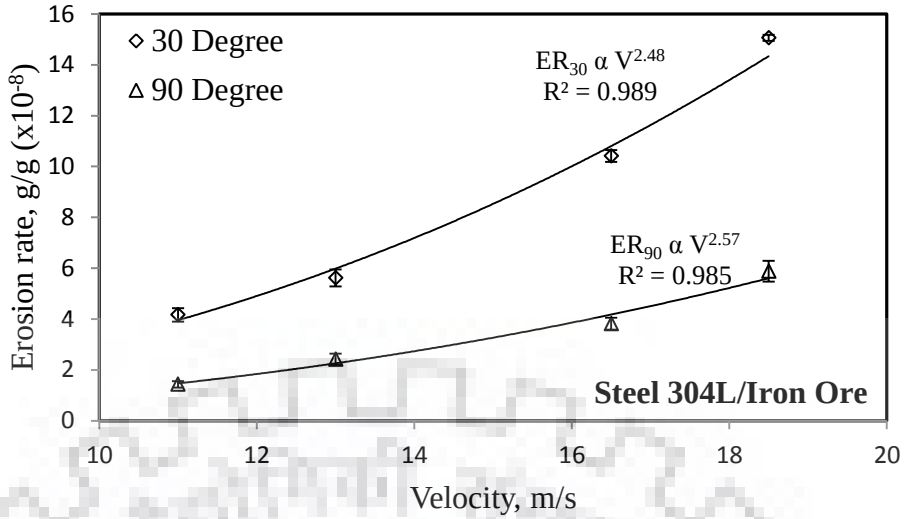

(a) Erosion of steel 304L in iron-ore water slurry

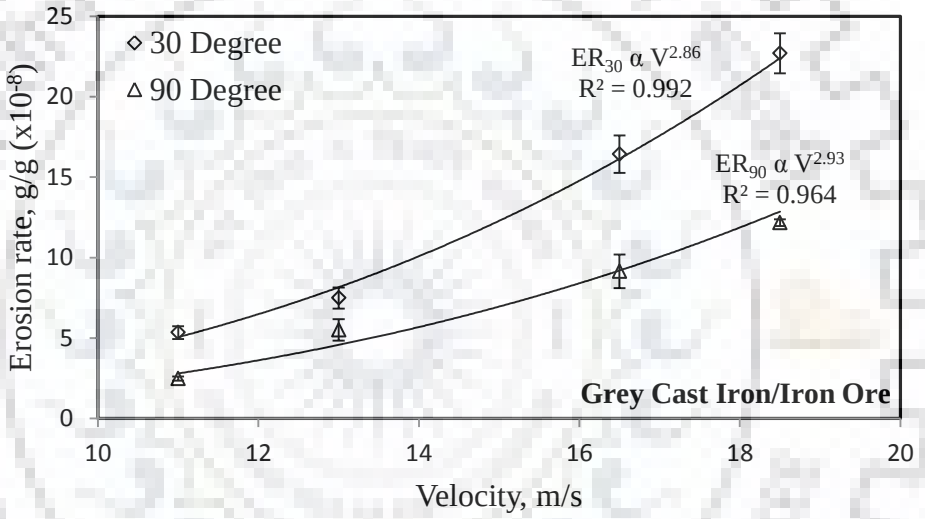

(b) Erosion of grey cast iron in iron-ore water slurry

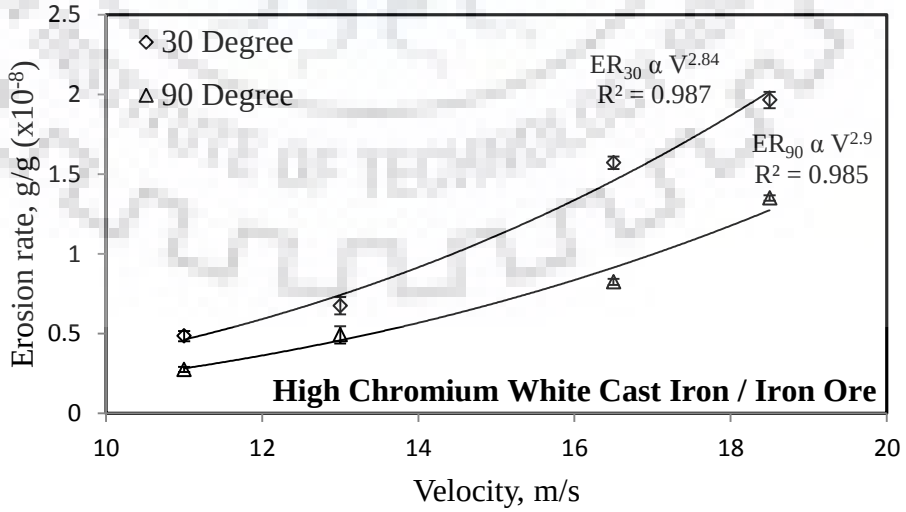

(c) Erosion of high chromium white cast iron in iron-ore water slurry

Fig. 5.12 Variation in erosion rate of different target materials with velocity for iron ore particulate slurry (a) Steel 304L, (b) Grey cast iron, and (c) High chromium white cast iron

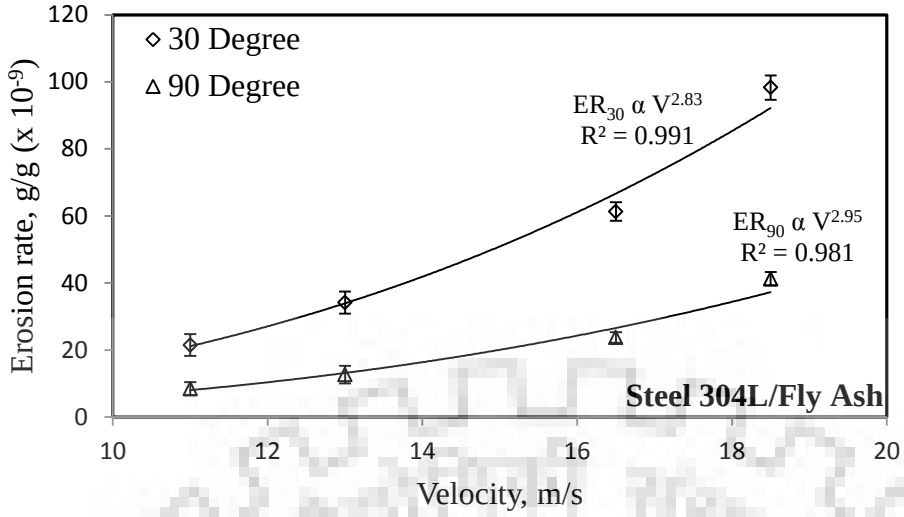

(a) Erosion of steel 304L in fly ash water slurry

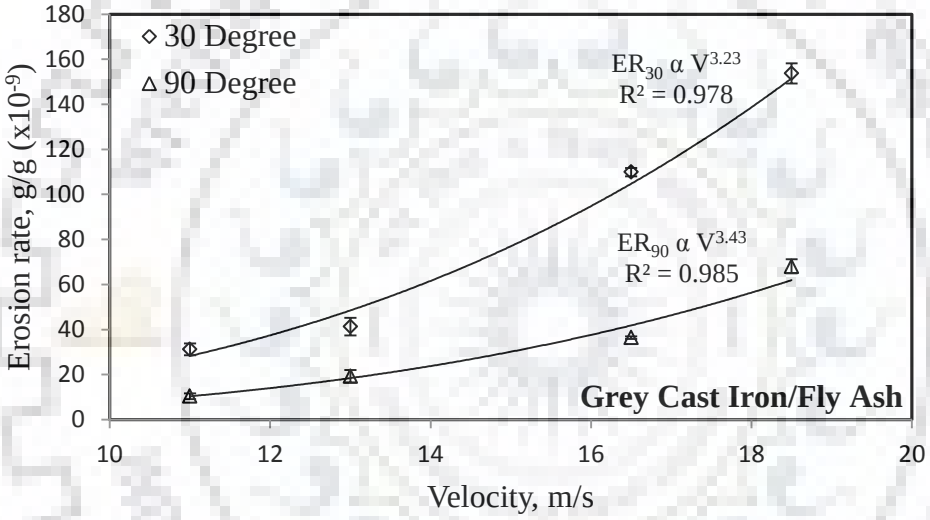

(b) Erosion of grey cast iron in fly ash water slurry

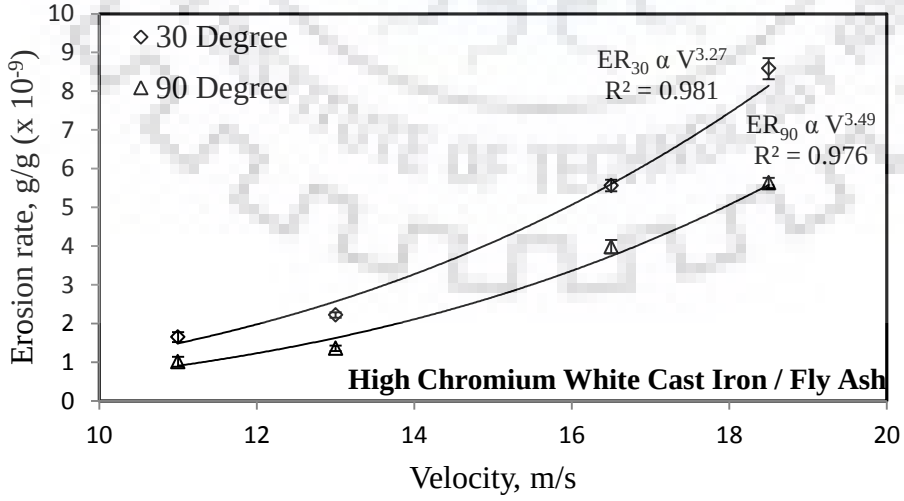

(c) Erosion of high chromium white cast iron in fly ash water slurry

Fig. 5.13 Variation in erosion rate of different target materials with velocity for fly ash particulate slurry (a) Steel 304L, (b) Grey cast iron, and (c) High chromium white cast iron

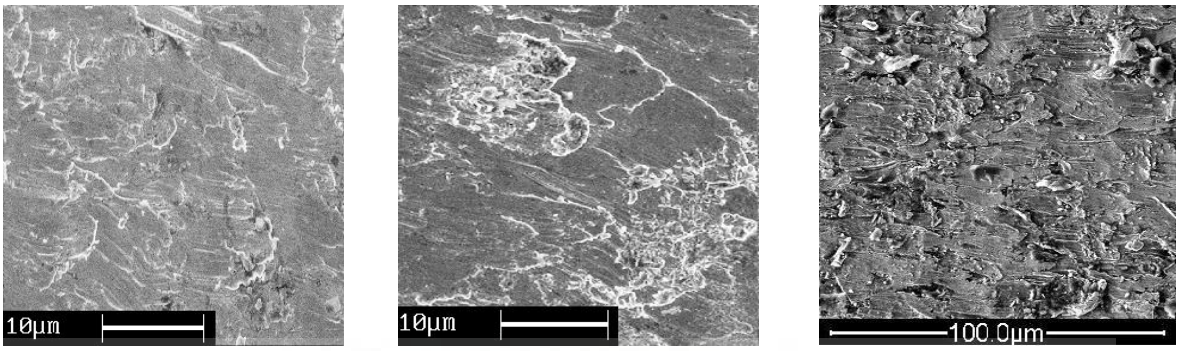

(a) Velocity = 9 m/s (b) Velocity = 13 m/s (c) Velocity = 18.5 m/s

(i) Orientation angle = 30^o

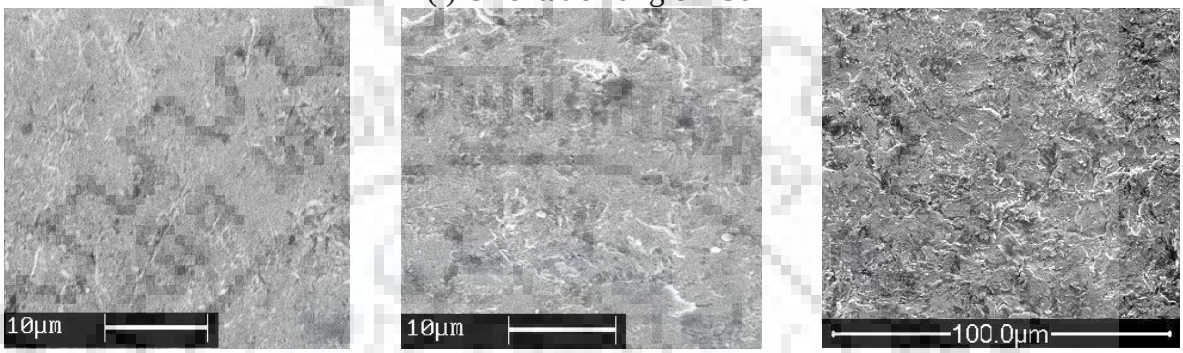

(d) Velocity = 9 m/s (e) Velocity = 13 m/s (f) Velocity = 18.5 m/s

(ii) Orientation angle = 90^o

Fig. 5.14 Effect of velocity on mechanism of surface failure of steel 304L at (i) 30^o and (ii) 90^o orientation angles with 655 µm size particles at 1% weight concentration

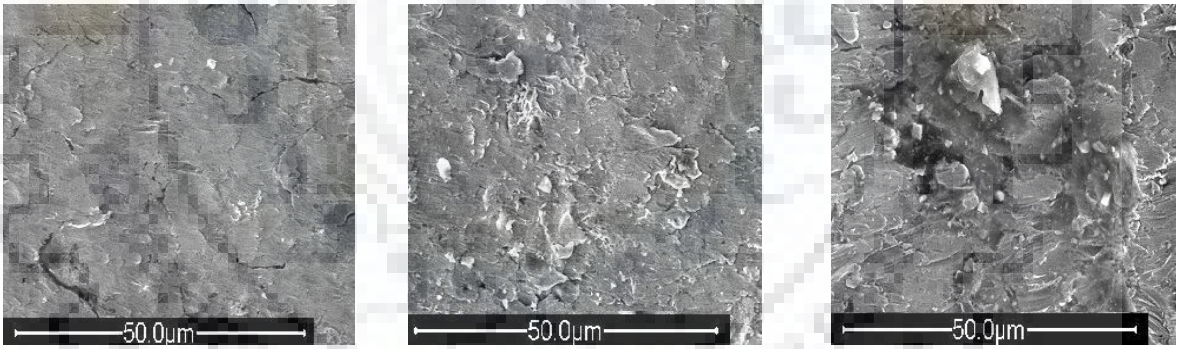

(a) Velocity = 9 m/s (b) Velocity = 13 m/s (c) Velocity = 18.5 m/s

(i) Orientation angle = 30^o

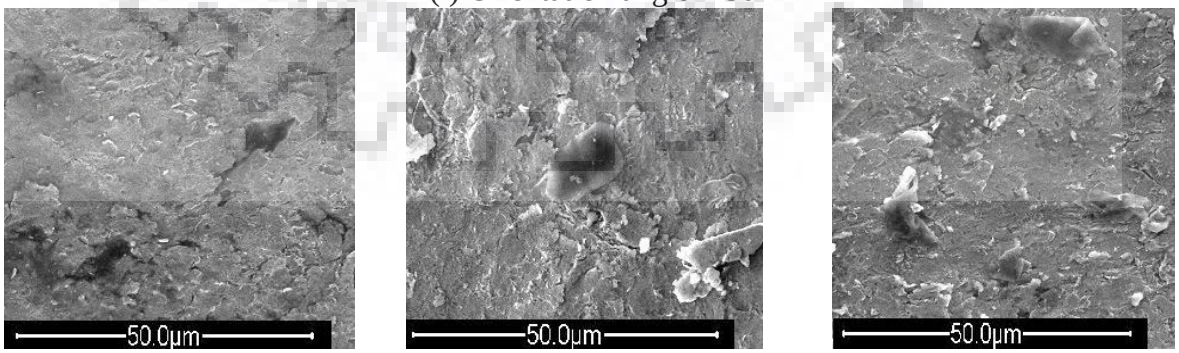

(d) Velocity = 9 m/s (e) Velocity = 13 m/s (f) Velocity = 18.5 m/s

(ii) Orientation angle = 90^o

Fig. 5.15 Effect of velocity on mechanism of surface failure of grey cast iron at (i) 30^o and (ii) 90^o orientation angles with 362.5 µm size particles at 1% weight concentration

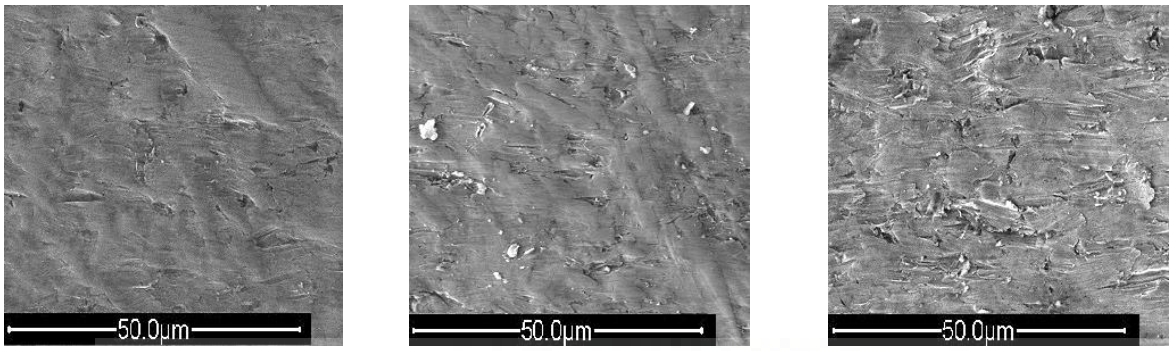

(a) Velocity = 11 m/s (b) Velocity = 13 m/s (c) Velocity = 18.5 m/s

(i) Orientation angle = 30°

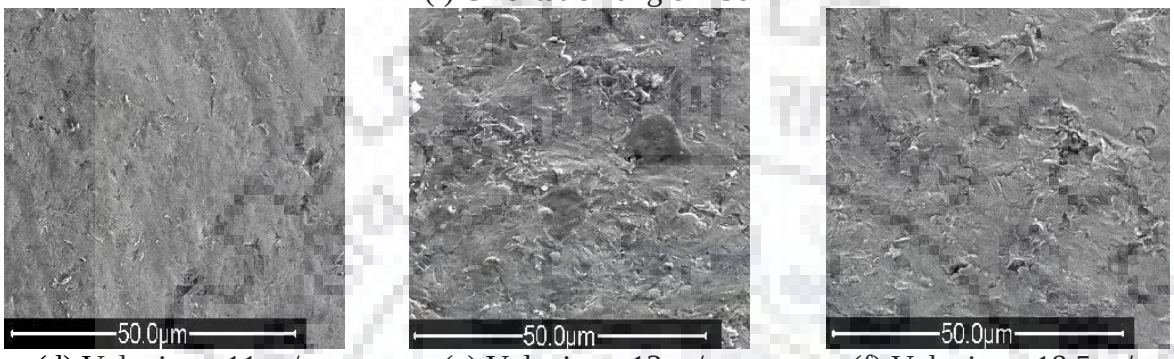

(d) Velocity = 11 m/s (e) Velocity = 13 m/s (f) Velocity = 18.5 m/s

(ii) Orientation angle = 90°

Fig. 5.16 Effect of velocity on mechanism of surface failure of high chromium white cast iron at (i) 30° and (ii) 90° orientation angles with 550 µm size particles at 1% weight concentration

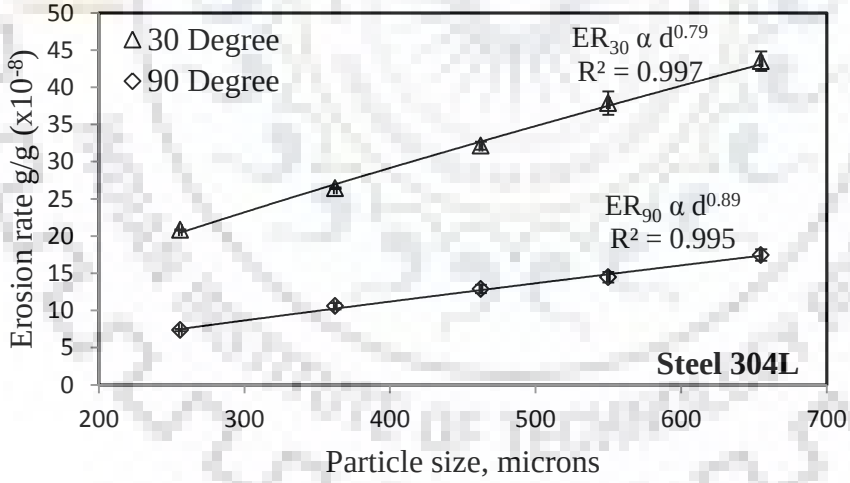

(a) Steel 304L

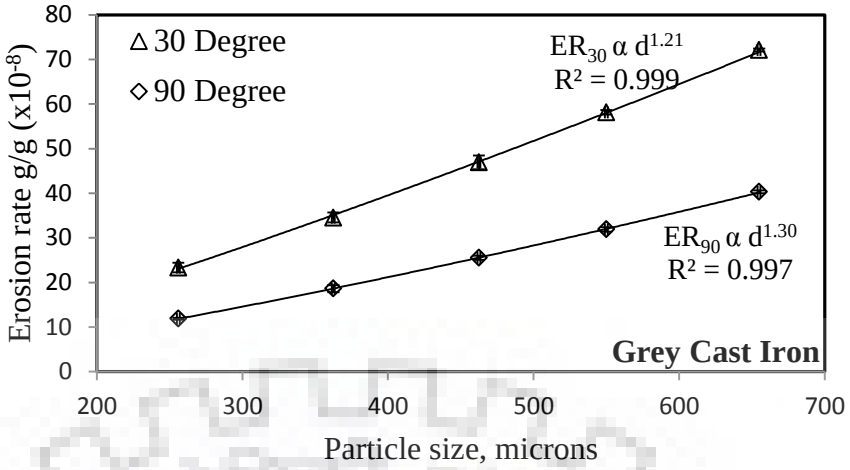

(b) Grey Cast Iron

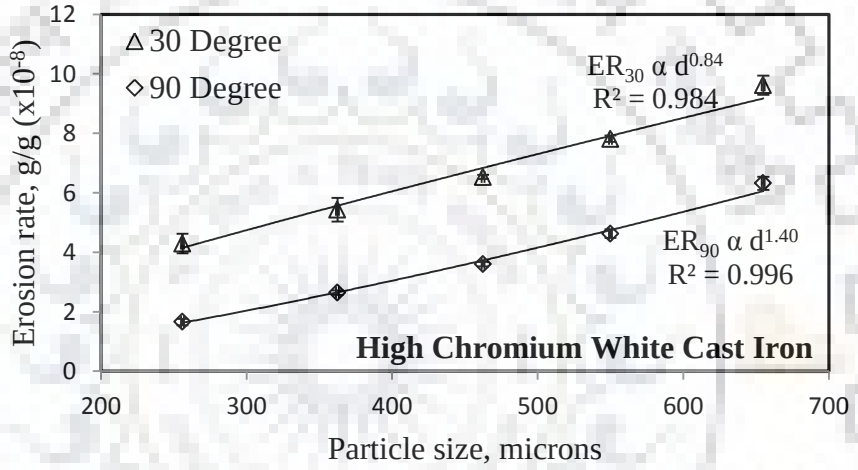

(c) High Chromium White Cast Iron

Fig. 5.17 Variation in erosion rate of different target materials with particle size (a) Steel 304L, (b) Grey cast iron, and (c) High chromium white cast iron

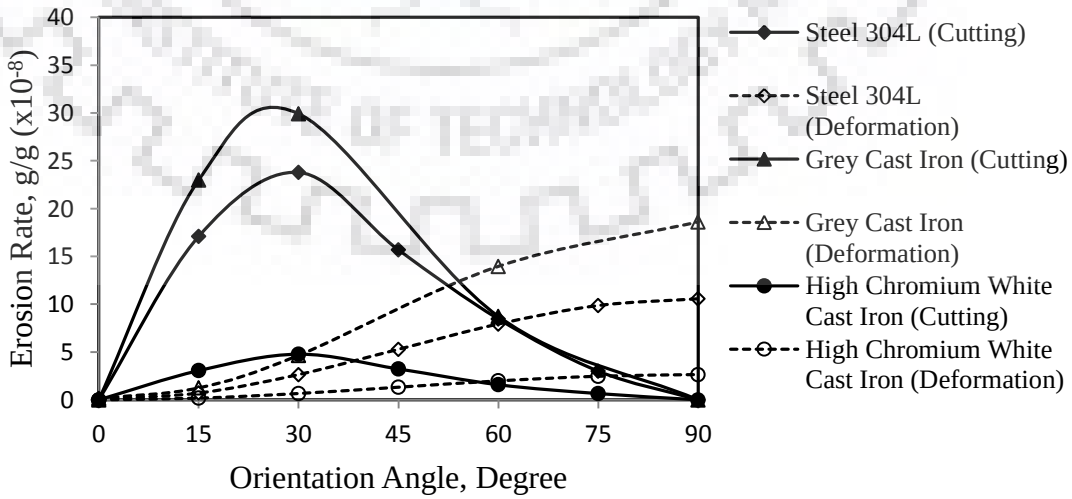

Fig. 5.18 Variation of erosion rate due to cutting and deformation with orientation angle at particle size = 362.5 μm, V = 13 m/s, and Cw = 1%.

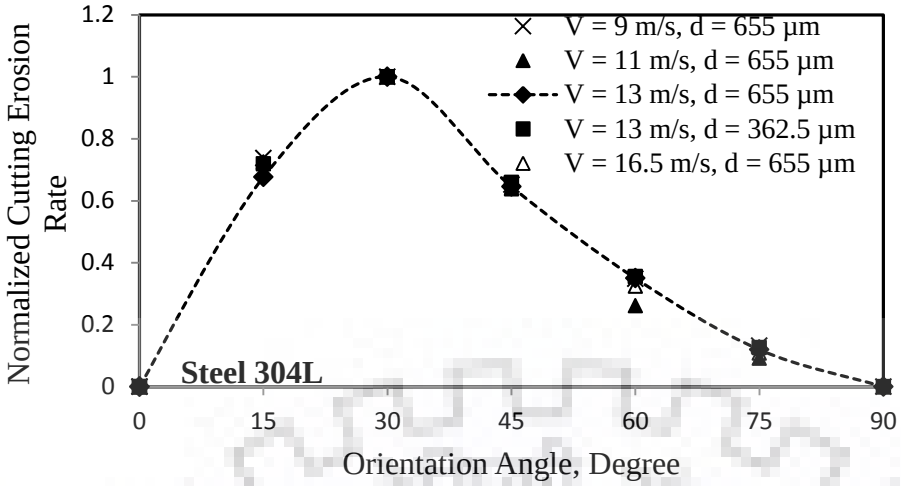

(a) Steel 304L

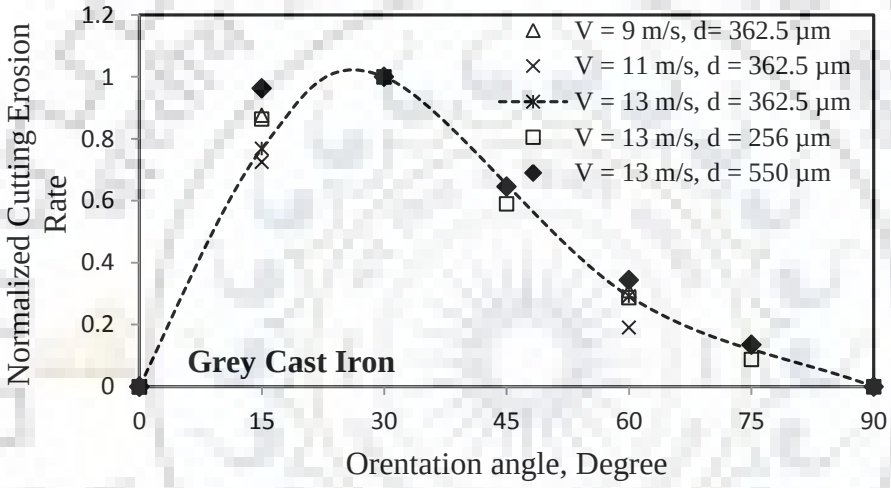

(b) Grey Cast Iron

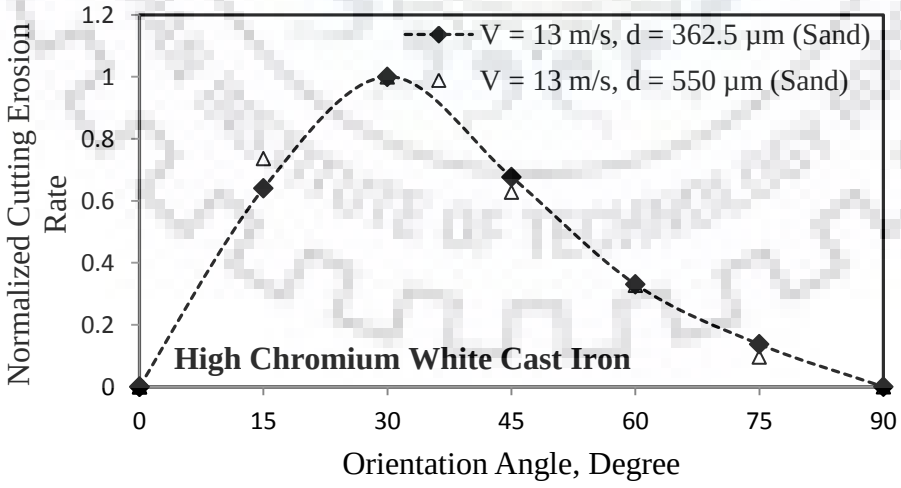

(c) High Chromium White Cast Iron

Fig. 5.19 Variation of normalized cutting erosion rate with orientation angle (a) Steel 304L, (b) Grey cast iron, and (c) High chromium white cast iron

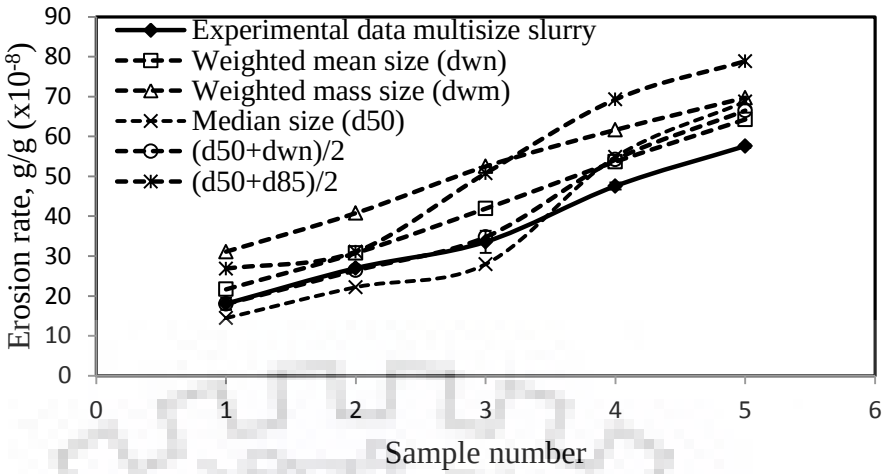

(a) Orientation angle = 30^o

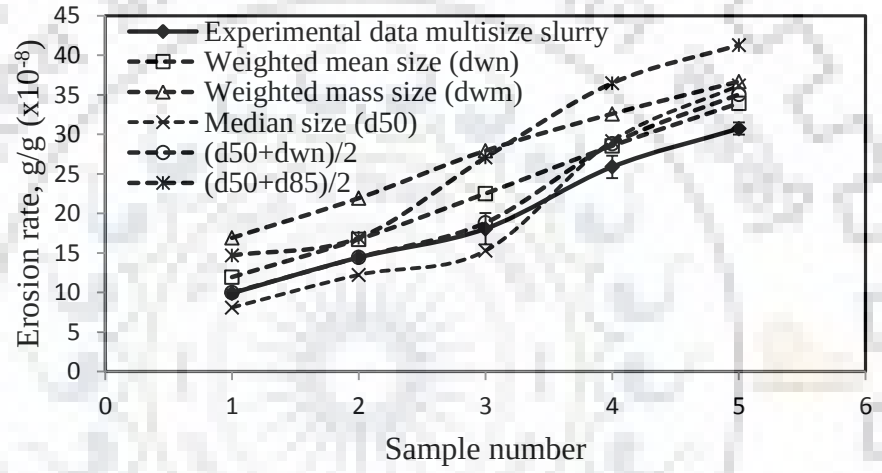

(b) Orientation angle = 90^o

Fig. 5.20 Experimental and predicted variation of erosion rate of grey cast iron with different samples of multi-sized slurry at (a) 30^o and (b) 90^o orientation angle at 13 m/s velocity and 1% weight concentration

CHAPTER 6: SLURRY EROSION OF CENTRIFUGAL SLURRY PUMP COMPONENTS

In slurry transportation systems, wetted components of centrifugal slurry pumps are prone to erosion which may lead to their replacement. Although erosion damage is considered unavoidable during the process, it can be mitigated significantly through optimized design, choosing high erosive resistance material and selecting proper operating conditions. Therefore, it is essential to understand the erosion behaviour of the pump components. It can be done in two ways. First is predicting the erosion rate of a component under certain operating condition, and secondly, the identification of the zone of the maximum erosion and the factors affecting it. This may help in optimization of design and estimating the service life.

In the present study, experiments are performed to investigate the pump casing erosion behaviour under different operating conditions. Thin wear specimens are used to paste on the casing wall to evaluate the erosion with the minimum flow disturbance. The wear samples are pasted along the centerline of the casing in order to develop an understanding of the dominant parameters affecting the casing erosion with change in pump operating conditions. To understand the mechanism of failure, the surface of the worn out wear specimens at different angular locations are analysed using scanning electron microscope.

Further, to investigate the erosive wear characteristic of the pump casing and impeller, three dimensional unsteady numerical simulation of a centrifugal slurry pump is performed. The Eulerian-Lagrangian approach has been applied to simulate the solid-liquid flow. The erosion rate of the components is estimated from the correlations developed through the pot tester. The measured centerline erosion profile of the pump casing is used for validation of the numerical model. The particulate flow field and its effect on erosion of casing and impeller blade surfaces is analysed and discussed for different flow rates and particle sizes.

6.1 Experimental Investigation of Centrifugal Slurry Pump Casing Wear

6.1.1 Experimental Setup and Procedure

Experiments are performed in a slurry pilot plant test rig available at the slurry research laboratory of Mechanical and Industrial Engineering Department, IIT Roorkee. A short loop of 50 mm pipe diameter is used in the present work for measurement of wear characteristics of "50M WILFLEY" pump casing. The details of pump geometry and experimental set up are already discussed in Chapter 3. The erosion profile of the pump casing is determined by affixing 100 μm thick wear specimens (1.5 x 1.5 cm^2) of AISI 304L steel along the centerline

of the casing wall. The chemical composition and hardness of the specimens are listed in Table 6.1. The casing material of the pump used is Ni-hard but the choice of material is not limited for its manufacturing and it may be of steel, cast iron, high chromium cast iron, ceramic, elastomer etc. [Xie et al., 2015]. The Ni-hard material has higher erosion resistance and is difficult to produce measurable erosion loss in short period of time in a laboratory under controlled conditions using close circuit test loop. Therefore, experiments are performed on the casing by inserting specimens of low erosion resistance material. To minimise the flow disturbances, thin (100 microns) wear specimens of steel 304L are pasted at selected locations inside the casing and the mass loss of the specimens are measured in a single test run of 90 minutes to minimise the effect of particle attrition and rounding-off. Fresh wear specimens are used for each experiment. The surface of the specimens is kept as received from the manufacturer (Bhandari Foils and Tubes Ltd, Dewas, India) and no additional surface treatment is performed. The average arithmetic mean roughness (Ra) of each specimen surface before the test is observed within 0.1 µm. The test specimens are cleaned with tap water, rinsed in acetone and dried with hot air blower before and after the test. The specimens are then glued at 14 different angular locations along the casing centerline as shown in Fig. 6.1. The locations '1' and '14' are at the discharge end of the casing, location '2' is close to the casing tongue (5^o) which was reported as one of the critical location [Pagalthivarthi et al., 2013; Noon and Kim, 2016], location '3' is 15^o downstream to location '2' to further understand the erosion close to the tongue and other locations are equally spaced at 30^o to each other to determine the variation in erosive wear of the casing along its flow path. The erosive wear of the specimens is determined by measuring the weight loss of the specimens before and after running the pump for a known period of time.

The performance of the pump is initially measured with water after affixing the specimens along the wetted wall of the casing. Thereafter, solid particles are added into the mixing tank and after proper mixing, the test is started at the desired operating conditions. During the test, slurry samples are collected at every half an hour duration to monitor the solid concentration. These samples are further analysed to check the particle attrition, if any. No significant change in the particle size is observed over the total duration of the tests. To evaluate the erosive wear at different locations of the casing centerline, weight loss of each wear specimen is measured using an electronic balance (least count of 0.1 mg) after running the pump for a period of 1.5 hours.

6.1.2 Material and Range of Parameters

The solid-liquid mixture is prepared by mixing Indian standard sand (IS 650:1991) with water. For the purpose of conducting the tests, the mean particle size of 400 µm (+ 300 –500), and 605 µm (+500 –710) are collected from sieving of solid particles using available sieve sizes. The numbers in the parenthesis represent the successive sieve sizes. The cases of different operating conditions at which the experiments are performed to study the casing wear are listed in Table 6.2. Flow rates corresponding to the best efficiency point (BEP) of the pump at 1200 rpm and 1050 rpm are 12 L/s and 10 L/s, respectively. The solid concentration at which the experiments are performed is kept nearly 10% by weight. To determine the effect of flow rate, the experiments are conducted with 605 µm size particles at 12 L/s and 9 L/s which are the BEP and 0.75 BEP conditions at 1200 rpm, respectively. Experiments are also performed with 400 µm size particles at 1200 rpm and BEP conditions to investigate the effect of particle size. Further to determine the effect of speed, experiments are performed at 1050 rpm with 400 µm size particles at BEP condition.

6.2 Numerical Modeling of Pump with Eulerian-Lagrangian approach for Slurry Flow

The advances in the numerical techniques have facilitated to analyse the flow field and particle impact conditions along the flow passages of complex geometries. Erosion modeling using CFD can be performed by following the steps as, the flow field simulation of the continuous phase, particle tracking, and applying the erosion model. In the present work, CFD code Fluent 17.2 is used to simulate the erosion of the pump components due to flow of solid-liquid mixture. It allows simulating the solid-liquid flow using Eulerian-Lagrangian frame of reference. The liquid is treated as a continuous phase to solve RANS equations in the Eulerian scheme and the secondary phase consisting of solid particles are dispersed in the continuous phase to track their motion in a Lagrangian framework with the application of Newton's second law.

6.2.1 Flow Modeling

Flow modeling is the initial step for CFD-based erosion modeling. It is used to identify the flow structure, velocity and turbulence which influence the movement and behaviour of particles in the flow. The predicted flow field is used as input for particle tracking to determine particle trajectories.

The continuity equation and the Navier-Stokes equations are utilized to define the flow medium. Equations of continuity and momentum are given as,

$$\frac{\partial \rho}{\partial t} + \nabla \bullet (\rho V) = 0 \tag{6.1}$$

$$\frac{\partial (\rho V)}{\partial t} + \nabla \bullet (\rho V V) = -\nabla p + \nabla \bullet \bar{\bar{\tau}} + \rho g + S_M \tag{6.2}$$

Where ρ is the liquid density, V is the instantaneous velocity vector, ∇p is the static pressure gradient, $\nabla \bullet \bar{\bar{\tau}}$ is the stress tensor, ρg is the gravitational body force and S_M is the added momentum transfer term for interaction between the continuous phase and the solid phase. It is figured out by probing the variation of the particle momentum when it moves through each control volume. It is calculated as:

$$S_M = \frac{-\sum (F_D + F_B + F_P + F_{VM} + F_R)}{V_{cell}} \tag{6.3}$$

Where F_D, F_B, F_P, F_{VM} and F_R represent the drag force, buoyancy force, pressure gradient force, virtual mass force and force due to rotation of reference frame, respectively: V_{cell} is the volume of the CFD cell.

In addition, the two-equation standard k-ε model is selected to simulate the turbulence, as it is the most extensively used in literature [Huang et al., 1997; Durate et al., 2015]. The flow in the near-wall region is modeled using standard wall function.

6.2.2 Dispersed Phase Modeling

Particle tracking is the second major step in CFD-based erosion simulation. It is performed through Lagrangian approach. The discrete phase model (DPM) is used to solve the motion equation for the discrete phase in a Lagrangian coordinates.

While performing the particle tracking, the following assumptions are made: (1) Particles are spherical in shape with no attrition effect during simulation (2) there is no modification in the geometry during the simulation. The governing equation of particle motion is expressed according to Newton's second law as below:

$$\frac{dV_s}{dt} = F_D + F_B + F_P + F_{VM} + F_R \tag{6.4}$$

The expression for drag force, buoyancy force, pressure gradient force, virtual mass force, and force due to rotation of reference frame in per unit mass are given as:

$$F_D = \frac{18\mu}{\rho_s d_s^2} \frac{C_D \, Re_p}{24} (V - V_s) \tag{6.5}$$

$$F_B = \frac{(\rho_s - \rho)g}{\rho_s} \tag{6.6}$$

$$F_P = \left(\frac{\rho}{\rho_s}\right) V_s \frac{\partial V}{\partial x} \tag{6.7}$$

$$F_{VM} = \frac{1}{2}\frac{\rho}{\rho_s}\frac{d}{dt}(V - V_s) \tag{6.8}$$

For rotation about the z axis,

$$F_R = F_{Rx}.\hat{n} + F_{Ry}.\hat{n} \tag{6.9}$$

$$F_{Rx} = \left(1 - \frac{\rho}{\rho_s}\right)\omega^2 x + 2\omega\left(V_{y,s} - \frac{\rho}{\rho_s}V_y\right) \tag{6.10}$$

$$F_{Ry} = \left(1 - \frac{\rho}{\rho_s}\right)\omega^2 y - 2\omega\left(V_{x,s} - \frac{\rho}{\rho_s}V_x\right) \tag{6.11}$$

($\hat{n}$ is the unit direction vector)

The drag coefficient C_D is taken as, $C_D = a_1 + \frac{a_2}{Re_p} + \frac{a_3}{Re_p^2}$ with a_1, a_2, a_3 are constants as given by Morsi and Alexander [1972], Re_p is the particle Reynolds number, $Re_p = \frac{\rho d_s |V_s - V|}{\mu}$, V_s is the particle velocity, d_s is the particle diameter, ρ_s is the density of particles, ρ is the fluid density and μ is the dynamic viscosity of the fluid.

The effect of turbulent eddies on the solid particles are predicted using the discrete random walk (DRW) model. The approach used is stochastic tracking which predicts the turbulent dispersion of particles by integrating the trajectory equations for individual particles, using the instantaneous fluid velocity, $v = V + v'(t)$, along the particle path. The fluctuating component of velocity is assumed to follow Gaussian distribution and determined as,

$$v' = \zeta\sqrt{\overline{(v')^2}} \tag{6.12}$$

Where ζ is the normally distributed random number.

For the k-ε model the local root mean square (RMS) value of velocity fluctuation is estimated as,

$$\sqrt{\overline{(v')^2}} = \sqrt{2k/3} \tag{6.13}$$

The characteristic life time of the eddy (T_e) is determined as,

$$T_e = 2T_L \tag{6.14}$$

Where T_L is the fluid Lagrangian integral time. For the k-ε model, which approximated as,

$$T_L \approx 0.15\frac{k}{\varepsilon} \tag{6.15}$$

The particle eddy crossing time (T_{cross}) is gives as:

$$T_{cross} = -T\ln\left[1-\left(\frac{L_e}{T|V-V_s|}\right)\right] \tag{6.16}$$

Where T is the particle relaxation time, L_e is the eddy length scale.

It is assumed that the particle interact with the continuous phase eddies over the smaller of the eddy lifetime and the eddy crossing time. After this time, a new value of the instantaneous velocity (v') is obtained by applying a new value of ζ.

The particles might collide against the wall and rebound back into the fluid domain during the flow. As the particle impacts on the wall, it loses some part of its energy and therefore, the velocity of the particle after the impact is less than that of the incidence. Therefore, particle wall interaction is an important phenomenon that needs be considered in DPM. The coefficient of restitution is used to account for this effect, which is the ratio the particle velocity after and before the impact as shown in Fig. 6.2.

The restitution coefficients in normal and tangential directions to the wall are defined as e_n and e_t, respectively and determined as below,

$$e_n = \frac{V_{pn1}}{V_{pn2}} \tag{6.17}$$

$$e_t = \frac{V_{pt1}}{V_{pt2}} \tag{6.18}$$

Where V_{pn} and V_{pt} are the normal and tangential velocity components of the particle, and the subscripts 1 and 2 denotes the conditions before and after the impact.

In this work, Forder et al. [1998] model is used to model the particle-wall rebound characteristic which was also used by Messa and Malavasi [2017]. The coefficient of restitution in the normal and tangential directions is given as:

$$e_n = 0.988 - 0.78\theta + 0.19\theta^2 - 0.024\theta^3 + 0.027\theta^4 \tag{6.19}$$

$$e_t = 1 - 0.78\theta + 0.84\theta^2 - 0.21\theta^3 + 0.028\theta^4 - 0.022\theta^5 \tag{6.20}$$

Where θ is the particle impact angle between the incident velocity and tangent to the surface

Further, the two-way coupling is applied to solve the interaction between the continuous phase and the discrete phase.

6.2.3 Erosion Modeling

Third and last step in CFD-based erosion prediction is calculation of the material loss. It occurs on a surface when the particle moves away from the fluid streamline and impacts on the wall. During particle impact, the particle impact information like the particle velocity and the impact angle are saved for each cell near the wall. Finally, the saved impact information is used to predict the erosion rate using the empirical correlation that can be incorporated in Fluent by either custom field function (CFF) or user defined function (UDF).

To predict the material removal rate (MRR) of the pump components, the correlations developed (See section 5.3) from pot tester data are used. A user defined function (UDF) is developed to incorporate these correlations in the CFD code Fluent 17.2. Details of the UDF made to estimate the MRR are presented in Appendix 1.

The MRR is defined as the mass loss of the target material per unit area per unit time. It is determined on walls by combining the damages done by each particle after the impact. It is given by

$$\mathrm{MRR} = \frac{1}{A_f}\sum_{\pi(f)} \dot{m}_{\pi} \mathrm{ER} \tag{6.21}$$

Where, A_f is the face area, $\dot{m}_{\pi}$ is the mass flow rate of particles that collide with the face and ER is the erosion rate, defined as the mass loss of target material over the erodent mass. The thickness loss per unit time of the target material due to erosion is determined by dividing the material removal rate (kg/m^2s) with the density of the target material ρ_t (kg/m^3) given as:

$$\text{Thickness loss rate } (\mu m/hr) = \frac{\mathrm{MRR}}{\rho_t} \times 3600 \mathrm{x} 10^6 \tag{6.22}$$

6.2.4 Model Implementation

A "50M WILFLEY" centrifugal slurry pump is selected for the present study. The details of pump geometry are discussed earlier (see Table 3.1). ANSYS ICEM is used to develop the mesh model of the complete pump. The relative motion between rotating and stationary components is modelled using a sliding mesh approach. The time step of 4.76×10^{-4}s and 4.16×10^{-4}s equivalent equal to 3 degree impeller rotation is set to perform the simulations at 1050 and 1200 rpm, respectively. To get the stable periodicity in the results, the simulations are initially performed for first ten impeller revolutions. The average data of the one complete impeller revolution (i.e. eleventh rotation) is used for the analysis. The velocity at the inlet and

pressure at the outlet are set as boundary conditions. SIMPLE algorithm is used for pressure-velocity coupling. Standard discretization schemes are used for the pressure terms and first-order upwind discretization scheme is used for the convection and diffusion terms. The under-relaxation factor of 0.3, 0.7, 0.5, 0.8 and 0.8 is set for pressure, momentum, volume fraction, turbulent kinetic energy and turbulent dissipation energy, respectively. Surface type of injection is used to release the particles at the impeller inlet at the same velocity as water. The mass flow rate of the particles is calculated from the solid concentration. The number of continuous phase iterations for each DPM iteration is set as 10. A total of 15,000 particles are simulated during DPM iteration. Increase in the number of particles for DPM simulation increases the computational time. Vieira et al. [2016] reported that the simulated results from DPM modeling of the solid-liquid mixture are unaffected after 10,000 numbers of particles.

6.2.5 Mesh Independency

Mesh independency check is performed to ensure mesh independent solution. Three different meshes named as m1, m2 and m3 are developed. The total numbers of elements with the corresponding meshes are 2.02 million, 2.72 million and 4.93 million, respectively. The details of the number of elements in the mesh for each component and the minimum orthogonal quality achieved with the complete mesh model are presented in Table 6.3. The simulation of different meshes is performed with 400 μm size particles (specific gravity = 2.65) of 10% weight concentration at 12 L/s flow rate for the pump speed of 1200 rpm. The predicted particle flow field along the casing centerline, particle velocity and volume fraction, with all the three meshes are shown in Fig. 6.3. It is seen that the casing centerline profile of particle velocity is not significantly affected with the increase in mesh density. However, different volume fraction profile is observed for the mesh m1 and m2, however, with further increase in mesh density to m3, no significant change in the profile is observed. Therefore, m2 mesh of elements 2.72 million with the minimum orthogonal quality of 0.32 is finalized for the simulation. With the present number of particles, DPM setup, rotor-stator interaction, and mesh size, the time required to get one result with eleven impeller revolution is nearly 9 days with a 28 core and 256 GB RAM workstation.

6.2.6 Model Validation

The numerically estimated particle tangential velocity at the location 13 (see Fig. 6.1a) is used to compare with experimental results of Furlan et al. [2015] as shown in Fig. 6.4. The simulation is performed with similar input parameters at which the experiments were conducted. Due to the difference in pump geometry, the results are compared by plotting the

variables in the non-dimensional form. The non-dimensional velocity along the width is plotted by dividing the particle tangential velocity with that at the middle plane. A good agreement between the predicted non-dimensional particle velocity profile along the width with the available experimental data is observed.

6.3 Casing Centerline Erosion and Its Variation with Operating Conditions

The average mass loss of the wear specimens affixed at different locations at the centerline of the casing for different operating conditions is listed in Table 6.4. The effect of flow rate, particle size and pump speed on the erosion, flow field and mechanism of erosion have been discussed in the following sections.

6.3.1 Effect of Flow Rate

The pump casing wear is experimentally evaluated at two flow rates, BEP and 0.75 BEP. The mass loss of the specimens due to erosion at different locations of the casing is presented in Fig. 6.5 for the particle size of 605 μm and pump speed of 1200 rpm at the two flow rates, 12 L/s (BEP) and 9 L/s (0.75BEP). It is observed that the erosion along the casing centerline is non-uniform in both the cases which may be attributed to variation of particulate flow field and the impact conditions. The secondary flows developed in the space between the impeller outlet and the casing also affects the flow field [Gandhi et al., 2001b]. Further, the maximum material loss for both the flow conditions is observed at the location '5' ($\theta = 80^o$) of the casing (see Fig. 6.5). It shows that the location of the maximum erosion along the centerline of the pump casing remains unaffected with the operating flow rate. Roudnev et al. [2009] also reported the zone of maximum erosion in the region 50^o-140^o from the casing tongue along the direction of impeller rotation. To further understand the casing erosion, the numerically predicted particle flow field along the casing centreline for same operating conditions are presented in Fig. 6.6 for particle velocity and volume fraction. It is observed that the particle velocity along the length of the casing do not vary much but a significant variation in the volume fraction of the particles along the centerline of the casing wall is observed. At 0.75 BEP flow rate, the mass loss of specimens along the casing wall is lower than that of the BEP flow rate at all the locations which may be attributed to the lower particle volume fraction. This observation is in line with Roco et al. [1984] and Walker et al. [1994], however, Gandhi et al. [2001b] observed nearly similar weight loss for the flow rates of 9 L/s and 18 L/s.

6.3.2 Effect of Particle Size

Particle size is one of the critical parameters during slurry handling that affects the extent of erosion. The effect of particle size on casing centerline erosion at nearly similar solid concentration (by weight) is presented in Fig. 6.7 for a pump speed of 1200 rpm and flow rate of 12 L/s (BEP) for two particle sizes of 605 μm and 400 μm. It is observed that the erosion pattern with these two particle sizes is almost similar, however, the magnitude of mass loss with 400 μm size particles is around 20-60% less as compared to that of the 605 μm size particles. The number of particles impacting at the surface is lower for 605 μm particle size as compared to 400 μm particle size for similar solid concentrations [Desale et al., 2009], however, the kinetic energy of the former is higher than the later due to 51.3% higher particle size. To further understand the effect of particle size on the casing erosion, the numerically simulated particle flow field is presented in Fig. 6.8. It is observed that change in the particle size at constant pump speed and flow rate does not significantly change the magnitude of particle impact velocity, however, the volumetric concentration of the particles increases with the reduction in particle size. This could be due to the increase in the uniformity of the particles along the casing width with the reduction in particle size. Thus the increase in kinetic energy of the impacting particles with an increase in particle size is partially balanced by the reduction in particle volume fraction. It may be one of the reasons for the lower increase in erosive wear as compared to the increase in kinetic energy due to the increase in particle size. However, the amount of mass loss of the specimens is dominated by the kinetic energy of the particles impacting the wear specimens. Thus the bigger size particles cause more erosion compared to the smaller size particles.

6.3.3 Effect of Pump Speed

The effect of pump operating speed on the casing wear is also investigated. Fig. 6.9 shows the effect of pump speed on the centerline erosion profile of the casing operating at BEP flow rate. It is observed that the mass loss of the specimens is normally decreased with the reduction in the pump speed. The magnitude of mass loss at 1050 rpm is around 25-65% less as compared to that of 1200 rpm. The dominant factor that may influence the mass loss of the specimens with the change in pump speed is analysed using the predicted particle flow field. The particle velocity and volume fraction at different locations of the casing is shown in Fig. 6.10. It shows that the volume fraction at different locations is nearly same at both the speeds, however, the particle impact velocity is less at lower speed except a small region just after the volute tongue. The decrease in particle impact velocity from 1200 rpm to 1050 rpm pump speed reduces the kinetic energy of the particles by around 10-35%. Thus the reduction in particle impact velocity

with the reduction in pump speed dominantly affects the erosion of the target surface. The rate of increase in mass loss of the target surface with the increase in particle velocity is dependent of the properties of the target surface and the impact conditions [Truscott, 1972; Finnie and Mcfadden, 1978; Lin and Shao, 1991b]. Truscott [1972] reported that the functional dependence of erosive wear of materials with velocity can be represented by a power-law relationship with power index value of 3.

6.3.4 Mechanisms of Material Removal

To observe the mechanism of material removal of casing wall, the worn out surface of wear specimens due to particles impacts are examined through scanning electron microscope (SEM) for all the cases under the present study. It is observed that the mechanism of material removal does not change much at any of the locations with change in operating conditions. For the sake of brevity, the photographs of the worn out specimens at six different casing locations for the cases I are shown in Fig. 6.11 (a-f). It is observed that the worn out surfaces of the specimens at different casing locations are not similar. At the location '2' which is near the casing tongue, the scratches and indentation marks are seen on the wear specimens. The mechanism of material removal due to indentation is generally associated with the condition of high impact angle of the particles. Minemura and Zhong [1995] also reported the impact angle of the particles near the casing tongue close to 90^{o} through numerical simulation. At other locations, the removal of material is observed due to cutting and ploughing. The mechanism of cutting and ploughing are generally associated with the low impact angle [Javaheria et al., 2018]. The intensity of surface failure due to cutting and ploughing is observed to vary with the location. It may be due to the variation in the kinetic energy transferred by the particles on the specimen surface with the change in the flow field. At the location '3', the material loss is less (see Fig. 6.5) which is also depicted by a few ploughing marks and scratches on the surface in the SEM image of the specimen. This is attributed to the low velocity and less number of particles hitting on the specimen surface at location '3' (see Fig. 6.6). At location '5', the material loss is observed as the maximum which is also visible from the SEM image of the specimen surface showing large cutting and deep ploughing marks (Fig. 6.11 (c)). This is attributed to the increase in the particle velocity and a number of particles hitting at the target surface (see Fig. 6.6). Further on observing the SEM images of the specimens at locations '7', '10', and '13', the mechanism of the mass loss appears to be cutting and ploughing of the surface. The observation of the surface failure of the casing at different locations is in line with the observations of Gandhi et al. [2001b]. They also reported that the impact angle of the particle at the volute

tongue is nearly 90^o and the impact angle of particles decreases with increase in the volute angle.

6.4 Comparison of the Measured and Predicted Mass Loss of a Pump Casing

In order to validate the procedure for numerical prediction of the pump erosion, the simulation of the pump with sand-water slurry is performed for the cases I-III (see Table 6.2) using the erosion model of steel 304L developed through the pot tester data. The experimentally measured mass loss data at 14 different locations along casing centerline are used for the comparison of predicted and measured mass loss results. The predicted mass loss of the specimens at each location is determined by assuming the constant erosion rate of the specimen within test duration. Figs. 6.12 (a-c) and Table 6.5 show the measured and predicted centerline erosion profiles of the pump casing for the case I, II and III respectively. The predicted erosion profile of the casing as well as the location of maximum erosion agrees reasonably well with the experimentally observed erosion profile for all the cases although the magnitude of predicted mass loss differs around 0.5 to 1.3 times of the measured mass loss. This difference may be attributed to some variation in simulation and experimental operating conditions. A similar comparison of erosion in pipe elbows were made by Chen et al. [2004], Vieira et al. [2016] and Pei et al. [2018] who observed the maximum deviation between the measured and predicted mass loss around 9 times, 1.5 times, and 0.8 times, respectively. This indicates that the present numerical modeling of the pump for erosion prediction using the correlation developed from pot tester data is reliable for predicting the erosion of the pump components and identification of location of maximum erosion for different operating conditions.

6.5 Numerical Simulation of Erosive Wear of Pump Components

To investigate the erosive wear distribution on the pump components, the numerical simulation of the pump with sand-water slurry is performed using the erosion model for target material of high chromium white cast iron developed through the pot tester data.

6.5.1 Range of Parameters

Two sets of numerical simulation of a pump are performed with sand-water slurry at 1200 rpm. In first set, the simulations are performed to establish the effect of flow rate on erosive wear of pump components at 10% weight concentration with 200 μm size particles for five different operating flow rates of 7.8 L/s, 10.2 L/s, 12 L/s, 13.8 L/s and 16.2 L/s which are 65%, 85%, 100%, 115% and 135% of BEP flow rate, respectively. In second set, the simulations are

performed to investigate the effect of particle size on erosive wear of pump components with five different particle sizes of 200 µm, 300 µm, 400 µm, 500 µm and 600 µm at 10% weight concentration and BEP flow rate.

6.5.2 Study on Zones of Maximum Erosion in Pump Components and its Variation with Operating Conditions

To study the erosive wear distribution of the pump components, the simulated results with 200 µm size particles at BEP flow rate are analysed. The erosion rate distribution and particle flow field data like impact velocity and concentration along the length and width of the casing and impeller blade surfaces are examined separately.

Fig. 6.13 (a-c) shows the distribution of particle impact velocity, concentration and erosion rate along the casing length and width. The casing length is measured from the volute tongue and the data at each angle along the flow direction are used to plot the velocity, concentration and thickness loss rate contours till the throat (see Fig. 6.1). To analyze the casing wall flow and erosion, non-dimensionalised width is presented with '0' for the front side and '1' for the back end. Fig. 6.13 (a) shows that the velocity is non-uniform across the width at all the casing angles. The velocity between the center and front side of the casing is observed to be higher than other regions along the whole length. The flow velocity is significantly low just after the tongue due to the separation of flow which increases with increase in the tongue angle. The maximum velocity is observed around 20 degree casing angle in the region between the centerline and front side. The distribution of particle volume fraction is highly non-uniform along the width of the casing at any volute angle as shown in Fig. 6.13 (b). This may be attributed to the presence of secondary flows in the casing flow passage [Gandhi et al., 2001b]. The high concentration of particles is observed near the back side region where the velocity of the particles is low.

Fig. 6.13 (c) shows the erosion rate distribution of the casing along its length and width. It is seen that the thickness loss of the casing is non-uniform along the length and width. The thickness loss of the casing is significantly less near the front side as compared to the centerline and back end though the velocity of the particles are more near the former as compared to other locations (Fig. 6.13a). This may be attributed to the low particulate concentration in the flow at the front side (Fig. 6.13b). The thickness loss rate at centerline is high near 80 degree and 300 degree casing angles. At the back side, the zone of maximum erosion is around 300 degree casing angle. A close observation of the erosive wear distribution of casing shows that the particulate concentration distribution dominates the erosive wear distribution of the casing as compared to the particle velocity distribution.

Further to study the erosive wear distribution of the impeller, the simulated results are plotted for the wall of one impeller blade passage namely pressure blade surface (PS), suction blade surface (SS), back shroud blade surface (BS) and front shroud blade surface (FS) (See Fig. 6.14).

To plot the variables, the blade surfaces are non- dimensionalised. The PS and SS are non-dimensionalised in axial (Z*) and radial (r*) directions. The FS and BS are non-dimensionalised in horizontal (X*) and vertical (Y*) directions. The non-dimensionalised distances are calculated as:

$$L^* = \frac{L - L_{min}}{L_{max} - L_{min}} \tag{6.23}$$

where L is either 'axial distance (Z)', 'radial distance (r)', ' horizontal distance (X)' or 'vertical distance (Y)' and the subscript 'min' and 'max' are the minimum and the maximum value corresponding to the distances being normalized. Thus, if the value of r* and Z* is 1, it corresponds to impeller eye and front shroud respectively and the corresponding value at impeller tip and back shroud is 0.

Fig. 6.15 (a-c) show the contours of particle impact velocity, distribution and thickness loss rate on impeller blade surfaces. It is seen that the particle flow field on the impeller blade surfaces is non-uniform (Figs. 6.15a,b). The particle impact velocity increases from blade inlet to outlet as the flow progresses (Fig. 6.15a). The particles are flowing more near the back shroud of the blade (Fig. 6.15b). From inlet to half of the blade, the concentration of particles is also more near the pressure side which reduces in remaining half and the particles are flowing more towards the suction side of the blade. This may attribute to the dominant outward centrifugal force that acts on the particles due to the rotation of the impeller which force the particles from pressure side to suction side.

Fig. 6.15 (c) shows the erosion rate distribution on the wall of the impeller blade. It is seen that the erosion of the blade surfaces is uneven. The variation in the impact velocity and solid distribution showed close resemblance to the erosion distribution of the surfaces. At the pressure side, the maximum thickness loss rate is observed near the blade inlet and close to the back shroud. This in line with experimentally obtained location of higher erosion rate reported by Ahmad et al. [1986]. At the blade surface of front shroud and back shroud, the location of higher thickness loss rate is near the blade outlet and close to the pressure side. This may be attributed to the higher impact velocity of the particles near the blade outlet and the higher particulate concentration close to the pressure side (see Figs. 6.15a ii,iii and 6.15b ii,iii). At the suction side of the blade, the rate of thickness loss is observed to be significantly less though

the particulate concentration is high near the blade outlet (Fig. 16b iv). This may be attributed to the low particle impact velocity on the suction side of the blade (see Fig. 16a iv).

6.5.2.1 Effect of Flow Rate

The pump is designed for BEP flow rate, however, it may run at other flow rates also depending on the operating condition. Therefore, it is important to determine the erosive wear characteristics of the pump components at different flow rates. To investigate the effect of flow rate, the numerical simulation of the pump is performed at five different operating flow rates varying from 65% BEP to 135% BEP. Fig. 6.16 shows variation in total mass loss rate for the impeller and casing of the pump operating at designed and off-designed conditions. The total mass loss rate of the components is calculated by multiplying the wetted surface area of the component (m^2) to the predicted average erosion rate (kg/m^2s) of the component. The wetted surface area of the impeller and casing is 0.12 m^2 and 0.24 m^2, respectively. It is observed from Fig. 6.16 that the mass loss rate of the casing is more as compared to the impeller. This shows agreement for the low specific speed (N_s =1345) design of the pump and the slower running of the impeller. Sellgren et al. [2005] reported that for the pump of low specific speed (around 1300), the service life of the impeller and side liner was higher as compared to the casing whereas for high specific speed pump (around 4000), the service life of the casing was higher as compared to impeller and side liner.

On comparing the mass loss rate of the pump components at designed and off-designed conditions (Fig. 6.16), it is seen that the mass loss rate of the components increases with the increase in flow rate. This attributed to the fact that the particulate concentration reduces near the wall of the components with the reduction in flow rate. The increase in mass loss rate of the pump casing with flow rate was also observed by Noon and Kim [2016].

Further to get the close understanding of the erosive wear distribution and location of the maximum erosion of the pump components with the change in flow rate, the contours of the thickness loss rate of the casing and impeller for different flow conditions are plotted as shown in the Fig. 6.17 (a-c) and Fig. 6.18 (a-c), respectively.

It is clearly observed from Fig. 6.17 (a-c) that the amount of thickness loss rate of the casing increases with the increase in flow rate. At lower flow rate (65% BEP), the thickness loss rate of the casing is highly uneven. The zones of maximum erosion are observed around 80 degree and 300 degree close to centerline and casing back end, respectively. No significant erosion of the casing is seen in between 0 degree to 120 degree casing angle close to casing front and back end. This may be attributed to the lower amount of recirculating flow [Gandhi et al. 2001b]. With increase in flow rate (85% BEP), the amount of recirculating flow increases and the

erosion of the casing is also seen near the tongue close to the back end (Fig. 6.17b). For 85% BEP, the zone of maximum erosion is around 80 degree casing angle near the centerline, whereas at the back end, the material loss is significantly more from 170 degree to 300 degree casing angle as compared to the other locations. At the front side, the erosion of the casing is not very significant. Further, the increase in flow rate to 100% BEP increases the uniformity in erosion distribution of the casing (see Fig. 6.13c). The locations of the maximum erosion are at centerline and casing back end around 80 degree and 300 degree casing angles, respectively. Further, operating the pump at flow rates higher than BEP (115% BEP), the material loss is higher at all the wetted flow passages of the casing except at the tongue region (Fig. 6.17c). The locations of higher erosion rate is near the front end from 0 to 110 degree casing angle and near the back end close to 300 degree casing angle.

Fig. 6.18 (a-c) shows the effect of pump operating flow rate on the erosion distribution of the impeller blade surfaces. It is seen that the erosion distribution of the blade surfaces significantly changes with the flow rate. At flow rate lower than BEP (65% BEP), no significant erosion at either FS or SS is observed, whereas the location of higher erosion rate of the PS and BS is observed close to the blade inlet and pressure side, respectively (Fig. 6.18a). With the increase in flow rate to 85% BEP and 100% BEP, no significant change in the location of maximum erosion of the blade surfaces is observed (See Figs. 6.18b and 6.15c) in comparison to the 65% BEP condition. At flow rate higher than BEP (115% BEP), the amount of material loss of the surfaces increases significantly and even the erosion of the surfaces at FS and SS are observed. The location of the maximum erosion of FS and SS is observed near the blade outlet close to the PS and FS, respectively. The erosion distribution and the zone of the maximum erosion are observed to be nearly same for PS and BS.

6.5.2.2 Effect of Particle Size

The particle size of the solids handled by the centrifugal slurry pumps generally varies for different applications. The trajectory of particles is significantly affected by its size for similar flow field [Fairbank, 1942]. Therefore the wear behaviour of the pump for different particle sizes is the prime interest of the designers. To investigate the effect of particle size, the numerical simulation of the pump is performed at BEP for the particle size varying from 200 µm to 600 µm. Fig. 6.19 shows variation of total mass loss rate for the impeller and casing of the pump operating with different particle sized slurry. It is observed that the increase in particle size increases the material loss rate which may be attributed to the increase in the kinetic energy of the particles.

Further to analyse the erosion distribution and the location of maximum erosion with particle size in detail, the contours of the thickness loss rate of the casing and impeller blade surfaces for 200 µm, 400 µm and 600 µm size particles are plotted in the Fig. 6.20 (a-c) and Fig. 6.21 (a-c), respectively. It is clearly seen that the increase in particle size increases the thickness loss rate of the casing and impeller blade surfaces.

The erosion contours of the casing in Fig. 6.20 (a-c) shows that the increase in particle size significantly changes the erosion distribution of the casing. This may be attributed to the increase in non-uniformity in the particle flow field with increase in size. As the particle size increases, the inertia force increases which oppose them to follow the liquid streamline, and produces random impact on the wall. The presence of secondary flows in the casing may also influence the impact characteristics of the particles. The smaller size particles may get trapped inside the vortices generated in the space between the impeller and the casing. For the larger particles, the influence of secondary flows on the particles decreases with respect to the inertia force. The inertia force drives the particles to impact directly on the casing wall and causes higher erosion.

For 200 µm size particle (Fig. 6.20a), the erosion is more uniform and the location of maximum erosion is around 300 degree casing angle close to the back end. For the particle size of 400 µm and 600 µm, the erosion of the casing is significantly more at the centerline and back end (Fig. 6.20b,c). The higher erosion at the centerline shows the direct impact of particles on the casing wall after exiting from the impeller outlet without much influence of the secondary flow. The increase in erosion at the back end with increase in the particle size may be attributed to the increase in particulate concentration.

Further, the variation in the erosion distribution at impeller blade surfaces is analysed for different particle sizes in Fig. 6.21 (a-c). It is observed that the erosion distribution of PS is dominantly influenced by the change in particle size as compared to other blade surfaces. For 200 µm size particles, the erosion of PS is observed close to blade inlet and no significant erosion in the upper half of the blade surface, whereas for the particle size of 400 µm and 600 µm, the erosion of PS is also observed in the upper half of the blade surface. This may be attributed to the non-uniform distribution of the particles along the blade passage. The small size particles tend to follow the fluid flow streamlines, whereas the coarse particles deviate from the fluid streamline and are shifted more towards the pressure side of the blade due to their higher inertial effect. The locations of the maximum erosion of the blade are at the back shroud and the blade inlet near the pressure side.

6.6 Concluding Remarks

The experimental and numerical investigation is performed to evaluate the centerline erosion profile of the casing and its variation with flow rate, particle size and pump speed. Further, the numerical modeling of the pump is performed using the erosion equations developed from the pot tester data to predict the erosive wear distribution and the locations of maximum wear and its variation with flow rate and particle size. Based on the study, the following conclusions can be drawn:

- The flow velocity in the centerline of the casing does not change significantly with the change in flow rate or particle size, however, the wear is affected by both the parameters. The lower flow rate reduces the particle volume fraction which reduces the wear. The bigger particles increase the wear due to higher kinetic energy, whereas, the smaller particles have a larger fraction of particles at the centerline.
- The reduction in pump speed reduces the flow velocity and thus the casing erosion is reduced significantly even if the particle volume fraction does not change.
- The mechanism of erosion of the casing is different at different locations. Around the casing tongue, cutting and deformation wear is dominant, whereas at other locations the cutting and ploughing are dominant. The location of the maximum erosion at the casing centerline is around 80^{o} from the casing tongue in the direction of impeller rotation.
- The comparison of the measured and predicted centerline erosion profile of the casing showed that the present numerical modeling of the pump along with the erosion equation developed through the pot tester data is useful to reasonably predict the erosion profile of the casing and to capture satisfactorily the erosion distribution of the pump components and its variation with the change in operating conditions.
- The higher mass loss rate of the casing compared to impeller concurs with the previous observations for low specific speed pumps. The increase in flow rate and particle size increases the mass loss rate of the components.
- The erosion distribution of the pump casing and impeller blade surfaces shows non-uniform variation along the length and width of the flow path. The non-uniformity in erosion distribution and the location of the maximum erosion are largely affected with the change in operating flow rate and particle size.
- Increase in flow rate increases the uniformity in the erosive wear distribution of the casing, whereas increase in particle size increases the non-uniformity in erosive wear distribution and higher erosion is observed at the casing centerline and back end. The

location of maximum erosion of the pump casing is around 80 degree and 300 degree casing angles near the centerline and back end, respectively.

- The erosive wear distribution on the impeller blade surfaces is not the same. The thickness loss rate of the blade pressure side and back shroud surfaces are more as compared to the blade suction side and front shroud surfaces. The location of the maximum erosion on the blade pressure side and back shroud is near the blade inlet and pressure side, respectively. Moreover, with the increase in particle size, the erosion distribution of the blade pressure side changes and the higher erosion is also seen on the upper half of the blade surface close to the back shroud.

Table 6.1: Properties of wear specimens

Material	Chemical composition (wt. %)	Hardness (Hv)
AISI SS304L	C-0.021, Mn-1.76, P-0.030, S-0.003, Si-0.22, Cr-18.08, Ni-8.06, Fe-bal.	160

Table 6.2: Operating conditions of the experiments

Case	Flow rate (lps)	Particle size (μm)	Pump speed (rpm)	Solid concentration (% by weight)	Duration (min)
I	12	605	1200	10.1	90
II	9	605	1200	9.4	90
III	12	400	1200	9.8	90
IV	10	400	1050	9.5	90

Table 6.3: Mesh parameters

Mesh type	Number of elements			Total number of elements	Mesh quality	Aspect ratio
	Impeller	Casing	Suction			
m1	1056115	290784	680084	2026983	0.35	15.41
m2	1056115	993667	680084	2729866	0.32	16.12
m3	2237111	1396978	1300437	4934526	0.29	24.28

Table 6.4: Experimental measured casing centerline erosion for different cases

Measuring Location	Measured Mass Loss (mg)			
	Case I	Case II	Case III	Case IV
1	2.2	0.3	1.97	1.5
2	2.1	0.8	0.8	2
3	6.2	2.4	4.8	3.1
4	16	6.2	9.9	5.5
5	32.6	17	21.4	10.4
6	14.6	6.8	7.2	6.8
7	20.1	8.9	13.1	13.1
8	14.7	8.4	10.4	6.9
9	13.7	7.3	6	6.2
10	22.2	15.6	17.1	11.1
11	15	6	9.7	5
12	12	5.3	11.6	7.4
13	18.9	6.4	15.3	8.6
14	2.9	0.7	2.7	0.9

Table 6.5: Comparison of measured and predicted casing centerline erosion rate

Measured Location	Erosion Rate (mg/hr)								
	Case I			Case II			Case III		
	Exp.	Num.	Pred. Factor	Exp.	Num.	Pred. Factor	Exp.	Num.	Pred. Factor
1	1.47	0.86	0.59	0.20	0.23	1.15	1.31	0.62	0.47
2	1.40	0.63	0.45	0.53	0.24	0.45	0.53	0.24	0.45
3	4.13	3.52	0.85	1.60	1.60	1.00	3.20	2.81	0.88
4	10.67	8.26	0.77	4.13	4.31	1.04	6.60	4.86	0.74
5	21.73	10.61	0.49	11.33	9.43	0.83	14.27	7.79	0.55
6	9.73	5.08	0.52	4.53	3.33	0.74	4.80	3.65	0.76
7	13.40	6.63	0.50	5.93	4.45	0.75	8.73	4.36	0.50
8	9.80	4.72	0.48	5.60	3.97	0.71	6.93	4.21	0.61
9	9.13	4.62	0.51	4.87	4.32	0.89	4.00	2.92	0.73
10	14.80	6.65	0.45	10.40	7.92	0.76	11.40	5.15	0.45
11	10.00	5.99	0.60	4.00	5.14	1.29	6.47	4.65	0.72
12	8.00	5.64	0.71	3.53	4.45	1.26	7.73	4.55	0.59
13	12.60	8.52	0.68	4.27	5.17	1.21	10.20	6.20	0.61
14	1.93	1.08	0.56	0.47	0.57	1.21	1.80	0.57	0.32

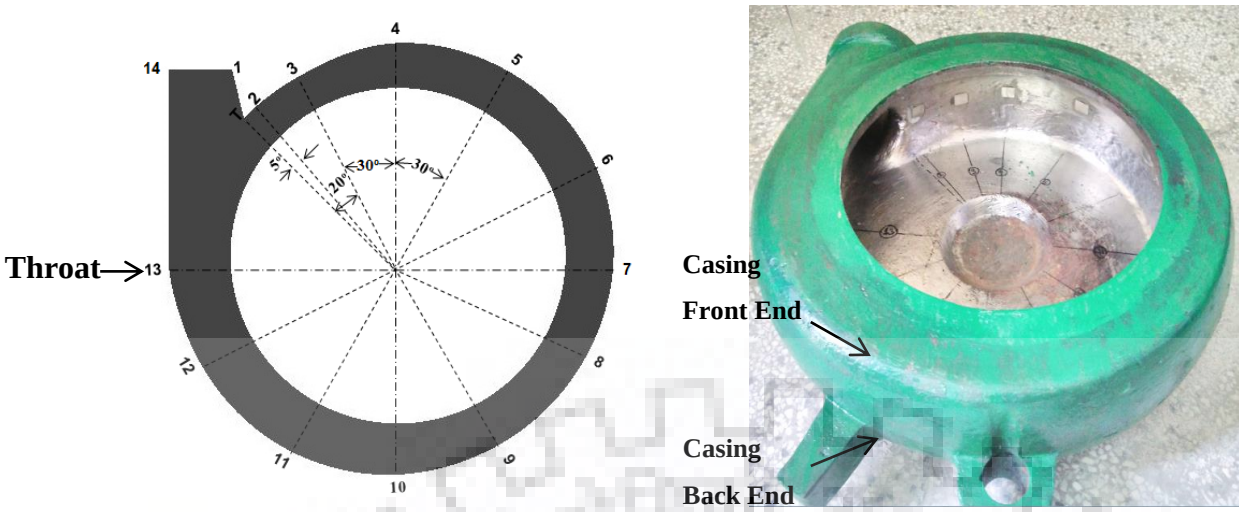

(a) Schematic view (b) Photographic view

Fig. 6.1 Slurry pump casing showing the locations of wear specimens

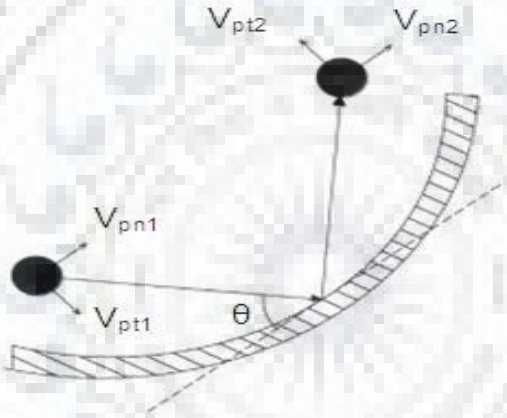

Fig. 6.2 Impact of a particle on casing wall

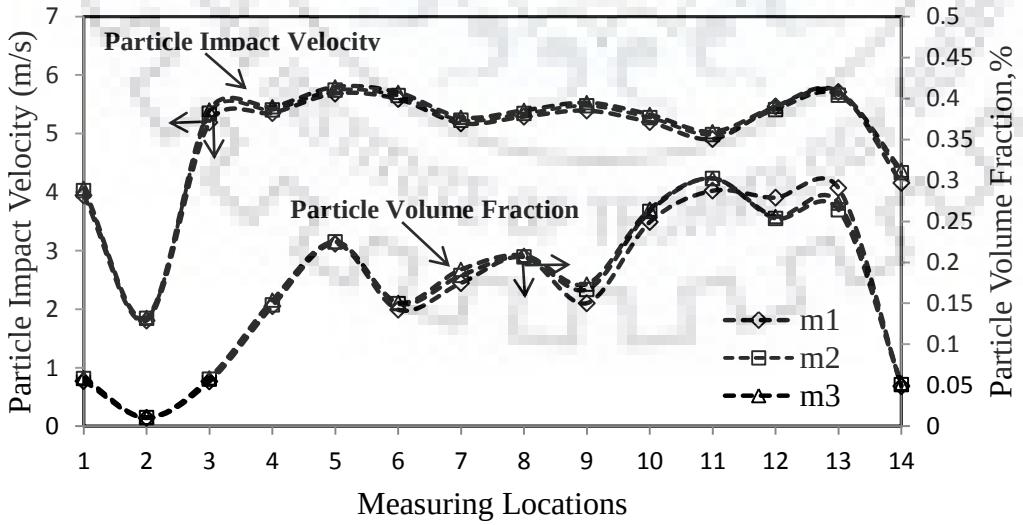

Fig. 6.3 Mesh independency test of particle flow field

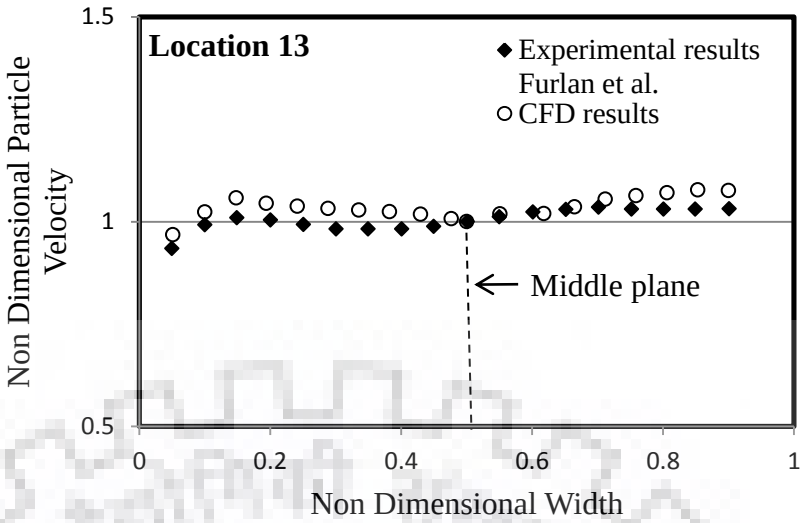

Fig. 6.4 Comparison of particle tangential velocity at the casing location 13 of Furlan et al. [2015] with the present CFD results

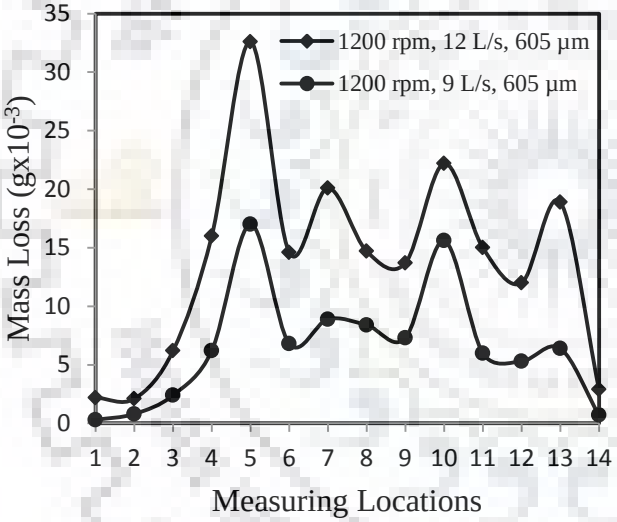

Fig. 6.5 Experimentally measured mass loss of the specimens at different casing locations for 12 L/s and 9 L/s operating flow rate with 605 µm particle size at 1200 rpm.

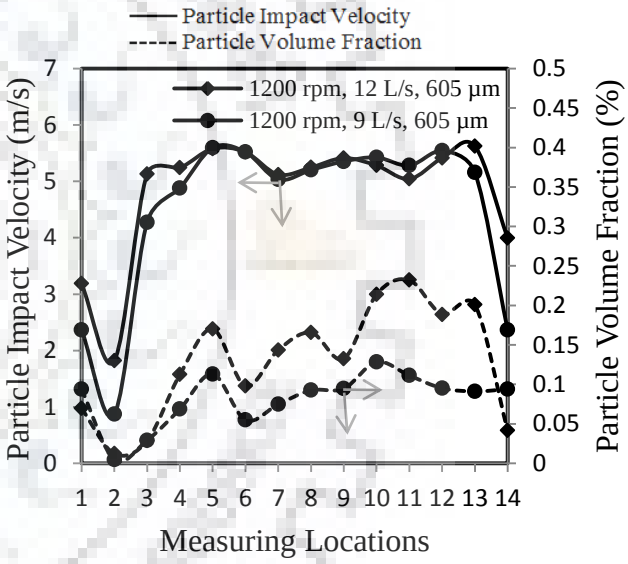

Fig. 6.6 Numerically predicted particle impact velocity and volume fraction at the centerline of the casing for 12 L/s and 9 L/s operating flow rate with 605 µm particle size at 1200 rpm.

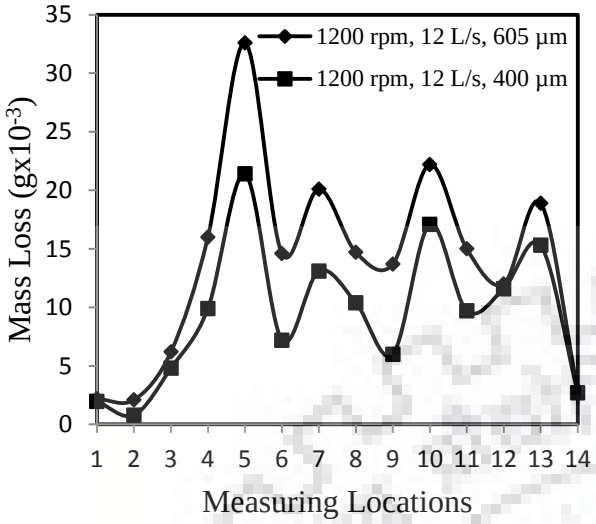

Fig. 6.7 Experimentally measured mass loss of the specimens at different casing locations for 12 L/s operating flow rate with 605 µm and 400 µm particle size at 1200 rpm.

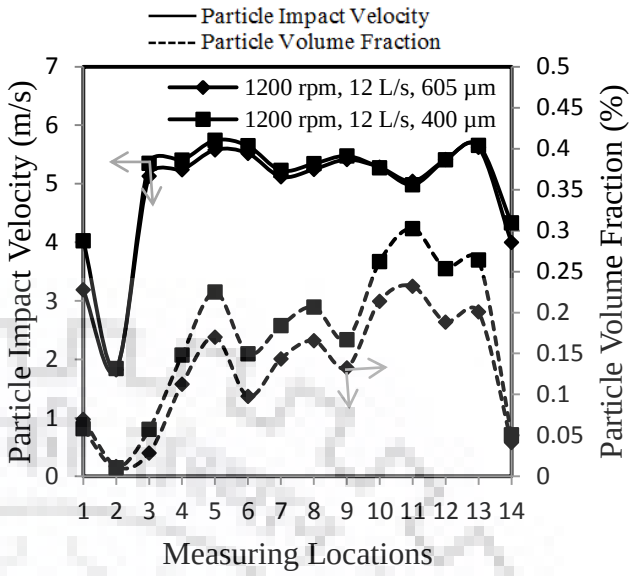

Fig. 6.8 Numerically predicted particle impact velocity and volume fraction at the centerline of the casing for 12 L/s operating flow rate with 605 µm and 400 µm particle size at 1200 rpm.

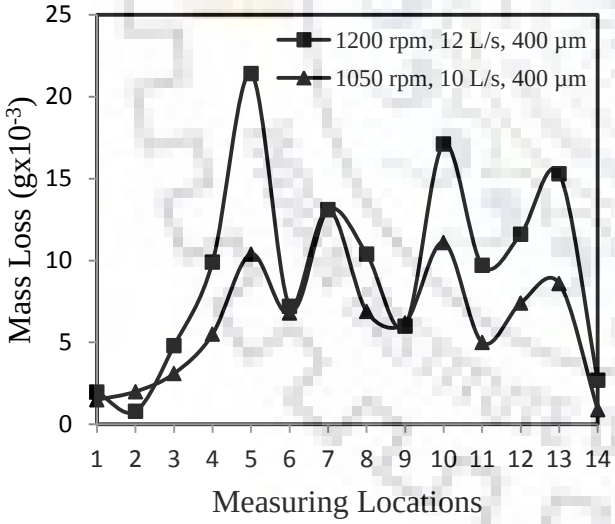

Fig. 6.9 Experimentally measured mass loss of the specimens at different casing locations for BEP flow rate with 400 µm particle size at 1050 rpm and 1200 rpm.

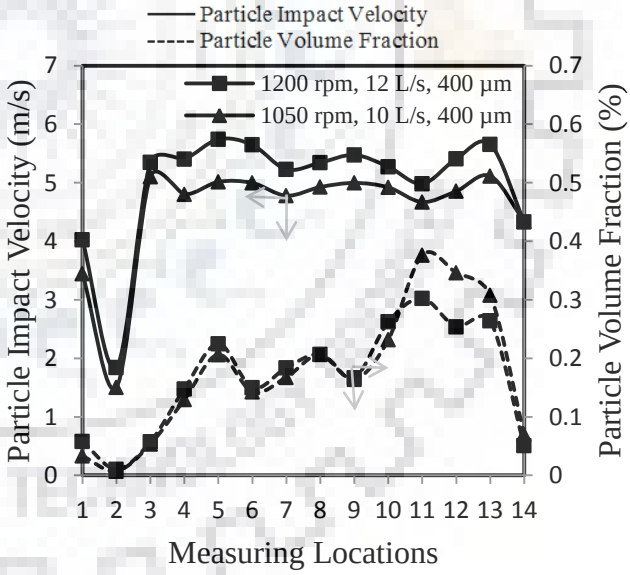

Fig. 6.10 Numerically predicted particle impact velocity and volume fraction at the centerline of the casing for BEP flow rate with 400 µm particle size at 1050 rpm and 1200 rpm.

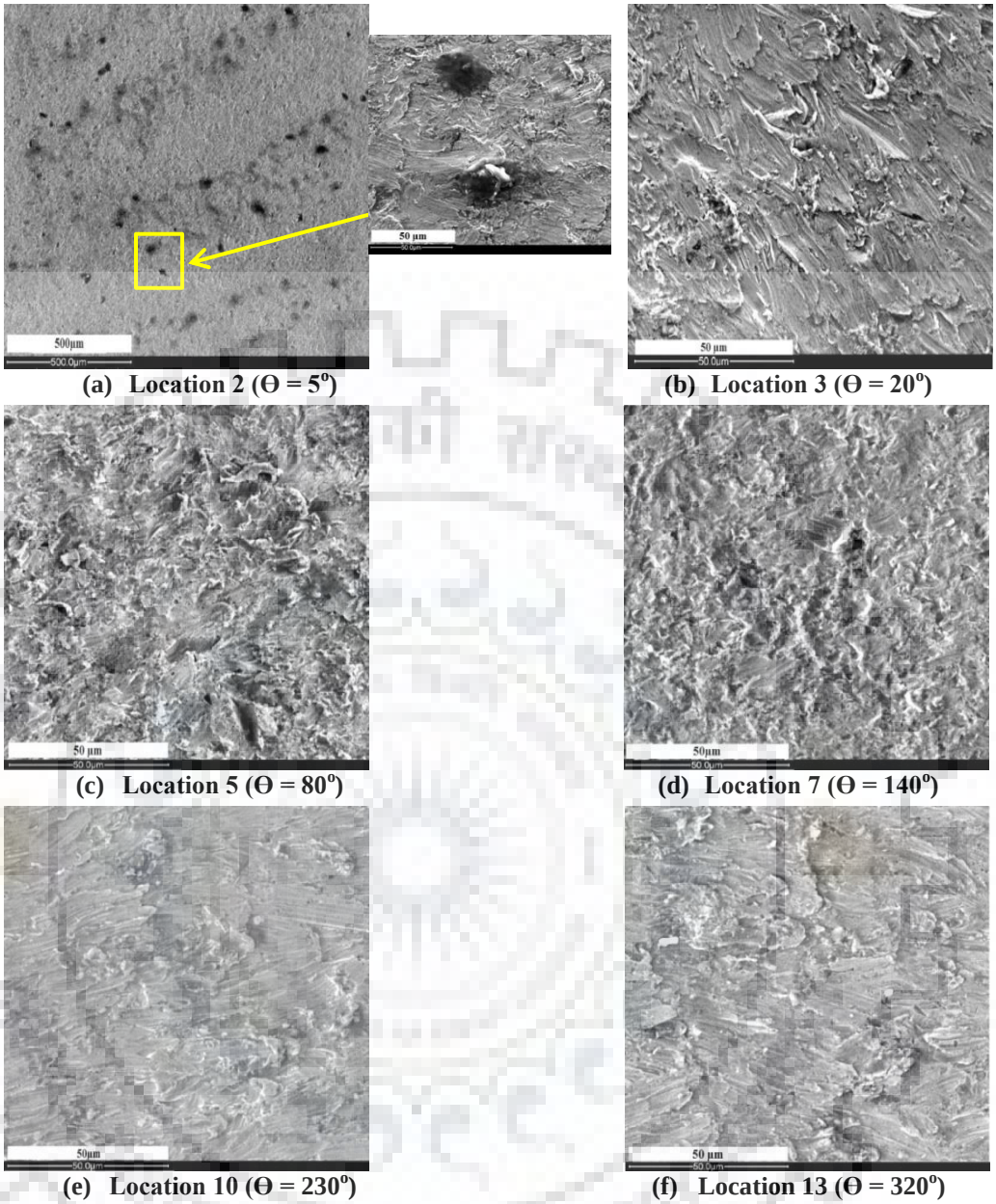

(a) Location 2 (Θ = 5°) (b) Location 3 (Θ = 20°)

(c) Location 5 (Θ = 80°) (d) Location 7 (Θ = 140°)

(e) Location 10 (Θ = 230°) (f) Location 13 (Θ = 320°)

Fig. 6.11 SEM micrographs of eroded surface of the wear samples affixed at different angular locations along the casing centerline for the pump operating at 12 L/s with 605 µm particle size, 10.1% weight concentration at1200 rpm.

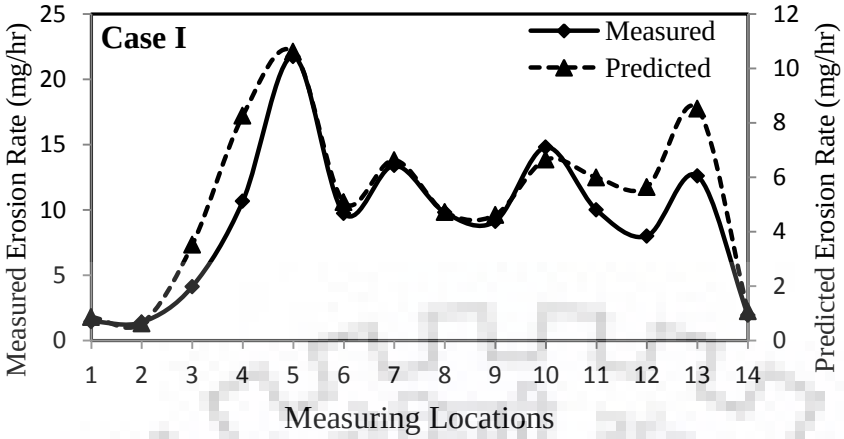

(a) **Case I**

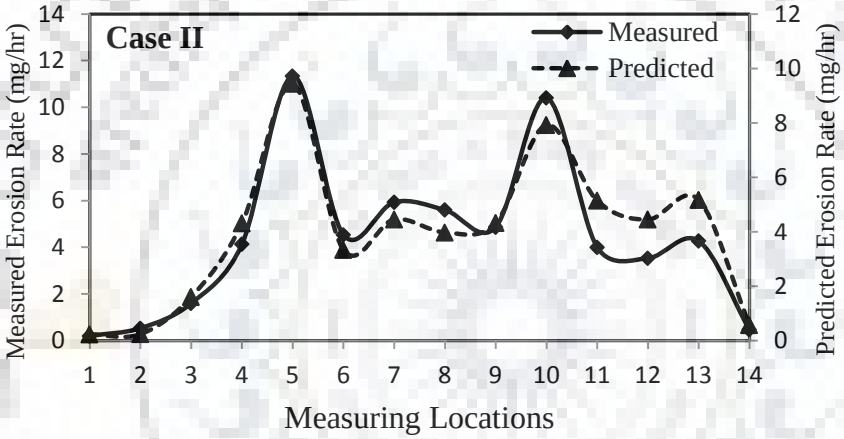

(b) **Case II**

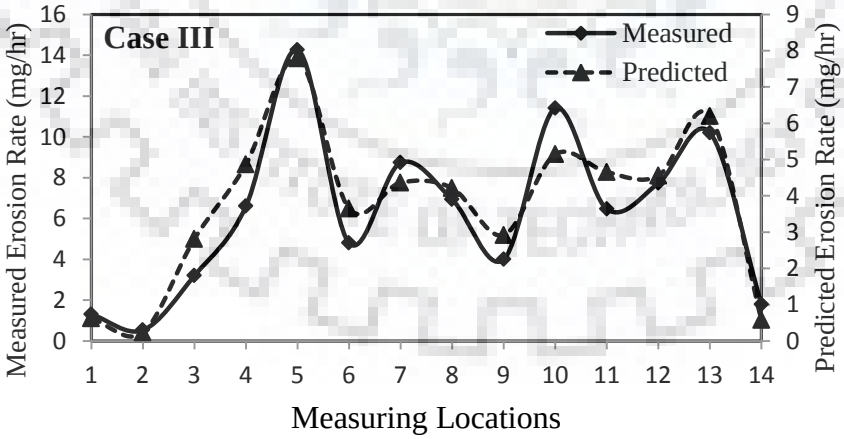

(c) **Case III**

Fig. 6.12 Comparison of predicted and measured centerline erosion profile of pump casing

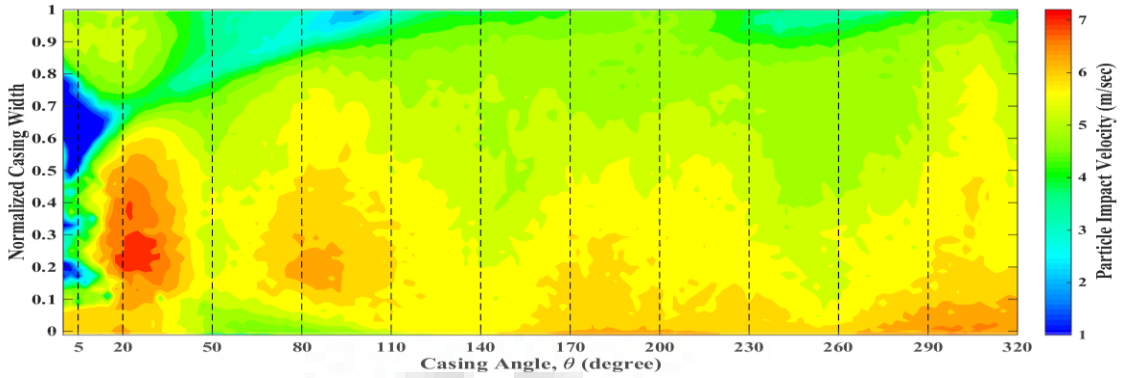

(a) Particle impact Velocity

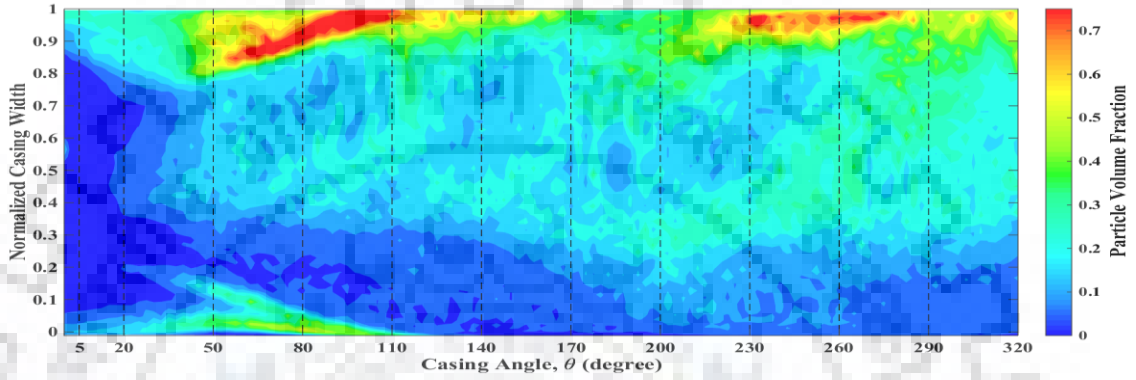

(b) Particle distribution

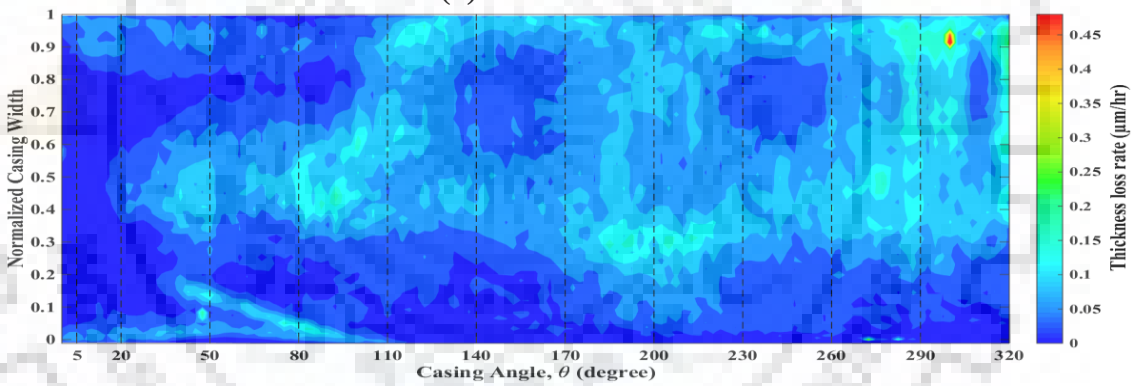

(c) Thickness loss rate

Fig. 6.13 Variation in particle impact velocity, distribution and thickness loss rate along length and width of the casing wall at BEP and C_w = 10% for 200 µm size particles

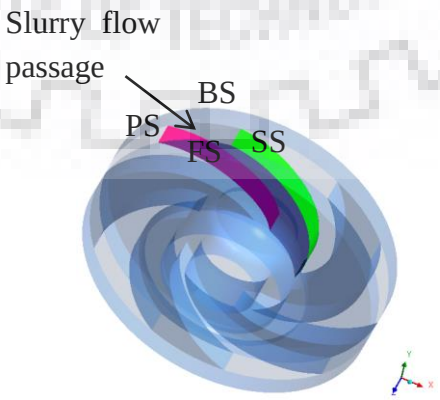

Fig. 6.14 Isometric view of impeller

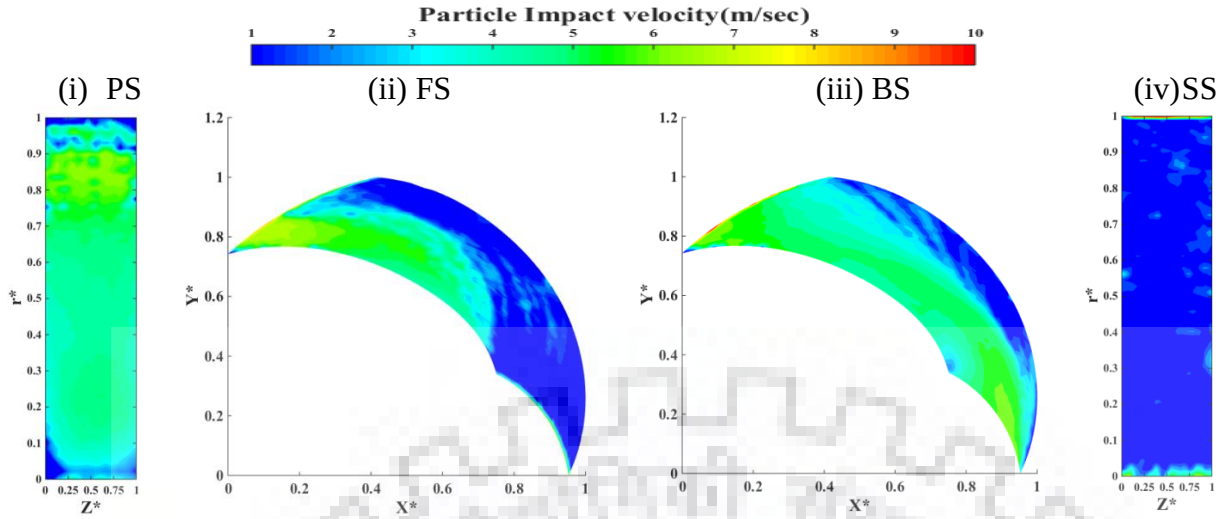

(a) Particle Impact Velocity

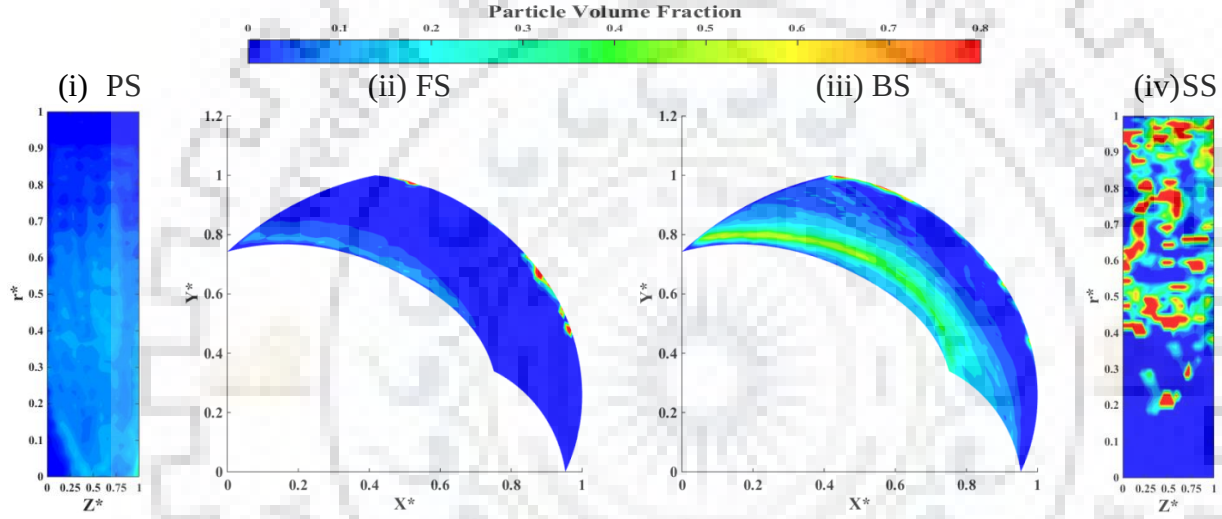

(b) Particle Distribution

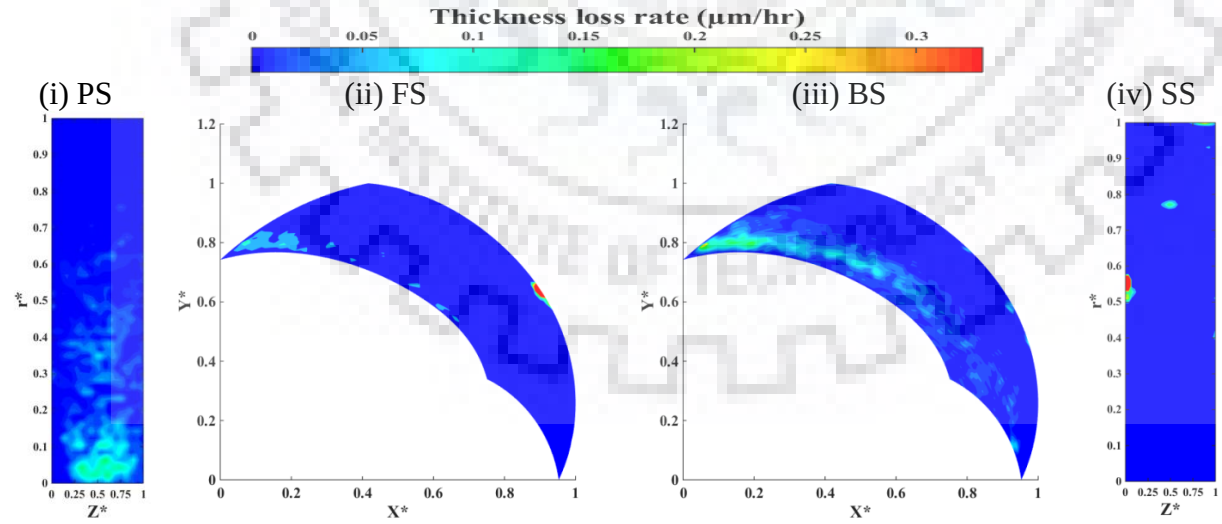

(c) Thickness loss rate

Fig. 6.15 Variation in particle impact velocity, distribution and thickness loss rate of impeller one blade surfaces at BEP and 10% weighted concentration for 200 µm size particles.

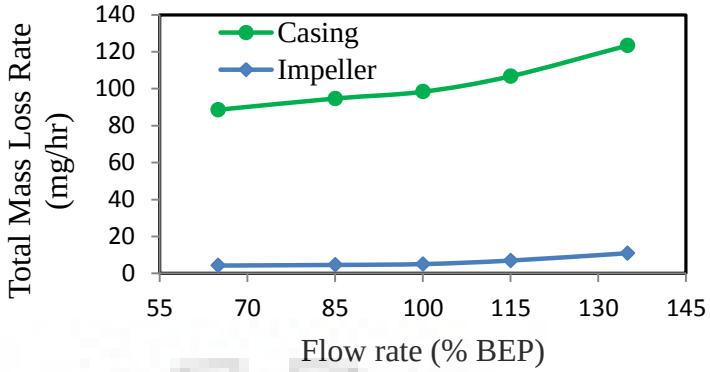

Fig. 6.16 Effect of flow rate on total mass loss rate of the pump impeller and casing

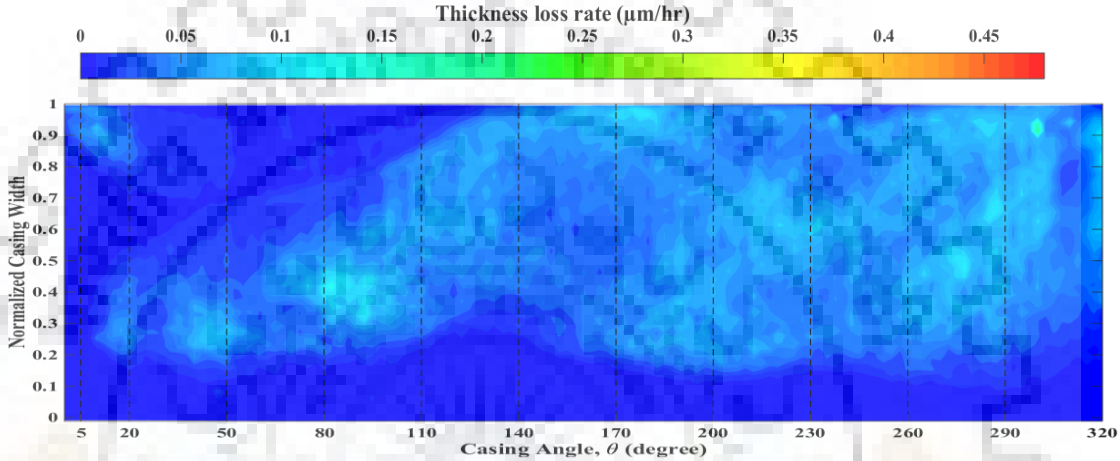

(a) Q = 65%Q_{bep}

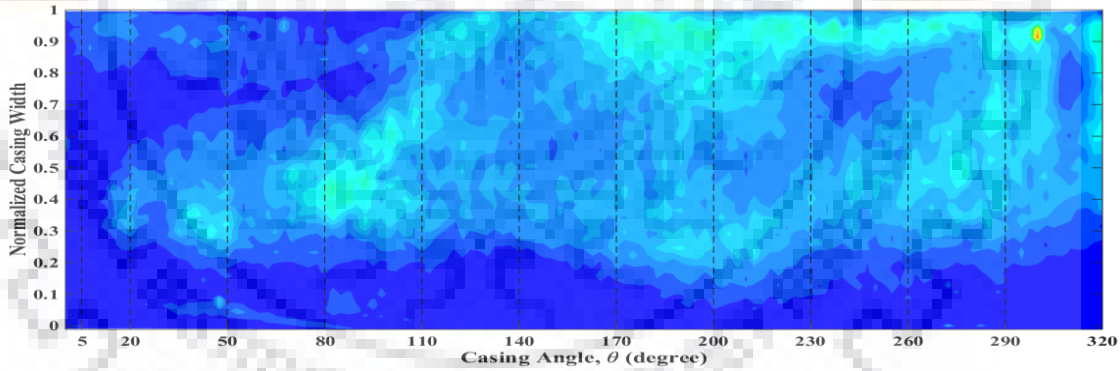

(b) Q = 85%Q_{bep}

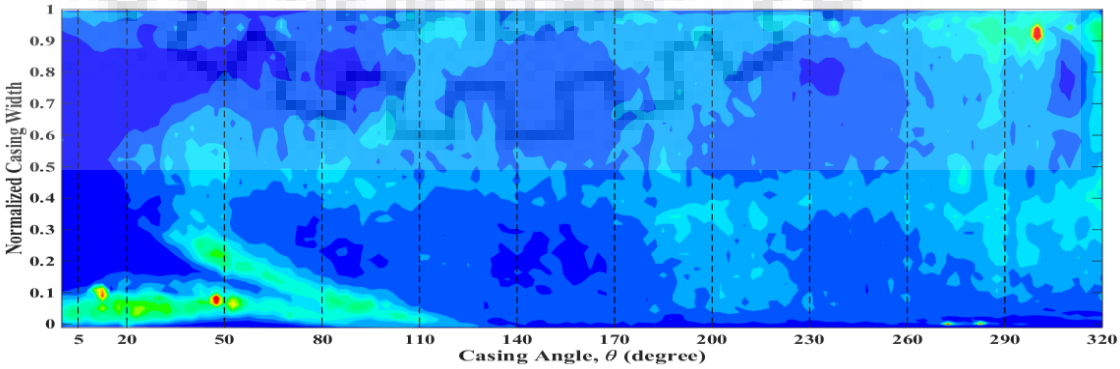

(c) Q = 115%Q_{bep}

Fig. 6.17 Variation in thickness loss rate along length and width of the casing wall with flow rate at 10% weighted concentration for 200 µm size particles.

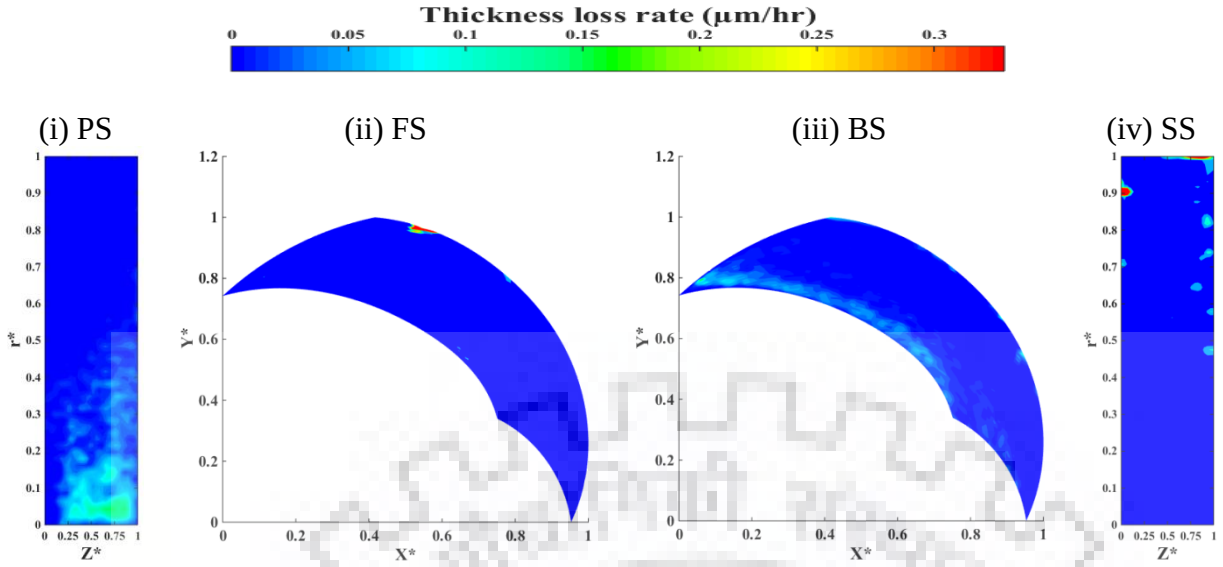

(a) Q = 65%Q_{bep}

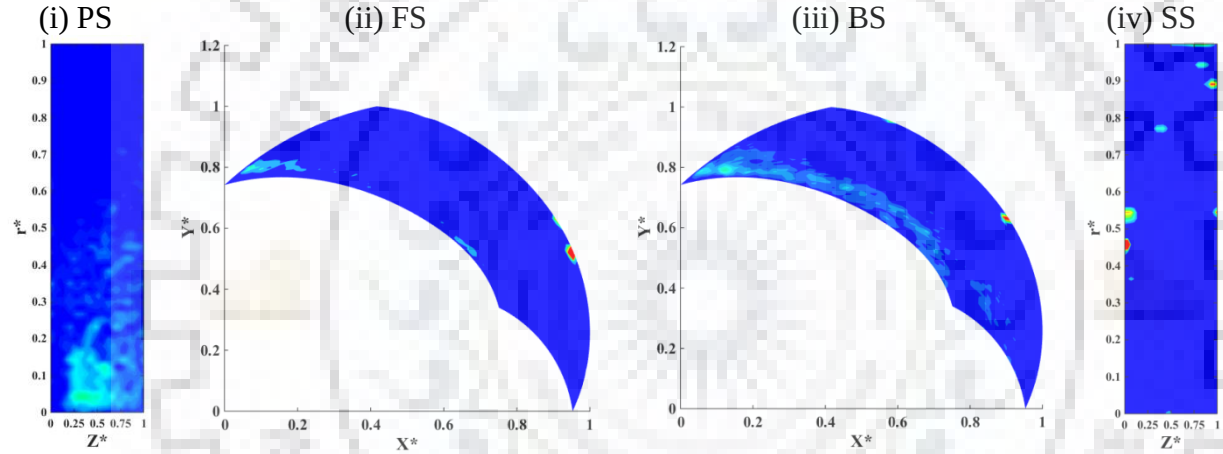

(b) Q = 85%Q_{bep}

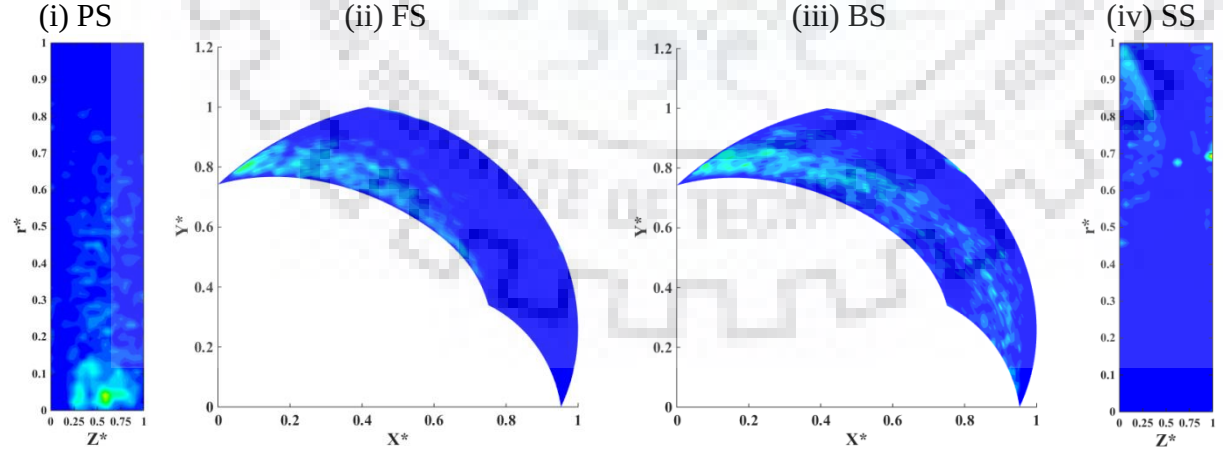

(c) Q = 115%Q_{bep}

Fig. 6.18 Variation in thickness loss rate of impeller one blade surfaces with flow rate at 10% weighted concentration for 200 µm size particles.

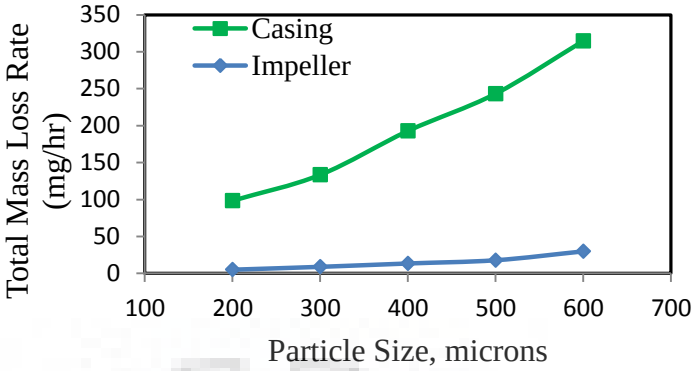

Fig. 6.19 Effect of particle size on total mass loss rate of the pump impeller and casing

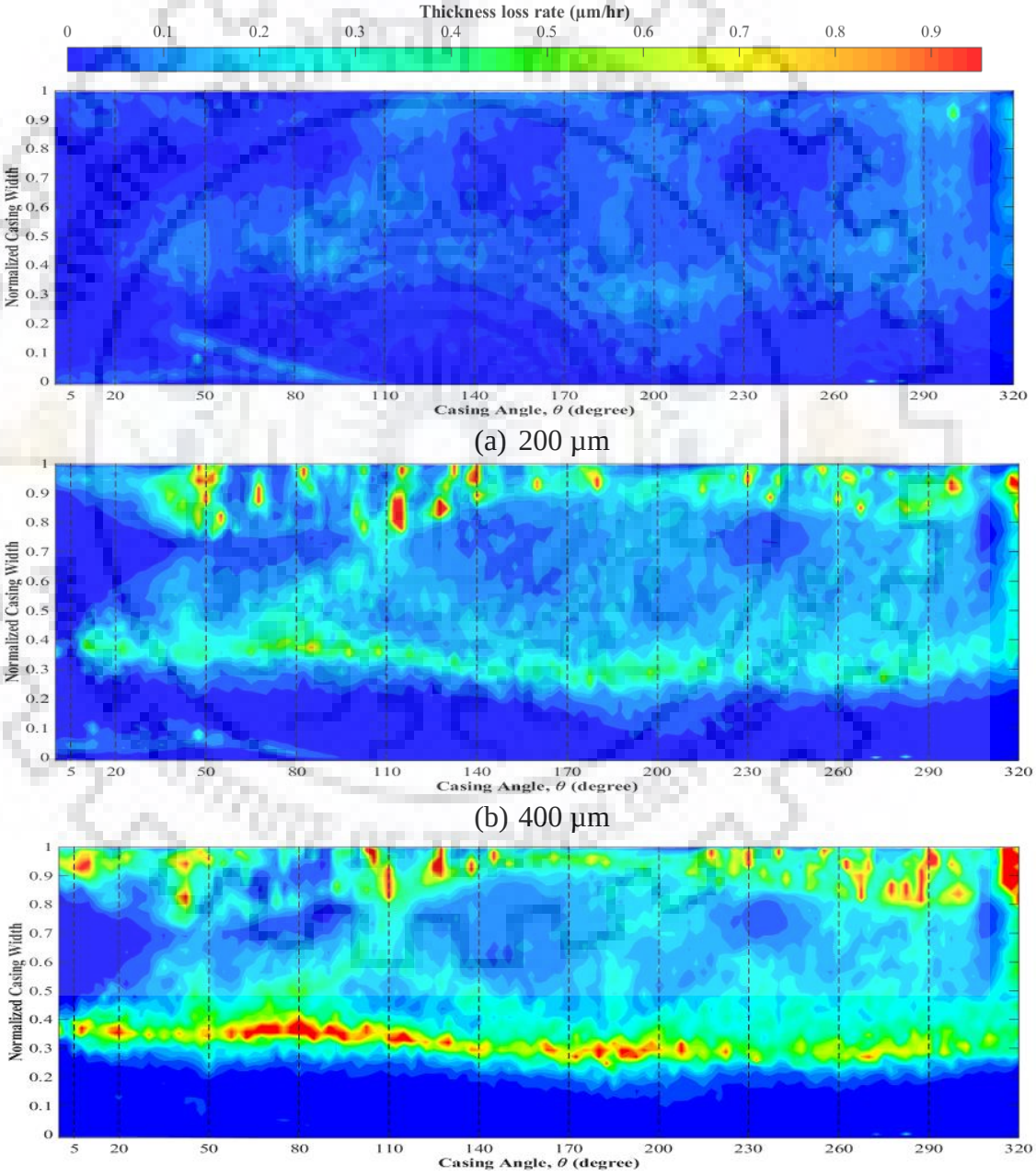

(a) 200 µm

(b) 400 µm

(c) 600 µm

Fig. 6.20 Variation in thickness loss rate along length and width of the casing wall with particle size at BEP flow rate and 10% weighted concentration.

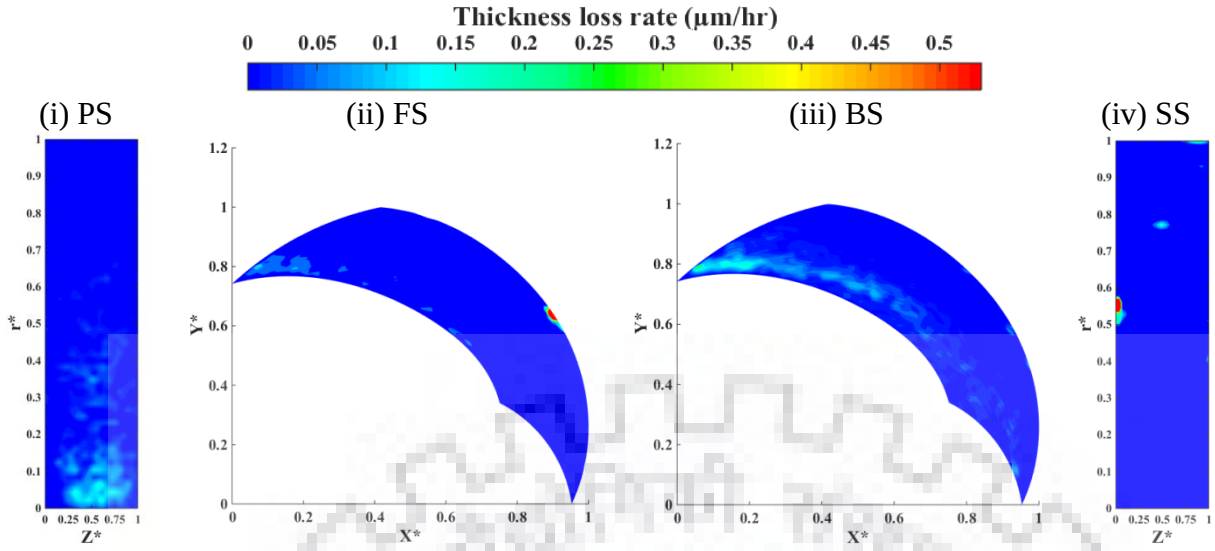

(a) 200 µm

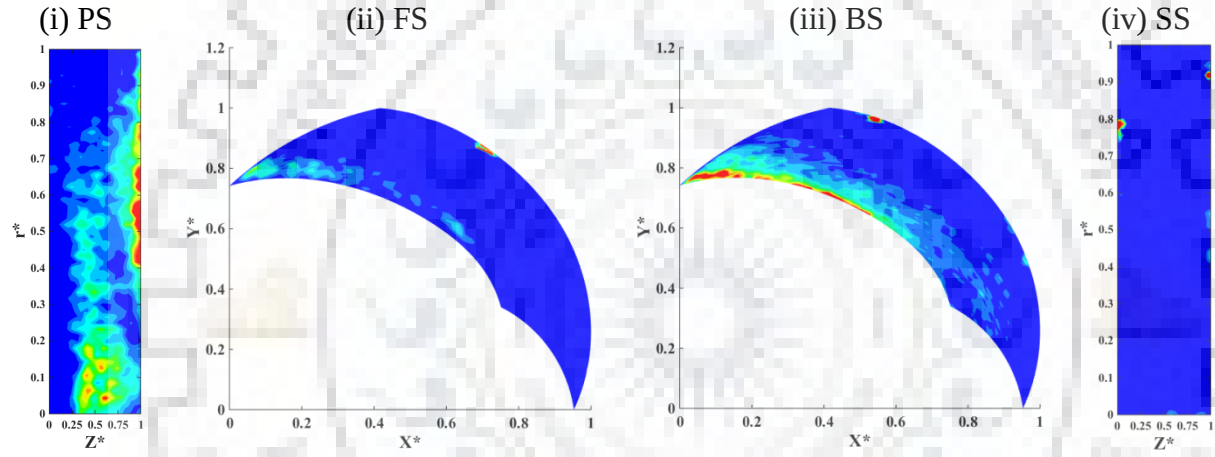

(b) 400 µm

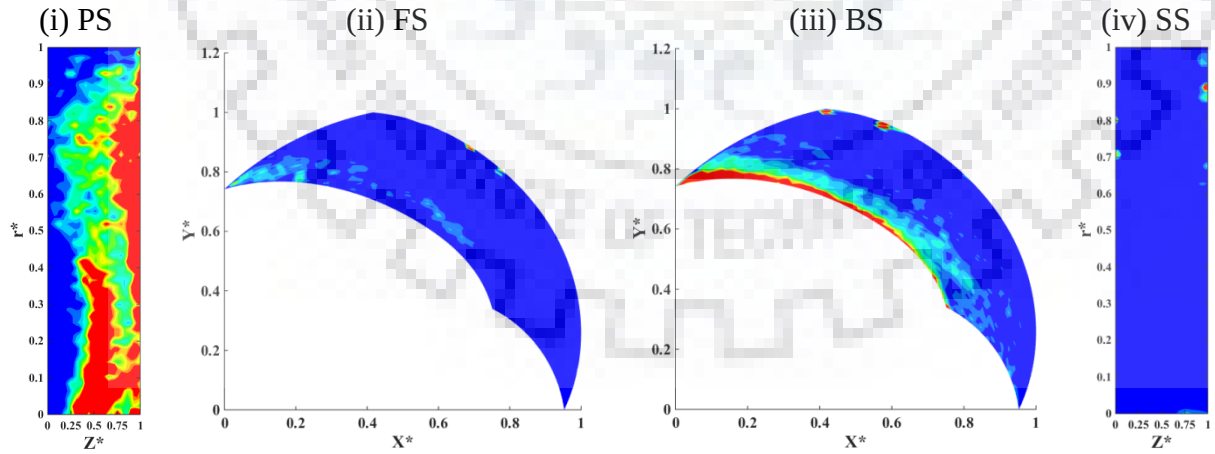

(c) 600 µm

Fig. 6.21 Variation in thickness loss rate of impeller one blade surfaces with particle size at BEP flow rate and 10% weighted concentration.

CHAPTER 7: CONCLUSIONS AND SCOPE FOR FUTURE WORK

7.1 Conclusions

Conclusions related to different aspects of the present work have been already discussed in individual chapters and hence are reiterated here in brief. The major outcomes from the present study on performance and erosive wear behaviour of the centrifugal slurry pump handling solid-liquid mixture are summarized below.

(1) The performance characteristic of centrifugal slurry pump is significantly influenced with the variation in particles and slurry properties. The drop in head and efficiency of the pump while handling solids is not the same which largely depends on the specific gravity of solids. The available empirical correlations in literature do not have good accuracy in prediction of effect of solids on pump performance.

(2) Three-dimensional numerical modeling of the pump handling solid-liquid mixture using Eulerian-Eulerian model with sliding mesh approach can predict the effect of solids on pump performance with reasonably good accuracy and can be used for the pump selection and design optimization.

(3) The velocity and concentration distribution of solids is non-uniform inside the impeller and casing of the pump. Zones of higher solid concentration are near the pressure side of the blade, impeller back shroud and casing backside. Operating the pump with smaller particle size and higher concentration may lead to homogenous particulate flow.

(4) The erosion of the materials showed dependence on target material properties, erodent properties, and impact conditions. The erosion resistance of high chromium white cast iron is better as compared to the steel 304L and grey cast iron. The erosion resistance of the materials is high for fly ash-water slurry as compared to the iron ore-water and sand-water slurry.

(5) The erosion rate of materials varies with the change in particle impact velocity and size according to a power law relationship with exponent as a function of target material properties and erosion mechanisms.

(6) CFD based correlations for predicting erosion rate at moderate velocities have been developed using a pot tester for steel 304L, grey cast iron and high chromium white cast iron for three different particulate slurries of sand, iron ore and fly ash.

(7) The experimentally determined localized erosion profile at the centerline of the pump casing is correlated with the numerically predicted particle flow field at different

operating conditions. The dominant parameters affecting the erosion profile of the casing at different operating conditions have been identified.

(8) Three-dimensional numerical modeling of the pump using discrete phase model with sliding mesh approach and the empirical correlations developed through the pot tester studies have been used to analyse the material loss distribution due to erosion of the pump components and its variation with the change in operating conditions. Thus, this methodology can be employed to predict the service life and design optimization of the pump components.

7.2 Scope for Future Work

The hydraulic performance and wear characteristics of centrifugal slurry pump depends on many factors and understanding the nature of impact of these parameters will improve the service life of the components and will help to reduce the running cost of slurry transportation. Based on the present work, the following studies can be undertaken in future to further improve the performance and erosion prediction of slurry transportation systems:

(1) The erosion modeling at higher solid concentration (>60% by weight) can be performed. It may help to predict the wear of the pump components for dense slurry flow applications.

(2) The effect of wear on the pump performance during continuous operation can be analysed by taking measurements at regular intervals. It may help to improve the operational stability of the slurry transportation system.

(3) Better numerical modeling techniques need to be developed to predict the time dependent erosion of the pump components which may help the designer to correctly estimate the service life of the pump components.

(4) The effect of geometrical and design parameters such as pump size, number of impeller blades, impeller-tongue, and impeller-volute clearance on pump performance and wear characteristics may be investigated with different particulate slurries to optimize the pump design and its selection for various industrial applications.

(5) The effect of solids on the pumping unit performance, as a whole, operating with multiple pumps in series and parallel modes of combination may be another area for investigation to resolve the operational issues.

APPENDIX - I

USER-DEFINED FUNCTION FOR EROSION PREDICTION

In the present work, UDF is developed to incorporate the erosion model in the CFD code Fluent 17.2 for erosion prediction of pump components. Fluent 17.2 offers different macros or interfaces to access its internal data structure. The UDF manual of Fluent 6.3 describes some of the macros and internal data structures. This appendix presents the developed UDF for erosion prediction in this work. The UDF can be used in any 3D geometry. In this, different user-defined memories were assigned to store information, like particle impact velocity, particle impact frequency, impact angle, and erosion rate, for each grid cell. The information stored in user-defined memory can be accessed in post-processing.

```
#include "udf.h"
#include "math.h"
#define MIN_IMPACT_VELO -1000.
        /* Minimum particle velocity normal to wall (m/s) to allow Accretion.*/
Domain *domain; /* Get the domain pointer and assign it later to domain*/
enum            /* Enumeration of used User-Defined Memory Locations. */
{
        NUM_OF_HITS,    /* Number of particle hits into wall face considered.*/
        AVG_DIAMETER,    /* Average diameter of particles that hit the wall. */
        AVG_VELO,
        ERSN_DEF,
        ERSN_CUT,
        NUM_OF_USED_UDM
};
int UDM_checked = 0;     /* Availability of UDMLs checked? */
void reset_UDM_s(void);  /* Function to follow below. */
int check_for_UDM(void)      /* Check for UDMLs' availability... */
{
        Thread *t;

        if (UDM_checked)
                return UDM_checked;
        thread_loop_c(t, domain)    /* We require all cell threads to.. */
        {                       /* provide space in memory for UDML */
                if(FLUID_THREAD_P(t))
                        if(NULLP(THREAD_STORAGE(t,SV_UDM_I)))
                                return 0;
        }
```

```
        UDM_checked = 1;     /* To make the following work properly... */
        reset_UDM_s();       /* This line will only be executed once, */
        return UDM_checked;  /* because check_for_UDM checks... */
}               /* ...for UDM_checked first. */
void reset_UDM_s(void)
{
        Thread *t;
        cell_t  c;
        face_t  f;
        int     i;

        if (!check_for_UDM())  /* Don't do it, if memory is not available. */
                return;
        Message("Resetting User Defined Memory...\n");
        thread_loop_f(t, domain)
        {
                if (NNULLP(THREAD_STORAGE(t,SV_UDM_I)))
                {
                        begin_f_loop(f, t)
                        {
                                for (i = 0; i < NUM_OF_USED_UDM; i++)
                                F_UDMI(f, t, i) = 0.;
                        }
                        end_f_loop(f, t)
                }
                else
                {
                        Message("  Skipping FACE thread no. %d..\n", THREAD_ID(t));
                }
        }
        thread_loop_c(t, domain)
        {
                if (NNULLP(THREAD_STORAGE(t,SV_UDM_I)))
                {
                        begin_c_loop(c, t)
                        {
                                for (i = 0; i < NUM_OF_USED_UDM; i++)
                                C_UDMI(c, t, i) = 0.;
                        }
                        end_c_loop(c, t)
                }
                else
                {
                        Message(" Skipping CELL thread no. %d..\n", THREAD_ID(t));
```

```
            }
        }           /* Skipping Cell Threads can happen if the user */
                    /* uses reset_UDM prior to initializing. */

        Message(" --- Done.\n");
}
DEFINE_DPM_SCALAR_UPDATE(dpm_scalup, c, t, if_init, p)
{
        if (if_init)
                P_USER_REAL(p, 0) = 0;    /* Simple initialization. Used later for
                                          * stopping trajectory calculation */
}
DEFINE_DPM_EROSION(erosn, p, t, f, normal, alpha, Vmag, Mdot)
/* p, t, f, normal, alpha, Vmag, Mdot are variables that are passed by the Fluent solver to the
UDF*/
{
        real A[ND_ND], area;
        real erdef90, erdef, ercut, ertot;
        real falpha, alphamax;
        real cutersn, defersn;
        int num_in_data;
        int i;
        Thread *t0;
        cell_t  c0;
        real thv, phv, shf;
        real cw, kpth;
        real part_dia;
        real imp_vel[3];
        NV_V( imp_vel, =, P_VEL(p));
        if (!UDM_checked)       /* We will need some UDM's, */
                if (!check_for_UDM()) /* so check for their availability.. */
                        check_for_UDM();            /* (Using int variable for speed, could */
                 /*  even just call check_for UDFM().) */
        c0 = F_C0(f,t);
        t0 = THREAD_T0(t);
        if( F_STORAGE_R(f,t,SV_DPMS_EROSION) == 0 )
        {
                F_UDMI(f, t, ERSN_DEF) = 0;
                F_UDMI(f, t, ERSN_CUT) = 0;
                F_UDMI(f, t, NUM_OF_HITS) = 0;
        }
        num_in_data = F_UDMI(f, t, NUM_OF_HITS);
        cutersn = F_UDMI(f,t, ERSN_CUT);
        defersn = F_UDMI(f,t, ERSN_DEF);
```

```
        /* Add particle to statistics: Calculate...: current_particle_property + earlier_particles_averaged_property * number_of_earlier_particles
        ------------------------------------------------------------------
          number_of_earlier_particles + 1                    */
        /* Average diameter of particles that hit the particular wall face:*/
        F_UDMI(f, t, AVG_DIAMETER) = (P_DIAM(p) +  num_in_data * F_UDMI(f, t, AVG_DIAMETER)) / (num_in_data + 1);
        C_UDMI(c0,t0,AVG_DIAMETER) = F_UDMI(f, t, AVG_DIAMETER);

        /* Average velocity normal to wall of particles hitting the wall:*/
        F_UDMI(f, t, AVG_VELO) = (Vmag +  num_in_data * F_UDMI(f, t, AVG_VELO)) / (num_in_data + 1);
        C_UDMI(c0,t0,AVG_VELO) = F_UDMI(f, t, AVG_VELO);
        F_UDMI(f, t, NUM_OF_HITS) = num_in_data + 1;
        C_UDMI(c0,t0,NUM_OF_HITS) = num_in_data + 1;
        F_AREA(A, f, t);
        area = NV_MAG(A);
        part_dia = P_DIAM(p);

        falpha = 0;
        thv = 210;
        phv = 1100;
        shf = 0.7007;
        cw = 0.0297;
        alphamax = 30 * M_PI / 180;

        if( alpha >= 0 && alpha <= alphamax )
        {
                falpha = pow( 0.99 * sin( M_PI / 2 * alpha / alphamax ), 0.92 );
        }
        if( alpha <= ( M_PI / 2 ) && alpha > alphamax )
        {
                falpha = pow( 0.68 * sin( M_PI / 2 * ( 1 - ( alpha - alphamax ) / ( M_PI / 2 - alphamax ) ) ), 1.89 );
        }

        erdef90 = 2.36 * pow( 10, -13 ) * pow( Vmag, 2.8 ) * pow( part_dia * 1000000, 0.98 ) ;
        erdef = erdef90 * sin( alpha ) * sin( alpha ) ;

        F_UDMI(f,t, ERSN_DEF) = defersn + erdef;
        C_UDMI(c0,t0,ERSN_DEF) = F_UDMI(f, t, ERSN_DEF);

ercut = 1.51 * pow( 10, -11 ) * falpha * pow( Vmag, 2.15 ) * pow( part_dia * 1000000, 0.71 );
```

```
        F_UDMI(f,t, ERSN_CUT) = cutersn + ercut;
        C_UDMI(c0,t0,ERSN_CUT) = F_UDMI(f, t, ERSN_CUT);
        ertot = erdef + ercut;
        F_STORAGE_R(f,t,SV_DPMS_EROSION) += ertot;
        // Message(" falpha  is %lf..\n", falpha);
        // Message(" erosion rate   is %lf..\n", F_STORAGE_R(f,t,SV_DPMS_EROSION));
}

DEFINE_ON_DEMAND(reset_UDM)
{
        /* assign domain pointer with global domain */
        domain = Get_Domain(1);
        reset_UDM_s();
}
```

REFERENCES

[1] Abd-Elrhman, Y.M., Abouel-Kasem, A., Emara, K.M., and Ahmed, S.M., (2014), "Effect of impact angle on slurry erosion behavior and mechanisms of carburized AISI 5117 steel", Journal of Tribology, 136, p. 011106.

[2] Abouel-Kasem, A., (2011), "Particle size effects on slurry erosion of 5117 steels", Journal of Tribology, 133, p. 014502.

[3] Abulnaga, B.E., (2002), "Slurry systems handbook", The McGraw-Hill Companies, New York.

[4] Addie, G.R., Grovetown, G., and Roco, M.C., (1987), "Experiences with a numerical method of calculating slurry pump casing wear", In 4th International Pump Symposium and Short Courses, pp. 27-34.

[5] Ahlert, K., (1994), "Effect of particle impingement angle and surface wetting on solid particle erosion of AISI 1018 steel", M.Sc. thesis, Department of Mechanical Engineering, The University of Tulsa, Oklahoma, United States.

[6] Ahmad, K., Baker, R.C., and Goulas, A., (1986), "Computation and experimental results of wear in a slurry pump impeller", Proceedings of the Institution of Mechanical Engineers, Part C: Journal of Mechanical Engineering Science, 200(6), pp. 439-445.

[7] Al-Bukhaiti, M.A., Abouel-Kasem, A., Emara, K.M., and Ahmed, S.M., (2016), "Particle shape and size effects on slurry erosion of AISI 5117 steels", Journal of Tribology, 138, p. 024503.

[8] Al-Bukhaiti, M.A., Abouel-Kasem, A., Emara, K.M., and Ahmed, S.M., (2017), "A study on slurry erosion behavior of high chromium white cast iron", Journal of Tribology, 139, p. 041102.

[9] Aminul Islam, M., and Farhat, Z.N., (2014), "Effect of impact angle and velocity on erosion of API X42 pipeline steel under high abrasive feed rate", Wear, 311, pp. 180-190.

[10] Barrio, R., Fernandez, J., Blanco, E., and Parrondo, J., (2011), "Estimation of radial load in centrifugal pumps using computational fluid dynamics", European Journal of Mechanics B/Fluids, 30, pp. 316-324.

[11] Barker, M.L., and Truscott, G.F. (1974), "The development and operation of a test facility for pipeline abrasive wear measurement", Hydrotransport 3, BHRA Fluid Engineering, 1500 Illinois Street Golden (United States), Paper J3.

[12] Batalovic, V., (2010), "Erosive wear model of slurry pump impeller", Journal of Tribology, 132(2), p. 021602.

[13] Baz, A., (1984), "Performance of irrigation pumps in muddy waters", Proceedings of International Conference on Multi-Phase Flow and Heat Transfer III, Part B: Application, Elsevier Science Publishers Ltd., Amsterdam, pp. 527-540.

[14] Benretem, A., Haddouche, A., Cheghib, H., and Saad, S., (2007), "Influence of solid particles on centrifugal pump characteristics", Journal of Engineering Applied Science, 2(1), pp. 244-247.

[15] Biswas, A., Gandhi, B.K., Singh, S.N., and Seshadri, V., (2000), "Characteristics of coal ash and their role in hydraulic design of ash disposal pipelines", Indian Journal of Engineering and Material Science, 7, pp. 1-7.
[16] Bitter, J.G.A., (1963a), "A study of erosion phenomena Part I", Wear, 6, pp. 5-21.
[17] Bitter, J.G.A., (1963b), "A study of erosion phenomena Part II", Wear, 6, pp. 169-190.
[18] Bree, S.E.M. de., Rosenbrand, W.F., and Gee, A.W.J. de., (1982), "On the erosion resistance in water-sand mixtures of steels for application in slurry pipelines", Hydrotransport 8, BHRA Fluid Engineering, Johannesburg (South Africa), Paper C3.
[19] Brown, R., Jun, E.J., and Edington, J.W., (1981), "Erosion of α-Fe by spherical glass particles", Wear, 70(3), pp. 347-363.
[20] Burgess, K.E., and Reizes, J.A., (1976), "The effect of sizing, specific gravity and concentration on the performance of centrifugal slurry pumps", Proceedings of the Institution of Mechanical Engineers, 190(1), pp. 391-399.
[21] Burstein, G.T., and Sasaki, K., (2000), "Effect of impact angle on the slurry erosion–corrosion of 304L stainless steel", Wear, 240, pp. 80-94.
[22] Cave, J., (1976), "Effect of suspended solids on the performance of centrifugal pumps", Hydrotransport 4, BHRA Fluid Engineering, Alberta (Canada), Paper H3.
[23] Chand, P., Adinarayana, B., and Singh, R.P., (1985), ''Effect of drag reducing polymers on slurry pump characteristics'', Bulk Solids Handling, 5(4), pp. 807-811.
[24] Chandel, S., Singh, S.N., and Seshadri, V., (2011), "A comparative study on the performance characteristics of centrifugal and progressive cavity slurry pumps with high concentration fly ash slurries", Particulate Science and Technology, 29(4), pp. 378-396.
[25] Cheah, K.W., Lee, T.S., Winoto, S.H., and Zhao, Z.M., (2007), "Numerical flow simulation in a centrifugal pump at design and off-design Conditions", International Journal of Rotating Machinery, 2007, pp. 1-8.
[26] Chen, L., Duan, Y., Pu, W., and Zhao, C., (2009), "CFD simulation of coal-water slurry flowing in horizontal pipelines", Korean Journal of Chemical Engineering, 26(4), pp. 1144-1154.
[27] Chen, X., McLaury, B.S., and Shirazi, S.A., (2004), "Application and experimental validation of a computational fluid dynamics (CFD)-based erosion prediction model in elbows and plugged tees", Computers & Fluids, 33, pp. 1251-1272.
[28] Cheng, H.P., and Song, P.Y., (2013), "A simple correlation equation to predict pump performance for slurry", Applied Mechanics and Materials, 365, pp. 365-369.
[29] Clark, H.M., (1991), "On the impact rate and impact energy of particles in a slurry pot erosion tester", Wear, 147, pp. 165-183.
[30] Clark, H.M., and Hartwich, R.B., (2001), "A re-examination of the particle size effect in slurry erosion", Wear, 248, pp. 147-161.
[31] Cox, E.P., (1927), "A method of assigning numerical and percentage values to the degree of roundness of sand grains", Journal of Paleontol, 1(3), pp. 179-183.
[32] Dalla Valle, J.M., (1948), "Micromeritics", Pitman, London.
[33] Davidson, G., (1987), "Considerations for proper sizing and material selection to optimize slurry pump performance", Proceedings of the Fourth International Pump Symposium, Texas A&M University, Houston, Texas, U.S.A., pp. 35-54.

[34] Deng, T., Chaudhry, A.R., Patel, M., Hutchings, I., and Bradley, M.S.A., (2005), "Effect of particle concentration on erosion rate of mild steel bends in a pneumatic conveyor", Wear, 258(1-4), pp. 480-487.
[35] Desale, G.R., Gandhi, B.K., and Jain, S.C., (2005), "Improvement in the design of a pot tester to simulate erosion wear due to solid-liquid mixture", Wear, 259(1-6), pp. 196-202.
[36] Desale, G.R., (2006), "Study on slurry erosion behaviour of ductile type materials and laser cladded surfaces", Ph.D. thesis, Indian Institute of Technology, Roorkee, India.
[37] Desale, G.R., Gandhi, B.K., and Jain, S.C., (2006), "Effect of erodent properties on erosion wear of ductile type materials", Wear, 261(7-8), pp. 914-921.
[38] Desale, G.R., Gandhi, B.K., and Jain, S.C., (2008), "Slurry erosion of ductile materials under normal impact condition", Wear, 264, pp. 322-330.
[39] Desale, G.R., Gandhi, B.K., and Jain, S.C., (2009), "Particle size effects on the slurry erosion of aluminium alloy (AA 6063)", Wear, 266, pp. 1066-1071.
[40] Desale, G.R., Gandhi, B.K., and Jain, S.C., (2011), "Development of correlations for predicting the slurry erosion of ductile materials", Journal of Tribology, 133, p. 031603.
[41] Ding, J., and Gidaspow, D., (1990), "A bubbling fluidization model using kinetic theory of granular flow", The American Institute of Chemical Engineers, 36(4), pp. 523-538.
[42] Divakar, M., Agarwal, V.K., and Singh, S.N., (2005), "Effect of the material surface hardness on the erosion of AISI 316", Wear, 259, pp. 110-117.
[43] Dong, J., Qian, Z., Thapa, B.S., Thapa, B., and Guo, Z., (2019), "Alternative design of double-suction centrifugal pump to reduce the effects of silt erosion", Energies, 12, p. 158.
[44] Dong, X., Zhang, H.L., and Wang, X.Y., (2009), "Finite element analysis of wear for centrifugal slurry pump", Procedia Earth and Planetary Science, 1(1), pp. 1532-1538.
[45] Duarte, C.A.R., Souza, F.J.de., and Santos, V.F.dos., (2015), "Numerical investigation of mass loading effects on elbow erosion", Powder Technology, 283, pp. 593-606.
[46] Elkholy, A., (1983), "Prediction of abrasion wear for slurry pump materials", Wear, 84, pp. 39-49.
[47] Engin, T., and Gur, M., (2001), "Performance characteristics of a centrifugal pump impeller with running tip clearance pumping solid-liquid mixtures", Journal of Fluids Engineering, 123(3), pp. 532-538.
[48] Engin, T., and Gur, M., (2003), "Comparative evaluation of some existing correlations to predict head degradation of centrifugal slurry pumps", Journal of Fluids Engineering, 125(1), pp. 149-157.
[49] Fact Sheet, May (2014), "Sludge pump selection and cost information", Fact Sheet Series, Australian Pork. https://australianpork.com.au
[50] Fairbank, L.C., (1942), ''Effect on the characteristics of centrifugal pumps'', Symposium Solids in Suspension, 107, Paper No. 2167, pp. 1563-1586.
[51] Feng, Z., and Ball, A., (1999), "The erosion of four materials using seven erodents-towards an understanding", Wear, 233-235, pp. 674-684.
[52] Finnie, I., (1960), "Erosion of surfaces by solid particles", Wear, 3, pp. 87-103.
[53] Finnie, I., (1972), "Some observation on the erosion of ductile materials", Wear, 19, pp. 81-90.

[54] Finnie, I., and Mcfadden, D.H., (1978), "On the velocity dependence of the erosion of ductile metals by solid particles at low angles of incidence", Wear, 48, pp. 181-190.
[55] Fluent 6.3, (2006), "User's guide", Fluent Incorporation, USA.
[56] Forder, A., Thew, M., and Harrison, D., (1998), "A numerical investigation of solid particle erosion experienced within oilfield control valves", Wear, 216, pp. 184-193.
[57] Furlan, J.M., Garman, M., Kadambi, J., Visintainer, R.J., and Pagalthivarthi, K.V., (2015), "Ultrasonic measurements of local particle velocity and concentration within the casing of a centrifugal pump", Proceedings of the Joint Fluids Engineering Conference AJKFluids, Seoul, Korea.
[58] Gahlot, V.K., Seshadri, V., and Malhotra, R.C., (1992), ''Effect of density, size distribution and concentration of solid on the characteristics of centrifugal pumps'', Journal of Fluids Engineering, 114(3), pp. 386-389.
[59] Gandhi, B.K., (1998), "Studies on performance and wear characteristics of centrifugal slurry pumps handling multi-sized concentrated particulate slurries", Ph.D. thesis, Indian Institute of Technology, Delhi, India.
[60] Gandhi, B.K., Singh, S.N., and Seshadri, V., (1999a), ''Head and efficiency ratio characteristics of a centrifugal slurry pump'', Proceedings of 26th National Conference of Fluid Mechanics and Fluid Power, Indian Institute of Technology, Kharagpur, India, pp. 630-635.
[61] Gandhi, B.K., Singh, S.N., and Seshadri, V., (1999b), "Study of the parametric dependence of erosion wear for the parallel flow of solid-liquid mixtures", Tribology International, 32, pp. 275-282.
[62] Gandhi, B.K., Singh, S.N., and Seshadri, V., (2000), "Improvement in the prediction of performance of centrifugal slurry pump handling slurries", Proceeding of Indian Journal of Mechanical Engineers, 214(A), pp. 473-486.
[63] Gandhi, B.K., Singh, S.N., and Seshadri, V., (2001a), "Performance characteristics of centrifugal slurry pumps", Journal of Fluids Engineering, 123(2), pp. 271-280.
[64] Gandhi, B.K., Singh, S.N., and Seshadri, V., (2001b), "Variation of wear along the volute casing of a centrifugal slurry pump", Japan Society of Mechanical Engineers International Journal Series B Fluids and Thermal Engineering, 44(2), pp. 231-237.
[65] Gandhi, B.K., Singh, S.N., and Seshadri, V., (2002), "Effect of speed on the performance characteristics of a centrifugal slurry pump", Journal of Hydraulic Engineering, 128(2), pp. 225-233.
[66] Gandhi, B.K., Singh, S.N., and Seshadri, V., (2003), "A study on the effect of surface orientation on erosion wear of flat specimens moving in a solid-liquid suspension", Wear, 254(12), pp. 1233-1238.
[67] Gandhi, B.K., and Borse, S.V., (2004), "Nominal particle size of multi-sized particulate slurries for evaluation of erosion wear and effect of fine particles", Wear, 257, pp. 73-79.
[68] Gandhi, B.K., (2015), "An accelerated erosion wear test rig for high impact velocities", International Conference on Hydropower for Sustainable Development, Dehradun, India, pp. 528-534.

[69] Garside, J., and Al-Dibouni, M.R., (1977), "Velocity-voidage relationships for fluidization and sedimentation", Industrial & Engineering Chemistry Process Design and Development, 16, pp. 206-214.
[70] Gidaspow, D., Bezburuah, R., and Ding, J., (1992), "Hydrodynamics of circulating fluidized beds, kinetic theory approach", In Fluidization VII, Proceedings of the 7th Engineering Foundation Conference on Fluidization, pp. 75-82.
[71] Gopaliya, M.K., and Kaushal, D.R., (2015), "Analysis of effect of grain size on various parameters of slurry flow through pipeline using CFD", Particulate Science and Technology, 33(4), pp. 369-384.
[72] Gonzalez, J., Fernandez, J., Blanco, E., and Santolaria, C., (2002), "Numerical simulation of the dynamic effects due to impeller-volute interaction in a centrifugal pump", Journal of Fluids Engineering, 124, pp. 348-355.
[73] Gonzalez, J., and Santolaria, C., (2006), "Unsteady flow structure and global variables in a centrifugal pump", Journal of Fluids Engineering, 128, pp. 937-946.
[74] Gupta, R., Singh, S.N., and Seshadri, V., (1995), "Prediction of uneven wear in a slurry pipeline on the basis of measurements in a pot tester", Wear, 184, pp.169-178.
[75] Harsha, A.P., and Thakre, A.A., (2007), "Investigation on solid particle erosion behaviour of polyetherimide and its composites", Wear, 262(7-8), pp. 807-818.
[76] Hasegawa, Yagi, and Tokunaga, July (1957), "Performance test of sand pump", Transportation Technical Research Institute, Monthly report 7 (6).
[77] Haugen, K., Kvernvold, O., Ronald, A., and Sandberg, R., (1995), "Sand erosion of wear-resistant materials: erosion in choke valves", Wear, 186-187 (Part I), pp. 179-188.
[78] Herbitch, and Vallentine, September (1961), "Characteristics of a model dredge pump", Leigh University Report Number 33 for U.S. Army Engineers.
[79] Huang, P., Bardina, J., and Coakley, T., April (1997), "Turbulence modeling validation, testing, and development", Technical Report, NASA, Ames Research Center, California, United States.
[80] Huang, C., Chiovelli, S., Minev, P., Luo, J., and Nandakumar, K., (2008), "A comprehensive phenomenological model for erosion of materials in jet flow", Powder Technology, 187, pp. 273-279.
[81] Hunt, W.A., and Faddick, R.R., (1971), "The effect of solids on centrifugal pump characteristics", In Advances in Solid-Liquid Flow in Pipes and its Application, Pergmon Press, New York, Paper No. 20, pp. 271-278.
[82] Hussainova, I., Kubarsepp, J., and Pirso, J., (2001), "Mechanical properties and features of erosion of cermets", Wear, 250(1-12), pp. 818-825.
[83] IEC 60041, (1991), "Field acceptance tests to determine the hydraulic performance of hydraulic turbines, storage pumps and pump-turbines", 3rd edition.
[84] Indian Bureau of Mines, July (2001), "Slurry transportation in Indian mines", Bulletin no. 40, Govt. of India, Ministry of Mines, Nagpur, India.
[85] Iwai, Y., and Nambu, K., (1997), "Slurry wear properties of pump lining materials", Wear, 210, pp. 211-219.
[86] Jacobs, B.E.A., (2005), "Design of slurry transport systems", Elsevier Applied Science, London and New York.

[87] Javaheria, V., Portera, D., and Kuokkala, V.T., (2018), "Slurry erosion of steel–review of tests, mechanisms and materials", Wear, 408-409, pp. 248-273.

[88] Jiang, W., Li, G., Liu, P.f., and Fu, L., (2016), "Numerical investigation of influence of the clocking effect on the unsteady pressure fluctuations and radial forces in the centrifugal pump with vaned diffuser", International Communications in Heat and Mass Transfer, 71, pp. 164-171.

[89] Kang, M.W., Park, N., and Suh, S.H., (2016), "Numerical study on sediment erosion of Francis turbine with different operating conditions and sediment inflow rates", Procedia Engineering, 157, pp. 457-464.

[90] Kazim, K.A., Maiti, B., and Chand, P., (1997), "A correlation to predict the performance characteristics of centrifugal pumps handling slurries", Proceedings of the Institution of Mechanical Engineers, Part A: Journal of Power and Energy, 211(2), pp. 147-157.

[91] Khalil, M.F., Kassab, S.Z., Naby, A.A.A., and Azouz, A., (2013), "Performance characteristics of centrifugal pump conveying soft slurry", American Journal of Mechanical Engineering, 1(5), pp. 103-112.

[92] Khanal, K., Neopane, H.P., Rai, S., Thapa, M., Bhatt, S., and Shrestha, R., (2016), "A methodology for designing Francis runner blade to find minimum sediment erosion using CFD", Renewable Energy, 87, pp. 307-316.

[93] Koirala, R., Thapa, B., Neopane, H.P., and Zhu, B., (2017), "A review on flow and sediment erosion in guide vanes of Francis turbines", Renewable and Sustainable Energy Reviews, 75, pp. 1054-1065.

[94] Krishnan, R.N., Vivek, S., Chatterjee, D., and Das, S.K., (2010), "Performance of numerical schemes in the simulation of two-phase free flows and wall bounded mini channel flows", Chemical Engineering Science, 65, pp. 5117-5136.

[95] Kruger, S., Martin, N., and Dupont, P., (2010), "Assessment of wear erosion in pump impellers", Proceedings of the Twenty-Sixth International Pump users Symposium, pp. 51-56.

[96] Kumar, U., Mishra, R., Singh, S.N., and Seshadri, V., (2003), "Effect of particle gradation on flow characteristics of ash disposal pipelines", Powder Technology, 132 (1), pp. 39-51.

[97] Kumar, S., Gandhi, B.K., and Mohapatra, S.K., (2014), "Performance characteristics of centrifugal slurry pump with multi-sized particulate bottom and fly ash mixtures", Particulate Science and Technology, 32(5), pp. 466-476.

[98] Lakshminarayana, B., (1991), "An assessment of computational fluid dynamic techniques in the analysis and design of turbomachinery - the 1990 freeman scholar lecture'', Journal of Fluids Engineering, 113, pp. 315–352.

[99] Launder, B.E., and Spalding, D.B., (1972), "Lectures in mathematical models of turbulence", Academic Press, London, England.

[100] Levy, A.V., and Chik, P., (1983), "The effects of erodent composition and shape on the erosion of steel", Wear, 89, pp. 151-162.

[101] Levy, A.V., and Yau, P., (1984), "Erosion of steels in liquid slurries", Wear, 98, pp. 163-182.

[102] Levy, A.V., (1986), "The platelet mechanism of erosion of ductile metals", Wear, 108, pp. 1-21.
[103] Li, Y., Zhu, Z., He, W., and He, Z., (2012), "Numerical simulation and experimental research on the influence of solid-phase characteristics on centrifugal pump performance", Chinese Journal of Mechanical Engineering, 25(6), pp. 1184-1189.
[104] Lin, F.Y., and Shao, H.S., (1991a), "Effect of impact velocity on slurry erosion and a new design of a slurry erosion tester", Wear, 143, pp. 231-240.
[105] Lin, F., and Shao, H., (1991b), "The effect of impingement angle on slurry erosion", Wear, 141, pp. 279-289.
[106] Lin, N., Arabnejad, H., Shirazi, S.A., McLaury, B.S., and Lan, H., (2018), "Experimental study of particle size, shape and particle flow rate on erosion of stainless steel", Powder Technology, 336(1), pp. 70-79.
[107] Lindgren, M., and Perolainen, J., (2014), "Slurry pot investigation of the influence of erodent characteristics on the erosion resistance of titanium", Wear, 321, pp. 64-69.
[108] Lindsley, B.A., and Marder, A.R., (1999), "The effect of velocity on the solid particle erosion rate of alloys", Wear, 225-229, pp. 510-516.
[109] Liu, J., Xu, Y., Wang, D., and Su, Q., (2009), "Analysis of liquid-solid two-phase turbulent flow in FGD system pump", In Computer-Aided Industrial Design & Conceptual Design, IEEE 10th International Conference, pp. 615-619.
[110] Lopez, D., Congote, J.P., Cano, J.R., Toro, A., and Tschiptschin, A.P., (2005), "Effect of particle velocity and impact angle on the corrosion–erosion of AISI 304 and AISI 420 stainless steels", Wear, 259, pp. 118-124.
[111] Lum, M., (2013), "Erosive wear mechanisms of rubber pump lining materials in minerals processing applications", Ph.D. thesis, The University of New South Wales, Sydney, Australia.
[112] Lun, C.K.K., Savage, S.B., Jefferey, D.J., and Chepurniy, N., (1984), "Kinetic theories for granular flow: inelastic particles in Couette flow and slightly inelastic particles in a general flow field", Journal of Fluid Mechanics, 140, pp. 223-256.
[113] Lynn, R.S., Wong, K.K., and Clark, H.M., (1991), "On the particle size effect in slurry erosion", Wear, 149, pp. 55-71.
[114] McDonald, L.G., and Kelley, J.E., (1994), "Erosive wear of potential valve materials for coal-conversion plants", U.S. Department of the Interior, Bureau of Mines, Report of Investigations No. 9490.
[115] Mano, (1955), "Conveyance of carbide slurry", Journal of Japan Society of Mechanical Engineers, 62(485), pp. 927-933.
[116] Maz, W., (1984), "The influence of solids concentration, solids density and grain size distribution on the working behavior of centrifugal pumps'', Hydrotransport 9, BHRA Fluid Engineering, Rome, Paper H1.
[117] Mens, I.W.M., and Gee, A.W.J. de, (1986), "Erosion in seawater sand slurries", Tribology International, 19, pp. 59-64.
[118] Messa, G.V., and Malavasi, S., (2017), "The effect of submodels and parameterizations in the simulation of abrasive jet impingement tests", Wear, 370-371, pp. 59-72.

[119] Minemura, K., and Zhong, Y., (1995), "Numerical prediction of erosion wear on pump casing under solid-water two phase flow", Proceedings of 2nd International Conference on Multiphase Flow, 95, pp. 1A3-7.
[120] Mishra. R., (1996), "A study on the flow of multisized particulate solid-liquid mixtures in horizontal pipelines", Ph.D. thesis, Indian Institute of Technology, Delhi, India.
[121] Mishra, R., Singh, S.N., and Seshadri, V., (1998), "Study of wear characteristics and solid distribution in constant area and erosion-resistant long-radius pipe bends for the flow of multisized particulate slurries", Wear, 217, pp. 297-306.
[122] Misra, A., and Finnie, I., (1981), "On the size effect in abrasive and erosive wear", Wear, 65, pp. 359-373.
[123] Morsi, S., and Alexander, A., (1972), "An investigation of particle trajectories in two-phase flow systems", Journal of Fluid Mechanics, 55, pp. 193-208.
[124] Mrinal, K.R., Siddique, M.H., and Samad, A., (2016), "Performance prediction of a centrifugal pump delivering non-Newtonian slurry", Particulate Science and Technology, pp. 1-8. DOI: 10.1080/02726351.2016.1205690
[125] Mueller, J.J., Wright, I.G., and Davis, D.E., (1978), "Erosion evaluation of materials for service in liquifaction coal slurry feed pumps", Proceedings of 3rd International Technical Conference on Slurry Transport, Las-Vegas, pp. 107-116.
[126] Nandre, B.D., and Desale, G.R., (2018), "The effects of constant kinetic energy of different impacting particles on slurry erosion wear of AA 6063", Journal of Tribology, 140, p. 031605.
[127] Neilson, J.H., and Gilchrist, A., (1968), "Erosion by a stream of solid particles", Wear, 11(2), pp. 111-122.
[128] Nguyen, Q.B., Nguyen, V.B., Lim, C.Y.H, Trinh, Q.T., Sankaranarayanan, S., Zhang, Y.W., and Gupta, M., (2014), "Effect of impact angle and testing time on erosion of stainless steel at higher velocities", Wear, 321, pp. 87-93.
[129] Nguyen, V.B., Nguyen, Q.B., Zhang, Y.W., Lim, C.Y.H., and Khoo, B.C., (2016), "Effect of particle size on erosion characteristics", Wear, 348-349, pp. 126-137.
[130] Ni, F., Vlasblom, W.J., and Zwartbol, A., (1999), ''Effect of high solid concentration on characteristics of a slurry pump'', Hydrotransport 14, BHRA Fluid Engineering, Maastricht, The Neatherland, pp. 141-149.
[131] Noon, A.A., and Kim, M.H., (2016), "Erosion wear on centrifugal pump casing due to slurry flow", Wear, 364-365, pp. 103-111.
[132] Oka, Y.I., Okamura, K., and Yoshida, T., (2005), "Practical estimation of erosion damage caused by solid particle impact part I: effects of impact parameters on a predictive equation", Wear, 259, pp. 95-101.
[133] Oka, Y.I., and Yoshida, T., (2005), "Practical estimation of erosion damage caused by solid particle impact, part II: mechanical properties of materials directly associated with erosion damage", Wear, 259(1-6), pp. 102-109.
[134] Okita, R., Zhang, Y., McLaury, B.S., and Shirazi, S.A., (2012), "Experimental and computational investigations to evaluate the effects of fluid viscosity and particle size on erosion damage", Journal of Fluids Engineering, 134, p. 061301.
[135] Padhy, M.K., and Saini, R.P., (2011), "Study of silt erosion on performance of a Pelton turbine", Energy, 36, pp. 141-147.

[136] Padhy, M.K., and Saini, R.P., (2012), "Study of silt erosion mechanism in Pelton turbine buckets", Energy, 39, pp. 286-293.

[137] Pagalthivarthi, K.V., and Hemly, F.W., (1992), "Applications of materials wear testing to solids transport via centrifugal slurry pumps", Wear Testing of Advanced Materials, ASTM STP 1167, American Society for Testing and Materials, Philadelphia, pp. 114-126.

[138] Pagalthivarthi, K.V., Furlan, J.M., and Visintainer, R.J., (2013), "Effect of particle size distribution on erosion wear in centrifugal pump casings", American Society of Mechanical Engineers, Fluids Engineering Division Summer Meeting, p. V01CT20A005.

[139] Parsi, M., Najmi, K., Najafifard, F., Hassani, S., McLaury, B.S., and Shirazi, S.A., (2014), "A comprehensive review of solid particle erosion modeling for oil and gas wells and pipelines applications", Journal of Natural Gas Science and Engineering, 21, pp. 850-873.

[140] Pei, J., Lui, A., Zhang, Q., Xiong, T., Jiang, P., and Wei, W., (2018), "Numerical investigation of the maximum erosion zone in elbows for liquid-particle flow", Powder Technology, 333, pp. 47-59.

[141] Peng, G.J., Luo, Y.Y., and Wang, Z.W., (2015), "Research on wear properties of centrifugal dredge pump based on liquid-solid two-phase fluid simulations", IOP Conference Series: Material Science and Engineering, 72, p. 042048.

[142] Rai, A.K., Kumar, A., and Staubli, T., (2017), "Hydro-abrasive erosion in Pelton buckets: Classification and field study", Wear, 392-393, pp. 8-20.

[143] Rawat, A., Singh, S.N., and Seshadri, V., (2017), "Erosion wear studies on high concentration fly ash slurries", Wear, 378-379, pp. 114-125.

[144] Rayan, M. A., and Shawky, M., (1989), "Evaluation of wear in a centrifugal slurry pump", Proceedings of the Institution of Mechanical Engineers, Part A: Journal of Power and Energy, 203(1), pp. 19-23.

[145] Read, E.N., (1982), "Experience gained with large dredge pumps in a sand mining operation", Hydrotransport 8, BHRA Fluid Engineering, Johannesburg (South Africa), Paper F1.

[146] Remisz, J., (1983), "Slurry pumps: transformation of characteristics and design", Proceedings of 8th Technical Conference of BPMA, Cambtidge(UK), Paper 2, pp. 13-22.

[147] Roco, M.C., Addie, G.R., Dennis, J., and Nair, P., (1984), "Modeling erosion wear in centrifugal slurry pumps", Hydrotransport 9, BHRA Fluid Engineering, Rome, Italy, Paper G1.

[148] Roco, M.C., Marsh, M., Addie, G.R., and Maffett, J.R., (1986), "Dredge pump performance prediction", Journal of Pipelines, 5, pp. 171-190.

[149] Roco, M.C., and Addie, G.R., (1987), "Erosion wear in slurry pumps and pipes", Powder Technology, 50(1), pp. 35-46.

[150] Roco, M.C., and Cader, T., (1988), "Numerical method to predict wear distribution in slurry pipelines", Advances in Pipeline Protection, BHRA, Cranfield, UK.

[151] Rohnisch, A. and Vollmer, E., (1970), "A method for the uniform evaluation of resistance to erosion of materials used for hydraulic structures", 1st International,

Conference, on the Hydraulic Transport of Solids in Pipes, Cranfield: British Hydromechanics Research Association, Australia, pp. 29-40.

[152] Roudnev, A.S., Bourgeois, R.J., and Kosmicki, R.J., (2009), "Slurry pump casing wear prediction using numerical multi-phase flow simulation", ASME Fluids Engineering Division Summer Meeting, pp. 515-523.

[153] Salik, J., Buckley, D., and Brainard, W.A., (1981), "The effect of mechanical surface and heat treatments on the erosion resistance of 6061 aluminum alloy", Wear, 65, pp. 351-358.

[154] Sasaki, Kato, Ueti, and Kajiwara, (1958), "Characteristics of pump pumping coal", Journal of Japanese Mining Industry Association, 74, p. 287.

[155] Salim, B., Bajawi, H.Y., and Suhaibani. Z., (2015), "Performance of a centrifugal slurry pump with clinker slurry", Indian Journal of Science and Technology, 8(12), pp. 1-9.

[156] Schaeffer, D.G., (1987), "Instability in the evolution equations describing incompressible granular flow", Journal of Differential Equations, 66(1), pp. 19-50.

[157] Sellgren, A., (1979), ''Performance of a centrifugal pump when pumping ores and industrial minerals'', Hydrotransport 6, BHRA Fluid Engineering, Canterbury, UK, Paper G1.

[158] Sellgren, A., and Vappling, L., (1986), "Effects of highly concentrated slurries on the performance of centrifugal pumps", International Symposium on Slurry Flows: Presented at the Winter Annual Meeting of the American Society of Mechanical Engineers, New York.

[159] Sellgren, A., and Addie, G., (1989), "Effect of solids on large centrifugal pumps head and efficiency", Paper CEDA Dredging Day, Central Dredging Association, Amsterdam, The Netherlands.

[160] Sellgren, A., Turner, T.M., and Addie, G.R., (1990), "Determination of the effect of solids on centrifugal slurry pumps", Fifth Annual AIME Regional Phosphate Conference, Lokeland, Florida.

[161] Sellgren, A., Addie, G., and Scott, S., (2000), "The effect of sand-clay slurries on the performance of centrifugal pumps", Canadian Journal of Chemical Engineering, 78 (4), pp. 764-769.

[162] Sellgren, A., Addie, G., Visintainer, R., and Pagalthivarthi, K., (2005), "Prediction of slurry pump component wear and cost", WEDA XXV-TAMU, 37.

[163] Senapati, P.K., (2009), "Studies on slurry transport characteristics of fly ash and fly ash-bottom ash mixtures at high concentrations", Ph.D. thesis, Utkal University, Bhubaneswar, India.

[164] Senapati, P.K., Panda, D., and Parida, A., (2009), "Predicting viscosity of limestone water slurry", International Journal of Minerals & Materials Characterization & Engineering, 8(3), pp. 203-221.

[165] Sharma, S., Tarodiya, R., and Gandhi, B.K., (2018), "Experimental investigation of flow field of a pot tester due to propeller rotation", 7th International conference of Fluid Mechanics and Fluid Power, IIT Bombay, p. 487.

[166] Shipway, P.H., and Hutchings, I.M., (1996), "The role of particle properties in the erosion of brittle materials", Wear, 193, pp. 105-113.

[167] Shukla, S.N., Khare, R., and Prasad, V., (2017), "Numerical prediction of NPSHR characteristics of double suction centrifugal pump", International Journal of Engineering and Technology, 9(2), pp. 1280-1287.

[168] Stack, M.M., Zhou, S., and Newman, R.C., (1996), "Effects of particle velocity and applied potential on erosion of mild steel in carbonate/bicarbonate slurry", Materials Science and Technology, 12, pp. 261-268.

[169] Stepanoff, A.J., (1965), "Pumps and blowers, two phase flow - flow and pumping of solids in suspension and fluid mixtures", John Wiley and Sons, London.

[170] Sundararajan, G., and Roy, M., (1997), "Solid particle erosion behaviour of metallic materials at room and elevated temperatures", Tribology International, 30, pp. 339-359.

[171] Syamlal, M., (1987), "The particle-particle drag term in a multi-particle model of fluidization", DOE/MC/21353-2373, NTIS/DE87006500, National Technical Information Service, Springfield,VA.

[172] Syamlal, M., Rogers, W., and O'Brien, T.J., (1993), "MFIX Documentation: Volume 1, Theory Guide", DOE/METC-9411004, NTIS/DE9400087, National Technical Information Service, Springfield, VA.

[173] Syamsundar, C., Chatterjee, D., Kamaraj, M., and Maiti, A.K., (2015), "Erosion characteristics of nanoparticle-reinforced polyurethane coatings on stainless steel substrate", Journal of Materials Engineering and Performance, 24, pp. 1391-1405.

[174] Tao, Y., Yuan, S., Liu, J., Zhang, F., and Tao, J., (2017), "The influence of the blade thickness on the pressure pulsations in a ceramic centrifugal slurry pump with annular volute", Proceedings of the Institution of Mechanical Engineers, Part A: Journal of Power and Energy, 231(5), pp. 415-431.

[175] Tarodiya, R., and Gandhi, B.K., (2016), "Effect of propeller off-bottom clearance and size on suspension of sand particles in a cylindrical tank: application to slurry pot tester", 6th International conference of Fluid Mechanics and Fluid Power, MNNIT Allahabad, p. 82.

[176] Tian, H.H., and Addie, G.R., (2005), "Experimental study on erosive wear of some metallic materials using Coriolis wear testing approach", Wear, 258, pp. 458-469.

[177] Truscott, G.F., (1972), "A literature survey on abrasive wear in hydraulic machinery", Wear, 20, pp. 29-50.

[178] Tsai, W., Humphrey, J.A.C., Carnet, I., and Levy, A.V., (1981), "Experimental measurement of accelerated erosion in slurry pot tester", Wear, 68, pp. 289-303.

[179] Turenne, S., Fiset, M., and Mansounave, J., (1989), "The effect of sand concentration on the erosion of materials by a slurry jet", Wear, 133, pp. 95-106.

[180] Vieira, R.E., Mansouri, A., McLaury, B.S., and Shirazi, S.A., (2016), "Experimental and computational study of erosion in elbows due to sand particles in air flow", Powder Technology, 288, pp. 339-353.

[181] Vocaldo, J.J., Koo, J.K., and Prang, A.J., (1974), ''Performance of centrifugal pumps in slurry service'', Hydrotransport 3, BHRA Fluid Engineering, Colorado, Paper J2.

[182] Voorde J.V., Dick, E., Vierendeels, J., and Serbmyns, S., (2002), "Performance prediction of centrifugal pumps with steady and unsteady CFD-methods", Advances in Fluid Mechanics IV-WIT Press, pp. 559-568.

[183] Walker, C.I., and Goulas, A., (1984), ‘‘Performance characteristics of centrifugal pumps when handling non-Newtonian homogeneous slurries’’, Proceedings of the Institution of Mechanical Engineers, 198 A(1), pp. 41-49.
[184] Walker, C.I., Wells, P.J., and Bodkin, G.C., (1994), “The effect of flow rate and solid particle size on the wear of centrifugal slurry pumps”, American Society of Mechanical Engineers, New York, United States.
[185] Walker, C.I., and Robbie, P., (2013), “Comparison of some laboratory wear tests and field wear in slurry pumps”, Wear, 302, pp. 1026-1034.
[186] Wang, P.W., Zhao, J., Zou, W.J., and Hu, S.G., (2012), “Experimental study and numerical simulation of the solid-phase particles influence on outside characteristics of slurry pump”, In IOP Conference Series: Earth and Environmental Science, 15(6), p. 062057.
[187] Wang, Z., and Qian, Z., (2017), “Effects of concentration and size of silt particles on the performance of a double-suction centrifugal pump”, Energy, 123, pp. 36-46.
[188] Want, F.M., (1980), “Centrifugal slurry pump wear-plant experience”, Hydrotransport 7, BHRA Fluid Engineering, Sendai, Japan, Paper H1.
[189] Wasp, E.J., Kenny, J.P., and Gandhi, R.L, (1977), “Solid-liquid flow slurry pipeline transportation”, Series in Bulk Solids Handling, 1, Trans Tech Publications, New York.
[190] Weinsink, H., and Elwenspoek, M.C., (2002), “A closer look at the ductile-brittle transition in solid particle erosion”, Wear, 253(9-10), pp. 1035-1043.
[191] Widenroth, W., (1970), “The influence of sand and gravel on the characteristics of centrifugal pumps, some aspects of wear in hydraulic transportation installations’’, Hydrotransport 1, BHRA Fluid Engineering, Warwick, UK, Paper E1.
[192] Widenroth, W., (1978), “Experimental work on the transportation of solid-liquid mixtures through pipelines and centrifugal pumps”, Hydrotransport 5, BHRA Fluid Engineering, Hannover(Germany), Paper A2.
[193] Widenroth, W., (1984), “Wear tests executed with a 125 mm I.D. loop and a model dredge pump”, Hydrotransport 9, BHRA Fluid Engineering, Rome(Italy), Paper G2.
[194] Widenroth, W., (1993), “The evaluation of the wear distribution of a dismountable impeller in a model-dredge pump”, Coal & Slurry Technology Association, Washington DC, United States.
[195] Wilfley, (2006), “Technical handbook”, A.R. Wilfley & Sons, Inc., Denver, Colorado.
[196] Willies, D.J., and Truscott, G.F., (1978), “Solids-handling Pumps: a survey of current practice, problems and developments”, Hydrotransport 5, BHRA Fluid Engineering, Hannover, Germany, Paper F6.
[197] Wilson, G., (1973), “Design aspects of centrifugal pumps for abrasive slurries”, Cim Bulletin, 66(733), pp. 91-102.
[198] Wilson, G., (1987), “The effects of slurries on centrifugal pump performance”, Proceedings of the Fourth International Pump Symposium, Texas A&M University, Houston, Texas, U.S.A., pp. 35-54.
[199] Wilson, K.C., Addie, G.R., and Clift, R., (1992), “Slurry transport using centrifugal pumps”, Elsevier Science, New York, United States.
[200] Wood, R.J.K., Jones, T.F., Ganeshalingam, J., and Miles, N.J., (2004), “Comparison of predicted and experimental erosion estimates in slurry ducts”, Wear, 256, pp. 937-947.

[201] Xie, Y., Jiang, J., Tufa, K.Y., and Yick, S., (2015), "Wear resistance of materials used for slurry transport", Wear, 332-333, pp. 1104-1110.
[202] Yao, J., Zhou, F., Zhao, Y., Yin, H., Guo, Q., and Li, N., (2015), "Experimental investigation of erosion of stainless steel by liquid-solid flow jet impingement", Procedia Engineering, 102, pp. 1083-1091.
[203] Yassine, K.C., Hammoud, A.H., and Khalil, M.F., (2010), "Experimental investigation for centrifugal slurry pump performance", In Proceedings of the 10th International Congress of Fluid Dynamics, pp. 16-19.
[204] Yildizli, K., Karamis, M.B., and Nair, F., (2006), "Erosion mechanisms of nodular and gray cast irons at different impact angles", Wear, 261, pp. 622-633.
[205] Yoganandh, J., Natarajan, S., and Kumaresh Babu, S.P., (2013), "Erosion behaviour of WC–Co–Cr thermal spray coated grey cast iron under mining environment", Transactions of the Indian Institute of Metals, 66(4), pp. 437-443.
[206] Yoganandh, J., Natarajan, S., and Kumaresh Babu, S.P., (2015), "Erosive wear behavior of high-alloy cast iron and duplex stainless steel under mining conditions", Journal of Materials Engineering and Performance, 24(9), pp. 3588-3598.
[207] Yuchuan, W., Lei, T., Baoshan, Z., ShuLiang, C., and Binbin, W., (2015), "Numerical investigation of influence of inlet guide vanes on unsteady flow in a centrifugal pump", Proceedings of the Institute of Mechanical Engineering Part C: Journal of Mechanical Engineering Science, 229(18), pp. 3405-3416.
[208] Zeng, L., Zhang, G.A., and Guo, X.P., (2014), "Erosion-corrosion at different locations of X65 carbon steel elbow", Corrosion Science, 85, pp. 318-330.
[209] Zhang, N., Yang, M., Gao, B., Li, Z., and Ni, D., (2016), "Investigation of rotor-stator interaction and flow unsteadiness in a low specific speed centrifugal pump", Journal of Mechanical Engineering, 62(1), pp. 21-31.
[210] Zhang, Y., Reuterfors, E.P., McLaury, B.S., Shirazi, S.A., and Rybicki, E.F., (2007), "Comparison of computed and measured particle velocities and erosion in water and air flows", Wear, 263, pp. 330-338.
[211] Zhang, Y., Li, Y., Cui, B., Zhu, Z., and Dou, H., (2013), "Numerical simulation and analysis of solid-liquid two-phase flow in centrifugal pump", Chinese Journal of Mechanical Engineering, 26(1), pp. 53-60.
[212] Zhao, B.J., Huang, Z.F., Chen, H.L., and Hou, D.H., (2012), "Numerical investigation of solid-liquid two phase flow in a non-clogging centrifugal pump at off-design conditions", In IOP Conference Series: Earth and Environmental Science, 15, p. 062020
[213] Zhong, Y., and Minemura, K., (1996), "Measurement of erosion due to particle impingement and numerical prediction of wear in pump casing", Wear, 199(1), pp. 36-44.
[214] Zhou, W., Zhao, Z., Lee, T.S., and Winoto, S.H., (2003), "Investigation of flow through centrifugal pump impellers using computational fluid dynamics", International Journal of Rotating Machinery, 9(1), pp. 49-61.
[215] Zikanov, O., (2010), "Essential computational fluid dynamics", John Wiley & Sons, Inc. Hoboken, New Jersey, United States.
[216] Zu, J.B., Hutchings, I.M., and Burstein, G.T., (1990), "Design of slurry erosion test rig", Wear, 140, pp. 331-344.

LIST OF PUBLICATIONS

International Journal

1. Rahul Tarodiya and Bhupendra K. Gandhi, Hydraulic Performance and Erosive Wear of Centrifugal Slurry Pumps - A review, Powder Technology, 305 (2017) 27-38.
2. Rahul Tarodiya and Bhupendra K. Gandhi, Experimental Investigation on Slurry Erosion Behavior of 304L Steel, Grey Cast Iron, and High Chromium White Cast Iron, ASME Journal of Tribology, 141 (2019) 091602.
3. Rahul Tarodiya and Bhupendra K. Gandhi, Experimental Investigation of Centrifugal Slurry Pump Casing Wear Handling Solid-Liquid Mixtures, Wear, 434-435 (2019) 202972.
4. Rahul Tarodiya and Bhupendra K. Gandhi, Numerical Simulation of A Centrifugal Slurry Pump Handling Solid-Liquid Mixture: Effect of Solids on Flow Field and Performance, Journal of Advanced Powder Technology, 30 (2019) 2225-2239.

International Conference

1. Rahul Tarodiya and Bhupendra K. Gandhi, Numerical Prediction of Casing Wear of a Centrifugal Slurry Pump Handling Solid-Liquid Mixture, 7th International conference of Fluid Mechanics and Fluid Power, IIT Bombay, 83, 2018.
2. Shubham Sharma, Rahul Tarodiya, and Bhupendra K. Gandhi, Experimental Investigation of Flow Field of a Pot Tester due to Propeller Rotation, 7th International conference of Fluid Mechanics and Fluid Power, IIT Bombay, 487, 2018.
3. Rahul Tarodiya and Bhupendra K. Gandhi, Effect of Propeller Off-Bottom Clearance and Size on Suspension of Sand Particles in a Cylindrical Tank: Application to Slurry Pot Tester, 6th International conference of Fluid Mechanics and Fluid Power, MNNIT Allahabad, 82, 2016.